Experimental investigations on turbulence and transport in tokamak plasmas

Laure Vermare

Mémoire en vue d'obtenir l'Habilitation à Diriger des Recherches

Experimental investigations on turbulence and transport in tokamak plasmas

Présenté par

Laure VERMARE
Laboratoire de Physique des Plasmas
CNRS, Ecole Polytechnique

Soutenu le 10/04/2018

à l' Université SORBONNE UNIVERSITE

Jury :

Mme. Teresa Estrada (Professeur, CIEMAT, Espagne)	*Rapporteur*
M. Evegeniy Gusakov (Professeur, Ioffe Institute, Russie)	*Rapporteur*
M. Etienne Gravier (Professeur, Institut Jean Lamour, Nancy)	*Rapporteur*
M. Bruno Després (Professeur, Lab. Jacques-Louis LIONS, Paris)	*Président*
M. Ambrogio Fasoli (Professeur, Swiss Plasma Center, Suisse)	*Examinateur*
M. Yann Camenen (Chargé de Recherche CNRS, PIIM, Marseille)	*Examinateur*
M. Xavier Garbet (Professeur,IRFM, CEA Cadarache)	*Examinateur*

Table des matières

List of Symbols and Acronyms

Acronyms

DBS	Doppler Back-Scattering
ECRH	Electron Cyclotron Resonnance Heating
ETG	Electron Temperature Gradient
GAMs	Geodesic Acoustic Modes
HFS	High Field Side
ICRH	Ion Cyclotron Resonnance Heating
ITG	Ion Temperature Gradient
KBM	Kinetic Ballooning Mode
LFS	Low Field Side
LH	Low Hybrid
NBI	Neutral Beam Injection
SOL	Scrape Of Layer
TEM	Trapped Electrons Mode
UHRS	Upper Hybrid Resonance Scattering
ZFs	Zonal Flows

Greek symbols

β	Ratio of the kinetic pressure over the magnetic pressure
β_c	Critical β value for the onset of electromagnetic instabilities
γ	Linear growth rate of a given instability
δ	Plasma triangularity
δn	Density fluctuations
ϵ	Aspect ratio of the tokamak (minor radius over the major radius)
η	Plasma resistivity
κ	Plasma elongation
θ	Poloidal angle
φ	Toroidal angle
$\nu_{i,e}$	Ion, Electron collisionality
ν^*	Collisionality normalized to the trapped ion bounce frequency
$\rho_{i,e}$	Ion, Electron gyroradius
ρ_s	Sound gyroradius
$\rho_\perp$	Ion or Sound gyroradius considering the perpendicular velocity
ρ^*	Gyroradius normalized to the minor radius of the plasma

τ_B	Bohm time
τ_E	Energy confinement time
τ_{th}	Thermal energy confinement time
Φ	Electrostatic potential
χ_B	Bohm diffusivity
$\chi_{i,e}$	Ion, Electron heat diffusivity
ψ	Poloidal flux
ω_{bi}	Trapped ion bounce angular frequency
Ω_{GAM}	Geodesic Acoustic Mode angular frequency
Ω_0	Cyclotron angular frequency at the magnetic axis

Symbols

a	Minor plasma radius
B	Total magnetic field
B_0	Toroidal magnetic field on axis
B_φ	Toroidal magnetic field
B_θ	Poloidal magnetic field
C_s	Ion sound speed
$E(k)$	Energy spectrum
E_r	Radial Electric Field
f_{GAM}	Geodesic Acoustic Mode frequency
k	Wavenumber of density fluctuations wavenumber generally expressed in cm^{-1} or normalized to gyroradius $k\rho$
$k_\perp$	Perpendicular wavenumber of density fluctuations (or more precisely density fluctuations wavenumber in the binormal direction that is perpendicular both to the magnetic field line and to the radial direction on the magnetic surface)
k_i	Wavenumber of incident probing wave
k_f	Wavenumber of the selected density fluctuations
k_θ	Poloidal wavenumber of density fluctuations
k_r	Radial wavenumber of density fluctuations
m	Poloidal mode number (number of periods in one poloidal circumference)
n	Toroidal mode number (number of periods in one toroidal circumference)
$n_{i,e}$	Ion, Electron density (generally expressed as m^{-3})
P_{add}	Additional (external) heating power (generally expressed as MW)
P_{fus}	Power generated by fusion reactions
P_{heat}	Total heating power (generally expressed as MW)
P_{OH}	Ohmic heating power (generally expressed as MW)
$p_{i,e}$	Ion, Electron kinetic pressure ($P_{i,e}$ corresponds to the pressure tensor)
q	Safety factor
R	Major radius of the tokamak
s	Magnetic shear
$S(k)$	Wavenumber spectrum of density fluctuations intensity
$T_{i,e}$	Temperature of ions, electron (generally expressed in keV)
$v_\perp$	Perpendicular velocity of density fluctuation
$v_{E\times B}$	$E \times B$ velocity
v_ϕ	Phase velocity of the selected density fluctuation
v_φ	Toroidal plasma velocity
v_θ	Poloidal plasma velocity
W	Total plasma energy content
W_{th}	Thermal plasma energy
Z_{eff}	Effective charge of the plasma ions

Magnetic confinement devices (mentionned in this report)

ATC	Adiabatic Toroidal Compressor Tokamak Princeton, USA (1972-)
AUG	ASDEX-Upgrade Tokamak Max-Planck Institut fü Plasmaphysik, Garching, Germany (1991)
DIII-D	Doublet-III Tokamak, General Atomic Company, San Diego, USA (1986)
FT-2	Ioffe, St Petersburg, Russian Federation (1979)
JET	Joint Europeen Tokamak installed in Culham, UK (1983)
JT-60	JAERI Tokamak-60, Naka Fusion Institute, Japan (1985-1989)
JT-60U	JT-60 Upgrade, Naka Fusion Institute, Japan (1991-2010)
MAST	Mega-Amp Spherical Tokamak, UKEAEA Culham Science Centre, UK (2000)
TCV	Tokamak (Tokamak à Configuration Variable), Centre de Recherches en Physique des Plasmas, Switzerland (1992)
TEXT	TEXT Tokamak, University of Texs, Austin, USA (1981)
TEXTOR	Tokamak EXperiment for Technology Oriented Research, Forschungszentrum, Jülich, Germany (1983-2013)
TJ-II	Flexible Heliac device, CIEMAT, Spain (1997)
Tore Supra	Tore Supra Tokamak, CEA Cadarache, France (1988)

1. Context

The principle of magnetic fusion is to use strong magnetic fields to confine a Deuterium-Tritium (DT) plasma and to heat its ions until a state in which enough nuclear fusion reactions occur to gain energy. In a Tokamak, the plasma is maintained in a toroidal vacuum vessel and confined through a strong toroidal magnetic field (several Teslas) generated by a set of magnetic coils and a smaller poloidal magnetic field, generated by a toroidal plasma current induced in the plasma by transformer action or by direct drive. The state, in which the plasma temperature is maintained by fusion reactions (i.e. α-particle heating), against the energy losses, is called ignition. In order to achieve this state, the triple product of the ion temperature T_i, the plasma density n and the *energy confinement time*, labelled τ_E (i.e. the ratio of global plasma energy content, W, and the applied total heating power P_{heat}), should exceed a certain minimum value. In toroidal geometry, charged particles flow more or less freely in the direction of the field lines while making a cyclotron motion around them. The tokamak geometry is such that particle orbits are well confined including their drifts. One obvious way the particles could be lost is by jumping from one field line to another through collisions with other particles. Neoclassical theory, which describes transport of particles, momentum and energy based on collisions, taking into account the particles trapped in the inhomogeneities of the magnetic field, predicts, in typical tokamak conditions and minor radius $a = 1m$, a global energy confinement time that should be in the range of $\tau_{E,neo} = [10 - 100]s$. For DT fusion reactions, the triple product $nT_i\tau_E$ is minimal for an ion temperature of around $10keV$. The plasma temperature reached by the ohmic-heating power P_{OH}, coming from the current that is induced inside the plasma, is limited, since the resistivity decreases proportionally with the temperature as $T^{-3/2}$. Thus, to increase the plasma temperature, two additional heating methods are commonly used : the injection of a beam of energetic neutrals (i.e. Neautral Beam Injection or NBI) and/or the resonant absorption of radio frequency (RF) electromagnetic waves. The three principal RF heating mechanisms involve waves at frequency around the ion cyclotron frequency (ICRH), the electron cyclotron frequency (ECRH), and the lower hybrid frequency (LH). These heating schemes allow the plasma to reach required temperatures.

However, the performance of fusion plasmas (i.e the energy confinement time) is limited by cross-field transport. This transport of energy (heat and particles), which typically exceeds neoclassical prediction by an order of magnitude or more, is usually attributed to turbulence. In fact, due to the strong gradients of density and temperature imposed by the magnetic confinement, turbulence at spatial scales that are small compared to the mean-free-path of plasma particles develops inside the plasma. This turbulence generates a radial transport of heat, particles and momentum. This so called *anomalous transport*, causes the core plasma to loose its energy and particles, orders of magnitude more rapidly than the base transport due to collisions. The tokamak presents a large variety of instabilities. Among them, the main micro-instabilities that underlie turbulent transport in the

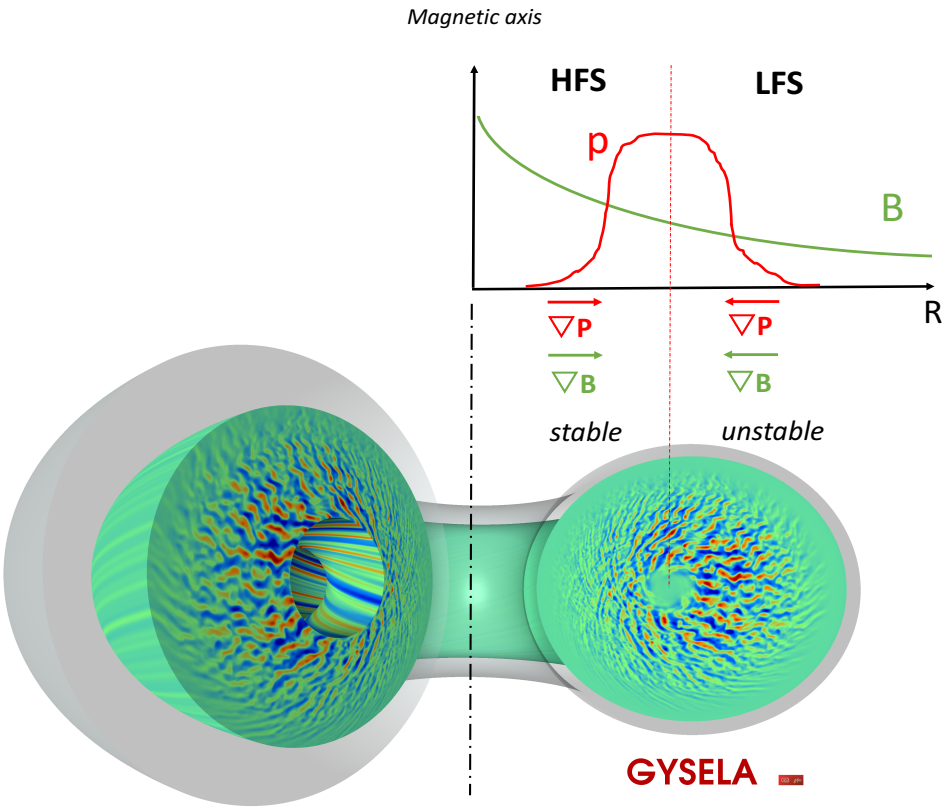

FIGURE 1.1. – Schematic illustration of the stability of a tokamak plasma with respect to the interchange instability. The magnetic field decreases with the major radius of the tokamak R, creating a High Field Side (HFS) and a Low Field Side (LFS) of the plasma, in which the magnetic field gradient and the pressure gradient are respectively co-aligned and counter-aligned. The bottom figure shows the balloonned fluctuations of the electrostatic potential from gyrokinetic simulation performed using GYSELA code

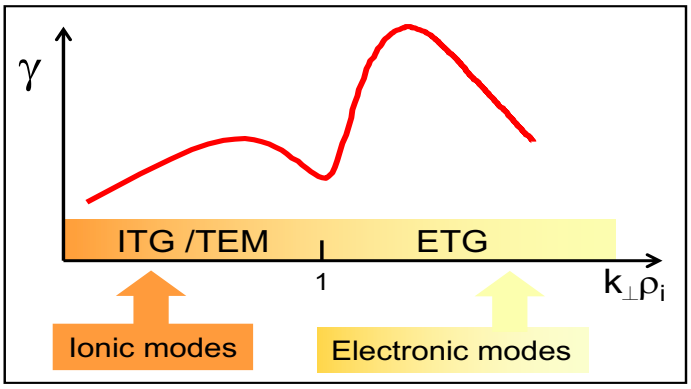

FIGURE 1.2. – Growth rate of the main micro-instalibities present in the confined tokamak plasmas as a function of the perpendicular wavenumber normalized to the inverse of Larmor radius ρ_i

core of fusion plasmas belong, in essence, to the family of interchange modes which are unstable when the gradient of magnetic field is aligned with the gradient of equilibrium pressure. In the tokamak configuration, this situation occurs on the low field side of the plasma (i.e on the external side of the torus since the toroidal magnetic field decreases with the major radius) while the interchange is locally stable on the high field side. Since field lines connect locally unstable to locally stable regions and modes tend to be aligned along the equilibrium magnetic field (due to the strong magnetic field), such modes belong to a class of *ballooning* modes (i.e with an amplitude varying in the poloidal direction). Figure1.1 illustrates the geometry of a tokamak with stable and unstable areas as well as the ballooning character of micro-turbulence that develops inside the plasma core via results from first principles numerical simulations of turbulence performed using gyrokinetic description of the plasma in which the fast cyclotronic motion of charged particles is averaged reducing the system from 6 dimensions (3 in positions and 3 in velocity) to 5 dimensions. These micro-instabilities, which are driven unstable by density and temperature gradients above a certain threshold, extend over a large range of spatial scales. As presented in Figure 1.2, at spatial scales of the order of the ion Larmor radius, typically $\rho_i = [1mm - 1cm]$, the main instabilities are the modes driven by the Ion Temperature Gradient (ITG) and Trapped Electron Modes (TEM), where the latter is driven by the electrons trapped in the low magnetic field side of the machine. At smaller scales (i.e. larger wavenumbers), there are modes driven by the Electron Temperature Gradient (ETG) with spatial scales around the electron Larmor radius (typically $\rho_e = [10\mu m - 100\mu m]$).

Non-linearly, turbulence self-organizes through energy transfer between different spatial scales. For a given spatial scale injection, related to a linear instability, the energy will be transferred to both smaller and larger scales to cover a wider spatial scale range, leading to a saturated state with a specific wavenumber spectrum. Among these mechanisms of non-linear transfer of energy, inverse cascade plays an important role and generates large-scale

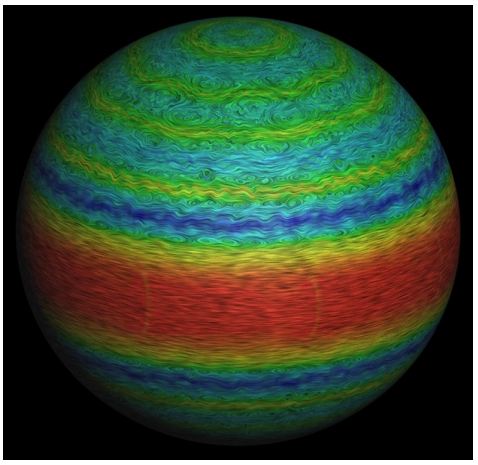

FIGURE 1.3. – Jupiter's zonal flows

structures extended in the radial direction that lead to a rapid increase of the ion heat transport. In addition, it is found experimentally that plasma turbulence self-organizes through nonlinear development of oscillating large-scale flows [1] that back-react on the small-scale fluctuations, which generate them, thus reducing the ion thermal transport. This picture is also supported by simulations [2]. Among these flows, zonal flows, which are similar to the flow structures observed in Jupiter's atmosphere (see Figure 1.3), are uniform along the toroidal and poloidal directions but strongly sheared in the radial direction in tokamaks. Closely related to these stationary zonal flows (ZFs) are the geodesic acoustic modes (GAMs), which are oscillations of the poloidal flow at the geodesic acoustic frequency. These modes are similarly turbulence-generated and appear in the form of a coupling between a ZF and an axisymmetric (m = 1) pressure sideband mode due to geodesic curvature.

The strong velocity shear associated with these large-scale flows (ZFs and GAMs), tends to decorrelate turbulent structures and in particular the radially elongated ones that are responsible for the turbulent transport (for a complete review see [3]). In Figure 1.4, this effect is illustrated via results from gyrokinetic simulations with the comparison of two cases : a case without ZF (left figure) in which turbulent structures are strongly radially extended and a case with ZF (right figure) in which the radial extend of as well as the intensity of turbulent stuctures are significantly reduced. The nonlinear decorrelation effect comes from the decrease of the radial correlation length, decrease of the fluctuation intensity as well as the change in the phase between density, temperature and potential fluctuations, as predicted initially by analytical theory [4]. This effect is general to any sheared flows that can be generated by turbulence (like ZFs and GAMs) or coming from the neoclassical profile of the radial electric field. The most remarkable experimental example of the turbulence reduction by velocity shear is the edge barrier that develops in the so-called H-mode (for High confinement) regime [5] that is accessed routinely on a wide variety of machines. The presence of this barrier at the edge, associated with a local increase of sheared flow and a reduction of the turbulence level allows higher density and temperature values in the plasma core than the standard L-mode regime (for "Low" confinement). When the barrier is well established (i.e in H-mode regime), there is a growing body of evidence

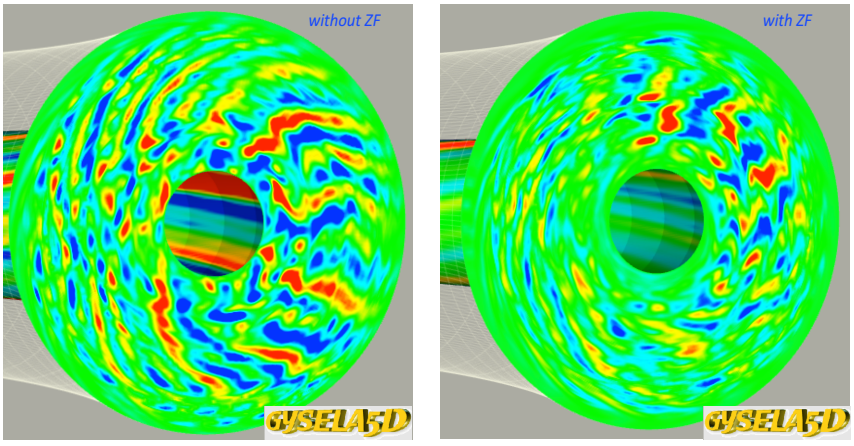

FIGURE 1.4. – Turbulent transport reduction by velocity shearing

from experiments showing that the mean flow responsible for the barrier is governed by force balance and well described by neoclassical theory [6, 7]. In essence, the neoclassical physics naturally forces the mean poloidal flow to relax towards a strongly sheared profile at the tokamak edge, resulting in strong gradients of both neoclassical coefficients and of pressure in the pedestal region. However the entire dynamical process and the time sequence of the formation of this barrier are not completely understood yet and the role of turbulence generated flows and their interaction with turbulence itself are commonly invoked as one of the key phenomena in the transition and the establishment of the barrier [8, 9]. The respective roles of neoclassical friction and turbulence generated flows remains an active and important subject of research. For example, it has been shown that accounting for the effect of collisional friction between trapped and passing particles on the radial electric field allows for the spontaneous formation of a transport barrier in flux-driven three-dimensional fluid simulations of resistive balooning turbulence [10]. An analysis of the roles of zonal-flows and force balance during the transition, shows that zonal flows provide temporary quenching of the turbulence via non-linear coupling, allowing for the mean flow to grow and form the barrier.

For future fusion reactors, prediction of confinement and scenario development are essential. Both require an excellent description of turbulent plasmas and therefore an improvement of our understanding on turbulent transport, its dependence on plasma parameters, its spatial scales as well as an improvement in our understanding on turbulence self-regulation mechanisms. In the magnetic fusion community, these subjects are addressed through various approaches from experiments to theory, from steering of the machine to fundamental understanding of precise physical mechanisms.

The approach I chose in my research work presented in this manuscript, is an experimental approach designed to highlight specific physical mechanisms invoked in turbulent transport to be compared with theory, via simple models and with high performance numerical simulations of plasma turbulence, performed mainly with gyrokinetic codes.

This report summarizes my main research contributions performed from the end of my

PhD and is articulated around six selected publications covering three research areas. In the first chapter, my post-doctoral research work on confinement and heat transport and their dependences with the parameter β in the ASDEX Upgrade tokamak is presented. The approach used, which consists of performing dedicated dimensionless scans, is particularly interesting in view of improving our understanding of some physical mechanisms, notably via comparisons with theory and numerical simulations. For this reason, this approach has been kept during a large part of my research work. Following this transport study, I will present my contribution on spatial scales repartition of turbulence (Chapter 4) and fluctuating or equilibrium flows (Chapter 5). The work presented in these two chapters are based on density fluctuations measurements using a Doppler Backscattering System that was installed on the Tore Supra tokamak. Some possible perspectives of my research contributions are proposed and discussed in the last chapter.

2. List of selected publications

Study of the β dependence of confinement and heat transport in ASDEX Upgrade

L. Vermare, F. Ryter, C. Angioni, A.G. Peeters, J. Stober, R. Bilato, L.D. Horton, B. Kurzan, C.F. Maggi, H. Meister, J. Schirmer, G. Tardini and the ASDEX Upgrade Team
Nuclear Fusion, volume 47, number 5, page 490, 2007

β dependence of micro-instabilities using linear gyrokinetic simulations

L. Vermare, C. Angioni, A. Bottino, A.G. Peeters and the ASDEX Upgrade Team
Conference Series, volume 123, number 1, page 012040, 2008

Wavenumber spectrum of micro-turbulence in tokamak plasmas

L. Vermare, Ö. D. Gürcan, P. Hennequin, C. Honoré, X. Garbet, J.C. Giacalone, R. Sabot, F. Clairet and the Tore Supra Team
Comptes Rendus Physique, volume 12, number 2, page 115 , 2011

Impact of collisionality on fluctuation characteristics of micro-turbulence

L. Vermare, P. Hennequin, Ö. D. Gürcan, C Bourdelle, F Clairet, X. Garbet and R. Sabot and the Tore Supra Team
Physics of Plasmas, volume 18, number 1, page 012306, 2011

Detection of Geodesic Acoustic Mode oscillations, using MUltiple Signal Classification analysis of Doppler backscattering signal on Tore Supra

L. Vermare, P. Hennequin, Ö. D. Gürcan and the Tore Supra Team
Nuclear Fusion, volume 52, number 6, page 063008, 2012

Poloidal asymmetries of flows in the Tore Supra tokamak

L. Vermare, P. Hennequin, Ö. D. Gürcan, X. Garbet, C. Honoré, F. Clairet, J.C. Giacalone, P. Morel, A.Storelli and the Tore Supra Team
Physics of Plasmas volume 25, number 2, page 020704, 2018

3. Dimensionless approach and dedicated scan experiments

One of the main experimental approaches that are used in the fusion community to characterize turbulence and transport issues while avoiding detailed physical mechanisms, is to determine the dependence of the global energy confinement time with respect to relevant plasma parameters. The basic approach consists of using empirical scaling laws which describe the global confinement time as a function of operating parameters such as the density, the plasma current, the additional power etc. For example, for H-mode plasmas, the scaling law the most commonly used is given in [11] and is written as :

$$\tau_{E,th}^{ELMy} = 0.0562 I_p^{0.93} B_0^{0.15} P_{LTH}^{-0.69} n^{0.41} M^{0.19} R^{1.97} \epsilon^{0.58} \kappa_a^{0.78} \tag{3.1}$$

in which the confinement time $\tau_{E,th} = W_{th}/P_{LTH}$ is in s and $P_{LTH} = P_L - P_{Floss}$ is the loss power corrected for charge exchange and unconfined orbit losses in MW, I_p is the plasma current in MA, B_0 is the toroidal magnetic field on geometrical axis in T, n is the central line average electron density in $10^{19} m^{-3}$, M is the effective atomic mass in AMU, R is the geometrical major radius of the tokamak in m, $\epsilon = a/R$ is the inverse aspect ratio (a is the minor radius) and $\kappa_a = area/(\pi a^2)$ is the elongation. This approach is simple, practical and allows predictions for the performance of the future devices such as ITER. However, while thinking in term of engineering parameters is convenient to design and operate experiments, the understanding in terms of physical processes involved in the turbulent transport is rather limited. Another approach consists on converting these engineering parameters in terms of dimensionless parameters.

The analysis of plasma energy transport in terms of dimensionless parameters [12, 13, 14] is a powerful technique widely used in the study of fusion plasmas. The idea is to use a reduced set of relevant dimensionless parameters, naturally built from the equations governing the system, instead of the "engineering" parameters. If the energy transport is dominated by plasma physics (i.e. does not depend on atomic physics), it has been shown that using the scale invariance approach, the normalized energy confinement time can be described as :

$$B_0 \tau_{th} = F(\rho^*, \beta, \nu*, q, \frac{a}{R}, \frac{m_e}{m_i}, \frac{T_e}{T_i}, Z_{eff}, \kappa, \delta, M_{rot}, ...) \tag{3.2}$$

where B_0 is the toroidal magnetic field on axis, τ_{th} is the thermal energy confinement time, $\rho* = \rho_i/a$ is the normalized ion Larmor radius, $\beta = 2\mu_0 p/B^2$ is the plasma pressure normalized to the magnetic pressure, $\nu^* = \nu_i/(\epsilon\omega_{bi})$ is the ratio of ion collision frequency to trapped ion bounce frequency $\omega_{bi} = v_{\perp i}/qR(r/2R)^{1/2}$, q is the cylindrical safety factor, T_i/T_e is the ion to electron temperature ratio, Z_{eff} is the effective charge of the plasma

ions, κ is the plasma elongation, δ is the plasma triangularity and $M_{rot} = V_{tor}/\sqrt{T_i/m_i}$ is the toroidal Mach number.

One can use a reduced set of dimensionless parameters composed of ρ^*, ν^* and β. In this case, the translation for the IPB98(y,2)(eq. 3.1), for H-mode plasmas gives :

$$B\tau_{th}^{98y2} \propto \rho^{*-2.7}\beta^{-0.90}\nu^{*-0.01}q^{-3.0} \tag{3.3}$$

Note that all these dimensionless parameters are normalized using a relevant quantity. The energy confinement time is generally normalized to the cyclotron frequency at the magnetic axis $\Omega = \frac{eB_0}{m}$ and is expressed as $B_0\tau_{th}$. This is coming from the normalization using the Bohm time $\tau_B \equiv a^2/\chi_B$ where $\chi_B = T/eB_0$ is the Bohm diffusivity.

These parameters are independently related to different physical aspects of the plasma dynamics. The ρ^* dependence gives informations on the scale of turbulent structures. Considering diffusive transport and taking the turbulence scale equal to ρ^* gives the so called gyro-Bohm scaling (while if turbulent structure is independant of ρ^*, the same approach gives a Bohm scaling). The normalized collisionality, ν^*, is related to collisional processes that will be discussed in the next chapter. The β, which is the ratio of the kinetic pressure over the magnetic pressure, mesures the significance of the electromagnetic component of the turbulence.

Therefore, studying separately the effect of these dimensionless quantities on the energy confinement and transport, provide indications about the relative weight of each mechanisms as compared to others. However, the accuracy of such an approach is largely questionable due to the correlation between engineering parameters. A more powerful approach is to perform dedicated dimensionless scan experiments. The principle of dimensionless scan is to vary one dimensionless parameters from one discharge to another keeping the others constant. Ideally, all dimensionless parameters but one should be kept constant on the entire radial profile. While this requirement is extremely demanding, it offers a powerful background for precise transport and turbulence studies and has been largely used in the community to verify the dependences exhibited in these empirical scaling laws.

Considering the effect of β on turbulent transport should provide indications about the nature of turbulence and in particular gives information about the role and weight of electromagnetic turbulence. For a long time the main instabilities responsible for turbulent transport in the core of fusion plasmas have been described using electrostatic approximation but this strong hypothesis should be constantly validated. In addition, because fusion power production P_{fus} increases with increasing β, there is large economic interest to operate reactors at β as high as possible. A robust knowledge of the dependence of the energy confinement time with β is therefore necessary to predict performances in future devices.

From a theoretical point of view, in the case of strongly unstable ITG mode (e.g. CYCLONE base case), linear electromagnetic simulations commonly show a stabilization of ITG modes and a destabilization of kinetic balooning modes (KBM) when increasing β. Thus, above a certain value of β, KBM prevails, leading to a strong β dependence of turbulent transport [15, 16, 17]. The β value necessary to destabilize KBM, is found to vary from the ideal MHD β limit [16] to half of this value [15] depending the approximations that are employed and generally remains above the experimental β range. Note that in the experiments, the β limit, labelled β_c is generally avoided and that all experimental

investigations on the β dependence range below this β_c value. In experiments, a weak improvement of the confinement time with β is expected until the critical β_c value.

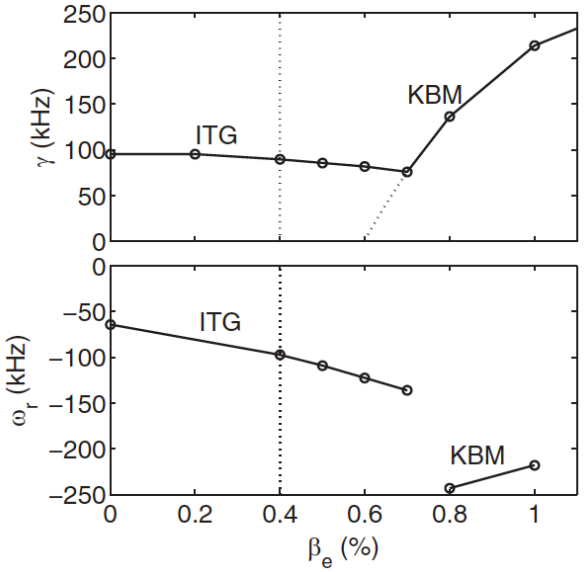

FIGURE 3.1. – β dependence of the linear growth rate (top panel) and real frequency (bottom panel) of $n = 20$ instability in the pedestal top region in GTC simulation. Vertical dotted line indicates the experimental value of β. Figure from [18]

In addition to these numerical results for CYCLONE base case, an electromagnetic stabilization of ITG, related to non-linear effects and fast ions, is observed in simulations with plasma conditions corresponding to JET discharges [19, 20]. The electromagnetic destabilization seems to be effective only at a ratio of β/β_c large enough [19].

However, concerning the experimentally observed β dependence, it is interesting to note that both scaling laws, for L-mode plasmas as well as for H-mode plasmas (eq.3.1) predict a clear and strong degradation with increasing β which is not beneficial for reactor perspectives. On the contrary, dedicated experiments have been performed in 2003 both in the DIII-D tokamak and the JET tokamak [21, 22] showing no β dependence of energy confinement or heat transport. Therefore, contradictions also exist between the empirical scaling laws and the results of dedicated experiments. The latter being, in principle, more reliable. In 2005, a new experiment performed in JT-60 [23] showed a moderate degradation of performances increasing β reinforcing the confusion on this question. This situation motivates to perform dedicated experiments in AUG.

The publication included next [Publication 1] presents the first dedicated β scan experiments performed in AUG. It found that the global confinement time strongly decreases while the local heat diffusivity significantly increases between $\rho = [0.5 - 0.75]$ with increasing β.

IOP Publishing and International Atomic Energy Agency Nuclear Fusion
Nucl. Fusion **47** (2007) 490–497 doi:10.1088/0029-5515/47/5/014

Study of the β dependence of confinement and heat transport in ASDEX Upgrade

L. Vermare, F. Ryter, C. Angioni, A.G. Peeters, J. Stober, R. Bilato, L.D. Horton, B. Kurzan, C.F. Maggi, H. Meister, J. Schirmer, G. Tardini and the ASDEX Upgrade Team

Max-Planck-Institut für Plasmaphysik, EURATOM Association, Garching D-85748, Germany

Received 15 December 2006, accepted for publication 12 April 2007
Published 8 May 2007
Online at stacks.iop.org/NF/47/490

Abstract
First β scan experiments have been made in ASDEX Upgrade in H-mode plasmas with type-I ELMs. Two sets of discharges, performed in different density ranges, scan β between $\beta_N = (1.4–2.2)$ and $\beta_N = (1.4–2)$. Global analysis of these dedicated experiments exhibits a strong unfavourable β scaling as $B\tau_{th} \propto \beta^{-0.9}$. This tendency is confirmed by a local analysis which shows an increase in the thermal heat diffusivity with increasing β as $\chi_{eff}/B \propto \beta^{0.65}$. These results are discussed and compared with studies made in DIII-D, JET and JT-60U.

PACS numbers: 52.55, Fa, 52.25, Fi, 28.52s

(Some figures in this article are in colour only in the electronic version)

1. Introduction

Both experimental and theoretical studies show that small scale plasma fluctuations (micro-turbulence), arising from instabilities driven by temperature and density gradients, can generate high levels of heat and particle transport, thus limiting fusion device performance. The understanding of the micro-turbulence induced transport and, consequently, the prediction of the confinement time plays a crucial role in determining the feasibility of a thermonuclear fusion reactor. The analysis of plasma energy transport in terms of dimensionless parameters [1, 2] is a powerful technique widely used in order to extrapolate from present day devices to next step experiments, like ITER. In addition to this, the experimental scaling of confinement time and local transport as a function of physically relevant quantities can provide useful insight about the nature of the instabilities responsible for the anomalous transport. This is particularly important for validating the different proposed theories of turbulent transport in tokamak plasmas.

Using the scale invariance approach it has been shown [2] that if the energy transport is dominated by plasma physics (i.e. does not depend on atomic physics) the normalized energy confinement time can be described by a set of dimensionless parameters and be written as

$$B\tau_{th} = F(\rho^*, \nu^*, \beta, q, \epsilon, \delta, \kappa, T_i/T_e, ...),$$

where B is the toroidal magnetic field on axis, τ_{th} is the thermal energy confinement time, $\rho^* = \rho_i/a$ is the normalized ion Larmor radius, $\nu^* = \nu_i/(\epsilon\omega_{bi})$ is the ion collision frequency normalized to the ion bounce frequency $\omega_{bi} = v_{\perp i}/qR(r/2R)^{1/2}$, $\beta = 2\mu_0 p/B^2$ is the normalized plasma pressure, q is the safety factor, $\epsilon = a/R$ is the inverse plasma aspect ratio, κ is the elongation, δ is the triangularity and T_i and T_e are, respectively, ion and electron temperature.

This paper focuses on the experimental study of the β scaling of transport in the ASDEX Upgrade tokamak. Since the fusion power production P_{fus} increases with increasing β, there is large economic interest to operate reactors at β as high as possible. Furthermore, the knowledge of the β dependence of confinement is also important to extrapolate present discharge scenarios to ITER.

In addition, a precise experimental characterization of the β dependence of transport may provide indications about the nature of turbulence. Electrostatic theories, in which finite β electromagnetic effects are neglected, predict a weak β dependence through geometrical effects like the Shafranov shift. For example, in drift wave theory, transport is expected to slightly decrease with increasing β due to the stabilizing β effect on ITG modes. On the other hand, approaching the ideal β limit, electromagnetic mechanisms not only affect electrostatic instabilities but also can destabilize electromagnetic modes, generally leading to a strong β dependence of turbulent transport [3–5].

Experimentally, the β dependence of transport is still a subject of controversy: contradictions exist between the prediction of empirical multi-machine scaling laws and the results of dedicated experiments. The widely used empirical

scaling law for high confinement mode (H-mode) plasmas with edge localized modes (ELMs), named IPB98(y, 2) [7], expressed in dimensionless parameters reads

$$B\tau_{\mathrm{th}}^{98y2} \propto \rho^{*-2.70}\beta^{-0.90}\nu^{*-0.01}q^{-3.0}.$$

This strongly negative β dependence suggests that electromagnetic effects may play a role in the turbulent transport process. In agreement with this negative β dependence, recent dedicated experiments in JT-60U [8] exhibited a degradation of global confinement time with increasing β as $B\tau_{\mathrm{th}} \propto \beta^{-0.6}$. In contrast, dedicated β scans performed in DIII-D [9] and JET [10] yielded no β dependence, in both global confinement time and local thermal diffusivities.

To contribute to clarifying these discrepancies, first β scaling experiments have been performed in ASDEX Upgrade. In the next section, experiments for the ASDEX Upgrade β scans are described and the results are presented in section 3. Differences in experimental conditions of β scans performed in DIII-D and JET as compared with ASDEX Upgrade and their possible impact on the results are discussed in section 4.

2. Experimental conditions

Dedicated β scan experiments on ASDEX Upgrade have been performed keeping ρ^*, ν^* (global and local values), the safety factor q and the plasma shape constant. The parameters ρ^*, ν^*, as well as the magnetic shear are known to have a strong impact on the plasma core instabilities, while a constant plasma shape is particularly important for the control of the edge behaviour. To vary β while keeping ρ^*, ν^*, the safety factor q and the plasma shape constant, the magnetic field B is varied in these discharges, and the main plasma parameters have to satisfy the following relationships:

$$I \propto B, \qquad n \propto B^4, \qquad T \propto B^2.$$

Following these requirements, β varies as B^4. As usual, in order to simplify the analysis and to compare with the empirical scaling law, we have made the assumption of considering a power law for the dependence of confinement time on β : $B\tau_{\mathrm{th}} \propto \beta^{-\alpha_\beta}F(\rho^*, \nu^*, ...)$. Therefore, the heating power must vary as $P_{\mathrm{h}} \propto B^{7+4\alpha_\beta}$. In the following, β will correspond to the total normalized pressure including fast particles, the thermal normalized pressure will be written as β_{th} and $\beta_{\mathrm{N}} \equiv \beta/(I/aB)$. Experimentally, the β range is limited by the L–H transition at low β ($\beta_{\mathrm{N}} \approx 1.1$) and by appearance of the neoclassical tearing modes (NTM) at high β ($\beta_{\mathrm{N}} \approx 2.5$). In addition, since the density has to vary as β ($\propto B^4$), another important limitation arises at low β from the natural density and at high β from the H/L transition close to the Greenwald density. In ASDEX Upgrade, the procedure to perform β scaling experiments was to first carry out a low β discharge at the lowest density reachable and at the lowest power needed to have type-I ELMs. From this discharge, the high β discharge was performed trying to reach simultaneously the density and the β required to match ρ^* and ν^*. All these experiments were performed in a single-null divertor plasma configuration and the shape parameters were chosen to closely match the plasma shape of JET and DIII-D experiments ($\delta \simeq 0.2$ and $\kappa \simeq 1.8$) and $q_{95} = 3.8$. The plasma was fuelled by deuterium gas puffing, heated by neutral beam injection (NBI) and in some cases with (H-minority) ICRH heating. The voltage of the NBI injectors was adjusted according to the density to match as well as possible the heating deposition profile between low and high β discharges. The divertor cryopump was used to control the plasma density in low density discharges and turned off to help reaching high density. The density profiles are calculated from interferometer and lithium beam data. The electron temperature profiles are measured by the Thomson scattering diagnostic. The charge exchange recombination spectroscopy (CXRS) during neutral beam injection provides a measure of the ion temperature and rotation profiles. Equilibria and q-profiles are reconstructed using the MHD equilibrium code CLISTE [12]. The heating deposition profiles for NBI and ICRH are calculated, respectively, by the Monte-Carlo code FAFNER [13] and the TORIC code [14]. The power balance analyses have been made using the ASTRA code [15] and comparisons carried out with the TRANSP code [16].

3. Experimental results

In the study presented here, two separate β scans in H-mode with Type-I ELMs have been performed in ASDEX Upgrade. The β ranges are $\beta_{\mathrm{N}} = (1.4\text{–}2.2)$ (scan A) and $\beta_{\mathrm{N}} = (1.4\text{–}2)$ (scan B) and cover two different density windows. The heating power was feedback-controlled to obtain a stationary phase at the required β. Engineering parameters as well as global dimensionless quantities of both scans are summarized in table 1. Global parameter calculations and analyses were performed over a stationary phase characterized by a time window width Δt. For discharges 21225 and 21226 Δt is comparable to the confinement time. However, during these discharges the time window was chosen at the maximum of β which correspond also to the maximum of the confinement time. Therefore, enlarging the time window leads to a stronger β degradation. The H factors of these discharges are close to 1 showing that the thermal confinement times are consistent with the IPB98(y, 2) scaling law. Considering only 'random' errors, the uncertainties on global parameters for both scans are estimated as 3.1% for ρ^*, 15.4% for ν^*, 3.2% for β and 9% for $B\tau_{\mathrm{th}}$. Global (deduced from stored energy) and local quantities such as ρ^*, ν^* and plasma shape parameters have to be well matched between discharges of the same scan in order to separate the β dependence of $B\tau_{\mathrm{th}}$ from the dependences induced by these parameters.

The first scan composed of one low β and three high β discharges was performed at high density, $\bar{n}_{\mathrm{e}_{19}} = (7.2\text{–}9.4)\ \mathrm{m}^{-3}$, which corresponds in terms of the Greenwald fraction, F_{GW}, to $F_{\mathrm{GW}} = (57\%\text{–}68\%)$. In this scan, in addition to NBI heating, ICRH was used in an attempt to adjust the heating profile deposition. Even without cryopump, it was difficult to reach the density required ($\overline{n}_{\mathrm{e}_{19}} = 9.7$) while keeping $\beta_{\mathrm{N}} = 2$. Thus, in scan A, there is a significant ν^* and ρ^* mismatch while q_{95}, κ and δ were well matched.

Scan B, composed of two discharges, was carried out at lower density than scan A, $\bar{n}_{\mathrm{e}_{19}} = (5.3\text{–}8)\ \mathrm{m}^{-3}$, or in terms of

Table 1. Engineering and dimensionless parameters for the two β scans. Parameters are averaged over time windows with a width Δt.

	Scan A				Scan B	
Pulse	20989	21101	21225	21226	21403	21426
Δt (ms)	2000	300	100	100	600	400
τ_{th} (ms)	135.5	94.81	67.86	60.67	160.9	89.47
B (T)	−2.10	−2.29	−2.28	−2.28	−2.12	−2.33
I (MA)	1.00	1.10	1.09	1.09	0.99	1.09
$\bar{n}_e$ (10^{19} m^{-3})	7.2	8.6	8.7	9.7	5.3	8
$\bar{n}_e/B^4$ (10^{19} m^{-3}/T^4)	0.37	0.31	0.32	0.36	0.26	0.27
F_{GW} (%)	57	64	63	68	43	54
P_{NBI} (MW)	2.4	7.75	7.5	10	2.6	8.75
P_{ICRH} (MW)	1.11	0.6	3.8	3.8	0	0
P_{tot}/B^7 (MW/T^7)	0.019	0.025	0.035	0.043	0.013	0.023
q_{95}	3.8	3.9	3.8	3.8	3.8	3.8
a/R	0.30	0.31	0.30	0.30	0.30	0.30
κ	1.84	1.79	1.84	1.83	1.82	1.86
δ	0.21	0.24	0.22	0.23	0.20	0.22
ρ^*	0.0061	0.0069	0.0066	0.0067	0.0070	0.0071
ν^*	0.610	0.300	0.396	0.388	0.243	0.279
β_N	1.41	2.22	1.97	2.22	1.41	2.05
β_{th}	1.32	2.07	1.87	2.09	1.30	1.93
$B\tau_{th}$	0.284	0.217	0.155	0.138	0.342	0.208
$H_{IPB98(y,2)}$	0.99	1.11	0.89	0.90	1.16	1.01

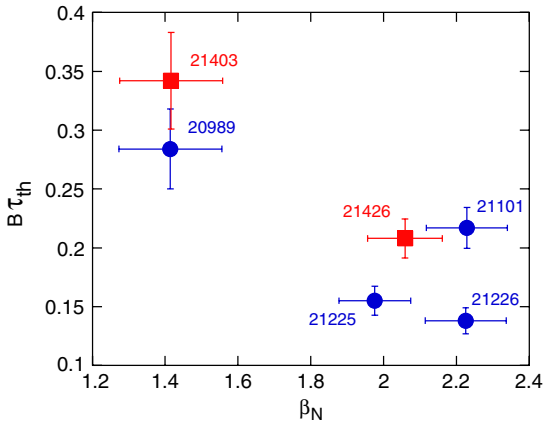

Figure 1. Normalized thermal energy confinement time as a function of β_N for the discharges given in table 1.

the Greenwald fraction, $F_{GW} = (43\%–57\%)$. Both discharges were performed with NBI heating only. Matching of global parameters (within 15% for ν^* and within 2% for ρ^* which are within the error-bars) as well as heating deposition profiles are clearly better than in scan A.

3.1. Global confinement time analysis

Figure 1 shows the normalized thermal energy confinement time $B\tau_{th}$ as a function of β_N for the six previously described discharges. For each scan, there is a clear degradation of the global confinement with increasing β. Linear regressions of each pair of discharges yield a β dependence of $B\tau_{th}$ which varies significantly from $\alpha_\beta = 0.6 \pm 0.4$ to $\alpha_\beta = 1.8 \pm 0.7$ (table 2). When all discharges of scan A are considered, $\alpha_\beta = 1.16$, while scan B (red) gives $B\tau_{th} \propto \beta_{th}^{-1.2\pm0.6}$. Although uncertainties on α_β are quite large , in particular when regression is made on only 2 points, α_β remains always positive within the error-bars. Note that the uncertainties reported in table 2 were calculated taking into account only the uncertainties on τ_{th} and β_{th}. The inclusion of ρ^* and ν^* uncertainties ($\Delta\rho^*$ and $\Delta\nu^*$) requires assumptions about the dependence of the global confinement time on ρ^* and ν^*. The Gyro–Bohm scaling $B\tau_{th} \propto \rho^{*-3}$ is well established in H-mode plasmas and has been verified on different tokamaks [17, 18]. The ν^* dependence in dedicated experiments was found to be weak, $\nu^{*-0.3}$, at low density [18, 19] and stronger, ν^{*-1}, at high density [20]. Since $\Delta\rho^*$ and $\Delta\nu^*$ are correlated via the stored energy and density uncertainties, $\Delta\alpha_\beta$ must be calculated using directly ΔW and Δn. For example, assuming $B\tau_{th} \propto \rho^{*-3}\nu^{*-1}$ for the pair 21403–21426, $\Delta\alpha_\beta = 0.9$. In contrast, assuming $B\tau_{th} \propto \rho^{*-3}\nu^{*-0.3}$, the uncertainty on α_β almost does not change as compared with the values reported in table 2.

As mentioned before, the ρ^* and ν^* matching between low and high β discharges is not perfect and differs significantly for each pair of discharge. Therefore, parameter mismatching affects each pair of discharges in a different way and may explain the large scattering of α_β values obtained. In order to compensate for these effects, the global confinement time can be corrected using its ρ^* and ν^* dependence obtained from previous experiments.

Corrections considering the dependences described above have been applied, separately and together, to each pair of discharges and the resulting β dependences are summarized in table 2. The ρ^* correction tends to decrease the β dependence for both scans. In contrast, the ν^* correction acts in opposite directions in scan A and scan B. In the first scan, the ν^* mismatch leads to an underestimate of α_β while it leads to an overestimate in scan B. Note that applying no ν^* correction and only the Gyro–Bohm scaling correspond almost to the dimensionless scaling obtained from the IPB98(y, 2).

For the first scan, the significant ρ^* and ν^* mismatches induce a strong influence of corrections and in particular of the choice of the ν^* correction. However, applying the corrections, the β scaling remains clearly unfavourable in both

Table 2. β dependence obtained from linear regressions performed on each pair of discharges listed in table 1 with and without mismatch corrections.

	20989–21101	20989–21225	20989–21226	21403–21426
α_β	0.6 ± 0.4	1.8 ± 0.7	1.6 ± 0.5	1.2 ± 0.6
With corrections				
ρ^{*-3}	−0.18	1.09	0.94	1.14
$\nu^{*-0.3}$	0.98	2.02	1.75	1.08
ν^{*-1}	1.86	2.61	2.18	0.69
$\rho^{*-3} * \nu^{*-0.3}$	0.26	1.16	1.13	0.94
$\rho^{*-3} * \nu^{*-1}$	1.08	1.93	1.56	0.58

scans. Considering the ν^* correction for high density, scan A leads to $B\tau_{\rm th} \propto \beta^{*-1.38}$ considering all discharges, while $\alpha_\beta = 1.08$ for the pair 20989–21101. The β dependence obtained for discharges 21225 and 21226 is clearly stronger (up to $\alpha_\beta = 1.93$). As mentioned above, in scan A, ICRH has been added to NBI. Applying ICRH has been shown to flatten the density profile [21], effect which increases with $P_{\rm ICRH}$. Therefore, in shots 21225 and 21226, the high ICRH power of 3.8 MW induced a stronger flattening of the density profile than in shots 21101 and 20889 with much lower ICRH powers. Consequently, in discharges 21225 and 21226 much stronger gas puffing was required to reach the desired line averaged density than in 21101. This produces an extremely flat density profile with very high pedestal density, inducing low pedestal ion temperature. In addition, the ELMs frequency is much higher 180 Hz compared with 90 Hz in 20989 and 21101.

For scan B, applying the low density correction ($B\tau_{\rm th} \propto \nu^{*-0.3}$) yields $B\tau_{\rm th} \propto \beta_{\rm th}^{-0.94}$ which agrees with the result from scan A (pair 20989–21101) using high density ν^* correction. The latter result is in accordance with the β dependence deduced from the IPB98(y, 2) [7] and the unfavourable β scaling found recently in JT-60U [8]. In order to cancel completely the β degradation in scan B, considering a Gyro–Bohm scaling, a ν^* dependence as $B\tau \propto \nu^{*-2}$ would be required. However, such ν^* dependence has never been found in ν^* scaling experiments or in empirical scaling laws.

3.2. Local heat transport analysis

In addition to matching the global normalized parameters, it is also important to verify that of local dimensionless quantities which are expected to play a role in heat transport. The local study of transport was performed on the best matched scan (scan B). All radial profiles presented in the following are plotted as a function of the normalized toroidal flux coordinate ρ_t. First of all, the heating deposition profiles normalized to B^7 (if $\alpha_\beta = 0$, $P_{\rm h} \propto B^7$) and plotted in figure 2(a) show that, in order to reach the β required, more additional power was needed than expected without β degradation. This behaviour agrees with the negative dependence found in the global analysis. Considering $\alpha_\beta = 1$, the profiles $P_{\rm h}/B^{7+4\alpha_\beta}$ are correctly matched as we can see in figure 2(b). The radial profiles of the kinetic normalized plasma pressure $\beta_{\rm kin}$ and of the quantity $\beta_{\rm kin}/B^4$ are shown in figure 3. The profile of the quantity $\beta_{\rm kin}/B^4$ is similar for low and high β discharges even at $\rho_{\rm t} = 0.85$. The H-mode edge pedestal and the core seem to vary in concert but in these discharges, no accurate edge

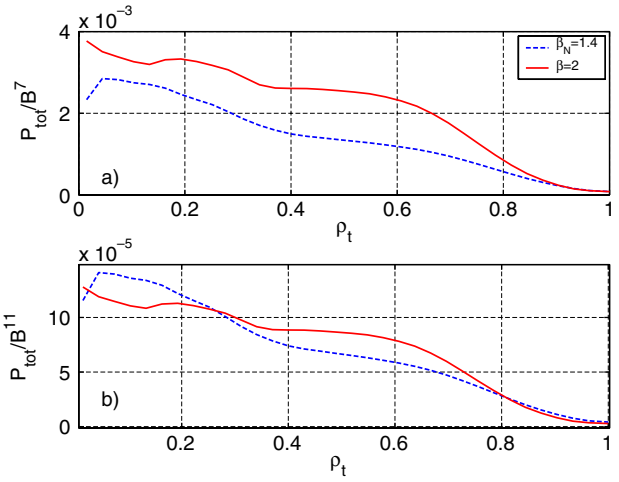

Figure 2. (a) Radial profiles of the heating power deposition normalized to B^7 as a function of the normalized toroidal flux coordinate for discharges 21403 ($\beta_{\rm N} = 1.4$) and 21426 ($\beta_{\rm N} = 2$). (b) Profiles of the heating power deposition normalized to $B^{7+4\alpha_\beta}$ with $\alpha_\beta = 1$

measurements were available. For this reason, in the following, all radial profiles will be plotted between $\rho_{\rm t} = (0–0.85)$ and no detailed analysis of the plasma edge will be done. On the profiles of $\beta_{\rm kin}/B^4$, only around $\rho_{\rm t} = 0.5$ there is a small gap, the high β discharge being slightly higher, but the difference is within the uncertainties.

The density and temperature profiles show that the normalized gradient lengths $R/L_{\rm n}$ and $R/L_{\rm T}$ (for ions and electrons) do not change significant between low and high β discharges. This feature suggests that core transport is governed by microinstabilities like ITG and TEMs, with consequent stiff behaviour of the temperature profiles in response to variations of the heat fluxes. Therefore, in these conditions the heat conductivity in the core might be strongly affected by the confinement at the plasma edge.

Figure 4 shows the profiles of the other relevant dimensionless quantities ρ^*, ν^*, $T_{\rm i}/T_{\rm e}$, q, effective ion charge $Z_{\rm eff}$, $v_{\rm rot}/(T_{\rm i}/m_{\rm i})^{1/2}$ and $R\nabla v_{\rm rot}/(T_{\rm i}/m_{\rm i})^{1/2}$. These profiles are well matched between the low and high β discharges except for $Z_{\rm eff}$. The mismatch does not exceed 5% for ρ^* and 20% for ν^* profiles. The small difference in the safety factor profiles at the centre is not really relevant because the uncertainties are quite large at this location due to the sawtooth activity. The ratio $T_{\rm i}/T_{\rm e}$ varies radially, the ion temperature is higher than electron temperature at the edge and the mismatch between the two discharges reaches at most 15%. Note that higher

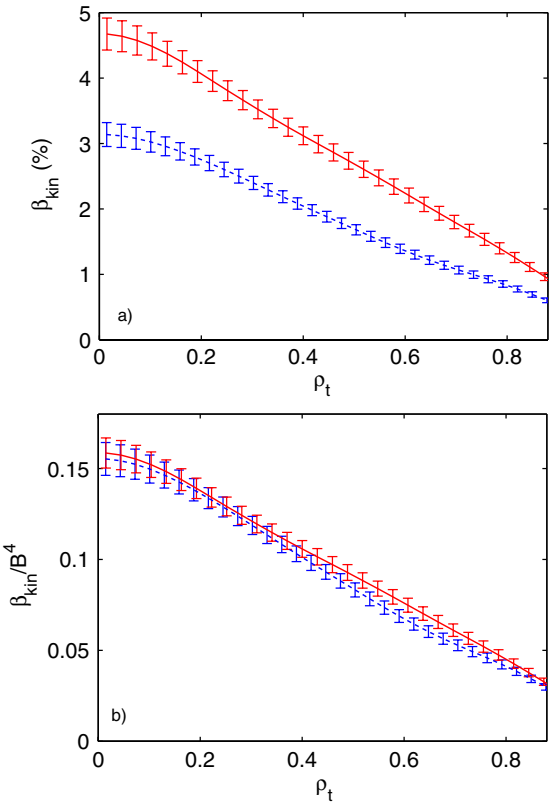

Figure 3. (*a*) Radial profiles of thermal normalized pressure β_{th} for discharges 21403 and 21426. (*b*) Radial profiles of β_{th} normalized to B^4 for discharges 21403 and 21426.

values of T_i/T_e are expected to stabilize electrostatic modes ITG [22].

The level of impurity is higher in the low β discharge for which Z_{eff} is around 2 while $Z_{eff} \simeq 1.5$ during the high β discharge. This general feature that Z_{eff} decreases with increasing density is commonly observed in ASDEX Upgrade ELMy H-mode plasmas [23]. In the local analysis, the effect of the dilution is taken into account computing the power balance using the experimental Z_{eff} profiles. Calculations have been made considering Carbon, Helium or Bore as main impurities. The relative behaviour of the thermal conductivity profiles (comparison of low and high β discharges) does not change from one impurity to another.

From theoretical standpoint, Z_{eff} affects the stability of ITG modes by ion dilution, such that increasing Z_{eff} has a stabilizing effect on ITG, stronger for light impurities than for heavy impurities [24, 25]. Therefore, the lower value of Z_{eff} in the high β discharge could amplify the β degradation. To estimate the Z_{eff} mismatch effect, we performed linear gyrokinetic simulations in the experimental conditions (GS2 code [26, 27]). They show that a change in Z_{eff} from 2 to 1.5 leads to an increase in the ITG growth rate of around 5% and a shift in the normalized gradient length (R/L_T) threshold of less than 0.5. Thus, the mismatch in Z_{eff} is expected to only play a minor role in the confinement and heat transport of the discussed experiments.

The rotational shear has a stabilizing effect on transport, therefore the relative influence of the toroidal rotational velocity v_{rot} must be kept constant during dimensionless scaling. Considering that v_{rot} is the dominant term in the radial electric field ($E_r \approx B_p v_{rot}$), the shearing rate may be written as $\omega_{E\times B} \approx \epsilon/q\, \nabla v_{rot}$. The radial profiles of $R\nabla v_{rot}/(T_i/m_i)^{1/2}$ plotted in figure 4 show that this quantity is slightly higher (6%) in the low β discharge than in the high β discharge. This mismatch is very small but means that the $E \times B$ stabilization is larger in the lower β. A recent experimental study on the role of T_i/T_e and ∇v_{rot} on ion heat transport in ASDEX Upgrade H-modes has presented the ITG threshold (R/L_{T_i}) dependence on $R\nabla v_{rot}/(T_i/m_i)^{1/2}$ [28]. In this reference it is shown that decreasing the quantity $R\nabla v_{rot}/(T_i/m_i)^{1/2}$ by 6% at fixed ratio T_i/T_e has a very weak effect on R/L_{T_i} and leads to a decrease of R/L_{T_i} smaller than 5%. Finally, this effect which affects only the ion channel may increase only very slightly the effective local transport.

To evaluate the β dependence of the local heat transport, experimental thermal diffusivities have been calculated from the radial power balance analysis. The heat flux has been assumed to be purely diffusive, therefore the thermal diffusivity is given by $\chi = -q/n\nabla T$. In the following, the effective heat diffusivity is defined by

$$\chi_{eff} = \frac{q_e + q_i}{n_e \nabla T_e + n_i \nabla T_i},$$

where q_e and q_i are, respectively, the electron and ion heat flux.

The total stored energy obtained by the equilibrium reconstruction and by the sum of kinetic energy from the experimental profiles and fast particle energy (from FAFNER) agrees within 5%. For comparison, the power balance calculations deduced using the TRANSP code yielded a similar β dependence of the thermal conductivity.

The normalized $\chi_{eff}/\chi_B \propto \chi_{eff}/B$ profiles, where χ_B is the Bohm diffusion coefficient, are plotted in figure 5. The error-bars reported in figure 5 were calculated as follows. First, for each of the two discharges of scan B, a set of $N = 500$ fitted profiles (T_e, T_i and n_e) has been generated by varying randomly (using a Gaussian distribution) the experimental points within their experimental errors. The latter were taken as 15% for T_e, 10% for T_i and 5% for n_e. Note that in the heat diffusivity, the largest uncertainties come from the temperature gradients. Secondly, for each set of the 500 profiles, a χ_{eff} profile was calculated by power balance. In this procedure, the heating deposition profiles are kept the same and have not been re-computed using FAFNER on the new set of profiles. However, FAFNER and ASTRA calculations show that varying density and temperature profiles in their error-bars lead at most to a change in χ_{eff} around 5%. The distribution of χ_{eff} obtained in this way is not symmetric. For this reason, the χ_{eff}/B plotted in figure 5 is taken at the maximum of the distribution function and the error-bars are the half-widths of each sides of this maximum. Following this procedure, the uncertainties are found to be around 15% at mid-radius and larger at the edge. The effective diffusivity is clearly higher for the high β discharge on a large radial area in the confinement zone ($\rho_t = 0.3$–0.9). For these profiles, the parameter α_β, defined as $\chi_{eff}/B \propto \beta^{\alpha_\beta}$, is plotted in figure 6.

The average β dependence of χ_{eff}/B from $\rho_t = 0.2$ to $\rho_t = 0.8$ corresponds to $\alpha_\beta = 0.65$. The β dependence

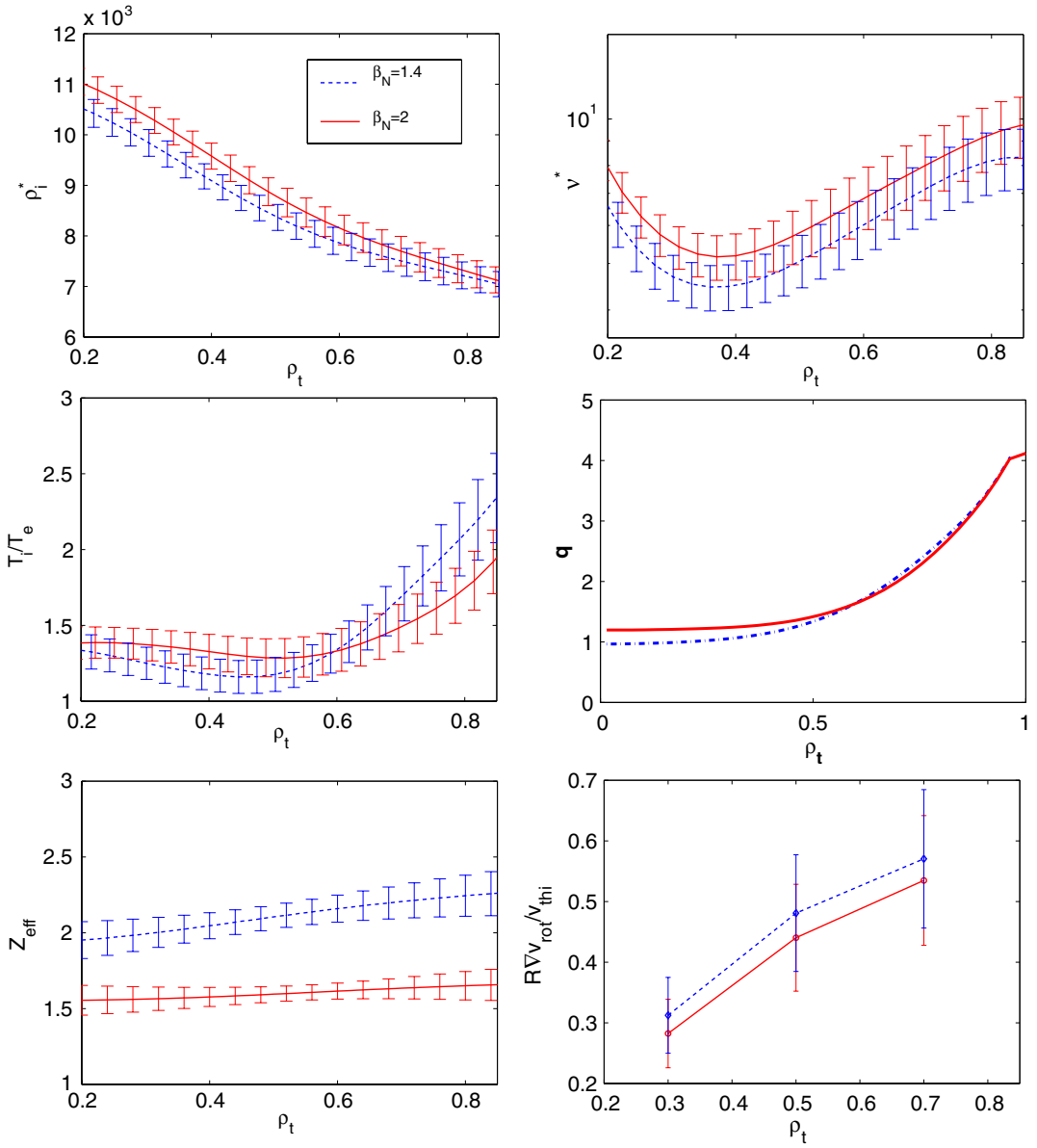

Figure 4. Radial profiles of ρ^*, ν^*, $T_\mathrm{i}/T_\mathrm{e}$, safety factor q, Z_eff and $R\nabla v_\mathrm{rot}/v_\mathrm{thi}$ for discharges 21403 and 21426.

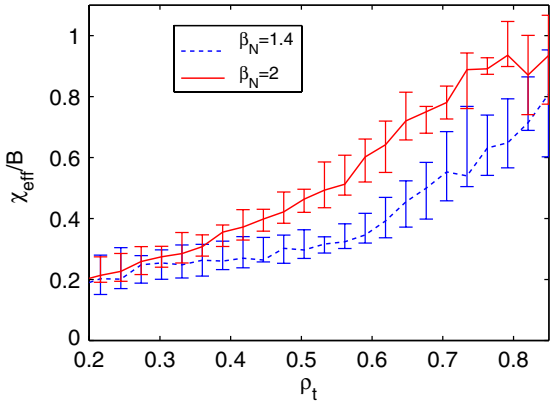

Figure 5. Radial profiles of the effective thermal diffusivity normalized to B for discharges 21403 and 21426.

changes significant with radius from $\alpha_\beta \simeq 0$ at $\rho_\mathrm{t} = 0.2$ to $\alpha_\beta \simeq 1$ in the range $\rho_\mathrm{t} = (0.5\text{–}0.7)$.

4. Conclusion

First dedicated experiments on β scaling in ASDEX Upgrade show a clearly unfavourable β dependence of transport in both global and local analyses. The global confinement time is found to vary as $B\tau_\mathrm{th} \propto \beta^{-1.2\pm0.6}$. Since in these experiments the ρ^* and ν^* profiles are not perfectly matched, attempts to correct these mismatches have been made. These corrections did not cancel the strong negative β degradation and lead to a β dependence as $B\tau_\mathrm{th} \propto \beta^{-0.9}$. In addition, the local effective heat diffusivity is enhanced with increasing β as $\chi_\mathrm{eff} \propto \beta^{0.65}$ (on average from $\rho_\mathrm{t} = 0.2$ to $\rho_\mathrm{t} = 0.8$). These results are in agreement with the β exponents derived from the ITER-IPB98(y, 2) scaling law and with the results of

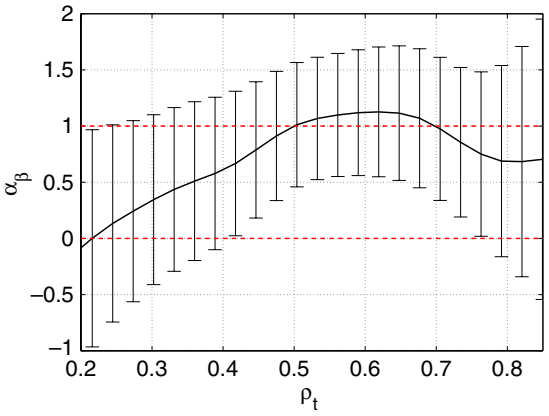

Figure 6. Radial profiles of α_β from χ_{eff}/B for discharges 21403 and 21426.

JT-60U dedicated experiments. However, they do not agree with DIII-D and JET experiments, in which no β dependence has been found. Although the experimental conditions of β scans performed in JET, DIII-D and ASDEX Upgrade are very similar, two main differences can be identified. The possible reasons for these differences are discussed in the following paragraphs.

Firstly, in ASDEX Upgrade, the collisionality is higher at $\rho_t = 0.5$ by a factor 5 as compared with JET and DIII-D experiments while the Greenwald fractions are in similar ranges (from 26% for the low β to 68% for the high β). According to the present results from dedicated experiments on the ν^* dependence of confinement time [18–20], the effect of collisionality via the ν^* mismatch cannot be responsible for the apparent β degradation, as it was shown in section 2.1. However, collisionality may play a role in the β scaling by changing the turbulence regime.

Secondly, a comparison of the plasma shapes in these β scans indicates that the elongation is the same in DIII-D and AUG ($\kappa \simeq 1.8$) while $\kappa = 1.6$ in JET experiments. The average triangularity is equal in JET and ASDEX Upgrade ($\delta = 0.2$) and slightly higher in DIII-D ($\delta \simeq 0.3$), but the upper triangularity δ_{up} is clearly smaller in AUG $\delta_{\text{up}}^{\text{AUG}} \simeq 0.06$ as compared with both DIII-D and JET ($\delta_{\text{up}}^{\text{DIII-D}} \simeq \delta_{\text{up}}^{\text{JET}} \simeq 0.2$) plasmas. The plasma shape is known to influence ELMs and H-mode pedestal properties. In particular, high triangularity shapes exhibit an increased edge pressure gradient and lead to a better confinement [32–35]. In addition, at high δ, confinement degradation with increasing density occurs at high density as compared to low δ plasmas [36]. These two effects can be linked to the observed β degradation in ASDEX Upgrade. As suggested in [37], the upper triangularity might play a role in the β dependence of transport. In this reference, from analysing an ASDEX Upgrade subset of the International Tokamak Physics Activity (ITPA) confinement database, a β degradation has been found and attributed to $\delta_{\text{up}} < 0$ plasmas. Although in the experiments presented here $\delta_{\text{up}} > 0$, the tendency is in the same direction.

The influence of the plasma shape suggest that the β dependence of confinement is a plasma edge effect. In contrast, the increase in the normalized thermal conductivity χ_{eff}/B with increasing β is not only localized at the edge but it is also visible at mid-radius. However, in the confinement region, density and temperature gradient lengths do not change significant between low and high β discharges. In these conditions, a strongly negative β dependence of the edge plasma may be sufficient to explain the increase in the thermal conductivity at mid-radius.

To investigate the role of the edge in the β scaling, new β scans with changing plasma shape with edge measurements are planned in ASDEX Upgrade.

Acknowledgments

The authors would like to acknowledge the valuable support of the whole AUG Team. One of the authors (LV) is grateful to A. Bottino for helpful suggestions and valuable discussions.

LV acknowledges financial support for this work from the EURATOM programme of the European Community in the form of a Individual Fellowship, Contract No FU06-028309.

References

[1] Kadomtsev B.B. 1975 *Sov. J. Plasma Phys.* **1** 295
[2] Connor J.W. and Taylor J.B. 1977 *Nucl. Fusion* **17** 1047
[3] Snyder B. and Hammett G.W. 2001 *Phys. Plasmas* **8** 744
[4] Candy J. 2005 *Phys. Plasmas* **12** 072307-1/072307-8
[5] Falchetto G.L., Vaclavik J. and Villard L. 2003 *Phys. Plasmas* **10** 1424
[6] Bourdelle C. *et al* 2003 *Phys. Plasmas* **10** 2881
[7] ITER Physics Expert Group on Confinement and Transport and Confinement Modelling and Database *et al* 1999 *Nucl. Fusion* **39** 2175
[8] Urano H. *et al* 2006 *Nucl. Fusion* **46** 781–7
[9] Petty C.C. *et al* 2004 *Phys. Plasmas* **11** 5
[10] McDonald D.C. *et al* 2004 *Plasma Phys. Control. Fusion* **46** A-215-A-225
[11] Mertens V. *et al* 1997 *Nucl. Fusion* **37** 1607–14
[12] Mc Carthy P.J. *et al* 2000 *27th EPS Conf. on Controlled Fusion and Plasma Physics (Budapest)* vol 24B P-440
[13] Lister G.G. 1985 FAFNER—A fully 3-D neutral beam injection code using Monte Carlo methods *IPP-Report* **4–222**
[14] Brambilla M. and Bilato R. 2006 *Nucl. Fusion* **46** S387–96
[15] Pereverzev G.V. and Yushmanov P.N. 2002 *IPP Report* 5/98
[16] Pankin A. *et al* 2004 *Comput. Phys. Commun.* **159** 157
[17] Petty C.C. *et al* 1995 *Phys. Plasmas* **2** 2342
[18] JET Team (Cordey J.G.) 1997 *Proc. 16th Int. Conf. on Fusion Energy 1996 (Montreal, 1996)* vol 1 p 611 (Vienna: IAEA)
[19] Shirai H. *et al* 2000 *Plasma Phys. Control. Fusion* **42** 1193
[20] Greenwald M. *et al* 1998 *Plasma Phys. Control. Fusion* **40** 789–92
[21] Stober J. *et al* 2001 *Plasma Phys. Control. Fusion* **43** A39–53
[22] Xu X.Q. and Rosenbluth M.N. 1991 *Phys. Fluids* B **3** 1807
[23] Meister H. *et al* 2003 *30th EPS Conf. on Controlled Fusion and Plasma Physics (St Petersburg)* vol 27A P-1.136
[24] Dominguez R.R. and Rosenbluth M.N. 1989 *Nucl. Fusion* **29** 844–8
[25] Paccagnella R., Romanelli R. and Briguglio S. 1990 *Nucl. Fusion* **30** 545–8
[26] Kotschenreuther M. *et al* 1995 *Comput. Phys. Commun.* **88** 128
[27] Dorland W. *et al* 2000 *Phys. Rev. Lett.* **85** 5579
[28] Manini A. *et al* 2006 *Nucl. Fusion* **46** 1047–53

[29] Jenko F. and Dorland W. 2001 *Plasma Phys. Control. Fusion* **43** A141–50
[30] Ryter F. *et al* 2005 *Phys. Rev. Lett.* **95** 085001
[31] Angioni C. 2003 *Phys. Plasmas* **10** 3225
[32] Suttrop W. *et al* 2000 *Plasma Phys. Control. Fusion* **42** A97–102
[33] Saibene G. *et al* 2002 *Plasma Phys. Control. Fusion* **44** 1796–9
[34] Osborne T.H. *et al* 2000 *Plasma Phys. Control. Fusion* **42** A175–84
[35] Lao L.L. *et al* 2001 *Nucl. Fusion* **41** 295–300
[36] Stober J. *et al* 2000 *Plasma Phys. Control. Fusion* **42** A211–16
[37] Takizuka T. *et al* 2006 *Plasma Phys. Control. Fusion* **48** 799–806

The possible reasons of this strong β degradation of the performances, notably as compared to DIII-D and JET experiments, were : collisionality which is higher in AUG experiment and/or a possible influence of the plasma shape and more precisely the upper triangularity, which is lower in AUG plasmas. Indeed, to improve our knowlegde in shape effect, we proposed and performed new experiments in DIII-D to compare β scalings using different shapes (DIII-D and AUG shapes performed in the DIII-D tokamak). Three β scans were achieved in the DIII-D tokamak : one in the AUG shape and two in the standard DIII-D shape, one at high rotation (standard case) and another at low rotation (using balanced NBI). Note that the new scan performed with the DIII-D shape at high rotation is expected to be similar to the previous experiments performed in DIII-D [21] in which no degradation was observed with increasing β. However, in all scans, a β degradation of the global confinement time was observed, going from $B_0\tau \propto \beta^{-0.7}$ for the AUG shape experiments to $B_0\tau \propto \beta^{-0.5}$ in the low rotation case and $B_0\tau \propto \beta^{-0.4}$ in the high rotation case. These results are then surprising.

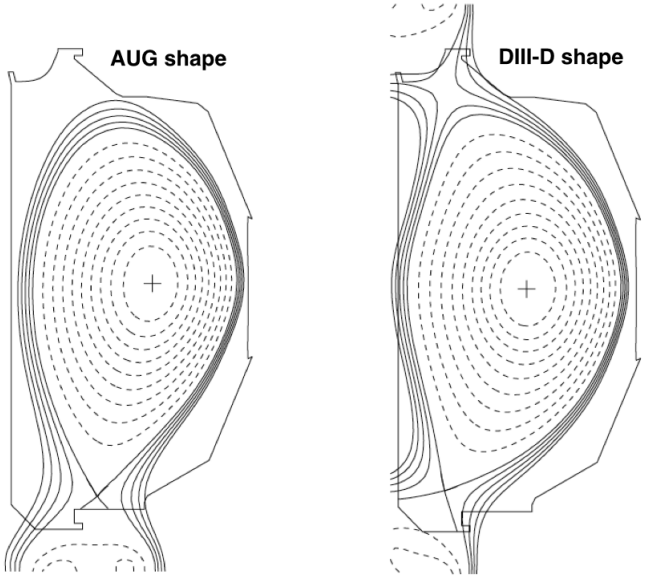

FIGURE 3.2. – Example of plasma shapes at low upper triangularity $\delta_u < 0.1$ labelled "AUG shape" (left) and at higher upper triangularity $\delta_u \sim 0.3$ labelled "DIII-D shape" (right)

However due to the high sensibility of the analysis with respect to the choice of the time sequence, none of these results were published. The discharges were not very stationary and displayed dependence on the selected time window for the analysis. Therefore upon matching between different parameters, the β degradation of the global confinement time changes significantly (still in the error-bars, since they are quite large). Therefore, no clear conclusion has been drawn after this set of experiments expect that this kind of experiments are quite sensitive and challenging.

In parallel to this experimental work, we performed a simple β scan, numerically. It consists of a linear stability analysis using gyrokinetic simulations with the GS2 code [24] in the experimental conditions (at least, using as much as possible, the experimental plasma

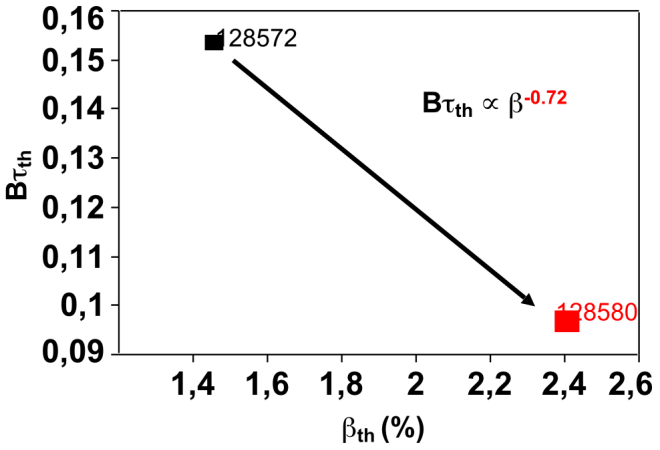

FIGURE 3.3. – Normalized confinement time as a function of the thermal β during dedicated β scan performed on DIII-D using the "AUG shape" (i.e $\delta_u \sim 0$)

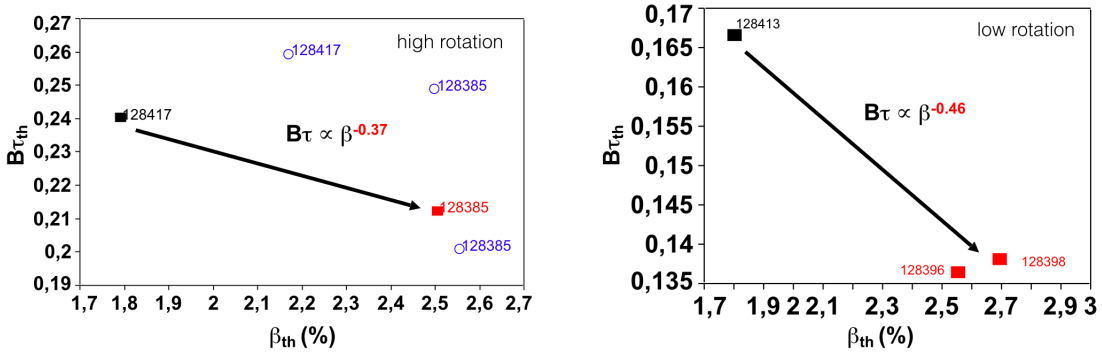

FIGURE 3.4. – Normalized confinement time as a function of the thermal β during dedicated β scans performed on DIII-D using the "DIII-D shape" at high rotation (left) and low rotation (right)

conditions as input parameters : local gradients, collision frequency, temperature ratio ...) of the dedicated β scan. This work is contained in the publication included in the following [Publication 2]. Note that most of the numerical studies on this topic are performed far from the linear threshold of the main instabilities (i.e. in the CYCLONE base case corresponding to extremely large normalized gradient lengths). These plasma conditions (of largely unstable situation), which are really useful to benchmark codes, remain far from real experimental conditions, in which naturally the temperature and density profiles are generally close to the threshold values (i.e. to marginal stability). This work shows that, in the AUG experimental condition of the β scan, the KBM are not destabilized at this range of β values, that the plasma triangularity does not modify the KBM stability and that microtearing modes (MTMs) are linearly destabilized and dominant for a certain range of wavenumber and gradient lengths (especially density gradient length). The latter, which have a very narrow radial extension, are supposed not to play a crucial role in turbulent transport.

In addition, in a recent publication [25], non-linear gyrokinetic simulations inlcuding both ETG modes and MTMs indicates that radially localized current-sheet structures of MTMs are strongly distorted by fine-scale $E \times B$ flows of ETG turbulence. Consequently, MTMs are suppressed by ETG turbulence.

On another side, the linear simulations performed in the context of AUG expetiments [Publication 2] show an interesting aspect, ITG modes are found to be slightly destabilized with increasing β. While this effect remains too weak to explain the β degradation obtained it highlights a different behavior of the stability of ITG modes depending on the distance from the linear threshold.

Journal of Physics: Conference Series **123** (2008) 012040 doi:10.1088/1742-6596/123/1/012040

β dependence of micro-instabilities using linear gyrokinetic simulations

L Vermare[1], C Angioni[1], A Bottino[1], A G Peeters[2] and ASDEX Upgrade Team

[1] Max-Planck-Institut für Plasmaphysik, EURATOM Association, Garching, Germany
[2] Centre for Fusion, Space and Astrophysics, University of Warwick, CV4 7AL Coventry, UK

E-mail: laure.vermare@lptp.polytechnique.fr

Abstract. The β scaling of micro-instabilities has been investigated by several authors using gyrofluid or gyrokinetic description in linear as well as in non-linear calculations. The typical picture well established now is that at low β, Ion Temperature Gradient (ITG) mode is stabilized with increasing β until Kinetic Ballooning modes become unstable. Such kind of numerical studies have been generally performed in plasma conditions close to the CYCLONE case, which means for ion temperature gradient length strongly above the ITG linear threshold and density gradient length around $R/L_n = 2.2$. However, in some standard H-mode plasmas, not only the ion temperature gradient length is closer to the ITG threshold but also the density gradient length can be rather small as compared to the CYCLONE case. In these conditions, the β scaling of micro-instabilities can significantly differ from the expected behavior described above. The goal of this paper is to investigate numerically the β scaling of micro-instabilities around such experimental conditions. Simulations have been performed using the gyrokinetic electromagnetic flux-tube code GS2 in its linear version and considering as reference, discharges from the dedicated β scaling experiments performed recently in ASDEX Upgrade. The effect of changing the gradient lengths (density and temperature) within experimental errors-bars is studied. It appears that for certain ranges of plasma parameters micro-tearing modes are the dominant micro-instability and coexist in the spectrum with ITG modes with a comparable growth rate. The effect of the plasma shape on the β scaling of micro-instabilities is also investigated. It is shown that the triangularity affects slightly the KBM branch which is destabilized at value of β clearly above the experimental range. However, it is found that at $\rho_t = 0.7$ Trapped Electron Modes are the most unstable instabilities and that such modes are destabilized with increasing β in agreement with results from dedicated β experiments performed in ASDEX Upgrade.

1. Introduction

The investigation on electromagnetic effects on micro-turbulence and heat transport is very challenging, in both, theoretical and experimental studies but is of primary importance considering the interest in operating at high β in future devices.

Experimental studies on β scaling of heat transport did not lead yet to a clear conclusion. The empirical scaling law IPB98(y,2) [1] exhibits a strong β degradation of the thermal confinement time τ_{th} as $B\tau_{th} \propto \beta^{-0.9}$. The dimensionless parameters dependence of the global confinement time are obtained by replacing the engineering parameters in the empirical scaling law by dimensionless parameters. Therefore, a little change in the exponents of engineering parameters can lead to a significant change in the exponents of the dimensionless parameters. In particular, the β dependence is very sensitive to the exponent of the additional power which is by itself subject to large uncertainties. The alternative approach consists in measuring directly the β dependence of confinement by performing dedicated experiments in which β is varied keeping the other dimensionless parameters (normalized Larmor radius ρ^*, normalized collisionality ν^*, the plasma shape, etc ...) constant. Such kind of experiments have been performed in DIII-D and JET and no β dependence was found [2, 3]. In contrast, more recent experiments carried out in JT-60U [4] and ASDEX Upgrade [5] found a β degradation comparable to the dependence predicted in the scaling law.

From a theoretical point of view, a substantial effort to include electromagnetic effects in numerical simulations has been undertaken. The study of finite β effects on core turbulence has been investigated by several authors using gyrofluid [6, 7, 8, 9], as well as gyrokinetic [10, 11, 12, 13, 14] descriptions. The plasma conditions used for these studies were close to the CYCLONE case (the normalized density gradient lenght $R/L_n = R\nabla n/n = 2.2$ where R is the major plasma radius, the normalized temperature gradient length $R/L_T = R\nabla T/T = 6.9$, the magnetic shear $\hat{s} = 0.78$, the electron and ion temperature ratio $T_e/T_i = 1$ and the safety factor $q = 1.4$), for which at low β the most unstable modes are Ion Temperature Gradient (ITG) modes with the maximum of the growth rate around $k_\theta \rho_i \simeq 0.3$ (where k_θ is the poloidal wavenumber and ρ_i the ion Larmor radius). As a general result, linear simulations show that finite β effects on ITG modes are stabilizing. With increasing β, a transition from nearly electrostatic ion drift turbulence to electromagnetic modes as Kinetic Ballooning modes (KBM) is observed. The transition occurs when β is increased above a threshold value generally smaller than the ideal MHD ballooning limit. Non-linear simulations at low β give a β dependence of transport which agrees with the linear results : far from the ideal ballooning limit, the ion heat conductivity decreases with β but it starts to increase strongly when β approaches the ideal ballooning limit. However, in high collisionality H-mode plasmas, not only the ion gradient length at mid-radius is closer to the linear ITG threshold ($R/L_T < 5$) but also the density gradient length can be rather small (around $R/L_n \sim 1$) as compared to the CYCLONE case ($R/L_n = 2.2$). In these conditions, the behavior of the β scaling of micro-instabilities could be different from the expected picture described above. The goal of this paper is to study the β dependence of micro-instabilities in these particular experimental conditions which are close to the β scaling discharges performed in ASDEX Upgrade. The tool used for simulations is the gyrokinetic electromagnetic flux-tube code GS2 [15, 16] in its linear version.

The remainder of this paper is organized as follows: in section 2 a description of the ASDEX Upgrade discharges [5] used as reference for the numerical simulation parameters is given. In section 3, β scans considering different density and temperature gradient lengths, within the experimental error-bars, are presented. Spectra of micro-instabilities for low and high β cases are shown in section 4. Section 5 is devoted to a discussion on the plasma conditions for which the micro-tearing modes are the most unstable modes in the system. In section 6, the β scaling of micro-instabilities at $\rho_t = 0.7$ (ρ_t is the normalized minor radius defined by the toroidal flux) and the effect of the triangularity are presented. Finally, in section 8, a brief summary is given.

2. Description of the reference discharge

As mentioned above, the reference input parameters used for the following simulations are based on the best pair of discharges from the dedicated β scaling experiments recently performed in ASDEX Upgrade [5]. These discharges (♯21403-♯21426) are in standard H-mode type-I ELMs regime with pure NBI heating (all details can be found in the latter reference). During this β scan experiment, ρ^*, ν^*, β/B^4, the safety factor q and the plasma shape were kept constant while only β was varied. This means that temperature and density gradient lengths as well as the ratio T_e/T_i were equal in both discharges. Temperature, density and safety factor profiles for the low β shot (♯21403) are plotted in figure 1.

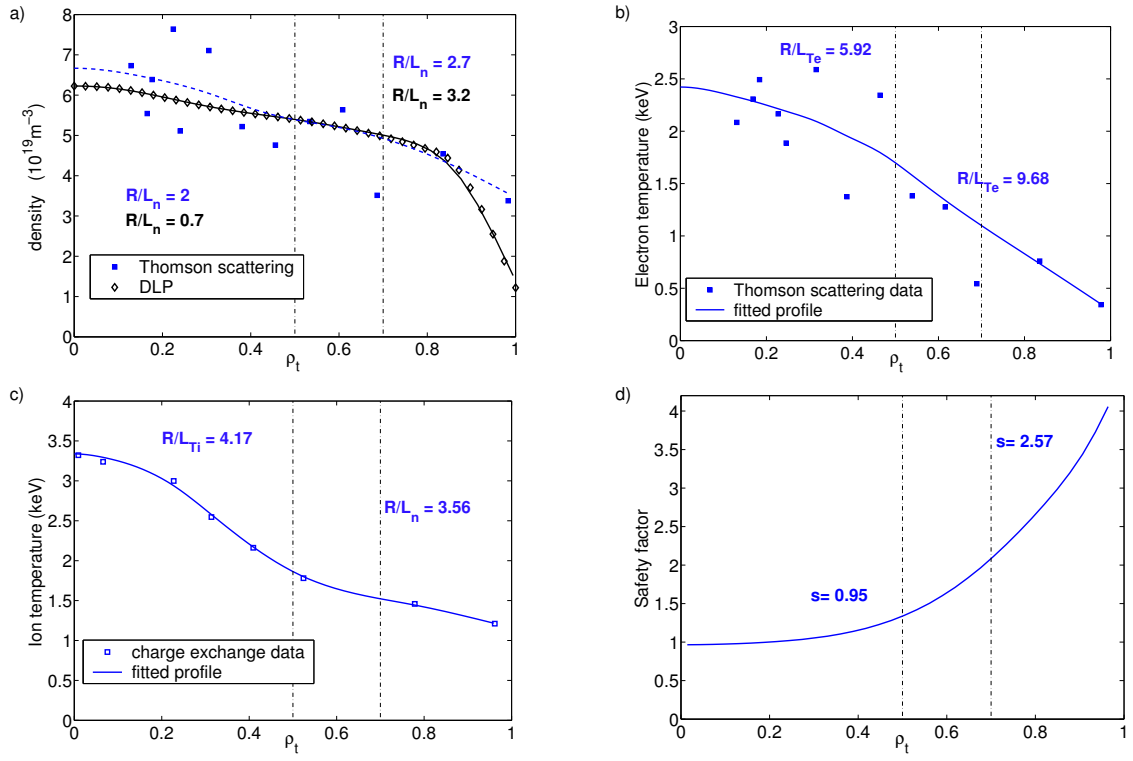

Figure 1. Toroidal radial profiles for the low β discharge ♯21403. Average from $t = [2.8 - 3.4]s$. a) Density profiles from interferometer data combined with lithium beam measurements (DLP) (full line) and from Thomson scattering measurements (dashed line). b) Electron temperature profile. c) Ion temperature profile. d) Safety factor profile.

The main input parameters for numerical simulations at $\rho_t = 0.5$ are : $T_e/T_i = 0.9$, $R/L_n = [0.7; 1.5; 2]$, $R/L_{Te} = 5.92$, $R/L_{Ti} = 4.17$, the electron collision frequency $\nu_e = 0.00279\, log\Lambda n/T_e^{3/2} a\sqrt{m_i/T_i} = 0.16$ and the ion collision frequency $\nu_i = \nu_e\sqrt{m_e/m_i}\,(T_e/T_i)^{3/2}$ with the density in 10^{19} and the temperature in keV. Note that the experimental uncertainty on the gradient length is relatively large. In particular, the estimate of the density gradient length depends on the diagnostic used (cf. figure 1) and may vary significantly (from $R/L_n = 0.7$ to $R/L_n = 2$ at $\rho_t = 0.5$). The Thomson scattering profile is flatter at the edge and more peaked in the core than the profile obtained by combined measurements of interferometer and lithium beam diagnostics. For comparison, the scaling law density peaking from Reference [17] predicts for this discharge $R/L_n \simeq 1.5$. The experimental local-β value ranges between $\beta(\rho_t = 0.5) = 0.88\%$ (low β discharge) and $\beta(\rho_t = 0.5) = 1.48\%$ (high β discharge). All simulations presented in the following have been performed using the GS2 [15, 16] code which solves the gyro-averaged

Vlasov equation coupled to the Maxwell equations. Dynamic of electrons and ions, passing and trapped, is resolved and perturbations of the magnetic field in all directions (i.e., perturbations both parallel $\delta B_{||}$ and perpendicular $\delta B_{\perp}$ to the equilibrium field) are included. Particle collisions are modeled using a Lorentz collision operator. The GS2 code uses the ballooning representation in which the coordinates follow the magnetic field lines (the ballooning angle is noted θ_b).

To reproduce closely the experimental equilibrium, the Miller local equilibrium model [18] was used. The equilibrium input parameters are : the normalized half-width of the flux surface $\rho_c = 0.17$, the local safety factor $q = 1.3$, the local derivative of the Shafranov shift $\Delta' = -0.15$, the local elongation $\kappa = 1.377$ and its derivative $\kappa' = 0.58$, the local triangularity $\delta = 0.03$ and its derivative $\delta' = 0.33$, the magnetic shear $\hat{s} = (\rho/q) \times (dq/d\rho) = 0.95$. For the low β case, $\beta(\rho_t = 0.5) = 0.88\%$ and its local derivative $\beta' = \beta \sum [nT(R/L_T + R/L_n)] = [-0.096; -0.110; -0.118]$ depending on the density gradient length chosen. For the high β case, $\beta(\rho_t = 0.5) = 1.48\%$ and $\beta' = [-0.161; -0.183; -0.197]$.

All simulations have been performed including collisions and only two species were retained which means that the deuterium density is imposed to match the electron density and to verify the quasi-neutrality condition.

3. β scan close to experimental conditions

The β scans presented in this section were performed at $k_\theta \rho_i = 0.4$ where ITG modes, which are supposed to play the main role in heat transport in tokamak plasmas, are strongly unstable. In these simulations β and β' are varied consistently while all other input parameters were kept constant. In the local Miller equilibrium model [18] we used, the Shafranov shift is determined by β', therefore it has also been changed consistently with β. In term of plasma conditions, there are several main differences comparing the present β scan to previous studies. Firstly, the value of the ion temperature gradient length R/L_{Ti} is here taken very close to the ITG threshold while generally $R/L_{Ti} = [6.9-9]$. Secondly, the collisionality in the present simulations is rather high ($\nu^* = \nu_i/(\epsilon\ \omega_{bi}) = 0.05$, where ω_{bi} is the ion bounce frequency). And as third difference, the value of the density gradient length is small (generally $R/L_n = 2 - 2.2$ while here in most of the simulations $R/L_n = 0.7 - 1.5$).

The β scaling of micro-instabilities is very sensitive to the density gradient length while experimentally the uncertainty on this value is rather large. For these reasons, we have analyzed three different values of $R/L_n = [0.7, 1.5, 2]$. The evolutions of the growth rate and the real frequency as a function of β are plotted in figure 2.

For $R/L_n = 2$, ITG modes are the most unstable modes from $\beta = 0$ to $\beta = 4.5\%$. Between $\beta = 4\%$ and $\beta = 4.5\%$, the real frequency as well as the growth rate shows a discontinuity corresponding to the destabilization of KBM. In these specific conditions (R/L_{Ti} close to the ITG threshold), ITG modes are not stabilized with increasing β and the growth rate is very weakly affected by any increase of β. Note that in this scan, β and β' were varied simultaneously, indeed the stabilizing effect of β is balanced by the destabilizing effect of β' (at low β'), via the Shafranov shift. This has been proven by repeating the same scan keeping β' constant : in this case the ITG growth rate clearly decreases with increasing β. For $R/L_n = 1.5$, the behavior of the β scaling of micro-instabilities is similar to the $R/L_n = 2$ case with a slight shift of the KBM threshold toward higher β values (around $\beta = 5\%$).

For $R/L_n < 2$, the behaviour of the growth rate is significantly different from the expected theoretical picture of ITG stabilization with β up to the critical limit where the electromagnetic modes (KBM) become unstable. For $R/L_n = 0.7$, at low β ($\beta = [0 - 1\%]$), the most unstable modes are ITG modes which are stabilized with increasing β. For $\beta > 1\%$, the most unstable modes rotate in the electron direction. Looking at the eigenfunctions of such modes (figure 3), it appears that the electrostatic potential (Φ) is asymmetric with respect to the ballooning coordinate and the electromagnetic potential (A) is symmetric. This is not consistent with ITG,

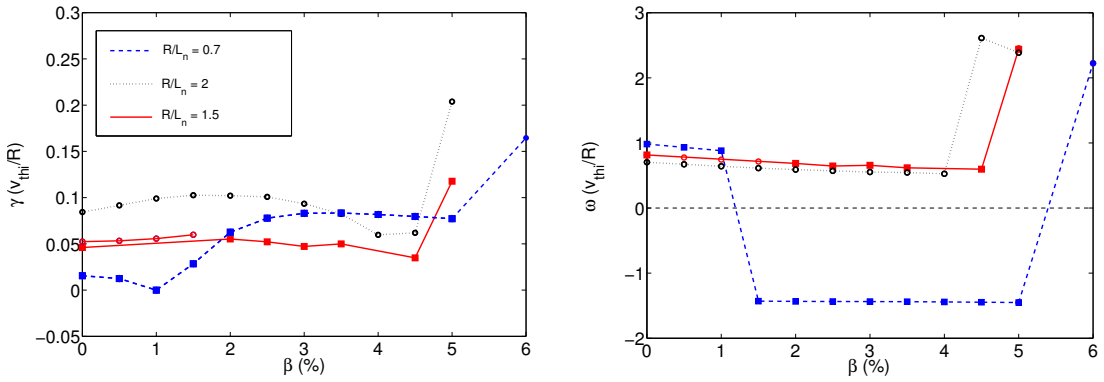

Figure 2. Growth rate and real frequency (normalized to v_{thi}/R where $v_{thi} = \sqrt{T_i/m_i}$ and R is the major radius) vs β for the experimental conditions of the reference shot ♯21403 at $\rho_t = 0.5$ for $R/L_n = 0.7$ (dashed line), $R/L_n = 1.5$ (full line) and $R/L_n = 2$ (dotted line). Simulations were performed on n = 15 toroidal turns (circle symbols) or on n = 79 toroidal turns (square symbols).

Trapped Electron Modes (TEM) or KBM instabilities for which the electrostatic potential (Φ) is symmetric and the electromagnetic potential (A) is asymmetric. This behaviour is the signature of micro-tearing modes which have been yet only detected, in experimental conditions, in high β simulations ($\beta = 10\%$) made for Spherical Tokamak plasmas [21, 22, 23, 24]. Micro-tearing modes are very extended in the ballooning coordinate (θ_b) meaning that they are extremely narrow in term of radial extension. Therefore, they required calculations on large boxes in term of θ_b (∼79 toroidal turns) to be correctly resolved.

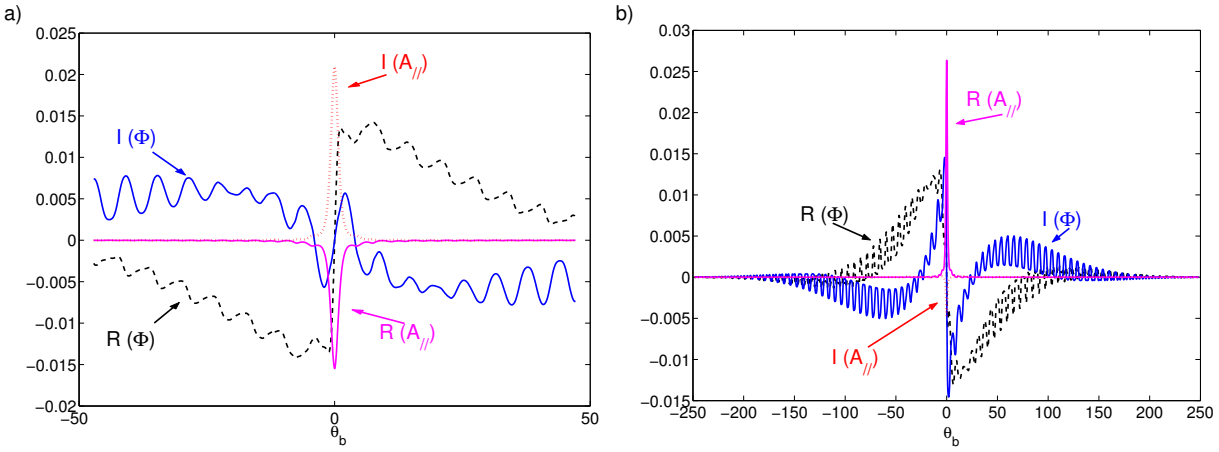

Figure 3. Eigenfunctions for $\beta = 2.5\%$ (a) for simulations performed on n = 15 toroidal turns and (b) for simulations performed on n = 79 toroidal turns as functions of the ballooning angle θ_b.

In calculations performed on narrow boxes, the growth rate of micro-tearing is overestimated and they can artificially appear as the most unstable modes in the system. Therefore, each time micro-tearing modes have been identified as the most unstable modes in a simulation, we have enlarged the box size until convergence was reached (θ_b grid extended up to a factor 5). In all the following figures, square symbols represent runs on large box while circle represent smaller box simulations.

Figure 2 shows that the growth rate of the micro-tearing modes, $\gamma_{\mu t}$, increases with increasing β until a saturation phase is reached, around $\beta \simeq 3\%$. The appearance of micro-tearing modes as most unstable modes is not only due to the ITG stabilization but also to the increase of the micro-tearing growth rate with β, for example, $\gamma_{\mu t}(\beta = 2\%) \gg \gamma_{ITG}(\beta = 0.5\%)$.

In this β scan, micro-tearing modes are the most unstable modes until $\beta = 6\%$ at which value a KBM is destabilized. However, a similar scan has been done with values of β' increased artificially by a factor 1.3 (not consistent with β and gradient length values) in which micro-tearing modes are the dominant micro-instabilities even at $\beta = 9\%$. KBMs have a stronger dependence on β than micro-tearing modes : when they become unstable, they become the most unstable modes as soon as β is slightly increased. This means that in such a case, where β' is artificially increased, KBM are still stable at $\beta = 9\%$.

The effect of changing the temperature gradient length within the experimental error-bars has been also investigated. Simulations of β scans at $k_\theta \rho_i = 0.4$ increasing R/L_{Ti} show that for $R/L_n = 1.5$, the expected β stabilizing effect on ITG is recovered for $R/L_{Ti} \geq 5$. For $R/L_n = 0.7$, the β range in which micro-tearing modes are the most unstable modes is reduced but still exists between $\beta = [2.5 - 4\%]$ even with $R/L_{Ti} = 7$. Similar simulations have been done to study the effect of the electron temperature gradient length R/L_{Te} on the β scaling of micro-instabilities. The results are presented in figure 4.

For $R/L_{Te} = 4$, the most unstable modes are ITG modes between $\beta = [0 - 2]\%$ for which the growth rate decreases with increasing β. For $\beta > 2\%$, the dominant instabilities become micro-tearing modes. Even at $\beta = 5\%$ no KBM is destabilized. Increasing slightly the electron temperature gradient length to $R/L_{Te} = 5$ has a destabilizing effect on ITG. The ITG growth rate increases slightly with increasing β and ITG modes stay the dominant instabilities between $\beta = [3.5 - 5]\%$ instead of micro-tearing modes. At $\beta = 5\%$, KBMs are destabilized. At low β, for $R/L_{Te} = 7$, simulations did not converge. For $\beta \geq 1.5\%$, the behavior of the dominant modes is similar to the β scan for the nominal value $R/L_{Te} = 5.9$ already discussed above. ITG modes which are the most unstable modes until $\beta = 4.5\%$ is very weakly affected by β.

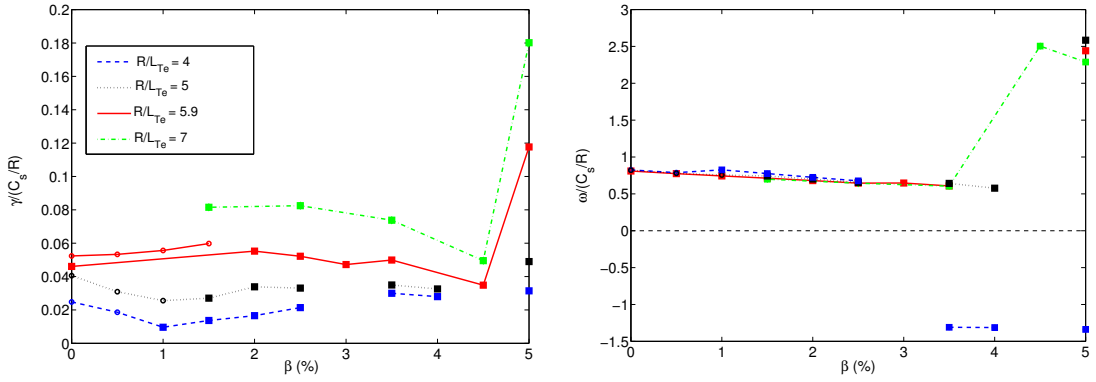

Figure 4. Growth rate and real frequency vs β for various values of R/L_{Te} for $R/L_n = 1.5$ and $k_\theta \rho_i = 0.4$.

From these simulations, the effect of R/L_{Te} on the β scaling of micro-instabilities is not very clear and surprising. In particular, ITG modes are found to be destabilized with increasing R/L_{te} which is not expected from collisionless simulations in which trapped electrons are affected by R/L_{Te} and lead to a stabilization of ITG with increasing R/L_{Te}.

Note that the AUG experiments, used as reference, cover the range $\beta(\rho_t = 0.5) = [0.88 - 1.48]\%$. Simulations show that in this range, the most unstable modes for $R/L_n = 1.5$ and $R/L_n = 2$ (considering nominal values for R/L_T) are ITG modes. The growth rate is slightly

increasing from the low β to the high β (by about 9%). For $R/L_n = 0.7$, at $\beta(\rho_t = 0.5) = 0.88\%$ the most unstable modes are also ITG modes (with a growth rate very close to zero) but for the high β case, micro-tearing modes are the most unstable modes. The appearance of micro-tearing for such small values of β ($\beta < 2$) is rather unexpected especially at wavenumber $k_\theta \rho_i = 0.4$ for which the ITG growth rate is close to its maximum value.

4. Spectrum of micro-instabilities

The simulations discussed in the previous section showed the presence of micro-tearing modes for $R/L_n = 0.7$ at $k_\theta \rho_i = 0.4$. This value of R/L_n is at the lower limit of the experimental error-bars and may be considered too small even for a high collisionality H-mode plasma in ASDEX Upgrade. Therefore in this section, we discuss the spectrum of micro-instabilities for $R/L_n = 1.5$.

Figure 5 shows the linear spectrum of the most unstable modes in the range $k_\theta \rho_i = [0.1 - 0.6]$ for both low and high β cases. ITG modes appeared to be the most unstable modes for $k_\theta \rho_i = [0.2 - 0.5]$ with a maximum in the growth rate at $k_\theta \rho_i = 0.3$ for both values of β. Surprisingly, at lower wavenumber (between $k_\theta \rho_i = [0.1 - 0.2]$) micro-tearing are the most unstable modes. This result shows that even with a standard value of density gradient length, micro-tearing modes may be unstable in H-mode plasmas at low β values. Furthermore, the growth rate of micro-tearing and ITG modes are comparable.

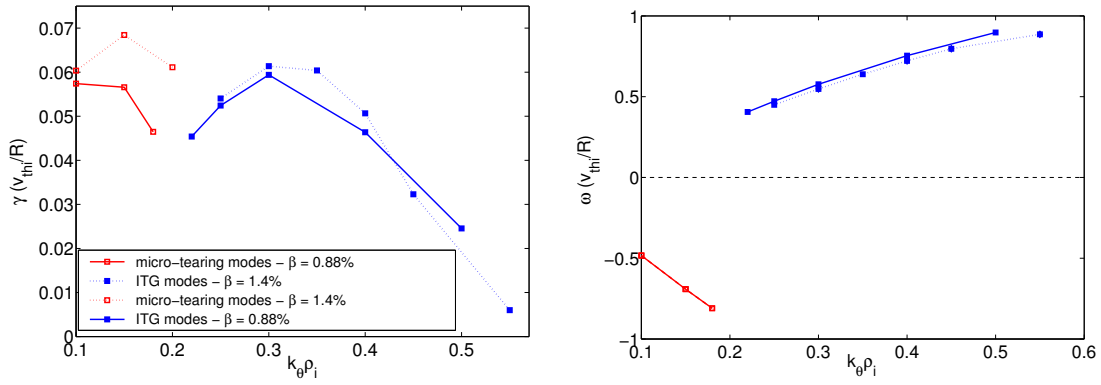

Figure 5. Spectrum for $R/L_n = 1.5$ for the low β case ($\beta = 0.88\%$) and for the high β case ($\beta = 1.4\%$).

However, it is important to underline that even if the poloidal wavenumber is smaller for micro-tearing than for ITG, the radial wavenumber of micro-tearing modes is much higher than the ITG one. This is due to the fact that micro-tearing have a very narrow radial extension. As a result, the average perpendicular wavenumber $k_\perp$, computed by GS2, is a factor of 5 higher for micro-tearing modes ($k_\perp \rho_i = 2.5$) as compared to ITG modes ($k_\perp \rho_i = 0.5$). According to the quasi-linear theory and the mixing length estimate ($\chi \propto \gamma / k_\perp^2$), ITG modes are therefore expected to play the dominant role in heat transport. However, it is well known that during the non-linear evolution, the spectrum of ITG turbulence is down shifted from $k_\theta \rho_i \simeq 0.3$ in the linear phase to $k_\theta \rho_i \simeq 0.15$ in the saturated non-linear phase [20]. In this spectral region, micro-tearing modes are linearly unstable and up to now the non-linear coupling of such modes with ITG modes is not completely understood. In reference [8], it has been shown when ITG modes are stabilized enough by the increase of β, the electron heat transport can become dominated by micro-tearing modes. In addition, it is apparently possible for micro-tearing to exhibit self-sustainment. On another hand, it is not certain that taking the perpendicular wavenumber of

the linear modes as an average yields a reasonable estimate of the transport coefficients especially for electromagnetic modes such as micro-tearing.

In figure 5, it can also be observed that, for both branches, the increase of β has a weak effect on the growth rate and does not affect the real frequency.

The computation of the spectrum for $R/L_n = 0.7$ at $\beta = 0.88\%$ shows that ITG modes are weakly unstable, with a very low growth rate, as seen in figure 2 for $k_\theta \rho_i = 0.4$. Thus, at low density gradient, the micro-tearing branch extends to higher wavenumbers as compared to the $R/L_n = 1.5$ case (between $k_\perp \rho_i = 0.1 - 0.3$), with a comparable value of the growth rate.

5. Stability conditions of micro-tearing

Starting from the input parameters of the low β case with $R/L_n = 1.5$ for $k_\theta \rho_i = 0.15$, we have tried to define the domain in which micro-tearing modes are the most unstable instabilities. It has been found that, in AUG conditions, micro-tearing modes appear to be the most unstable modes when $R/L_{Te} \geq 3$. A minimum of $\beta = 0.4\%$ is required to obtain $\gamma_{\mu t} > \gamma_{ITG}$ and for $\beta > 6\%$ KBMs start to be dominant instabilities even at $k_\theta \rho_i = 0.15$. The micro-tearing threshold in term of collisionality has been found to be between $\nu_e = 0.066$ and $\nu_e = 0.1$.

Up to now, micro-tearing modes have been identified as the dominant micro-instabilities in gyrokinetic simulations applied to experimental discharges [21, 22, 23, 24] only for plasma conditions of the Spherical Tokamak (ST). The plasma parameters of ST discharges are rather different from AUG plasmas conditions. In particular, the plasma shape is different as compared to conventional tokamaks and very high β can be reached in ST (up to a factor 10 higher than in AUG plasmas). The number of parameters which may play a role in the stability of micro-tearing, ITG and TEMs is so large that it is very difficult to make a direct and complete comparison of the present study with MAST [23, 24] publications. However, we would like to underline some specific differences and agreements. The first difference is that, in AUG simulations, micro-tearing modes are the most unstable modes only for a limited part of the spectrum (around $k_\theta \rho_i = 0.15$) and coexist with ITG while on MAST they are dominant over the entire poloidal wavenumber range ($k_\theta \rho_i = [0 - 1]$) with a clear maximum of the growth rate localized around $k_\theta \rho_i = 0.8$. Secondly, the β scaling of the micro-tearing growth rate in MAST conditions exhibits a maximum at $\beta = 15\%$ [24] but these modes are almost completely stable at $\beta = 5\%$. The maximum of the growth rate of micro-tearing modes in MAST is around $\gamma = 7.56 \times 10^5 s^{-1}$ while in AUG simulation, $\gamma = 5.48 \times 10^5 s^{-1}$. These comparable amplitudes at very different β values show that the β scaling of micro-tearing is strongly affected by other plasma parameters. For example, micro-tearing stability is strongly dependent on collisionality [24] and in AUG simulations, ν_e is lower by about a factor of 3 as compared to the MAST case.

6. Effect of the triangularity at $\rho_t = 0.7$

Experimentally, the plasma shape is known to play a role in the quality of the confinement in tokamak plasmas. The increase of the elongation κ and of the triangularity δ is favorable in experiments. For example, it provides a significant increase in the β stability limit in DIII-D [25, 26] and the increase of triangularity changes the plasma edge dynamics (such as ELMs) and leads to an increased edge pressure gradient and consequently to an increase of the confinement time [27]. The effect of plasma shaping has been investigate numerically by several authors [28, 29, 30, 31]. As general results, it has been found that the elongation has a stabilizing effect on ITG mode and TEM while the effect of the triangularity seems to depend itself on the value of the elongation. In the electrostatic limit, δ has been found to be destabilizing at moderate κ and stabilizing at high κ [31]. In electromagnetic simulations, δ is also found to have a stabilizing effect on KBM by increasing the threshold of such modes.

The impact of increasing triangularity, in the conditions of the AUG β scaling experiments, on the micro-instabilities β scaling is explored in this section. As plasma shape affects more the edge, even if in this work we investigate core turbulence, triangularity effects have been study at $\rho_t = 0.7$ to use plasma parameters closer to the edge conditions. The main input parameters at $\rho_t = 0.7$ are : $T_e/T_i = 0.71$, $R/L_n = 3.26$, $R/L_{Te} = 9.68$, $R/L_{Ti} = 3.56$, $\nu_i = 0.0036$ and $\nu_e = 0.35$. For the low β case, $\beta(\rho_t = 0.7) = 0.68\%$ and its local derivative $\beta' = -0.109$. For the high β case, $\beta(\rho_t = 0.7) = 1.08\%$.

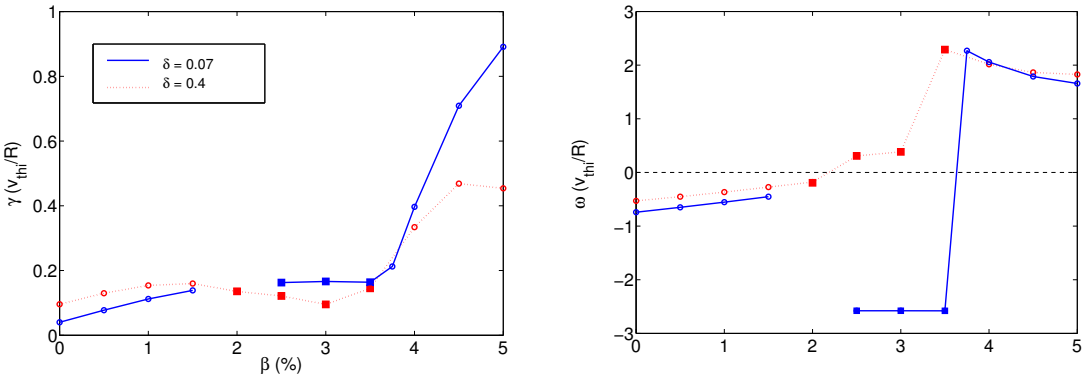

Figure 6. β scaling of the growth rate and the ral frequency at $\rho_t = 0.7$ for $\delta = 0.07$ (full line) and $\delta = 0.4$ (dotted line)

Figure 6 shows the growth rate and the real frequency of the most unstable modes at $\rho_t = 0.7$ for two values of triangularity ($\delta = 0.07$ which is the nominal value in the reference discharge and $\delta = 0.4$ corresponding to the experimental value of a high triangularity AUG plasma). Firstly, in the β scaling under experimental conditions at $\rho_t = 0.7$ ($\delta = 0.07$), it appears that TEMs are the most unstable modes from the electrostatic limit to $\beta = 1.5\%$ and that TEMs are destabilized with increasing β. The fact that TEMs are the most unstable modes for these conditions of low density and high density gradient is not unexpected. It has been found from linear gyrokinetic simulations that in ASDEX Upgrade discharges, with similar gradient lengths than in this present study, TEMs are the dominant instabilities [32]. However, the influence of β on TEMs are not well known and the destabilization of TEM with increasing β is an interesting result which requires deeper investigations.

Note that the experimental range of β values is in the regime of dominant TEM. The growth rate increases by about 30% from the low β ($\beta(\rho_t = 0.7) = 0.68\%$) to the high β case ($\beta(\rho_t = 0.7) = 1.08\%$) while the perpendicular wavenumber computed by GS2, $k_\perp$ decreases from $k_\perp = 5.37$ to $k_\perp = 5.03$. This behavior leads to an increase of the mixing length estimate $\chi \propto \gamma/k_\perp^2$ of about 50%. The simulation performed at $\beta = 2\%$ did not converge and we can observed a jump of the absolute value of the real frequency between $\beta = 1.5\%$ and $\beta = 2.5\%$ which means that the nature of the most unstable modes changed. At $\beta = 2.5\%$, micro-tearing modes are again the dominant instabilities (in these simulations, $k_\theta \rho_i = 0.4$). Another transition appears around $\beta = 4\%$, this time, the real frequency as well as the value of the growth rate jumps. The dominant modes, which rotate in the ion direction, are KBMs.

Now, increasing artificially the triangularity (keeping its derivative constant as compared to the low δ case), no micro-tearing modes appear as the most unstable modes at any value of β. TEMs are also the dominant micro-instabilities at low β and destabilized with increasing β. The β value for which the KBM becomes the dominant instability is not strongly affected by the change of the triangularity.

7. Summary

The β dependence of micro-instabilities have been studied using linear gyrokinetic simulations in experimental conditions of the ASDEX Upgrade dedicated β scan discharges. In such high density H-mode plasmas with low density gradient, it is found that when the ion temperature gradient length is close to the linear ITG threshold, β scaling of micro-instabilities is very sensitive to the density gradient length. The β scaling of micro-instabilities can significantly differ from the expected behaviour in which at low β, ITG modes are stabilized with increasing β until KBMs start to become unstable.

From linear gyrokinetic simulations, KBMs seem not to play a role in the β degradation observed in dedicated ASDEX Upgrade experiements. First, it is found that KBMs are destabilized at value of β clearly above the experimental β range. Even changing the density gradient length and the temperature gradient length within the error-bars do not change this result. The effect of the plasma triangularity on the KBM branch has been also investigated. It shows that at $\rho_t = 0.7$, the increase of the triangularity does not affect strongly the KBMs stability.

It is also shown that for low density gradient length, micro-tearing modes are the most unstable modes already for $\beta = 1\%$. Such modes are dominant at $k_\theta \rho_i = 0.4$ for the specific case of very low density gradient length ($R/L_n = 0.7$) but are also found to coexist with ITG modes for higher value of R/L_n ($R/L_n = 1.5$) at $k_\theta \rho_i = 0.15$ with similar value of the growth rate. These modes, which have a very narrow radial extension, are supposed not to play a crucial role in the turbulent heat transport observed in tokamak plasmas . However, non-linear evolution of such modes and their coupling with ITG modes are not completely understood. Therefore, their role in the β dependence of heat transport is not excluded and deeper investigations are required.

In addition to this, it has been found that, for values of R/L_{Ti} close to the linear ITG threshold, the β dependence of ITG modes is rather different from expected. In these conditions, β has a very weak effect on ITG stability. At low β ($\beta < 2\%$), ITG modes are slightly destabilized with increasing β while the stabilizing effect of β slowly starts for $\beta \geq 2\%$. Even if, in the experimental β range, ITG modes are destabilized with increasing β, the absolute effect is very weak and the perpendicular wavenumber decreases in the same time as the growth rate increases leading to a change in the mixing length estimate which is not in agreement with the observed experimental β degradation.

Finally, the study of the β scaling of micro-instabilities at $\rho_t = 0.7$ has shown that TEMs are the dominant modes and that β has a destabilizing effect on TEM. In this case, not only the growth rate increases with increasing β but also the perpendicular wavenumber decreases. In the experimental β range, the mixing length estimate $\chi \propto \gamma/k_\perp^2$ changes by about 50% from the low β to the high β case. Therefore, TEMs may play a role in the β degradation observed in ASDEX Upgrade.

Acknowledgments

The authors would like to acknowledge W. Dorland and M. Kotschenreuther for providing the gyrokinetic code GS2 and financial support for this work from the EURATOM programme of the European Community in the form of a Individual Fellowship, Contract No FU06-028309.

References

[1] ITER Physics Basis and ITER Physics Expert Groups 1999 *Nuclear Fusion* **39** 2175
[2] Petty C C, Luce T C, McDonald D C *et al.* 2004 *Phys. Plasmas* **11** 5
[3] McDonald D C *et al.* 2004 *Plasma Phys. and Control. Fusion* **46** A-215
[4] Urano H, Takizuaka T *et al.* 2006 *Nuclear Fusion* **46** 781
[5] Vermare L, Ryter F, Angioni C, Peeters A G *et al.* 2007 *Nuclear Fusion* **47** 490
[6] Scott B D 1997 *Plasma Phys. and Control. Fusion* **39** 1635

[7] Snyder P B and Hammett G W 2001 *Phys. Plasmas* **5** 3 744
[8] B.D. Scott 2003 *Plasma Phys. and Control. Fusion* **45** A385
[9] Scott B D 2006 *Plasma Phys. and Control. Fusion* **48** B277
[10] Jenko F and Dorland W 2001 *Plasma Phys. and Control. Fusion* **43** A141
[11] Falchetto G L, Vaclavik J and Villard L 2003 *Phys. Plasmas* **10** 5 1424
[12] Chen Y, Parker S E *et al.* 2003 *Nuclear Fusion* **43** 1121
[13] Parker S E, Chen Y *et al.* 2004 *Phys. Plasmas* **11** 5 2594
[14] Candy J 2005 *Physics of Plasmas* **12** 072307
[15] Kotschenreuther M, Rewoldt G and Tang W M 1995 *Comput. Phys. Commun* **88** 128
[16] Dorland W, Jenko F, Kotschenreuther M and Rogers B N 2000 *Phys. Rev. Lett.* **85** 5579
[17] Angioni C, Weisen H, Kardaun O J W F *et al.* 2007 *Nuclear Fusion* **47** 1326
[18] Miller R L, Chu M S, Greene J M, Lin-Liu Y R and Waltz R E 1998 *Phys. Plasmas* **5** 973
[19] Bourdelle C *et al.* 2003 *Phys. Plasmas* **10** 7 2881
[20] Lin Z and Hahm T S 2004 *Phys. Plasmas* **11** 1099
[21] Redi M H *et al.* 2003 *in Proceedings of 30th EPS Conference on Controlled Fusion and Plasma Physics, St Petersburg*, edited by R. Koch and S. Lebedev (Europoean Physical Society, Mulhouse), ECA Vol. 27A, P4.94
[22] Wilson H R *et al.* 2004 *Nuclear Fusion* **44** 917
[23] Applegate D J and Roach C M *et al.* 2004 *Physics of Plasmas* **11** 11 5085
[24] Applegate D J and Roach C M 2007 *Plasma Phys. and Control. Fusion* **49** 1113
[25] Lazarus E A, Chu M S, Ferron J R *et al.* 1991 *Phys. Fluids B* **3** 2220
[26] Ferron J R, Casper T A *et al.* 2005 *Physics of Plasmas* **13** 056126
[27] Suttrop W *et al.* 2000 *Plasma Phys. and Control. Fusion* **42** A97
[28] Rewoldt G, Tang W M, and Chance M S 1982 *Phys. Fluids* **25** 480
[29] Hua D D, Xu X Q, and Fowler T K 1992 *Phys. Fluids B* **4** 3216
[30] Waltz R E and Miller R L 1999 *Physics of Plasmas* **6** 4265
[31] Belli E A 2006 *PhD thesis*
[32] Peeters A G, Angioni C *et al.* 2005 *Physics of Plasmas* **12** 022505

From this entire work, it appears difficult to clearly conclude about the β dependence of confinement and heat transport. However, since all experiments performed during this study exhibit a β degradation, it is unlikely that β has no impact at all in turbulent transport in actual tokamak plasmas and performance degradation could be expected in future devices. In addition, it should be noted that new experiments have been performed in JET (without my participation) exhibiting a clear β degradation [26]. Therefore, in 2008 all tokamaks which have investigated β scaling have shown a β degradation, while in 2005, DIII-D and JET experiments, cited as reference, claimed that no β degradation is observed in tokamaks. Unfortunately, I do not believe that this turnaround is the result of progress in performing this kind of experiments (even if for sure, progress have been made, notably to measure and control the plasma) but translates the large sensitivity of such dedicated scans. As mentioned above, errors bars on the power indexes deduced from these experiments are quite large (reaching sometimes 100% of the index, which makes no sense). Another important limitation of dedicated dimensionless scans, comes from the fact that such experiments are designed to study the core plasma. However, in H-mode plasmas, the formation and the subsistence of the density pedestal strongly constraints these experiments. In order to match the global and local quantities, the density is largely increased during the high β plasma of such scans, leading to the excessive use of gas puffing, which degrades the edge conditions strongly. Also, the potential role of plasma shape observed in dedicated dimensionless scans, is probably an "edge effect" since the profiles of dimensionless parameters are usually not well matched at the edge.

4. Wavenumber spectrum of density fluctuations

The shape of wavenumber spectrum represents the distribution of fluctuation energy over different spatial scales. In other words, it represents how different spatial scales of turbulence interact and exchange energy with each other. It contains detailed information about the character of underlying instabilities and the mechanisms involved in energy transfer between different scales. The knowledge of the wavenumber spectrum can help us to identify which instability is the dominant one, and to determine which mechanisms cause the cascade of energy (or some other conserved quantity such as enstrophy, free energy etc.). As a result, wavenumber spectrum is one of the few quantities which allow us a high detail comparison (i.e. a "lower order" in contrast to a comparison, merely of χ_i) between experiment and theory. This latter feature, is the main motivation of the work performed on this topic.

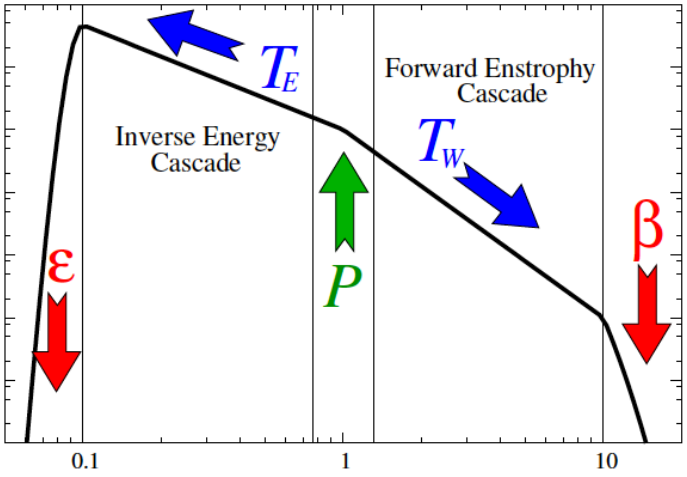

FIGURE 4.1. – Cartoon of the usual 2D cascade assuming that the turbulence is isotropic and homogeneous. Figure is taken from [27]

The fluid theory is interesting here to get a simple understanding of the non-linear dynamics of turbulence, which determines the shape of the wavenumber spectrum. In fluid theory, the wavenumber spectrum is derived using a dimensional analysis. This formulation requires a conserved quantity and the existence of *an inertial range*, a range of scales, for which the production and dissipation of this conserved quantity can be neglected. In 2D, the injection of energy is expected at a given limited scale while the energy is transferred to larger scales via inverse energy cascade or to smaller scales via forward enstrophy cascade, to be dissipated, respectively at larger and smaller scales (see. cartoon presented in figure

4.1). For 2D Euler turbulence, considering the vorticity conservation equation and energy and enstrophy as conserved quantities, the dimensional analysis gives a forward enstrophy cascade range in which the energy scales as $E(k) \propto \beta^{2/3}k^{-3}$ and an inverse energy cascade range in which the energy spectrum is $E(k) \propto \epsilon^{2/3}k^{-5/3}$, corresponding to the well-known Kraichnan-Kolmogorov spectra. It should be noted that in the context of comparison with fluctuations measurements, instead of spectral energy, one has to use fluctuation intensity. Since for Euler turbulence, the spectral energy $E(k) \propto kv^2$ and $v \propto k\phi$, then $E(k) \propto \phi^2/k^3$ and the fluctuations intensity becomes $|\tilde{\phi}_k|^2 \propto k^{-14/3}, k^{-6}$.

It should be emphasised that the existence of an inertial range, in fusion plasmas, is highly questionable. First, the injection is not really localized and there exists a multitude of linear instabilities injecting turbulence energy in various different scales. In addition, dissipation is not truly localized in fusion plasmas either, since the main processes that dissipate turbulence energy are Landau damping and the existence of linearly damped large scale structures (such as zonal flows and GAMs) that feed on turbulence. Both of these may extract energy from micro-turbulence over a wide range of spatial scales.

From a diagnostic point of view, measurements of the wavenumber spectrum (k-spectrum) in fusion plasmas is challenging since it requires a scale selectivity over a certain range of scales and access to the hot, confined plasma without perturbing it. Therefore, there are relatively few measurements of the k-spectrum. Most of the measurements of density fluctuations are based on the detection of radiation mainly coming from the scattering of a probing, electromagnetic beam on the density fluctuations. Micro-waves, with or without cut-off in the plasma, or shorter wavelength beams such as Far-Infra-Red (FIR) ($\lambda = 1.22mm$) [28] or CO_2 ($\lambda = 10.6\mu m$) lasers [29] can be used as probing beams. For example, first measurements of wavenumber spectrum in the range of medium to large wavenumbers (typically $k \sim [5-15]cm^{-1}$) were obtained in 1976 [30] using wave scattering in the ATC (Adiabatic Toroidal Compressor) machine. This technique uses forward scattering of micro-waves to probe the plasma without a cut-off layer in the plasma (unlike the standard reflectometry technique). More common techniques based on forward scattering of electromagnetic waves using lasers have been largely used leading to the first measurements of both poloidal and radial wavenumber spectrum, in 1987, in the TEXT tokamak [31]. This measurement, using FIR laser, exhibits an anisotropy of large scale structures ($k < 5cm^{-1}$) which has been also observed using Beam Emission Spectroscopy (BES) [32, 33], which measures the local density by observing the collisionally excited emission from the deuterium beam particles as they traverse the plasma, interacting with plasma electrons and ions. This anisotropy, at small wavenumbers, is such that while the poloidal wavenumber spectrum peaks around $k_\theta\rho_s = 0.1-0.3$ (corresponding approximatively to $2cm^{-1}$), the radial wavenumber spectrum does not exhibit any maximum at the observed range and decreases continuously from $k_r\rho_s = 0$. This anisotropy is well recovered in gyrokinetic simulations [34] and is coherent with the existence of radially elongated turbulent structures which generate significant energy transport in the radial direction.

Considering a wider wavenumber range, the perpendicular wavenumber spectrum has been measured using laser scattering on Tore Supra [35] between $k_\perp\rho_s = [0.5-2.5]$. Note that here and in the following, the "perpendicular" direction refers to the binormal direction which is defined as the direction that is perpendicular both to the magnetic field line and to the radial direction on the magnetic surface. At small k ($k\rho_\perp \lesssim 1$), it is found to

decrease as $k_\perp^{-3}$, in agreement with early measurements in the tokamak Microtor [36] (using FIR) which found a decrease as $k_\perp^{-3.5}$. Thanks to the improvement of turbulence simulations through the development of gyro-kinetic description and of computing capabilities, comparisons between experiments and simulations in more and more realistic conditions become possible. In particular, a precise comparison has been performed using gyrokinetic simulations, for ion turbulence scales ($k\rho_i \lesssim 1$), and using experimental plasma conditions (as much as possible) of the Tore Supra experiments [37]. The comparison of the perpendicular wavenumber spectrum shows an encouraging agreement in this wavenumber range. Note that the precise comparison required an adequate treatment of the simulation results in order to be consistent with the diagnostic selectivity (integration on the same radial wavenumber range). This specific aspect motivates a subject of research on synthetic diagnostic [38].

The radial wavenumber spectrum has also been measured in Tore Supra in L-mode plasmas using fast sweep reflectometry [39, 40]. At small k (i.e. $k_r\rho_s < 2$), it is found to decrease slightly more slowly than the perpendicular wavenumber spectrum, as $k_r^{-2.5\pm0.25}$, also in agreement with the gyrokinetic simulations mentioned above [37]. However, it was shown that the probing of the edge plasma using micro-wave in X-mode polarization may be affected by non-linear effects of wave propagation leading to a flattening of the measured spectrum [39]. This issue has been addressed using both analytic and numerical studies [41, 42, 43] showing that above a certain threshold (depending mainly on amplitude and correlation length of the density fluctuation and on the probing frequency), the detected signal is largely affected by small angle multi-scattering. This aspect must be kept in mind when studying wavenumber spectra measured using micro-wave scattering.

For $k_\perp\rho_i \geq 1$, the level of fluctuations turns out to decrease much faster for scales smaller than ρ_i, typically with a power law $S(k_\perp) \propto k_\perp^{-6}$. The transition is observed for $1 < k_\perp\rho_i < 2$ [35]. This first observation of a fast decrease was surprising and was not confirmed by numerical simulations, which had to resolve smaller scales in order to adress this issue. These aspects motivate, both, new experimental and theoretical approaches. The latter lead to the derivation of spectral models for drift-wave based on the Hasegawa-Mima [44] and Hasegawa-Wakatani [45] models that include interactions between fluctuations and large scale flow structures. When interaction between a large scale mode (such as zonal flows for example) and the disparate scales are dominant, the steady state spectrum is found to have the form [46] :

$$\delta n^2 \propto k^2/(1+k^2)^2 \tag{4.1}$$

A generalized form, more flexible and permitting the application of the fitting procedure is obtained using, for example an "i-delta" model to relax the adiabatic condition in the Hasegawa-Wakatani model :

$$A_3 \frac{k^{-3}}{(1+\alpha_1 k^2)^2 + \beta_1 k^2} \tag{4.2}$$

It is interesting to mention that using the dimensional analysis for 2D fluid, as discussed above for Kraichnan-Kolmogorov spectrum, the k-dependence of Eq.4.1 can be recovered. This is obtained by adding non-local interactions (in term of wavenumbers) with a single dominant mode (see illustratiion in figure 4.2) and using the Hasegawa-Mima model. While

this approach is not completely rigourous (since different scales are involved), it allows one to emphasise that the main ingredient to obtain this k-spectrum shape is the non-local interaction and the simple model of drift wave turbulence. For a nice and more detailed description of shell model for wavenumber spectrum resolution, one can refer to [27].

Note that in the variety of existing theoretical models that address the question of the shape of the wavenumber spectrum in plasma turbulence, other mechanisms are considered such as damped modes which may play the role of dissipation for small wavenumbers [47, 48] and kinetic effects such as phase mixing (similar to Landau damping) that will create a "transfer" in the phase velocity space [49, 50] in the transfer region of the spectrum ($k_\perp \rho_i \geq 1$). The critical balance hypothesis is then used to couple the parallel and perpedicuar wavenumbers and is also used in the low wavenumber range [51].

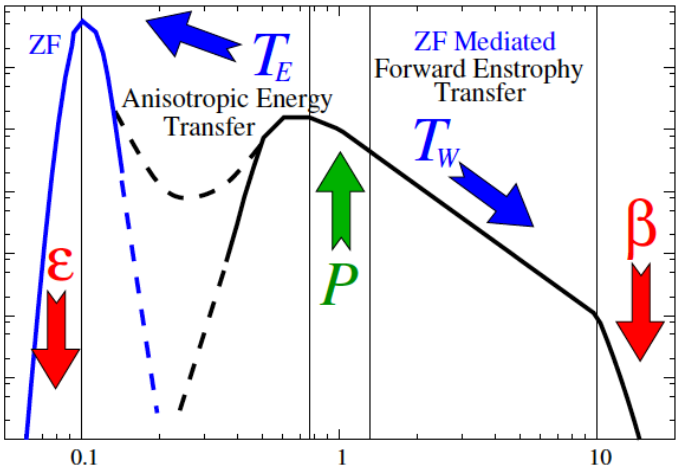

FIGURE 4.2. – The cartoon of the Zonal Flows (ZF) mediated 2D "cascade". Figure is taken from [27]

The novel experimental approach consists of developping a Doppler Back-scattering (DBS) system [52, 53] in order to perform, among other objectives, a specific study of the wavenumber spectrum in L-mode plasmas of the Tore Supra tokamak. The Doppler backscattering system allows the detection of density fluctuations with a high sensitivity, combining advantages from both reflectometry and scattering techniques, namely a good spatial localization and a good scale selectivity, respectively. This technique is detailed in the Annex A.

A first encouraging attempt of DBS measurement was previously performed on Tore Supra [54]. The main part of the system used in the work presented in this manuscript was installed on Tore Supra in 2003. It has two channels in the equatorial plane : one of which operates in the V-band frequency range (50-75 GHz) in ordinary polarization (i.e. O-mode) and a second one covers the W-band (75-110 GHz) in extra-ordinary polarization (i.e. X-mode) [52, 53]. In addition, in 2010, a complementary channel has been installed on the top of the machine with a vertical line of sight. The latter operates in the V-band with an ordinary polarization and has been used essentially in the study presented in the next chapter. Note that in parallel to the DBS development, Upper Hybrid Resonance Scattering (UHRS) [55] system were developed and installed on the small tokamak FT-2

[56]. This system is able to probe small scale density fluctuations using the presence of the resonance, were probing wavenumber and electric field amplitude increase strongly. Performing radial correlation between two close probing frequency channels, one can recover the radial wavenumber spectrum over a large wavenumber range (typically from $k_r\rho_s = 1$ to $k_r\rho_s = 10$). The wavenumber spectrum obtained in FT-2 shows a faster decrease, as k_r^{-7}, for $k_r\rho_s > 2$ [57, 58](figure 4.4), similar to the behavior of the perpendicular wavenumber spectrum [35]. In addition, later on, DBS systems were also installed on AUG and DIII-D tokamaks [59, 60] and on TJ-II stellerator [61]. In AUG, k-spectrum were measured and no fast decrease was observed in the wavenumber range k, reinforcing the necessity of a new investigation on Tore Supra, in which long stationary phase in L-mode plasmas allows detailed turbulence measurements. The experimental study of the k-spectrum performed using DBS in Tore Supra plasmas is presented in the publication included next [Publication 3].

C. R. Physique 12 (2011) 115–122

Contents lists available at ScienceDirect

Comptes Rendus Physique

www.sciencedirect.com

Propagation and plasmas: new challenges, new applications

Wavenumber spectrum of micro-turbulence in tokamak plasmas

Spectre en nombre d'onde de la micro-turbulence dans les plasmas de tokamak

L. Vermare [a,*], Ö.D. Gürcan [a], P. Hennequin [a], C. Honoré [a], X. Garbet [b], J.C. Giacalone [b], R. Sabot [b], F. Clairet [b], Tore Supra Team [b]

[a] *École polytechnique, LPP, CNRS UMR 7648, 91128 Palaiseau cedex, France*
[b] *CEA, IRFM, 13108 Saint-Paul-lez-Durance, France*

ARTICLE INFO

Article history:
Available online 17 March 2011

Keywords:
Tokamak plasma
Micro-turbulence

Mots-clés :
Plasma de tokamak
Micro-turbulence

ABSTRACT

A better understanding of turbulent transport in a tokamak plasma requires precise comparisons between experimental observation and theoretical prediction of micro-turbulence characteristics. The repartition of fluctuation energy over different spatial scales, which contains detailed information about the character of underlying instabilities and the mechanisms involved in energy transfer between different scales, is one of the few quantities allowing a high detail comparison. The present article reports the investigation performed on the Tore Supra tokamak on the wavenumber spectrum of micro-turbulence using Doppler backscattering. The theoretical approach consists of the derivation of spectral models that include interactions between fluctuations and large scale flow structures.

RÉSUMÉ

Une meilleure compréhension du transport turbulent dans les plasmas de tokamak exige des comparaisons précises entre les observations expérimentales et les prédictions théoriques des caractéristiques de la micro-turbulence. La répartition de l'énergie des fluctuations sur les différentes échelles spatiales, qui contient des informations sur le type instabilités sous-jacentes et sur les mécanismes de transfert d'énergie entre échelles spatiales, est l'une des rares quantités permettant une comparaison de niveau élevé. Cet article présente le travail mené sur le tokamak Tore Supra sur l'étude du spectre en nombre d'onde de la micro-turbulence mesuré par rétro-diffusion Doppler. L'approche théorique consiste en la dérivation de modéles spectraux qui inclut les interactions entre les fluctuations et les structures d'écoulement de grandes échelles.

1. Introduction

The performance of most recent tokamaks are limited by the existence of turbulent transport (also denoted as *anomalous transport*) that results in loss of heat, faster than only through the effect of collisions. The main instabilities that underlie turbulent transport in fusion plasmas are now well identified. The spectrum of such instabilities is quite rich and extend over a large range of spatial scales. At the "large scales" of the micro-turbulence range (i.e. relatively smaller wavenumbers),

* Corresponding author.
E-mail address: laure.vermare@lpp.polytechnique.fr (L. Vermare).

1631-0705/$ – see front matter
doi:10.1016/j.crhy.2010.11.003

the main instabilities are the modes driven by the Ion Temperature Gradient (ITG) and Trapped Electron Modes (TEM), where the latter is driven by the electrons trapped in the low magnetic field side of the machine. Both of these modes develop at spatial scales of the order of the ion Larmor radius (typically $\rho_i = [1\text{ mm}–1\text{ cm}]$). At even smaller scales, there are modes driven by the Electron Temperature Gradient (ETG) with spatial scales around the electron Larmor radius (typically $\rho_e = [10\ \mu\text{m}–100\ \mu\text{m}]$). These micro-instabilities are all driven unstable by density and temperature gradients above a certain threshold.

Nonlinearly, turbulence in the core of tokamak plasmas self-organises through the development of large scale structures that back-react on small scale fluctuations. In particular, two kinds of structures have been identified from numerical simulations of turbulence. In the case of ITG turbulence, the linear instability has a so-called ballooning structure that is extended in the radial direction, commonly named streamers, and leads to rapid rise of the ion heat transport. As back-reaction, large scale sheared flows, called "zonal flows" are nonlinearly generated. These tend to regulate the ion heat transport by shearing apart radially elongated linear structures [1]. The existence of such zonal flows has been confirmed by several observations on different machines (for a complete review see [2]) however their roles in the saturated state still remains to be investigated. In addition, while the experimental level of ion heat transport may roughly be explained by the ITG modes, the role of TEM and ETG in the observed electron heat and particle transport also remain an open question.

A better understanding of turbulent transport requires precise comparisons between experimental observations and theoretical predictions. The repartition of fluctuation energy over different spatial scales, as represented by the wavenumber spectrum, contains detailed information about the character of underlying instabilities and the mechanisms involved in energy transfer between different scales. As a result, wavenumber spectrum is one of the few quantities which allow us a high detail comparison (i.e. a "lower order" in contrast to a comparison, merely of χ_i) between experiment and theory.

The first observations of wavenumber spectra of density fluctuations made in the early eighties, showed that the fluctuation energy is concentrated at ion scales, (i.e. at relatively small wavenumbers, $k\rho_i < 1$) [3–7], which correspond to the range for which ITG/TEM are unstable. At these scales, a difference between the radial direction and the poloidal direction is highlighted [3,5,8]. While the anisotropy is clearly manifest for smaller wavenumbers ($k < 2\ \text{cm}^{-1}$), for the larger wavenumbers, the fluctuation energy follows, in both directions, a power law $S(k) = \delta n^2 \propto k^{-\alpha}$ such as $\alpha \approx -3.5 \pm 1$ [9–13]. This behaviour is generally observed for $k\rho_i \lesssim 1$. Thanks to the extension of the spatial scale range of the measurements, a faster decrease of the energy of fluctuations at higher wavenumbers has been observed, for the first time on the Tore Supra tokamak: the spectrum is composed of two power laws, at small k, $S(k) = k^{-3}$ while from $k\rho_i = [1 - 2]$ $S(k) = k^{-6}$ [14]. Similar spectra have, then, been also observed in W7-AS ($k^{-2.8}$ and $k^{-8.5}$) [15] and in FT-2 ($k^{-2.5}$ and k^{-7}) [16]. This kind of spectrum evokes two-dimensional fluid turbulence in which, in addition to a direct cascade that transfer energy from large to small structures, an inverse cascade takes place. However, the similarity between fluid and magnetized plasma turbulence is rather limited. First, in plasmas, injection appears at various different scales. Secondly, as mentioned above, the development of large-scale structures that interact with the background fluctuations is known to impact the saturated state of turbulence possibly more profoundly than the case of fluid turbulence.

Thanks to the impressive improvement of turbulence simulations through the development of gyro-kinetic description and of computing capabilities, comparisons between experiments and simulations in more and more realistic conditions become possible. In particular, it has been recently shown that wavenumber spectrum obtained from gyrokinetic simulations is consistent with experimental observations [17] for ion turbulence scales ($k\rho_i \lesssim 1$). However, the behaviour of the wavenumber spectrum at smaller scales still remains unresolved.

In this article we present the investigation on the wavenumber spectrum shape that we have performed on the Tore Supra tokamak. In order to increase our understanding of plasma turbulence, we use the experimental and the theoretical approaches, in parallel. The theoretical approach involves the use of simple turbulence model, which allows us to isolate specific mechanisms and to study the impact of these mechanisms separately. Thus, on the one hand, we derive spectral shell models to describe the evolution of turbulence spectrum that include large scale flow structures and the interactions between these structures and fluctuations [18]. On the other hand, we extensively used an efficient and flexible diagnostic, during dedicated experiments, to determine wavenumber spectrum with a combined spatial localization and wavenumber resolution over a large spatial scale range and during a single discharge.

Theoretical background and a description of these spectral shell models are given in Section 2. The experimental approach is then detailed in Section 3. We first present the Doppler back-scattering system installed on Tore Supra and the observation of wavenumber spectrum of density fluctuations and how it compares with theoretical results. Then a discussion on perspective works is proposed in the last section.

2. Theoretical considerations

Theoretical understanding of the form of the wavenumber spectrum in plasma turbulence is nowhere near the understanding of wavenumber spectrum in fluid turbulence. There are different approaches, with different implications about the form of the spectrum, some of which are incompatible with each-other. The quasi-linear approach, which involves balancing the linear growth with a weak-turbulence quasi-linear transfer rate [19,20], gives a spectrum in the linearly driven region and explains roughly the shape of the spectrum near the region of the drive ($k_\perp \rho_s \lesssim 0.5$). However especially near, and just beyond $k_\perp \rho_s \sim 1$, the linear growth linked to ITG/TEM modes (the primary sources of energy injection), is almost completely irrelevant. For instance, for the standard ITG mode, nonlinear transfer dominates over the linear growth

approximately around $k_\perp \rho_s > 0.6$ [17], beyond which the spectrum becomes clearly isotropic. This has various interesting implications. First, if we consider a given scale, the energy that enters that scale does not come directly from the instability (i.e. the for which the background gradient is the free energy source), but rather from the nonlinear transfer. The transfer in plasma turbulence involves a process akin to the standard cascade processes of fluid turbulence. However, in addition disparate scale interactions with large scale structures such as Zonal Flows, Geodesic Acoustic Modes (GAMs) or convective cells, are also likely to play a role in the form of the spectrum.

In order to obtain a simple description, it is common to take plasma turbulence as being two dimensional. This is justified by the fact that the fluctuations are generally rather elongated in the direction parallel to the strong confining magnetic field, and have a locally two-dimensional character for the spatial scales of interest. It is also common to take the electron response as being adiabatic for further simplification when one is concerned with the ion Larmor radius scales. This means that the plasma maintains $\frac{\tilde{n}}{n_0} \approx \frac{e\tilde{\Phi}}{T_e}$, so that the parallel force on electrons is zero. If a fluctuation deviates from this, the electrons move rapidly in the parallel direction and re-establish this state. Note the contradiction here, however. We take the plasma as being 2D (i.e. $\nabla_\parallel \approx 0$), yet we say that in order for the force ($F \approx -T_e \nabla_\parallel (\frac{\tilde{n}}{n_0} - \frac{e\tilde{\Phi}}{T_e})$) to vanish it has to be that $\frac{\tilde{n}}{n_0} \approx \frac{e\tilde{\Phi}}{T_e}$. This is in fact resolved by separating the $k_\parallel = 0$ modes (large scale structures, denoted here by $\bar{\Phi}$), from those that have small but nonzero $k_\parallel$ (denoted actually by $\tilde{\Phi}$), that is $\Phi = \bar{\Phi} + \tilde{\Phi}$, and compute the force only from this fluctuating component whose $k_\parallel$ is small but nonvanishing.

2.1. Potential vorticity conservation

The simplest two-dimensional theoretical models of plasma turbulence are reduced fluid models, such as Hasegawa–Mima [21], or Hasegawa–Wakatani [22] models, which are akin to some of the simplest geophysical fluid dynamics (GFD) models such as the Charney model (see for instance [23] for the detailed analogy). The mathematical similarity between these two physically very different systems can be emphasized in particular by using potential vorticity (PV) description. It can be shown that, nonlinear dynamics in these reduced systems conserve potential vorticity.

In the case of fusion plasmas, the potential vorticity defined as $h \equiv n_i^{gc} \approx n - \rho_s^2 \nabla^2 (\frac{e\Phi}{T_e})$ (and is linked to the ion guiding center density n_i^{gc}) is indeed conserved:

$$\frac{\mathrm{d}h}{\mathrm{d}t} = 0$$

In principle, after solving for h, the adiabatic electron response $\frac{\tilde{n}}{n_0} \approx \frac{e\tilde{\Phi}}{T_e}$ can be used to revert the solution that is found for PV in terms of density:

$$\tilde{h}_k = \left(1 + k^2\right)\tilde{\Phi}_k$$

in normalized units (i.e. $x \to x'/\rho_s$, $t = t'\Omega_i$, $\Phi \to e\Phi'/T_e$, $n \to n'/n_0$ etc. where the primed coordinates have physical units). We shall use the conservation of potential vorticity in order to formulate our simple shell model that permits a computation of the wavenumber spectrum when the interaction with the large scale flows are dominant.

2.2. Shell model and wavenumber spectrum

Once it is established that PV conservation is a good approximation to turbulent plasma dynamics, one can use it to build a simple shell model. Such models, which are based on homogeneous, isotropic turbulence, and local interactions are used commonly in fluid dynamics and they can be used to

1. obtain the steady state spectrum by finding the fixed points of the shell model
2. study nonlinear dynamics, intermittency etc. by numerically integrating them in time

In order to be applicable to fusion plasma systems we include local as well as disparate scale interactions. Since we are interested mainly on the small scales, we integrate over the large scale structures as a single $k_\parallel = 0$ mode with an average perpendicular wavenumber denoted by q.

Nonlinear interactions in a PV conserving system, or the particular example of Hasegawa–Mima model, conserve energy and generalized enstrophy. Similarly the nonlinear interactions in Hasegawa–Wakatani model conserve kinetic and internal energies and a generalized helicity-like term involving both density and electrostatic potential. When the disparate scale interactions with a large scale flow are allowed, the main conserved quantity takes the form of potential enstrophy (i.e. $W = h^2$). Note that it is the "total" potential enstrophy (fluctuations + large scale flows) that is conserved, which suggests that it is in fact potential enstrophy that is exchanged between fluctuations and large scale flows.

Taking $k_n = g^n k_0$ where $g > 1$ is a parameter denoting shell spacing, above observations allow us to build a shell model that conserves potential enstrophy. The model has the form [18,24]:

$$\frac{\partial}{\partial t} h_n - \gamma_n h_n - \alpha p k_n \left(\bar{\Phi} h_{n+1} - g^{-1} \bar{\Phi} h_{n-1}\right) = \alpha p k_n \left(\bar{h} \Phi_{n+1} - g^{-1} \bar{h} \Phi_{n-1}\right) + C(h, \Phi) \tag{1}$$

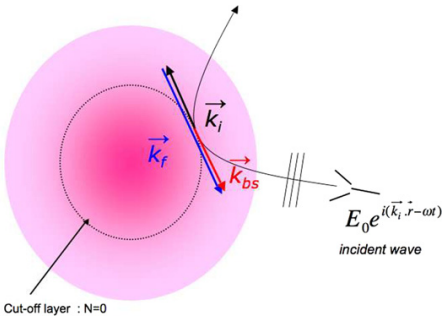

Fig. 1. Illustration of the principle of the Doppler backscattering system.

where γ_n represent linear growth and α is a "free" parameter for the shell-model, representing the strength of the nonlinear term. Here the wave collision term:

$$C(h,\Phi) \equiv \alpha' k_n^2 \left\{ g^{-3}(\Phi_{n-2}h_{n-1} - \Phi_{n-1}h_{n-2}) - g^{-1}(\Phi_{n-1}h_{n+1} - \Phi_{n+1}h_{n-1}) + g(\Phi_{n+1}h_{n+2} - \Phi_{n+2}h_{n+1}) \right\} \tag{2}$$

describes the local cascade. The mean PV equation can be written as:

$$\frac{\partial}{\partial t}\bar{h} - \sum_n \alpha g^{-1} k_n (\Phi_n h_{n-1} - \Phi_{n-1} h_n) = 0 \tag{3}$$

The model as given by (1)–(3), describes the coupled evolution of large and small scales. Of course one should also add a damping term (or take γ_n as being negative) for large n (i.e. large k). If we use $h_n \sim \Phi_n(1+k_n^2)$ one can show that $\Phi_n \sim k_n^{-4/3}$ and $\Phi_n \sim k_n^{-2}$ make $C(h,\Phi)$ vanish exactly. This means that the solution when the local interactions dominate has the basic form $E(k) \propto \{k^{-5}, k^{-11/3}\}(1+k^2)$. In contrast, when the disparate scale interactions with $\bar{\Phi}$ are dominant we find that $h_n \propto k^{-1/2}$, which gives $W(k) \propto k^{-2}$. If we interpret potential enstrophy as enstrophy and link it to the Euler 2D problem, this is apparently equivalent to the Saffman's solution [25] written for enstrophy. Now if we relate $W(k)$ to the discrete Fourier transform, and note that $W(k) \sim |h_{\mathbf{k}}^2|k$, where $h_{\mathbf{k}} \propto (1+k^2)\Phi_{\mathbf{k}}$ and that $\Phi_{\mathbf{k}} \approx n_{\mathbf{k}}$ we find that

$$|n_{\mathbf{k}}|^2 \propto |\Phi_{\mathbf{k}}|^2 \propto \frac{k^{-3}}{(1+k^2)^2} \tag{4}$$

This is the spectrum, when the disparate scale interactions dominate over the local interactions in plasma turbulence. We obtained it here as the solution of a simple shell model in the limit when the local interactions are dropped. In fact, the result is more generic, and is simply due to the form of the nonlinearity as modified by the fact that the electrons cannot respond to large scale modes and the nonlinear interactions are mediated by the large scale flows.

3. Doppler back-scattering system

Different types of diagnostic systems are generally used in order to measure and characterize density fluctuations in hot magnetized plasmas where probes and cameras are not usable. Among those are two major diagnostic families which rely on scattering of electromagnetic waves on plasma fluctuations. On one hand, there is reflectometry that uses microwave frequency range to obtain a cut-off layer inside the plasma. In this case, the probing wave reflected from the plasma is detected and analysed to extract information about the density fluctuations in the vicinity of the cut-off layer (the layer where the refractive index vanishes and the probing wave gets reflected). Major advantages of this method are high sensitivity and excellent localization of the measurement. On the other hand, there are wave-scattering systems based on the detection of probing waves scattered by the fluctuations of the plasma [3,26,27]. The choice of the angle between the emitter and the receptor, permits selecting the spatial scale of the detected fluctuations (elastic scattering). This selectivity in wavenumber is the main advantage of this kind of system.

The Doppler backscattering system combines advantages from both reflectometry and scattering techniques. It is based on the detection of the field backscattered on density fluctuations in the vicinity of the cut-off layer. In practice, the probing wave is chosen in the microwave range and is launched in oblique incidence with respect to the normal of iso-index surfaces (angle α) thereby only the back-scattered signal (no or little reflected signal is received) is detected by the emitter antenna, which also serves as a receptor. The fluctuations whose wavenumber matches the Bragg rule $\vec{k}_f = -2\vec{k}_i$ are selected exclusively, where $\vec{k}_i$ and $\vec{k}_f$ are the local wave-vectors of the probing beam and the density fluctuations respectively (cf. Fig. 1). This technique thus provides the instantaneous spatial Fourier analysis of density fluctuations, $\tilde{n}(\vec{k},t) = \int_V n(\vec{r},t)e^{i\vec{k}\cdot\vec{r}}d\vec{r}$, acting as a band pass filter in k-space around $k = k_0 \sin\alpha$ at the cut-off layer. The radial localization of the measurements

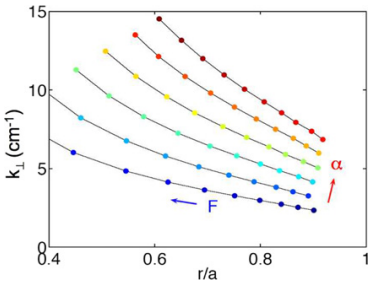

Fig. 2. Mapping r/a vs. k of Doppler backscattering system (V-band, O-mode) measurements for a typical Tore Supra discharge.

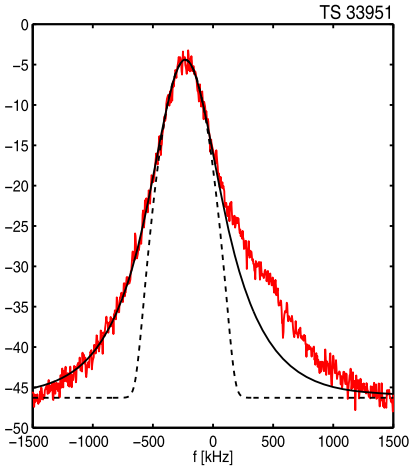

Fig. 3. Frequency spectrum of density fluctuations measured using Doppler backscattering system. The spectrum is Doppler shifted with $V_\perp = 2\pi f_D$.

is provided by two combined effects: a propagation effect and an effect linked to an intrinsic characteristic of the plasma turbulence. First, back-scattering processes are strongly amplified close to the cut-off layer due to swelling of the incident field near the cut-off layer. Secondly, the physical fluctuation energy in the large radial wavenumbers (that interact with the incident beam along the beam trajectory towards the cut-off layer) is quite low, leading to a good localization of the measurement.

The system installed on Tore Supra has two channels [28]: one channel operates in V-band range of frequencies in ordinary polarisation while the second one covers the W-band in extra-ordinary polarisation. These channels allow us, respectively, to probe the plasma from $r/a = 0.5$ to $r/a = 0.9$ (where $r/a = 0$ is the center of the plasma and $r/a = 1$ corresponds to the last closed flux surface) for wavenumber $k = 3$–20 cm^{-1} and from $r/a = 0.85$ to $r/a = 1$ with $k = 2$–25 cm^{-1}. Gaussian optics are used to control the scattering volume (for more details see [29]). However, due to the long distance between the antenna and the plasma, the waist of the Gaussian beam remains distant from the scattering zone in contrast with the conditions of the analysis of optical mixing in scattering experiments reported in [30] and with other similar systems [31,32].

The radial position and the wavenumber of the probing wave at the cut-off layer are determined using a 3D beam tracing code [33] simulating the propagation of a Gaussian beam in a stationary plasma represented by a radial density profile (measured using fast-sweep reflectometers [34]) and an equilibrium profile of the magnetic field (only needed in the case of extra-ordinary polarisation). An example of measurements mapping for a typical Tore Supra discharge is shown on Fig. 2. The wavenumber selectivity $\triangle k$ is related to the refraction of the Gaussian beam during its propagation and can be evaluated directly from the beam tracing code [35,36].

The power spectral density is Doppler shifted $\triangle\omega = \vec{k}_f.\vec{v}_f$ due to the perpendicular (to the field lines) movement of density fluctuations (cf. Fig. 3). This property allows us to determine the fluctuation velocity at the cut-off layer and is the most currently used property by present Doppler systems for studying plasma flows [37], radial electric field profile [38,39] and instantaneous velocity field [31,40].

The integration of the power spectral density gives the power of fluctuations contained at a radial position and at a specific spatial scale. The measurement of spectra at a large number of couple $(F, \alpha) \leftrightarrow (r, k)$ allow us to resolve the

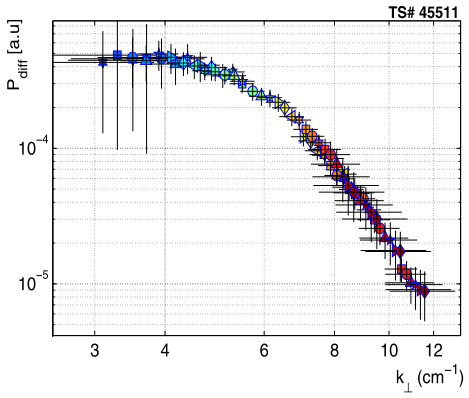

Fig. 4. Example of wavenumber spectrum measured on Tore Supra discharge.

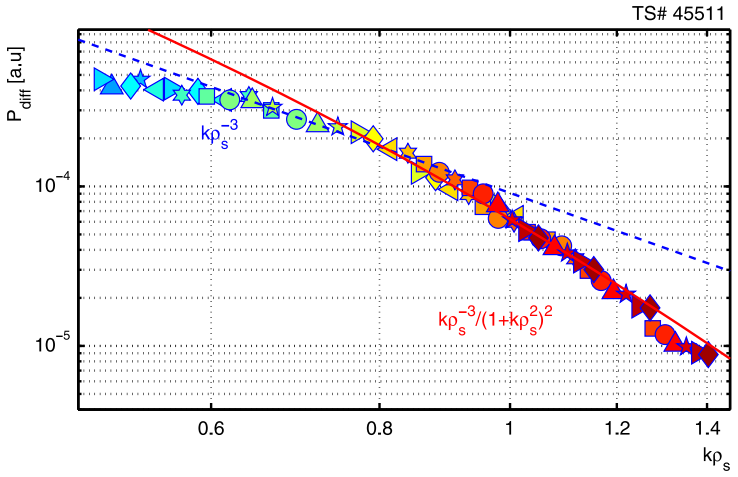

Fig. 5. Experimental wavenumber spectrum of density fluctuations during the discharge 45 511 compared with power law $k\rho_s^{-3}$ (in blue) and the shell model $k\rho_s^{-3}/(1+k\rho_s^2)^2$ (in red).

wavenumber spectrum with a very high discretization such as the one plotted in Fig. 4. Error-bars reported on this figure are evaluated as follows. As mentioned just above the selectivity in k is evaluated directly from the beam tracing code. Then uncertainties on the radial density profile must be also taken into account to determine the resolution in k. The evaluation of the uncertainties on the δn^2 is less trivial. First, there is an impact of the amplitude of the incident signal that differs for each probing frequency. This is corrected using a calibration technique which is not completely perfect and that must be included in the evaluation of the error bars. Secondly, the efficiency of back-scattering processes may be wavenumber dependent. This effect seems to be relevant, only for very small wavenumbers [41–43]. Finally, a small uncertainty coming from the integration process must be included as well.

4. Shape of the wavenumber spectrum

Thanks to the steady-state operation of the Tore Supra tokamak and to the flexibility of the Doppler backscattering system installed on it, we can scan a large number of probing frequency and incident angle pairs (F, α) and obtain the wavenumber spectrum with a high level of resolution in terms of wavenumber discretization. Fig. 5 presents the wavenumber spectrum of density fluctuations measured around $r/a = 0.8 \pm 0.08$ during the discharge #45 511. This spectrum corresponds to a typical discharge of Tore Supra at $B = 3.8$ T, in which the plasma is heated using Ion Cyclotron Resonance Heating system and performed during dedicated experiments (to study the impact of dimensionless parameters such as $\nu*$ on transport and turbulence). As shown in Fig. 5, at small wavenumber ($k\rho_s \leqslant 0.6$) the spectrum seems to saturate. This behaviour corresponds to the characteristic feature of the linear part of the spectrum as discussed in Section 2 and is roughly consistent with a Gaussian shape, thought to be linked to the linear growth rate of the ITG/TEM mode. In

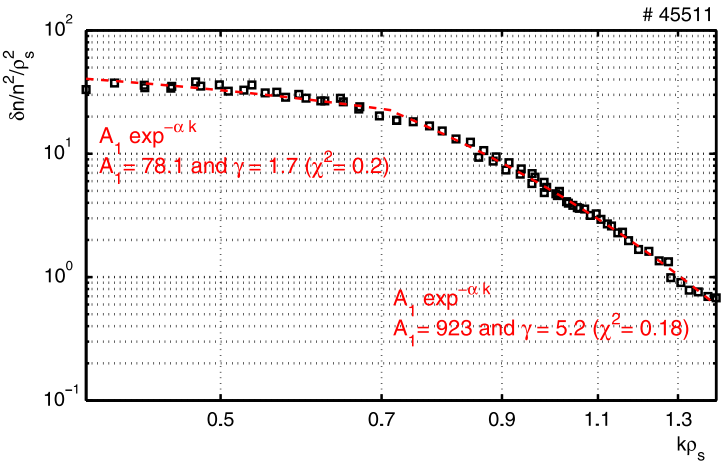

Fig. 6. Experimental wavenumber spectrum of density fluctuations of the discharge 45 511 (in black squares) fitted using two exponential functions.

contrast, for the range of wavenumbers $k\rho_s = [0.6–0.9]$, it follows a power law as $s(k) \propto k^{-3}$ and starts to decrease faster for higher wavenumbers, consistently with previous observations [14]. This form is correctly described using the shell model (4) for $k\rho_s = [0.7–1.2]$. Note that the shell model expression does not have any fitting parameters (apart from the fluctuation level). Therefore, the correct agreement between experiment and this model is remarkable and suggests that interaction between disparate scales including zonal flows is an important ingredient to determine the wavenumber spectrum shape. As already noticed in [14], the wavenumber spectrum may also be fitted using exponential functions. Fig. 6 presents the same wavenumber spectrum as before, but this time fitted using two separate exponential functions. For the smaller wavenumber ($k\rho_s < 0.7$), the measurements are well fitted using an exponential as $e^{-1.7k\rho_s}$. This wavenumber range corresponds to the anisotropic part of the spectrum and is labelled in the figure as the "linear part". Although nonlinear processes inevitably affect this region as well, it appears mainly as the region of energy injection from the plasma micro-instability, driven unstable by gradients in background profiles. In the range of larger wavenumbers, where the nonlinear interactions and the energy transfer dominate, the spectrum has the form: $e^{-5.2k\rho_s}$. This region is akin to the inertial range in fluid turbulence, even though the dominant mechanism for energy transfer may be different and some residual instabilities may exist in this region, due to the final form of the spectrum, the energy these instabilities can inject (i.e. $\propto \gamma_k P$) is quite small.

5. Results and discussion

The wavenumber spectrum gives the repartition of fluctuation energy over different spatial scales. In the present study, we use the wavenumber spectrum of density fluctuations to obtain detailed information about the character of underlying instabilities and to study the mechanisms involved in energy transfer between different scales. For this end, we employed an experimental approach using the Doppler backscattering system installed on the Tore Supra tokamak, which allow us to diagnose the shape of the wavenumber spectrum, accurately, over various discharges. In addition, we employed a theoretical approach based on the study of nonlinear transfer using simple shell models, derived from reduced descriptions of plasma turbulence based on conservation of potential vorticity. During the experimental studies, where various plasma conditions are tested, two main characteristics of the spectrum has been noted. We observed first that the wavenumber spectrum is composed of two regions: at the smaller wavenumbers ($k\rho_s < 0.7$), a region of energy injection from the main instability/instabilities where the spectrum is rather flat and decreases slowly in our range of observation; at larger wavenumbers ($k\rho_s > 0.7$), a region of energy transfer in which the spectrum decreases in a steady fashion. Secondly, the shape of the spectrum in this energy transfer range is found to be well described by the simple form $k^{-3}/(1+k^2)^2$ (Eq. (4)) suggesting that the interactions between large scale flow structures and fluctuations may play an important role in determining the wavenumber spectrum shape. However, note that this part of the spectrum is also well represented by an exponential function. These results lead to a picture of wavenumber spectrum different from that of fluid turbulence. While in the standard picture of fluid turbulence, the energy transfer takes place mainly via local cascade processes, in magnetized plasmas, nonlocal interactions between disparate scales seem to play a dominant role in determining the form of the spectrum. In particular the interactions between small scale fluctuations and large scale flow structures that are driven by the turbulence/instabilities themselves appear to be rather important. In addition, in plasma turbulence, the injection of energy is intrinsic, driven by micro-instabilities and may be important at various different scales while in the standard fluid dynamical study of turbulence the energy injection is usually taken to be well localized in k-space and is assumed to be externally sustained. Another difference between turbulence spectrum in fluids and plasmas comes from the dissipation processes: in fluid turbulence, dissipation of the forward cascading conserved quantity (such as energy for 3D turbulence or enstrophy

for 2D turbulence) affects only small scales while in plasmas, kinetic effects such as Landau damping may appear at various scales depending on the details of parallel dynamics. Finally, the conserved quantities are different. In 2D fluid description, the enstrophy is the main invariant that cascades forward, whereas in plasma turbulence, formulated as a reduced 2D turbulence problem, it is the potential enstrophy that is conserved. In order to characterize the energy injection range and the effects of changing the energy injection on the energy transfer range (or more accurately, potential enstrophy transfer range) one should investigate the effects of changing various plasma parameters. Studying the impact of relevant plasma parameters (such as collisionality, normalized Larmor radius etc.) on the wavenumber spectrum shape, will allow future research to identify the importance of linear phenomena (which is sensitive to plasma parameters) vs. nonlinear processes (which is insensitive to plasma parameters). Moreover, the question of electron thermal transport, and therefore the detection of small scale turbulence, linked possibly to ETG modes at a detail and resolution comparable to that of ion turbulence remains as an important and interesting challenge.

Acknowledgements

This work was carried out within the framework the European Fusion Development Agreement (EFDA) and the French Research Federation for Fusion Studies (FR-FCM). It is supported by the European Communities under the contract of Association between Euratom and CEA. The views and opinions expressed herein do not necessarily reflect those of the European Commission. Financial support was also received from Agence Nationale de la Recherche under contract ANR-06-BLAN-0084.

References

[1] Z. Lin, T.S. Hahm, W.W. Lee, W.M. Tang, R.B. White, Science 281 (1998) 1835.
[2] G.R. Tynan, A. Fujisawa, G. McKee, Plasma Physics and Controlled Fusion 51 (2009) 113001.
[3] C. Surko, R. Slusher, Phys. Rev. Lett. 37 (1976) 1747.
[4] R. Watterson, R. Slusher, C. Surko, Phys. Fluids 28 (1985).
[5] C. Ritz, D. Brower, T. Rhodes, R. Bengtson, S. Levinson, J.N.C. Luhmann, W. Peebles, E. Powers, Nuclear Fusion 27 (1987).
[6] D. Brower, W. Peebles, J.N.C. Luhmann, Nuclear Fusion 27 (1987).
[7] H. Weisen, C. Hollenstein, R. Behn, Plasma Physics and Controlled Fusion 30 (1988) 293.
[8] R.J. Fonck, G. Cosby, R.D. Durst, et al., Phys. Rev. Lett. 70 (1993) 3736.
[9] A. Semet, A. Mase, W.A. Peebles, N.C. Luhmann, S. Zweben, Phys. Rev. Lett. 45 (1980) 445.
[10] TFR-Group, A. Truc, Plasma Physics and Controlled Fusion 26 (1984) 1045.
[11] P. de Simone, D. Frigione, F. Orsitto, Plasma Physics and Controlled Fusion 28 (1986) 751.
[12] F. Gervais, in: 19th EPS Conf. Plasma Phys., 1992.
[13] S. Paul, N. Bretz, R. Durst, R. Fonck, Y. Kim, E. Mazzucato, R. Nazikian, Phys. Fluids B 4 (1992).
[14] P. Hennequin, R. Sabot, C. Honoré, et al., Plasma Physics and Controlled Fusion 46 (2004) B121.
[15] N. Basse, IEEE Trans. Plasma Sci. 36 (2008) 458.
[16] A.D. Gurchenko, E.Z. Gusakov, D.V. Kouprienko, S. Leerink, A.B. Altukhov, J.A. Heikkinen, S.I. Lashkul, L.A. Esipov, A.Y. Stepanov, Plasma Physics and Controlled Fusion 52 (2010) 035010.
[17] A. Casati, T. Gerbaud, P. Hennequin, C. Bourdelle, J. Candy, F. Clairet, X. Garbet, V. Grandgirard, O.D. Gürcan, S. Heuraux, et al., Phys. Rev. Lett. 102 (2009) 165005.
[18] Ö.D. Gürcan, P. Hennequin, L. Vermare, X. Garbet, P.H. Diamond, Plasma Physics and Controlled Fusion 52 (2009) 045002.
[19] T.S. Hahm, W.M. Tang, Phys. Fluids B 3 (1991) 989.
[20] N. Mattor, P.H. Diamond, Phys. Fluids B 1 (1989) 1980.
[21] A. Hasegawa, K. Mima, Phys. Fluids 21 (1978) 87.
[22] A. Hasegawa, M. Wakatani, Phys. Rev. Lett. 50 (1983) 682.
[23] W. Horton, A. Hasegawa, Chaos: An Interdisciplinary Journal of Nonlinear Science 4 (1994) 227.
[24] Ö.D. Gürcan, X. Garbet, P. Hennequin, P.H. Diamond, A. Casati, G.L. Falchetto, Phys. Rev. Lett. 102 (2009) 255002.
[25] P.G. Saffman, Studies in Applied Mathematics 50 (1971) 377.
[26] E. Mazzucato, Phys. Rev. Lett. 36 (1976) 792.
[27] A. Truc, A. Quemeneur, P. Hennequin, et al., Rev. Sci. Inst. 63 (1992) 3716.
[28] P. Hennequin, C. Honoré, A. Truc, et al., Rev. Sci. Inst. 75 (2004) 3881.
[29] P. Hennequin, C. Honoré, A. Truc, A. Quéméneur, C. Fenzi-Bonizec, C. Bourdelle, X. Garbet, G. Hoang, the Tore Supra Team, Nuclear Fusion 46 (2006) S771.
[30] E. Holzhauer, J. Massig, Plasma Physics 20 (1978) 867.
[31] M. Hirsch, E. Holzhauer, Plasma Physics and Controlled Fusion 46 (2004) 593.
[32] V. Bulanin, M. Efanov, Plasma Physics Reports 32 (2006) 47.
[33] C. Honoré, P. Hennequin, A. Truc, A. Quemeneur, Nuclear Fusion 46 (2006) S809.
[34] F. Clairet, C. Bottereau, J. Chareau, R. Sabot, Rev. Sci. Inst. 74 (2003) 1481.
[35] M. Hirsch, E. Holzhauer, J. Baldzuhn, B. Kurzan, Rev. Sci. Inst. 72 (2001) 324.
[36] V. Bulanin, in: 29th EPS Conf. Plasma Phys., vol. 26B, 2002.
[37] P. Hennequin, in: 26th EPS Conf. Plasma Phys., 1999.
[38] G.D. Conway, J. Schirmer, S. Klenge, W. Suttrop, E. Holzhauer, the ASDEX Upgrade Team, Plasma Physics and Controlled Fusion 46 (2004) 951.
[39] E. Trier, L.G. Eriksson, P. Hennequin, C. Fenzi, C. Bourdelle, G. Falchetto, X. Garbet, T. Aniel, F. Clairet, R. Sabot, Nuclear Fusion 48 (2008).
[40] V. Bulanin, A. Petrov, M. 'Yefanov, in: 30th EPS Conf. Plasma Phys., vol. 27J, 2003.
[41] F. da Silva, S. Heuraux, N. Lemoine, C. Honoré, P. Hennequin, M. Manso, R. Sabot, Rev. Sci. Inst. 75 (2004) 3816.
[42] E. Blanco, T. Estrada, Plasma Physics and Controlled Fusion 50 (2008) 095011.
[43] C. Lechte, IEEE Trans. Plasma Sci. 37 (2009) 1099.

4. Wavenumber spectrum of density fluctuations

The first main results of this work is that the general behavior of the k-spectrum is coherent with the previously observed spectra [35] ; the wavenumber spectrum is composed of two regions : at the smaller wavenumbers ($k\rho_s < 0.7$) the spectrum is rather flat and decreases slowly corresponding to a region of energy injection from the main instabilities while at larger wavenumbers($k\rho_s > 0.7$), a region of energy transfer, the spectrum decreases faster. The fact that the shape of the spectrum measured using two different systems (scattering of CO_2 laser and DBS) is similar gives confidence in the reliability and reproducibility of the measurement. Notably, with regards to the possibility of non-linear effects of the propagation of micro-waves.

The second main result of the paper presented above, is that the shape of the spectrum in this energy transfer range is found to be well described by the simple form $k^{-3}/(1+k^2)^2$ obtained from a theoretical approach consisting of the derivation of spectral models that include interactions between fluctuations and large scale flow structures [46]. This result suggests that these latter may play an important role in determining the wavenumber spectrum shape.

4.1. Effect of collisionality on the wavenumber spectrum shape

To investigate deeper the role of large scales structures in turbulence saturation, we study the effect of collisionality on the wavenumber spectrum. In fact, it is well known that collisionality plays an important role on the dynamics of such large-scale structures whether they are zonal flows (ZF) or geodesic acoustic modes (GAMs). It is commonly argued for instance that the effect of collisionality on zonal flows might lead to an increase rather than a decrease of the fluctuation levels when the level of collisions is increased. The argument is based on the idea that the fluctuation level is usually set by the turbulence reduction by shearing via zonal flows [62] and not by the collisional dissipation. Thus, for instance, if the collisionality is increased, the zonal flow level should decrease which should then lead to the turbulence fluctuation levels to increase. In reality, of course collisions are expected to play a dual role, since increasing collisionality would also lead to stronger damping on the fluctuations and a larger range of wave-numbers where the energy is dissipated (i.e. smaller “inertial” range). It is not a priori known which of these effects would be the dominant one in real experimental conditions. Moreover, collisions may also change the nature of the linear instability mechanism and thus the character of energy injection. In contrast, increasing the collisionality should not change the nature of the nonlinear interactions. It would change however, the slow nonlinear dynamics, represented by predator-prey oscillations.

Knowing the advantages of the dimensionless approach, we performed dedicated ν^* scans in the Tore Supra tokamak. Analysis and interpretation of the best scan obtained is presented in the following publication [Publication 4].

Impact of collisionality on fluctuation characteristics of micro-turbulence

L. Vermare,[1] P. Hennequin,[1] Ö. D. Gürcan,[1] C. Bourdelle,[2] F. Clairet,[2] X. Garbet,[2] R. Sabot,[2] and the Tore Supra Team
[1]*Ecole Polytechnique, LPP, CNRS UMR 7648, 91128 Palaiseau, France*
[2]*CEA, IRFM, F-13108 Saint-Paul-lez-Durance, France*

(Received 24 September 2010; accepted 20 December 2010; published online 14 January 2011)

The influence of changing collisionality on density fluctuation characteristics is studied during dedicated $\nu*$ scaling experiments, using Doppler backscattering system. First, the repartition of fluctuation energy over different spatial scales, as represented by the wavenumber spectrum, is investigated and a modification of the shape of the perpendicular wavenumber spectrum in the low wavenumber part of the spectrum is observed when changing collisionality. In addition, a new procedure to evaluate the dispersion relation of micro-turbulence is presented. From the behavior of the perpendicular mean velocity of density fluctuations with the perpendicular wavenumber, different dispersion relations are obtained between low and high collisionality cases. © *2011 American Institute of Physics*. [doi:10.1063/1.3536648]

I. INTRODUCTION

Particle and heat transport induced by micro-turbulence largely determine the performances of modern day tokamaks. Turbulent transport modeling is thus the main challenge for the study and realization of magnetic fusion energy. There are three different methods that allow predicting confinement performances for next step devices such as ITER and DEMO (DEMOnstration Power Plant). One commonly used technique is based on extrapolating global empirical scaling laws obtained from existing experimental multimachine databases.[1] However, the degree of confidence in this approach is unsatisfactory, and as a result, its predictive capabilities are limited. Another approach for confinement prediction, which in principle promises higher degree of confidence, is to use first principle models retaining comprehensive physics. Direct numerical simulations using gyrokinetic description appear as the main tools for this purpose. However, these codes should be carefully validated against experiment in order to be useful for actual prediction. One way this can be done is to perform precise comparisons between experimental observations and theoretical predictions,[2–4] in particular via studies of parametric dependencies of turbulence characteristics. The description of plasma dynamics using dimensionless parameters is another powerful and commonly used tool to extrapolate from present day devices to next step experiments.[5,6] The dependence of turbulent transport on dimensionless parameters such as $\rho*$, β, and $\nu*$ can be studied by performing dedicated scan experiments in which one of these parameters is varied while the others are kept constant (also keeping the geometry of the plasma unchanged). These kinds of experiments constitute an excellent framework to perform comparisons between the observed characteristics of micro-turbulence and the results from simple theoretical models and gyrokinetic simulations.

The repartition of fluctuation energy over different spatial scales, as represented by the wavenumber spectrum, is one of the few quantities which allow a high detail comparison (i.e., a "lower order" in contrast to a comparison, merely of χ_i) between experiment and theory. The perpendicular wavenumber spectrum contains specific information about the character of underlying instabilities and the mechanisms involved in energy transfer between different scales. It has been suggested that the interactions between fluctuations and large scale flow structures that are driven by turbulence may play an important role in the energy transfer mechanism, since measured wavenumber spectra are found to agree with the simple cascade model for drift waves in the limit of solely disparate scale interactions.[7,8] While such an agreement may be coincidental, it is consistent with the basic understanding of plasma turbulence based on large scale flows mediating nonlinear interactions. It is also well known that collisionality plays an important role on the dynamics of such large scale structures whether they are zonal flows or geodesic acoustic modes (GAMs). It is commonly argued for instance that the effect of collisionality on zonal flows might lead to an increase rather than a decrease of the fluctuation levels when the level of collisions is increased. The argument is based on the idea that the fluctuation level is usually set by the turbulence reduction by shearing via zonal flows[9] and not by the collisional dissipation. Thus, for instance, if the collisionality is increased, the zonal flow level should decrease which should then lead to the turbulence fluctuation levels to increase.[10]

In reality, of course collisions are expected to play a dual role, since increasing collisionality would also lead to stronger damping on the fluctuations and a larger range of wavenumbers where the energy can be dissipated. It is not *a priori* known which of these effects would be the dominant one in real experimental conditions. Moreover, collisions may also change the nature of the linear instability mechanism and thus the character of energy injection. In contrast, increasing the collisionality should not change the nature of the nonlinear interactions. It would change however, the slow nonlinear "dynamics," represented by predator-prey oscillations.

In the present paper, we investigate the shape of the perpendicular wavenumber spectrum using Doppler back-

scattering system.[11] In order to isolate the specific effect of the collisionality on micro-turbulence characteristics, we performed this study during dedicated ν^* scaling experiments. The Doppler backscattering technique, also called Doppler reflectometry, is based on scattering of electromagnetic waves in the vicinity of a cut-off layer. In addition to providing access to the spatial scales of density fluctuations, this technique also allows us to probe the dispersion relation of micro-turbulence through the representation of the perpendicular velocity as a function of the wavenumber. It is found that for $k\rho_s < 0.7$, the wavenumber spectrum of density fluctuations gets flatter when increasing collisionality while for $k\rho_s > 0.7$, the shape of the spectrum does not change. At the same time, the behavior of the dispersion relation is modified: at high collisionality, the phase velocity is found to decrease with the wavenumber while at low collisionality, the phase velocity remains rather constant over the full wavenumber range.

A short description of the Doppler backscattering system is given in Sec. II. The study of the perpendicular wavenumber spectrum is then detailed in Sec. III. First, after an introduction, the shape of the wavenumber spectrum commonly observed on Tore Supra is presented. Second, the effect of collisionality on the shape of the spectrum highlighted during the ν^* scans is given. Section IV is dedicated to the wavenumber dependence of the perpendicular velocity of density fluctuations. The impact of changing the collisionality in the behavior of the dispersion relation of micro-turbulence is presented. Finally, a discussion is proposed in the last section.

II. DOPPLER BACKSCATTERING SYSTEM ON TORE SUPRA

The Doppler backscattering system combines advantages of both reflectometry and scattering techniques. It is based on the detection of the field backscattered on density fluctuations in the vicinity of the cut-off layer. In practice, the probing wave is chosen in the microwave range and is launched in oblique incidence with respect to the normal vector to the surfaces of isoindex-of-refraction (α being the angle of incidence with the normal vector to the isoindex-of-refraction surface), thereby only the backscattered signal (little or no reflected signal is received) is detected by the emitter antenna which also serves as a receptor. The fluctuations whose wavenumber matches the Bragg rule $\vec{k}_f = -2\vec{k}_i$ are selected exclusively, where $\vec{k}_i$ and $\vec{k}_f$ are, respectively, the local probing wave-vector and the density fluctuations wave-vector. This technique thus provides the instantaneous spatial Fourier analysis of density fluctuations, $\tilde{n}(\vec{k},t) = \int_V n(\vec{r},t) e^{i\vec{k}.\vec{r}} d\vec{r}$, acting as a band pass filter in k-space around $k = k_0 \sin\alpha$ at the cut-off layer.

The system installed on Tore Supra has two channels: one channel operates in the V-band frequency range in ordinary polarization (i.e., O-mode) while the second one covers the W-band in extraordinary polarization (i.e., X-mode). These channels allow us to probe the plasma from $r/a = 0.5$ to $r/a = 0.9$ (where a is the minor radius) for wavenumber $k = 3-20$ cm^{-1} and from $r/a = 0.85$ to $r/a \geq 1$ with $k = 2-25$ cm^{-1}, respectively. Note that for this wavenumber range, the efficiency of the backscattering processes is expected to remain constant.[12–14] The scattering volume is controlled by using Gaussian optics. However, due to the long distance between the antenna and the plasma, the waist of the Gaussian beam remains distant from the scattering zone and the wavenumber selectivity Δk is thus related to the refraction of the Gaussian beam[15,16] (for more details see Ref. 17). The radial position and the wavenumber of the probing wave at the cut-off layer are determined using a three-dimensional beam tracing code[18] simulating the propagation of a Gaussian beam in a stationary plasma represented by a radial density profile (measured using fast-sweep reflectometers[19]) and a radial profile of the magnetic field (only used in the case of extraordinary polarization). Note that here we assume that the collected signal comes essentially from backscattering processes occurring in the vicinity of the cut-off layer.

The power spectral density that is detected is Doppler shifted by $\Delta\omega = \vec{k}_f . \vec{v}_f$ due to the movement of density fluctuations perpendicular to the field lines. This allows us to determine the fluctuation velocity at the cut-off layer and is currently used, mostly for studying plasma flows,[20] radial electric field profiles,[21,22] and instantaneous velocity fields[23,24] by present Doppler systems. In addition to the flow profile, the Doppler reflectometers can be used to obtain the wavenumber spectra, locally, since the integration of the power spectral density gives the power of density fluctuations contained at a radial position and at a specific spatial scale. Using different incident angles and different probing frequencies, the wavenumber spectrum can be reconstructed at a corresponding radial position. In the following, only the results from the ordinary channel will be presented. Note that in O-mode, the selected wavenumber at the cut-off is mainly in $\hat{\mathbf{b}} \times \hat{\mathbf{r}}$ direction (where $\hat{\mathbf{b}}$ is along the field lines and $\hat{\mathbf{r}}$ is radially outward).

Note that the incident probing beam amplitude (and thus the measured raw signal amplitude) is sensitive to various factors such as reflection, antenna coupling, mixer response, conversion losses, etc. We use a well defined calibration procedure which permits us to measure these losses for each probing frequency and correct for those. The net effect of this calibration procedure is to reduce the unphysical spread in the data, and bring the curves corresponding to different frequencies together. Regarding the frequencies used in this paper, the correction due to this calibration procedure is up to about 30%.

III. COLLISIONALITY DEPENDENCE OF DENSITY FLUCTUATIONS CHARACTERISTICS

A. Shape of the wavenumber spectrum

In simple, two-dimensional fluid turbulence, theory predicts that k-spectrum follows a power law in the ranges of wavenumbers where drive and damping are unimportant (commonly called the inertial ranges), due to cascades of conserved quantities: energy and enstrophy (e.g., Ref. 25). In the case of tokamak plasmas, the drive is not expected to be well localized in k-space since several modes, corresponding to various different scales are possibly linearly unstable.

Among these, the ion temperature gradient (ITG) driven mode and the trapped electron mode (TEM) are known to play important roles in the heat and particle transport in tokamaks. The ITG mode, for which the free energy source is the ITG, has a linearly most unstable mode at around $k_\perp \rho_s \approx 0.3$, which tends to be shifted nonlinearly toward even smaller wavenumbers.[26] It has negligible linear growth or energy injection beyond roughly $k_\perp \rho_s \approx 0.6$. TEM in contrast usually appears in conjunction with the ITG mode and has a characteristic scale of roughly $k_\perp \rho_s \sim 1$. There are other instabilities associated to electron gyroradius scales such as the electron temperature gradient driven mode. However the energy injected by these modes is expected to be relatively weak in the range of wavenumbers considered. In addition to these different kinds of instabilities, the interactions with zonal flows act as a damping process on turbulence on a wide range of scales. This means that the concept of inertial range is not really applicable to fusion plasmas, since drive and damping affect almost all scales. As a result, making a simple theoretical prediction for the k-spectrum is nontrivial. Experimentally, the determination of the wavenumber spectrum is also very challenging since the fluctuations must be measured on a wide range of scales in the core of the plasma (which is usually not accessible with probes). Such measurements are usually done using scattering of electromagnetic waves.[27–29]

Early density fluctuations measurements showed that the fluctuation energy is concentrated at ion scales.[30–34] These scales correspond to relatively small wavenumbers, $k\rho_i < 1$ where the ITG and TEM modes are unstable. At the largest scales measured ($k < 2$ cm^{-1}), an anisotropy is observed between the radial and the poloidal directions[30,32,35] while for higher wavenumbers (but still $k\rho_i \lesssim 1$) the fluctuation energy follows, in both directions, a power law $S(k) = \delta n^2 \propto k^{-\alpha}$ where $\alpha \approx -3.5 \pm 1$.[36–40] Thanks to the extension of the spatial scale range of the measurements, a faster decrease of the energy of fluctuations at high wavenumbers has been observed, first on Tore Supra using CO2 laser scattering system: the spectrum is composed of two power laws, at small k, $S(k) = k^{-3}$ while from $k\rho_i = [1-2]$, $S(k) = k^{-6}$.[28] This observation has been confirmed on W7-AS ($k^{-2.8}$ and $k^{-8.5}$) (Ref. 41) and on FT-2 ($k^{-2.5}$ and k^{-7}) (Ref. 42) in which spectra with similar shape have been observed as well as on Tore Supra using Doppler backscattering system.[17] The decrease in the form of a power law with $\alpha \approx -3$ in the large scale range has been compared against gyrokinetic simulations between $k\rho_s = [0.5-1]$ and found to be in fair agreement with numerical results when using similar data processing.[3] The faster decrease of the spectrum at higher wavenumbers is found to be in rough agreement with a family of simple spectral shell models for drift waves.[7,8] When disparate scale interactions (in particular, interactions with zonal flows) are dominant, this model gives

$$\delta n_k^2 = \Phi_k^2 = k^{-3}/(1+k^2)^2 \tag{1}$$

in standard normalized units ($\delta n_k = n_k'/n_0(\rho_s/L_n)^{-1}$, $\phi_k = e\phi_k'/T_e(\rho_s/L)_n^{-1}$, $k = \rho_s k'$, etc. where primed quantities are in physical units.)

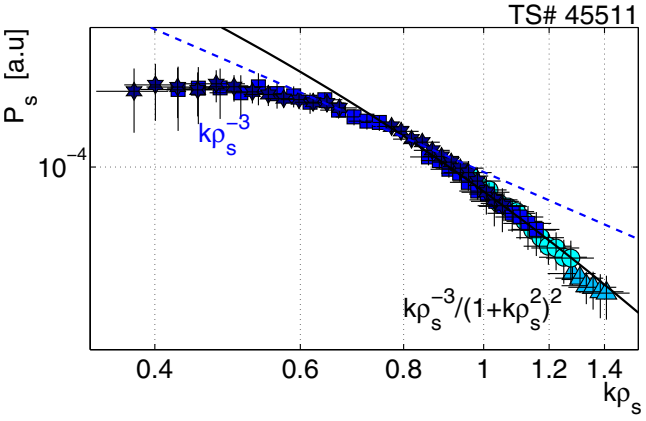

FIG. 1. (Color online) Example of k-spectrum resolved with small k-step measured using Doppler backscattering system and the probing frequencies 49 GHz (stars), 53 GHz (squares), 55 GHz (circles), and 58 GHz (triangles).

In the present work, we focus on the effect of collisionality on the shape of the perpendicular wavenumber spectrum during dedicated ν^* scan experiments using the Doppler backscattering system. Thanks to the steady-state operation of the Tore Supra tokamak and to the flexibility of the Doppler backscattering system installed on it, we can scan a large number of $(F,\alpha) \leftrightarrow (r,k)$ pairs (F being the probing frequency and α the angle of incidence) and thus obtain the wavenumber spectrum with a high level of resolution in terms of wavenumber discretization. Figure 1 presents the wavenumber spectrum of density fluctuations measured around $r/a = 0.8 \pm 0.08$ during a typical discharge of Tore Supra at $B = 3.8$ T, in which the plasma is heated using ion cyclotron resonance heating system. Errors on the perpendicular wavenumber spectrum, as reported in Fig. 1, come essentially from uncertainties in the integration of the power spectral density $\delta n^2(k,\omega)$ to evaluate $\delta n^2(k)$, and from the slight variations of plasma conditions (though all measurements presented here are made during stationary phase) that may affect both the level and the localization.

The error-bars are then evaluated by comparing values of δn^2 obtained using different integration procedures (from the raw spectra versus from using different fitting functions, etc.) and from the dispersion of δn^2 measured at a given wavenumber using different probing frequencies in a narrow radial window (e.g., $\Delta(r/a) = 0.08$). Note that in this dispersion, the impact of the change of the amplitude of the incident signal between each probing frequency which is not perfectly corrected by the calibration procedure (described in Sec. II) is also taken into account. The error-bars on the perpendicular wavenumber have been evaluated directly from the beam tracing code by considering the possible modification of the propagation due to the uncertainty on the radial profile of density. In addition, the uncertainties coming from the evaluation of the local ρ_s is also taken into account.

In the lowest wavenumber range, the spectrum is rather flat and seems to saturate while for higher wavenumbers, the shape of the spectrum is similar to previous observations made on Tore Supra.[17,28] In the wavenumber range around $k\rho_s = 0.6-0.8$, the spectrum is compatible with a power law

$S(k) \propto k^{-\alpha}$ with a spectral index $\alpha \approx -3$ while this power law representation starts to break down around $k\rho_s \sim 0.8$ and the spectral power decreases much faster ($\alpha \approx -6$). This form is consistent with the shell model expression (1) for $k\rho_s = [0.7-1.2]$. Note that the shell model expression does not have any fitting parameters (apart from the fluctuation level). Therefore, the agreement between experiment and this model is remarkable and suggests that interaction between disparate scales including zonal flows may be an important ingredient to determine the wavenumber spectrum shape.

As already mentioned in Sec. I and in Ref. 28, this kind of k-spectrum is not consistent with well known theories of neutral fluid turbulence.[25] Two-dimensional (2D) turbulence theory provides a mechanism of dual cascade. In the inertial range, the kinetic energy at the scale $1/k$ varies as $E(k) \propto k^{-3}$ (direct cascade) while in the enstrophy inertial range, $E(k) \propto k^{-5/3}$ (inverse cascade). However, assuming adiabatic electrons, the slopes expected for the spectral power of density fluctuations from these predictions, respectively, $S(k) = |\widetilde{n(k)}|^2 \propto k^{-6}$ and $S(k) = |\widetilde{n(k)}|^2 \propto k^{-14/3}$ differ significantly from what is observed. In addition, in the case of 2D turbulence, the transition should be expected around the energy injection scale. However, the main instabilities in tokamak plasmas appear at different scales with a predominance in numerous experiments of ITG modes expected around $k\rho_s \sim 0.1$ while the change of slope which can be considered as a transition is observed for $k\rho_s \sim [1-2]$.

More generally, through wavenumber spectra measured in various plasma conditions, it is observed that the wavenumber spectrum is composed of two regions: at the smaller wavenumbers ($k\rho_s < 0.7$), a region of energy injection from the main instability/instabilities (corresponding to the anisotropic part[30,32,35]) in which the spectrum is rather flat and/or decreases slowly; at larger wavenumbers ($k\rho_s > 0.7$), a region in which nonlinear interactions and the energy transfer dominate and the spectrum decreases roughly as a power law.

B. Impact of ν^* on the shape of the wavenumber spectrum

During the dedicated ν^* scan experiments, the entire radial profile of the collisionality has been varied by more than a factor 4 between two different discharges (i.e., 45494 and 45511, see Fig. 2). In order to keep the dimensionless parameters $\rho*$ and β constant, we varied the magnetic field B between both discharges, while density profiles are maintained unchanged and the electron temperature profiles are varied following $T \propto B^{-1}$ adjusting the power of ion cyclotron resonance heating system with keeping a central deposition. The plasma current is also varied in order to keep the same safety factor profile (especially at the edge). The wavenumber spectra of density fluctuations during these discharges have been measured using the same probing frequencies (49, 52, and 55 GHz) and are compared in Fig. 3. Using the mixing length approximation, the relative fluctuation level $\delta n/n$ scales as $1/(\langle k_\perp \rangle L_n)$, where L_n is the density gradient length[3] and considering that the turbulence scale length is related to the gyroradius $\langle k_\perp \rangle \equiv 1/\rho_i$ (gyro-Bohm scaling), $\delta n/n \equiv \rho_i/L_n$.

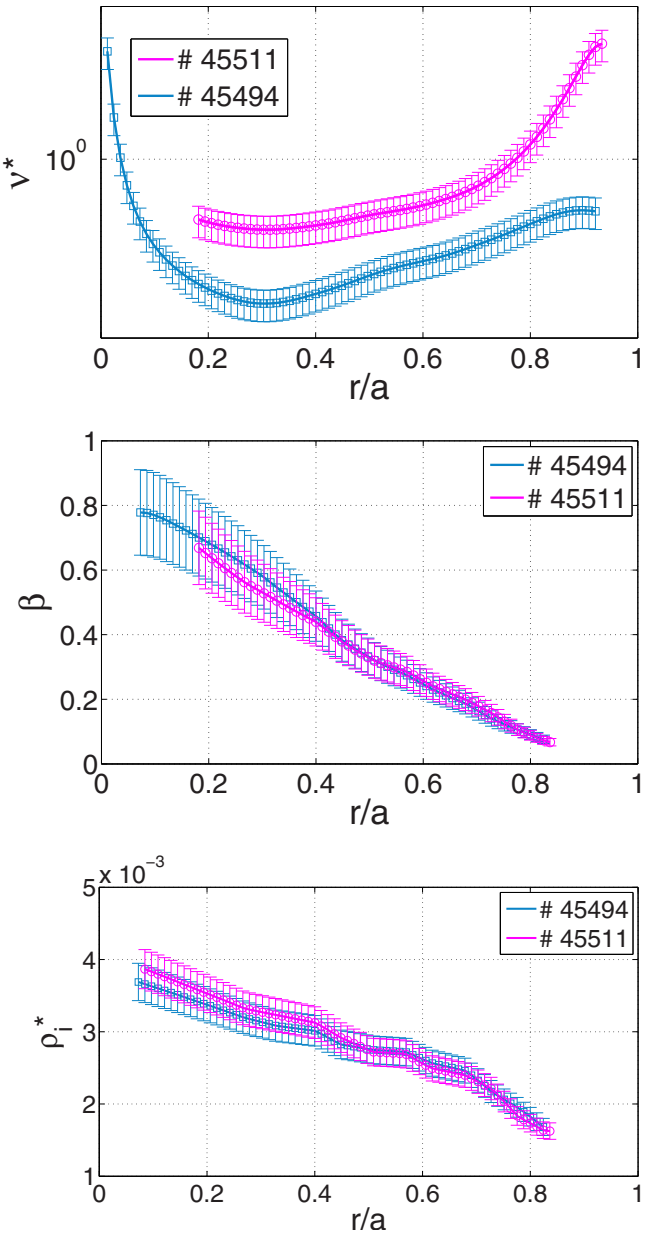

FIG. 2. (Color online) Radial profiles of ν^*, β, and ρ_i during the discharges of the dedicated dimensionless scan.

Since density profiles and $\rho*$ profiles are kept constant between these discharges, here the wavenumber spectra are compared without any normalizations.

A clear impact of the change of ν^* is observable on the wavenumber spectrum: at low k, the amplitude of the spectrum is similar in both cases, while the shape differs such that during the low ν^* discharge, the spectrum decreases faster than during the high ν^* discharge. The difference on the spectrum shape at small k generates a gap between both spectra that persist in the higher wavenumber range even though the shapes remain quite similar for $k\rho_s > 0.7$. We would like to point out that the comparison in terms of amplitude remains rather limited since the energy is mostly contained by the smaller wavenumbers, which are not measured here. Thus, for instance, it is impossible to say, as we go to

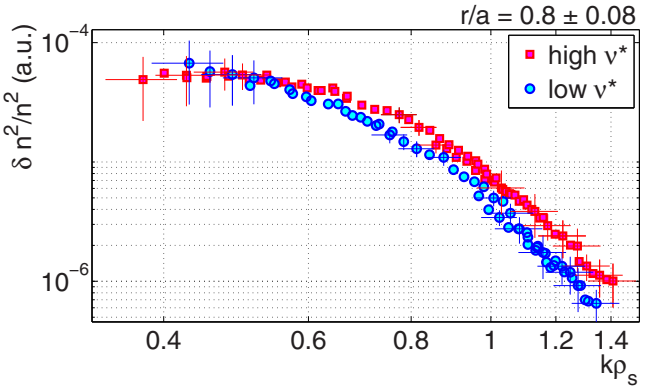

FIG. 3. (Color online) Comparison of the perpendicular wavenumber spectra, normalized to $\delta n^2/n^2$, between low $\nu*$ discharge 45494 and high $\nu*$ discharge 45511 at $r/a=0.8\pm0.08$.

smaller k, if the spectrum continues to increase in the case of low ν^* and becomes higher than that of the high ν^* discharge, or not.

In the following, we will focus on the form of the spectrum, and in order to quantify the effect of collisionality on the wavenumber spectrum shape we use a rigorous fitting procedure. The best agreements occur when treating the two wavenumber ranges $k\rho_s<0.7$ and $k\rho_s>0.7$ of the spectrum separately using exponential $A_1e^{-\gamma k}$ functions (or a Gaussian $A_2e^{-\xi k^2}$ for the low-k region), or a generalized expression of the spectral model for drift waves [Eq. (1)] mentioned above

$$A_3\frac{k^{-3}}{(1+\alpha k^2)^2+\beta k^2}. \tag{2}$$

The derivation of this expression will be given in a future paper. This generalized form is more flexible and permits the application of the fitting procedure while the standard form [Eq. (1)] has no fitting parameters.

The results from the fitting procedure for both low and high collisionality cases are presented in Fig. 4. For the smaller wavenumber range ($k\rho_s<0.7$), the spectrum is well described, for both cases, by Gaussian and exponential functions. Note that for small value of k, both functions are similar and cannot be distinguished. Note that the justification for the Gaussian function comes from the shape of the linear growth rate of the main instabilities. The quasilinear approach, which involves balancing the linear growth with a quasilinear transfer rate, gives a spectrum in the linearly driven region and explains roughly the shape of the spectrum near the region of the drive ($k_\perp\rho_s\lesssim0.5$). The change of the value of $\nu*$ affects this region in a way that decreasing $\nu*$ the spectrum decreases faster. This effect can be quantified by comparing the fitting parameter ξ of the Gaussian function. For the low $\nu*$ discharge $\xi=3.3$ while for the low $\nu*$ discharge $\xi=1.6$. In the higher wavenumber range, the spectrum is well fitted using the generalized form of the spectral shell model [Eq. (2)] as well as by the exponential function (fitting curves cannot be distinguished) and is almost not affected by the variation of $\nu*$. Comparing the exponential parameters $\gamma=5.8$ for the high $\nu*$ case while $\gamma=5.2$ for the low $\nu*$ case and comparing the parameters from shell model expression, $\alpha=1.1$ and $\beta=-3.6$ for the high $\nu*$ case while $\alpha=1.2$ and $\beta=-4$ for the low $\nu*$ case.

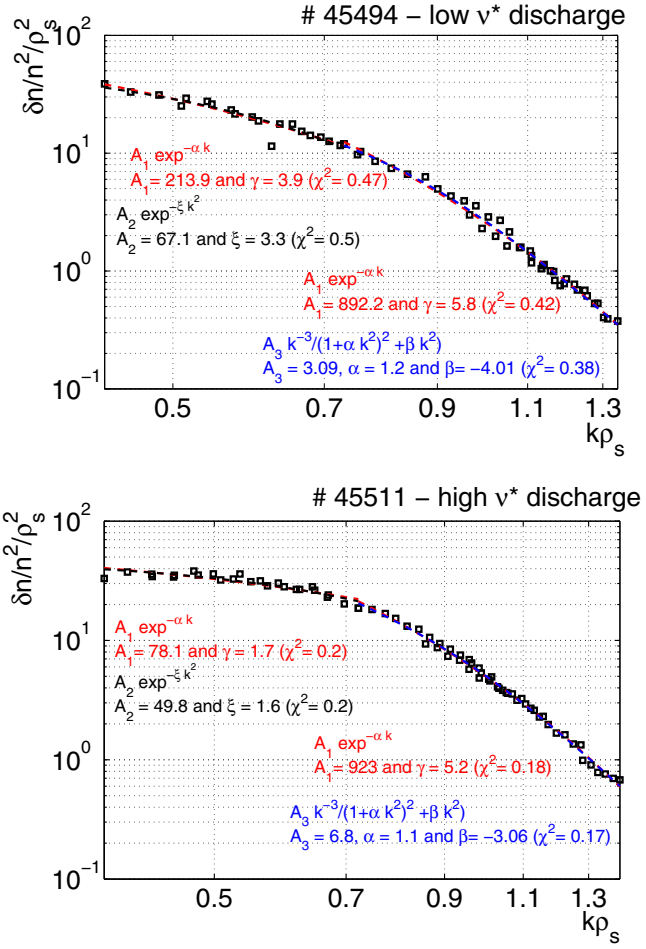

FIG. 4. (Color online) Fitting of the wavenumber spectra considering separately the wavenumber range $k\rho_s<0.7$ and $k\rho_s>0.7$ for both discharges 45494 (top) and 45511 (bottom).

C. Evolution of the dispersion relation

In addition to the spatial scales of micro-turbulence, Doppler backscattering system also permits to access the dynamics of the density fluctuations. The Doppler shift of the spectral density power $S_{k,r}(f)$ gives the perpendicular velocity of density fluctuations in the laboratory frame: $V_\perp=v_{E\times B\perp}+v_{\rm fluc}$, where $v_{E\times B\perp}=-E_r/B$ (E_r being the radial electric field) and $v_{\rm fluc}$ is the mean phase velocity of the density fluctuations. For all the discharges presented in this paper, the Doppler shift is in the electron diamagnetic direction (negative frequency) as it is almost always the case in Tore Supra plasmas [except for very specific conditions[43] or in the Scrape of Layer (SOL)]. For reasons of simplicity, we will consider in the following the absolute value of $V_\perp$, which corresponds to convention that $V>0$ means in the electron direction and $V<0$ means in the ion direction. The mean phase velocity of the density fluctuations $v_{\rm fluc}$ is known to be small as compared to $v_{E\times B\perp}$ (Refs. 17, 22, and 44) therefore extracting its value from $V_\perp$ requires a precise

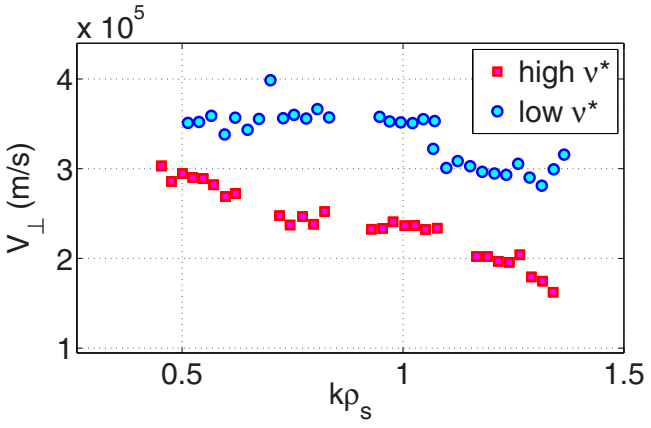

FIG. 5. (Color online) Evolution of the mean perpendicular velocity of density fluctuations (in electron diamagnetic direction) vs the normalized perpendicular wavenumber for low $\nu*$ discharge 45494 and high $\nu*$ discharge 45511 at $r/a=0.8\pm0.025$.

measurement/determination of toroidal and poloidal velocities and ion pressure gradient using the radial force balance relation: $E_r=v_\phi B_\theta - v_\theta B_\phi - \nabla P_i/nq_i$. The toroidal velocity of the carbon can be measured on Tore Supra discharges using the charge exchange diagnostic. However no direct measurements or reliable theoretical predictions permit the evaluation of the poloidal velocity sufficiently accurately to determine v_{fluc} with some confidence using this scheme. Nevertheless, $v_{E\times B\perp}$, which is a global quantity, does not depend on the wavenumber. Therefore, the dependence of the perpendicular velocity $V_\perp$ (measured at a given radius) with the perpendicular wavenumber gives an indication on the dependence of v_{fluc} with $k_\perp$. This then gives us important information on the dispersion relation $\omega_{\text{fluc}}(k_\perp)$ from $v_{\text{fluc}}=\omega_{\text{fluc}}/k_\perp$. The $k_\perp$ dependence of the Doppler velocity $V_\perp$ for the discharges presented above measured at the same radial location ($r/a=0.8\pm0.025$) is shown in Fig. 5. In other words the technique gives us access, directly to the dispersion relation apart from an unknown "offset" that depends on the radial electric field. Note that the data points are selected in a radial window $\Delta r/a=0.025$, narrower than for the wavenumber spectrum (in which $\Delta r/a=0.08$) in order to minimize the impact of the radial dependence of $v_{E\times B\perp}$.

A clear difference in the behavior of $V_\perp(k_\perp)$ is observed between both discharges: for the high $\nu*$ discharge, $V_\perp$ decreases with increasing $k_\perp$ while $V_\perp(k_\perp)$ remains rather flat during the low $\nu*$ discharge. In the high collisionality discharge, the behavior of the perpendicular velocity with the wavenumber can be interpreted/translated as follows. If we consider that the density fluctuations are dominated by ion turbulence $v_{\text{fluc}}<0$, the decrease of $V_\perp$ with $k_\perp$ means that v_{fluc} increases with increasing $k_\perp$. This led to a dispersion relation such as $\omega_{\text{fluc}}(k_\perp)=k_\perp v_{\text{fluc}}\propto k_\perp^\alpha$ with $\alpha>1$. On the opposite, if we consider that $v_{\text{fluc}}>0$ (electron turbulence), the decrease of $V_\perp$ with $k_\perp$ means that v_{fluc} decreases with increasing $k_\perp$ leading to $\omega_{\text{fluc}}(k_\perp)=k_\perp v_{\text{fluc}}\propto k_\perp^\alpha$ with $\alpha<1$. Now, if we consider the low $\nu*$ discharge, the $k_\perp$ dependence of $V_\perp$ indicates that regardless of the type of turbulence (pure ion mode or pure electron mode), $\omega_{\text{fluc}}(k_\perp)=k_\perp v_{\text{fluc}}\propto k_\perp$. One can also imagine a case of mixed ion and electron turbulence that generates density fluctuations in both ion and electron diamagnetic directions at the same spatial scales leading to a Doppler shift associated to the mean of both components (ion and electron components, respectively, shifted in the negative and positive directions with respect to the $v_{E\times B\perp}$ component).

We would like to point out the fact that when scanning the wavenumber (by varying the incident angle of the probing wave), the radial position of the measurements also slightly changes. Even if we use very narrow radial window to extract $V_\perp(k_\perp)$, the radial dependence of $v_{E\times B\perp}$ may still affect the results. In particular, in presence of a strong velocity shear it may be difficult to distinguish which effect—the $k_\perp$ dependence of v_{fluc} or the radial dependence of $v_{E\times B\perp}$—dominates.

IV. DISCUSSION

In the present paper, we used Doppler backscattering system to study certain micro-turbulence characteristics such as perpendicular wavenumber spectrum and perpendicular velocity of density fluctuations, and their collisionality dependence. The wavenumber spectrum gives the repartition of fluctuation energy over different spatial scales and allows us to access detailed information about the character of underlying instabilities and to the mechanisms involved in energy transfer between different scales. At a basic level, its form seems to be a robust feature of all wavenumber spectra measured in various plasma conditions. We observed that the wavenumber spectrum is composed of two regions: at the smaller wavenumbers ($k\rho_s<0.7$), a region of energy injection from the main instability/instabilities in which the spectrum is rather flat and/or decreases slowly; at larger wavenumbers ($k\rho_s>0.7$), a region of energy transfer in which the spectrum decreases in a regular fashion. In the range of small k (referenced as the linear part of the spectrum), the shape of the spectrum is well represented by Gaussian functions. At larger k, the form is correctly described by the simple form $k^{-3}/(1+k^2)^2$ [from the shell model Eq. (1)] suggesting that the interactions between large scale flow structures and fluctuations may play an important role in determining the wavenumber spectrum shape in this energy transfer region. This part of the spectrum is also well fitted using a generalized form of the shell model [Eq. (2)] or using an exponential function $A_1 e^{-\gamma k}$ (with typically $\gamma\simeq 5-6$).

During dedicated $\nu*$ scan experiments it is found that the shape of the perpendicular wavenumber is affected by changing the collisionality: in the linear part, the spectrum decreases faster with decreasing $\nu*$. In contrast, no impact was observed at larger wavenumbers. On one hand, considering the impact of zonal flows, it is expected that a decrease of $\nu*$ would reduce the damping on zonal flows, which would lead to a decrease of energy content on small wavenumbers due to the shearing by large scale structures.[45] This would give a flatter wavenumber spectrum when decreasing $\nu*$. On the other hand, considering the role of TEM, the increase of $\nu*$ is supposed to stabilize TEM and then is expected to peak the spectrum (since only the ITG "peak" remains). Both ex-

planations seem to contradict the present observation suggesting that the effect of collisions on turbulence may be more complicated than we think. This motivates further investigations, especially on the possibility that the TEM may cause a reduction of the zonal flow activity[46,47] or on the role of GAMs as a second predator species feeding on the main instability.[48]

In addition to the effect of collisionality on the wavenumber spectrum, an impact is also observed in the behavior of the perpendicular velocity of density fluctuations. Doppler backscattering system permits access to the wavenumber dependence of the perpendicular velocity which can then be used to obtain information about the dispersion relation of the micro-turbulence measured inside the plasma. While the measurements are indicative of a change of the behavior of $V_\perp(k_\perp)$ between the two $\nu*$ discharges, the results are not conclusive. We present it as an illustration of this powerful procedure to evaluate the form of the dispersion relation, which can then be compared with theoretical predictions from simple models as well as from complete gyrokinetic simulations.

ACKNOWLEDGMENTS

This work was carried out within the framework the European Fusion Development Agreement (EFDA) and the French Research Federation for Fusion Studies (FR-FCM). It is supported by the European Communities under the contract of association between Euratom and CEA. The views and opinions expressed herein do not necessarily reflect those of the European Commission. Financial support was also received from Agence Nationale de la Recherche under Contract No. ANR-06-BLAN-0084.

[1] ITER Physics Expert Groups, Nucl. Fusion **39**, 2175 (1999).
[2] A. E. White, L. Schmitz, G. McKee, C. Holland, W. A. Peebles, T. A. Carter, M. W. Shafer, M. E. Austin, K. H. Burrell, J. Candy, J. C. DeBoo, E. J. Doyle, M. A. Makowski, R. Prater, T. L. Rhodes, G. M. Staebler, G. R. Tynan, R. E. Waltz, and G. Wang, Phys. Plasmas **15**, 056116 (2008).
[3] A. Casati, T. Gerbaud, P. Hennequin, C. Bourdelle, J. Candy, F. Clairet, X. Garbet, V. Grandgirard, O. D. Gürcan, S. Heuraux, G. T. Hoang, C. Honoré, F. Imbeaux, R. Sabot, Y. Sarazin, L. Vermare, and R. E. Waltz, Phys. Rev. Lett. **102**, 165005 (2009).
[4] L. Lin, M. Porkolab, E. Edlund, J. C. Rost, M. Greenwald, N. Tsujii, J. Candy, R. E. Waltz, and D. R. Mikkelsen, Plasma Phys. Controlled Fusion **51**, 065006 (2009).
[5] B. B. Kadomtsev, Sov. J. Plasma Phys. **1**, 295 (1975).
[6] J. Connor and J. Taylor, Nucl. Fusion **17**, 1047 (1977).
[7] Ö. D. Gürcan, X. Garbet, P. Hennequin, P. H. Diamond, A. Casati, and G. Falchetto, Phys. Rev. Lett. **102**, 255002 (2009).
[8] Ö. D. Gürcan, P. Hennequin, L. Vermare, X. Garbet, and P. H. Diamond, Plasma Phys. Controlled Fusion **52**, 045002 (2010).
[9] Z. Lin, T. S. Hahm, W. W. Lee, W. M. Tang, and R. B. White, Science **281**, 1835 (1998).
[10] Z. Lin, T. S. Hahm, W. W. Lee, W. M. Tang, and P. H. Diamond, Phys. Rev. Lett. **83**, 3645 (1999).
[11] P. Hennequin, C. Honoré, A. Truc, A. Quéméneur, N. Lemoine, J.-M. Chareau, and R. Sabot, Rev. Sci. Instrum. **75**, 3881 (2004).
[12] F. da Silva, S. Heuraux, N. Lemoine, C. Honoré, P. Hennequin, M. Manso, and R. Sabot, Rev. Sci. Instrum. **75**, 3816 (2004).
[13] E. Blanco and T. Estrada, Plasma Phys. Controlled Fusion **50**, 095011 (2008).
[14] C. Lechte, IEEE Trans. Plasma Sci. **37**, 1099 (2009).
[15] M. Hirsch, E. Holzhauer, J. Baldzuhn, and B. Kurzan, Rev. Sci. Instrum. **72**, 324 (2001).
[16] V. Bulanin, E. Z. Gusakov, A. V. Petrov, and M. V. Yefanov, Proceedings of the 29th EPS Conference on Plasma Physics, Montreux, 2002, Vol. 26B, p. 2.121.
[17] P. Hennequin, C. Honoré, A. Truc, A. Quéméneur, C. Fenzi-Bonizec, C. Bourdelle, X. Garbet, and G. Hoang, Nucl. Fusion **46**, S771 (2006).
[18] C. Honoré, P. Hennequin, A. Truc, and A. Quéméneur, Nucl. Fusion **46**, S809 (2006).
[19] F. Clairet, Rev. Sci. Instrum. **81**, 10D903 (2010).
[20] P. Hennequin, C. Honoré, A. Quéméneur, A. Truc, F. Gervais, C. Fenzi, and R. Sabot, Proceedings of the 23th EPS Conference on Plasma Physics, Maastricht, 1999.
[21] G. D. Conway, J. Schirmer, S. Klenge, W. Suttrop, E. Holzhauer, and the ASDEX Upgrade Team, Plasma Phys. Controlled Fusion **46**, 951 (2004).
[22] E. Trier, L. G. Eriksson, P. Hennequin, C. Fenzi, C. Bourdelle, G. Falchetto, X. Garbet, T. Aniel, F. Clairet, and R. Sabot, Nucl. Fusion **48**, 092001 (2008).
[23] M. Hirsch and E. Holzhauer, Plasma Phys. Controlled Fusion **46**, 593 (2004).
[24] V. Bulanin, A. Petrov, and M. Yefanov, Proceedings of the 30th EPS Conference on Plasma Physics, St. Petersburg, 2003, Vol. 27J, p. 2.55.
[25] R. H. Kraichnan, Phys. Fluids **10**, 1417 (1967).
[26] A. M. Dimits, G. Bateman, M. A. Beer, B. I. Cohen, W. Dorland, G. W. Hammett, C. Kim, J. E. Kinsey, M. Kotschenreuther, A. H. Kritz, L. L. Lao, J. Mandrekas, W. M. Nevins, S. E. Parker, A. J. Redd, D. E. Shumaker, R. Sydora, and J. Weiland, Phys. Plasmas **7**, 969 (2000).
[27] E. Mazzucato, Phys. Rev. Lett. **36**, 792 (1976).
[28] P. Hennequin, R. Sabot, C. Honoré, G. Hoang, X. Garbet, A. Truc, C. Fenzi, and A. Quéméneur, Plasma Phys. Controlled Fusion **46**, B121 (2004).
[29] E. Gusakov, A. Gurchenko, A. Altukhov, A. Y. Stepanov, L. A. Esipov, M. Y. Kantor, and D. V. Kouprienko, Plasma Phys. Controlled Fusion **48**, B443 (2006).
[30] C. Surko and R. Slusher, Phys. Rev. Lett. **37**, 1747 (1976).
[31] R. Watterson, R. Slusher, and C. Surko, Phys. Fluids **28**, 2857 (1985).
[32] C. Ritz, D. Brower, T. Rhodes, R. Bengtson, S. Levinson, J. N. C. Luhmann, W. Peebles, and E. Powers, Nucl. Fusion **27**, 1125 (1987).
[33] D. Brower, W. Peebles, and J. N. C. Luhmann, Nucl. Fusion **27**, 2055 (1987).
[34] H. Weisen, C. Hollenstein, and R. Behn, Plasma Phys. Controlled Fusion **30**, 293 (1988).
[35] R. J. Fonck, G. Cosby, R. D. Durst, S. Paul, N. Brtez, S. Scott, E. Synakowski, and G. Taylor, Phys. Rev. Lett. **70**, 3736 (1993).
[36] A. Semet, A. Mase, W. A. Peebles, N. C. Luhmann, and S. Zweben, Phys. Rev. Lett. **45**, 445 (1980).
[37] A. Truc, Plasma Phys. Controlled Fusion **26**, 1045 (1984).
[38] P. de Simone, D. Frigione, and F. Orsitto, Plasma Phys. Controlled Fusion **28**, 751 (1986).
[39] F. Gervais, D. Grésillon, P. Hennequin, A. Quéméneur, A. Truc, P. Devynck, X. Garbet, J. Payan, C. Laviron, and S. Saha, Proceedings of the 19th EPS Conference on Plasma Physics, Innsbruck, 1992, Vol. 16C-II, p. 1079.
[40] S. Paul, N. Bretz, R. Durst, R. Fonck, Y. Kim, E. Mazzucato, and R. Nazikian, Phys. Fluids B **4**, 2922 (1992).
[41] N. Basse, IEEE Trans. Plasma Sci. **36**, 458 (2008).
[42] A. D. Gurchenko, E. Z. Gusakov, D. V. Kouprienko, S. Leerink, A. B. Altukhov, J. A. Heikkinen, S. I. Lashkul, L. A. Esipov, and A. Y. Stepanov, Plasma Phys. Controlled Fusion **52**, 035010 (2010).
[43] E. Trier, P. Hennequin, C. Fenzi, Ö. D. Gürcan, R. Sabot, P. Maget, J. Bucalossi, X. Garbet, F. Clairet, L. Vermare, C. Bourdelle, Z. O. Guimarães-Filho, G. Falchetto, and G. Huysmans, Proceedings of the 36th EPS Conference on Plasma Physics, Sofia, 2009.
[44] M. Hirsch, E. Holzhauer, J. Baldzuhn, B. Kurzan, and B. Scott, Plasma Phys. Controlled Fusion **43**, 1641 (2001).
[45] F. L. Hinton and M. N. Rosenbluth, Plasma Phys. Controlled Fusion **41**, A653 (1999).
[46] W. Wang, P. Diamond, T. Hahm, S. Ethier, G. Rewoldt, and W. M. Tang, Phys. Plasmas **17**, 072511 (2010).
[47] F. Merz and F. Jenko, Nucl. Fusion **50**, 054005 (2010).
[48] K. Miki and P. Diamond, Phys. Plasmas **17**, 032309 (2010).

4. Wavenumber spectrum of density fluctuations

From this work, it is found that, at small wavenumbers ($k\rho_s < 0.7$) where energy injection from the main instabilities takes place, the perpendicular wavenumber varies when collisionality is changed. In this region, the shape of the spectrum is well represented by a Gaussian function and the spectrum decreases faster with decreasing ν^*. In contrast, no impact of changing the collisionality was observed at larger wavenumbers and its shape remains correctly described by the simple form $k^{-3}/(1+k^2)^2$ from the shell model [46]. This part of the spectrum is also well fitted using a generalized form of the shell model or using an exponential function $A_1 e^{-\gamma k}$ (with typically $\gamma = 5-6$).

The interpretation of such observation is not straightforward. On the one hand, considering the impact of zonal flows, it is expected that a decrease of ν^* would reduce the damping on zonal flows, which would lead to a decrease of energy content on small wavenumbers due to the shearing by large scale structures [63]. This would give a flatter wavenumber spectrum when decreasing ν^*. On the other hand, considering the role of TEM, the increase of ν^* is supposed to stabilize TEM and then is expected to peak the spectrum (since only the ITG "peak" remains). Both explanations seem to contradict the present observation suggesting that the effect of collisions on turbulence may be more complicated than we think. This motivates further investigations, especially on the possibility that the TEM may cause a reduction of the zonal flow activity [64, 65] or on the role of GAMs as a second predator species feeding on the main instability [66].

From this study, new observations of wavenumber spectrum have been obtained in other fusion plasma devices such as TJ-II [67, 68], DIII-D [69], AUG [70] and in the spherical tokamak MAST [71]. The strong decrease in the region of energy transfer is also observed during L-mode plasmas in TJ-II (c.f. figure 4.3) and MAST (the k-spectrum varies as k^{-5}). Note that in MAST, due to the low magnetic field, wavenumbers that are probed are very large ($k_\perp \rho_s = 7-11$) as compared to other experimental works, except the measurements performed in FT-2 [57, 58, 72] plasmas, in which the radial wavenumber spectrum is evaluated between $k_r \rho_s = [1-15]$.

However, the shape of k-spectrum such as k^{-3} up to about $k\rho_s < 1$ and a faster decrease at higher k was not seen in DIII-D and depending the radial location and on the plasma conditions, not always observed in TJ-II [73] and AUG [59, 74] either. The spectra measured appeared flatter than the shape described above and some incoherence is found when compared with gyrokinetic simulations [70]. This specific behavior is related to non-linear effects of micro-wave propagation in a turbulent plasma. The detailed study lead by Happel et al. [75] clarifies this point. The comparison of wavenumber spectrum measured using X-mode and O-mode DBS systems (at the same radial location and same plasma conditions) exhibits a strong difference in the spectral indexes such that the spectrum obtained using X-mode polarization are flatter than the one coming from O-mode measurements (c.f left figure 4.5). The comparison of these experimental spectra to the result from a gyrokinetic simulation (performed using the experimental plasma conditions) shows an agreement with k-spectrum measured with O-mode. In addition, 2D full-wave simulations have been performed using the turbulence field obtained via gyrokinetic simulations. Again, the comparison of k-spectrum obtained for X and O-mode, shows an impressive difference : the X-mode spectrum is flat until $k_\perp = 11 cm^{-1}$ while O-mode spectrum starts a fast decrease, such as $k_\perp^{-8.8}$ from $k = 5 cm^{-1}$ (c.f right figure 4.5). The flattening of the X-mode spectrum seems to result from a saturation of the scattering response. This explanation is supported by

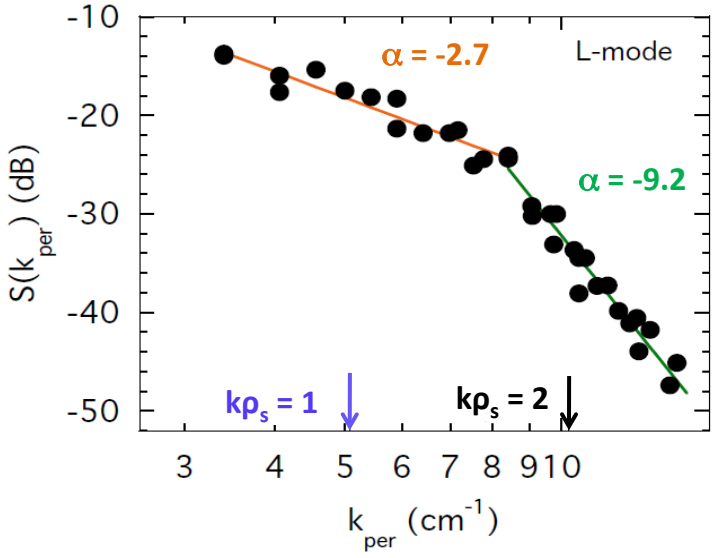

FIGURE 4.3. – Perpendicular wavenumber spectrum measured on TJ-II using DBS [67]

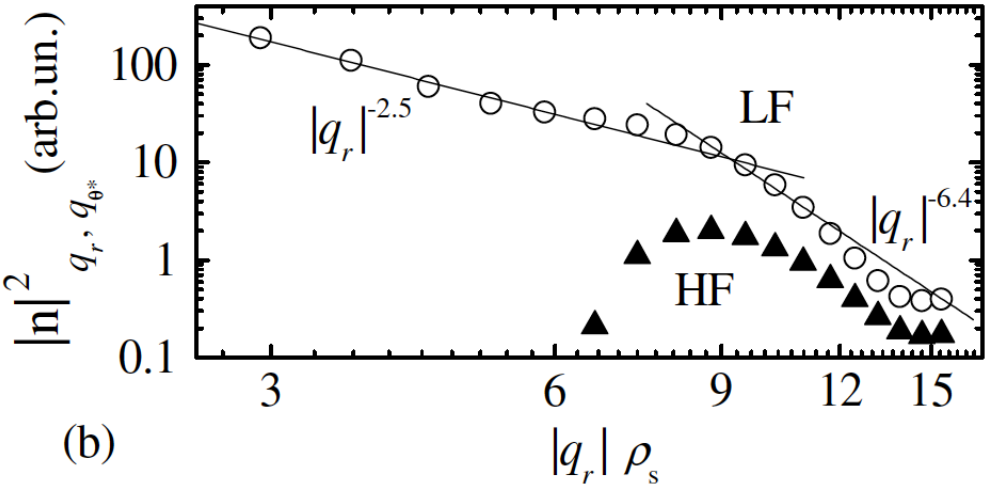

FIGURE 4.4. – Radial wavenumber spectra measured on FT-2 using UHRS

the fact that nonlinear processes are indeed expected to appear at lower turbulence levels when probing fluctuations with X-mode polarization [76]. These findings show that DBS in O-mode is better suited than X-mode polarization for k-spectrum measurement and more generally for turbulence amplitude investigations. However, it should be noted that comparing full-wave spectrum with direct (applied lowest synthetic diagnostic) spectrum, it is obvious that neither the wavenumber spectrum measured with O-mode nor the one measured with X-mode wave polarization reproduces directly the wavenumber spectrum of the input exactly.

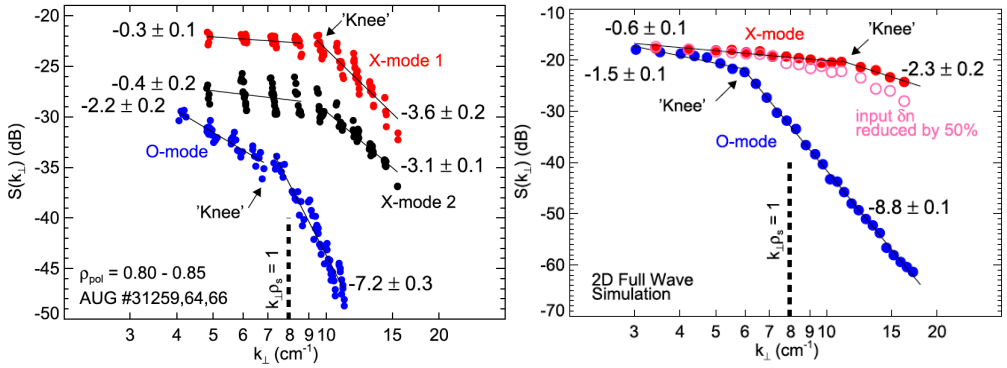

FIGURE 4.5. – Perpendicular wavenumber spectra measured on AUG using DBS in O-mode and X-mode polarisation (left) and spectra obtained using 2D full-wave code and gyrokinetic simulations (right)

In addition to the results on the wavenumber spectrum, the measurement of the perpendicular velocity of density fluctuations (using also the DBS system) during the dedicated ν^* scan allows us to observe an interesting behavior of this velocity. For a given radius, here $r/a = 0.8$, the measured velocity is found to strongly vary with the wavenumber of the probed density fluctuations, suggesting that the phase velocity is not always negligible. This work, presented in the *section C* of the [Publication 4], is discussed in the next section.

5. Dynamics of the plasma via the dynamics of density fluctuations

In this chapter, we present the results related to the dynamics of density fluctuations obtained using the DBS systems. This system, presented in the Annex A, gives access to the perpendicular velocity of density fluctuations in the laboratory frame, which is the sum of the "plasma velocity" plus the apparent (i.e phase) velocity of the fluctuations in the plasma frame. In most cases, density fluctuations are used as "tracers" to evaluate the "mean or equilibrium" plasma dynamics in the perpendicular direction. Since the presence of a strong shear in the perpendicular velocity tends to decorrelate the turbulent structures and thus reduce the turbulent transport (see for example [9]), research on rotation and flows that develop inside the confined plasmas is of major interest. This nonlinear decorrelation effect comes from mean/equilibrium velocity profile as well as from large-scale flows (ZFs and GAMs) generated by the turbulence itself. In the following, both kinds of flows are studied. Depending on the time integration of the data analysis, DBS gives access to the "mean" or "equilibrium" perpendicular plasma velocity or to a kind of "instantaneous" velocity, which allows an observation of velocity fluctuations at a given frequency as in the case for example, for geodesic acoustic modes (typically few kHz). In this chapter, the choice is made to first present a study on the fluctuations of plasma velocity related to the Geodesic Acoustic Modes (GAMs), while in a second section, the "mean" or "equilibrium" velocity investigations are presented after a brief reminder of the different components of the fluid plasma velocity.

5.1. GAMs

Geodesic Acoustic Modes (GAMs), in their basic form, are oscillations of the poloidal flow at the geodesic acoustic frequency, appearing in the form of a coupling between a zonal flows ($m = 0, n = 0$) and an axisymmetric ($m = \pm 1, n = 0$) pressure sideband mode due to geodesic curvature. Similar to stationary zonal flows, the flow (or radial electric field) structure of GAMs is symmetric around the magnetic axis, (i.e. $m = n = 0$) while they have a poloidally asymmetric from (with $m = 1$) for density fluctuations. The physical mechanism can be understood considering an electric field perturbation $\tilde{E}$ which causes a perpendicular flow perturbation $\tilde{v_\perp} = \tilde{E} \times B/B^2$. Since the magnetic field has a dependence as $1/R$, this perturbating flow will lead to an accumulation of the density such as $\tilde{n} \propto -\nabla \cdot \tilde{v_\perp}$. This density perturbation causes a radial current $\tilde{J} \propto (B \times \nabla \tilde{n})/B^2$, which tends to counteract the initial $\tilde{E}$, leading to an oscillation at the GAM frequency.

ZFs and GAMs have been intensively studied, from a theoretical perspective, over the last five decades since these axisymmetric large scale sheared flow structures back-react on small scale turbulence that drives them [77] and tend to regulate the turbulent transport

by shearing apart radially elongated structure of the underlying instability. While GAMs are not expected to reduce turbulence intensity as much as low-frequency ZFs [78], they are believed to exchange energy with ZF and drift-wave turbulence, acting as a third player in a possible predator-prey dynamics [79, 80]. As a result of this, it could be a key ingredient in the L-H transition [81]. Knowing precise properties of GAMs and comparing them with simulations may help in understanding the different parts of the puzzle, which may in turn help predicting, and potentially increasing, the performance of future machines.

The GAM was first predicted based on an ideal magnetohydrodynamic (MHD) model [82], which, for a large aspect ratio, circular plasma, gives the GAM frequency as :

$$\omega_{GAM} = \frac{C_s}{R}\sqrt{2 + \frac{1}{q^2}} \tag{5.1}$$

where R is the major radius, C_s is the sound velocity $C_s = \sqrt{\Gamma_i T_i + \Gamma_e T_e}$ with Γ_i and Γ_e the adiabatic coefficients respectively for ion and electrons and T_i and T_e the ion and electron temperature, and q is the safety factor. This prediction for ω_{GAM} neglects geometrical effects (i.e shape effects), impurities, kinetic and finite Larmor radius effects. Electromagnetic components are also neglected. Therefore, from this first investigation, several models for GAMs have been derived to take into account the plasma geometry [83] or gyrokinetic description [84, 85, 86] leading to slightly different frequency predictions. To give an order of magnitude, in the edge of a medium-sized tokamak, the value of GAMs frequency is typically of the order of $10 - 20kHz$. This frequency range makes them easier to detect as compared to stationary, or very low frequency ($f \approx 0$), zonal flows (ZF).

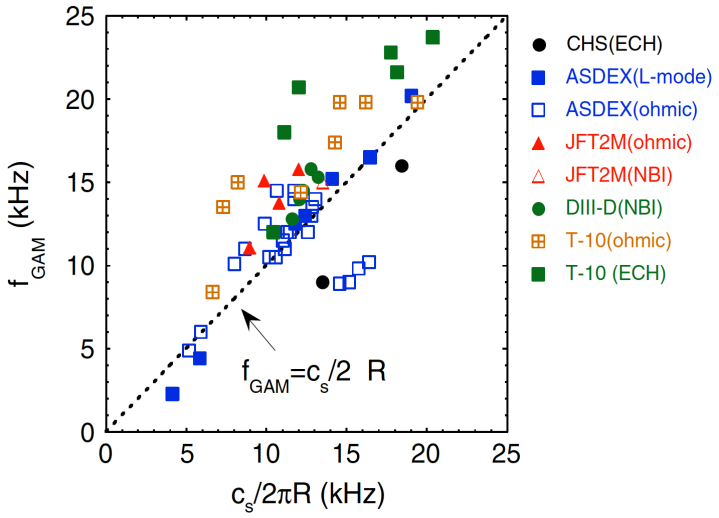

FIGURE 5.1. – Interdevice comparison of GAM frequencies between experiments and prediction from Ref.[87]. The GAM frequency roughly satisfies the relation $f_{GAM} \propto C_s/R$

Experimentally, GAMs appear as quasi-coherent symmetric oscillations of the plasma flows and are identified mainly via their frequency, their poloidal symmetry and in only few experiments via a complete symmetry, namely in both toroidal and poloidal numbers

($n = m = 0$) [88, 89, 90, 91]. After the pioneering works on the H1 heliac device [92, 93], GAMs are usually detected in the plasma edge (typically $\rho = 0.8 - 1$) of tokamak plasmas coherently with the fact that GAMs should experience Landau damping, which roughly varies as $exp(-q^2)$. Observations of GAMs have been reported from a number of toroidal devices, notably using DBS on AUG [94], DIII-D [95, 96] and FT-2 [97]. A more complete review, including a larger number of diagnostic techniques, can be found in Ref. [98]. The GAM frequency is generally found to be close to $C_s/(2\pi R)$ (see Figure 5.1), following the trend of the sound speed C_s, with a dependence on the plasma shape, especially on the plasma elongation [99]. However, an interesting aspect is that GAMs are observed with two significantly different behavior. Namely they either follow the local sound speed [94, 100], or have a fixed frequency over a wide radial domain [101, 96, 102] (for example, $\rho = [0.86 - 0.9]$ in DIII-D and $\rho = [0.75 - 0.95]$ in TCV). This latter behaviour is also observed in gyrokinetic simulations using the code ORB5[103]. In certain cases, the radial profile of GAM frequency exhibits some *"plateau"* (step frequency over $\rho = [0.86 - 0.88]$) [99] as discrete change in the frequency with the formation of several radial layers of GAMs. These different behaviors can be seen as corresponding to a GAM as a continuum (with varying frequency on each flux surface) or as an "eigenmode" structure (i.e a mode at a given frequency with a radial extension) [104, 105].

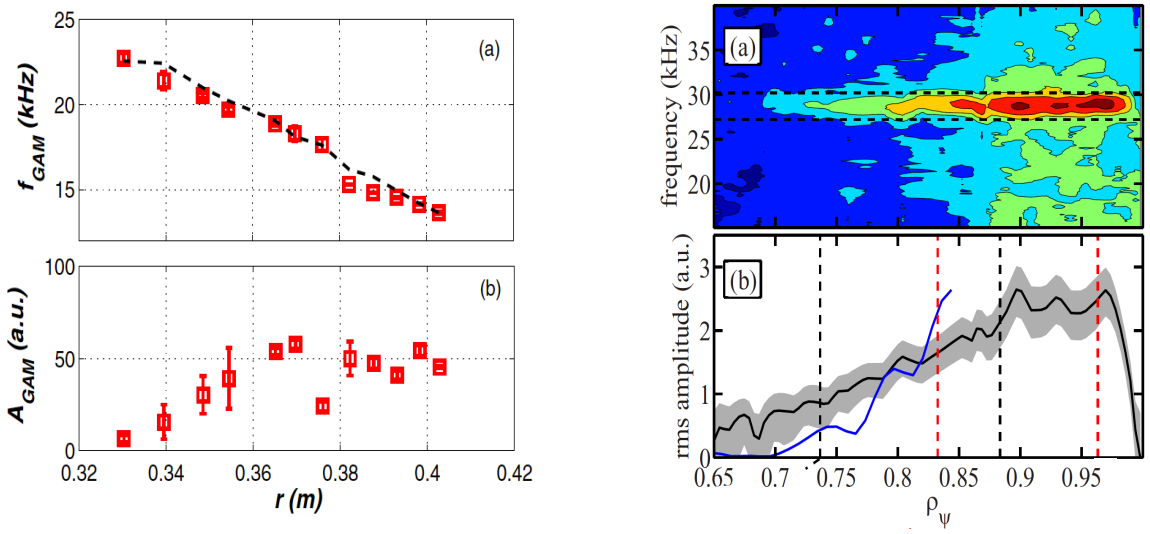

FIGURE 5.2. – Radial profile of the GAM frequency and amplitude in TEXTOR from Ref.[100] (left). Auto-power spectrum of electron density fluctuations and radial profile of the GAM amplitude in TCV from Ref.[102] (right) .

The tokamak Tore Supra had a complementary set of reflectometry systems, with an ultra-fast-sweep reflectometer [106] as well as a fixed frequency system [107] and two Doppler backscattering systems [53]. However, until 2010, no GAMs have been observed on Tore Supra plasmas while it was already largely detected in the other tokamaks [108, 109, 94, 110, 95]. The question of "why GAMs are not observed in Tore Supra plasmas ?" was puzzling. Is it due to an intrinsic property of the machine (i.e. large ripple, circular cross-section, lack of the dynamics leading to the L-H transition) or due to a

lack in detection systems ? Therefore, after intensive studies on characterization of density fluctuations using several scattering and reflectometry systems [111, 40, 112], dedicated analysis of electric field fluctuations from Doppler backscattering measurements have been performed. Exploiting the recently installed DBS acquisition system, the diagnostics were set up in order to acquire data with a long-time sequence (over 50 ms) and we have expanded our data analysis to include new data processing which extends considerably our capabilities in terms of Doppler velocity measurements. In addition, specific experiments have been designed and performed on Tore Supra looking for GAMs. These experimental studies allowed, for the first time, the detection of GAMs on Tore Supra plasmas and are presented in the following paper [Publication 5].

IOP Publishing and International Atomic Energy Agency Nuclear Fusion
Nucl. Fusion **52** (2012) 063008 (13pp) doi:10.1088/0029-5515/52/6/063008

Detection of geodesic acoustic mode oscillations, using multiple signal classification analysis of Doppler backscattering signal on Tore Supra

L. Vermare[1], P. Hennequin[1], Ö.D. Gürcan[1] and the Tore Supra Team[2]

[1] Ecole Polytechnique, LPP, CNRS UMR 7648,91128 Palaiseau, France
[2] CEA, IRFM, F-13108 Saint-Paul-lez-Durance, France

Received 21 October 2011, accepted for publication 7 March 2012
Published 17 April 2012
Online at stacks.iop.org/NF/52/063008

Abstract
This paper presents the first observation of geodesic acoustic modes (GAMs) on Tore Supra plasmas. Using the Doppler backscattering system, the oscillations of the plasma flow velocity, localized between $r/a = 0.85$ and $r/a = 0.95$, and with a frequency, typically around 10 kHz, have been observed at the plasma edge in numerous discharges. When the additional heating power is varied, the frequency is found to scale with C_s/R. The MUltiple SIgnal Classification (MUSIC) algorithm is employed to access the temporal evolution of the perpendicular velocity of density fluctuations. The method is presented in some detail, and is validated and compared against standard methods, such as the conventional fast Fourier transform method, using a synthetic signal. It stands out as a powerful data analysis method to follow the Doppler frequency with a high temporal resolution, which is important in order to extract the dynamics of GAMs.

(Some figures may appear in colour only in the online journal)

1. Introduction

The performances of today's tokamaks are limited by the micro-turbulence in the confined plasma that generates radial transport of heat and particles. The main instabilities that underlie this turbulent transport are drift instabilities driven unstable by density and temperature gradients. Non-linearly, the turbulence in the core of tokamak plasmas self-organizes by forming large-scale structures, and in particular, large scale sheared flows called 'zonal flows' that back-react on small scale turbulence that drives them [1]. These axisymmetric sheared flow structures tend to regulate the anomalous transport by shearing apart radially elongated mode structure of the underlying instability. Closely related to these zonal flows (ZFs) are the oscillations of the poloidal flow at the geodesic acoustic frequency, called geodesic acoustic modes (GAMs), which are similarly turbulence-generated and appear in the form of a coupling between a ZF and an axisymmetric ($m = 1$) pressure sideband mode due to geodesic curvature. ZFs and GAMs have been intensively studied over the last decade both theoretically and experimentally. The detection of such structures is quite challenging since it requires direct measurements of plasma flow or electric field with high temporal and spatial resolution. In particular the stationary ZFs, which evolve at a very low frequency ($f \approx 0$) are virtually impossible to detect with only one localized system and requires long distance correlation analysis between separate and distant systems. ZFs can be directly detected in the plasma core by measuring the electrostatic potential using heavy ion beam probes (HIBP) [2, 3] and at the plasma edge from floating potential measured using Langmuir probes [4–6]. Because GAMs have a frequency typically of the order of a few kHz, they are easier to detect and have been observed on several tokamaks such as DIII-D [7–9], JIPP T-IIU [10], ASDEX Upgrade (AUG) [11], JFT-2M [12], T-10 [13], TEXTOR [14], HL-2A [15] using beam emission spectroscopy (BES), HIBP, Doppler backscattering systems (also referred to as Doppler reflectometry) and Langmuir probes.

The tokamak Tore Supra has a complementary set of reflectometry systems, with an ultra-fast-sweep reflectometer [16] as well as a fixed frequency system [17] and two Doppler backscattering systems [18, 19]. However, until recently, no GAMs have been observed on Tore Supra plasmas. Whether this was due to an intrinsic property of the machine (i.e. large ripple, circular cross-section, lack of the dynamics leading to the L–H transition), has been a question for the scattering

community, which has finally been resolved in this paper. The detection in Tore Supra has proved difficult due to a variety of reasons: the standard reflectometry systems are located in the equatorial plane (where the density fluctuations due to GAM cannot be observed); the Doppler system was not adapted to the detection of GAMs because of the poor flexibility of the acquisition system and it operated mostly in the ordinary (O)-mode. In short, the scientific focus was on the wavenumber spectrum of density fluctuations and on radial profiles of the mean radial electric field studies, which require a set-up, which is not suitable for the detection of GAMs.

Therefore, after intensive studies on characterization of density fluctuations [20–23] using several scattering and reflectometry systems, dedicated analysis of electric field fluctuations from Doppler backscattering measurements have been performed which allowed, for the first time, the detection of GAMs on Tore Supra plasmas. Taking advantage of a new acquisition system, the diagnostics were set up in order to acquire data with a long time sequence (over 50 ms). Various data analysis methods for determining the instantaneous Doppler frequency and therefore the instantaneous velocity of density fluctuations are considered. Among those methods that have been tested are the calculation of the frequency as the derivative of the phase of the complex signal, use of the fast Fourier transform (FFT) on reduced time sliding window (SWFFT) and the multiple signal classification (MUSIC) algorithm [24]. The latter is a power spectral estimation method based on the eigenmode analysis of data vectors, which can provide a fine estimation of the frequency content of the signal, with high temporal resolution [25–27] (i.e. using a small number of data points, see for instance [28] for a recent review that contrasts modern power spectral density estimate methods). The key advantage of this algorithm is its ability to separate the information contained in the data into distinct signal and noise sub-spaces by determining the eigenvectors of the auto-correlation matrix. In this decomposition, the projection of each frequency component on the noise eigenvectors becomes minimum at the frequencies of the signal (e.g. the Doppler frequency in our case). A spectral (or frequency) estimator is thus formed by taking the inverse of this projection, which yields sharp peaks at the frequencies of the signal [29]. From our study, presented in the following, the MUSIC method has been determined to be the most efficient technique for detecting GAMs. In particular, the flexibility of this method in terms of determining the GAM frequency with a relatively low number of points from the Doppler backscattering signal, admits a high resolution characterization of GAM dynamics such as frequency modulations of GAM oscillations.

This paper is devoted to the first observations of GAMs on Tore Supra plasmas and the MUSIC method that can be used for detecting them. After this short introduction, a brief description of the Doppler backscattering system, used in the following, is given in section 2. Section 3 is dedicated to the data analysis technique. The MUSIC method, which we choose for our study, is described, tested and compared with the better known methods, such as, the derivative of the phase and SWFFT using a synthetic signal. Then, the oscillations observed in the velocity of the density fluctuations during ion cyclotron resonance heated (ICRH) L-mode plasmas are presented in section 4. Finally, a discussion gives perspectives of this work in section 5. Appendices A and B describe the mathematical foundation and the practical implementation of the MUSIC algorithm used in this paper.

2. Doppler backscattering system on Tore Supra

Doppler backscattering system allows measurements of density fluctuations with good spatial localization and an excellent wavenumber selectivity. This technique combines the advantages of both the reflectometry and the scattering techniques. The probing wave which is chosen in the microwave range, in order to reach a cut-off layer inside the plasma, is launched in oblique incidence with respect to the normal vector to the surfaces of iso-index-of-refraction. In this configuration, only the field backscattered on density fluctuations in the vicinity of the cut-off layer is detected by the emitter antenna, which also serves as a receptor. The fluctuations whose wavenumber matches the Bragg rule $\vec{k}_\mathrm{f} = -2\vec{k}_\mathrm{i}$ are selected exclusively, where $\vec{k}_\mathrm{i}$ is the local probing wavevector close to the cutoff and $\vec{k}_\mathrm{f}$ is the wavevector of density fluctuations. This technique thus provides the instantaneous spatial Fourier analysis of density fluctuations, $\tilde{n}(\vec{k},t) = \int_V n(\vec{r},t)\mathrm{e}^{\mathrm{i}\vec{k}.\vec{r}}\,\mathrm{d}\vec{r}$, at the wavenumber $k = k_\mathrm{f}$. Due to the movement of density fluctuations perpendicular to the field lines, in the $\hat{\boldsymbol{b}} \times \hat{\boldsymbol{r}}$ direction, the detected signal is Doppler shifted by $\triangle\omega = \vec{k}_\mathrm{f}.\vec{v}_f$. This allows the determination of the velocity at the cut-off layer, which corresponds to the speed of movement of the density fluctuations in laboratory frame, mainly due to the $E \times B$ drift, written as $v_\mathrm{f} = v_{E\times B} + v_\mathrm{ph}$ where $v_{E\times B}$ is the $E \times B$ velocity and v_ph is the phase velocity of density fluctuations.

The system installed on Tore Supra has two channels: one of which operates in the V-band frequency range in ordinary polarization (i.e. O-mode) while the second one covers the W-band in extra-ordinary polarization (i.e. X-mode). The scattering volume is controlled by Gaussian optics and the antenna is motorized in order to vary the tilt angle during a single discharge. This allows us to probe the plasma from $r/a = 0.5$ to $r/a = 0.9$ (where a is the minor radius) with wavenumber $k_\perp = 3$–$20\,\mathrm{cm}^{-1}$ (for the O-mode) and from $r/a = 0.85$ to $r/a \geqslant 1$ with $k_\perp = 2$–$25\,\mathrm{cm}^{-1}$ (for the X-mode). The radial position and the wavenumber of the probing wave at the cut-off layer are determined using a 3D beam tracing code [30] simulating the propagation of a Gaussian beam in a stationary plasma. In-phase ($I = A\cos\phi$) and quadrature ($Q = A\sin\phi$) signals are sampled at 10 MHz (and possibly up to 100 MHz). More detailed description of this system can be found in [31]. In this paper, we have used data from the X-mode system.

3. Data analysis

In the past, the capabilities of Doppler backscattering system [18, 32], installed on Tore Supra have been mainly used for studying the dynamics of the mean plasma flows and the radial electric fields. In order to do that, both I and Q signals are acquired over a time sequence of around typically 5 ms, for a given fixed probing frequency and a fixed tilt angle. The power

spectrum density is then obtained by a FFT of the complex signal $z(t) = I(t) + \mathrm{i}Q(t) = A(t)\mathrm{e}^{\mathrm{i}\phi(t)}$ over the total time sequence giving access to the 'mean' flow velocity, via the Doppler shift of the maximum of this power spectrum.

In order to obtain the temporal evolution of the flow velocity, or in other words, the 'instantaneous' velocity, several data analysis techniques can be used. The simplest and the fastest method is to determine the Doppler shift frequency directly from the phase derivative of the complex signal [33]. The limitation of this technique comes from its inability to treat signals when the signal amplitude varies rapidly (from high to near zero levels), which makes it difficult to determine the complex phase as distinct from the amplitude variations. A second method consists of applying FFT to the complex signal $z(t)$, on a small, sliding window in time and taking either the simple weighted spectral mean, or the maximum of the Doppler peak (using a fitting process) as the instantaneous Doppler shift. This technique has been intensively used to study GAMs on ASDEX Upgrade [9, 11, 34–36]. Here we will introduce another technique for the detection of GAMs. This method, well known in the signal analysis community, is called the MUSIC algorithm [24]. It is used in various applications from speech recognition [37] to estimating locations, directions and speeds of moving objects via radar/microwave signals [38], in particular in direction finding, and source localization using sensor arrays in a wide variety of applications such as mobile communication and wireless network arrays [39], volcano seismology [40], ultrasound imaging [41] and applications such as mapping of the human brain using magnetoencephalography [42].

3.1. The MUSIC technique

The MUSIC algorithm [24] is a frequency estimation algorithm, which is based on the idea that a large variety of observed signals can be represented by a finite number n_f of frequency components plus an incoherent noise part:

$$x(t) = x^{(s)}(t) + n(t) = \sum_{k=1}^{n_\mathrm{f}} B_k \mathrm{e}^{-\mathrm{i}2\pi f_k t} + n(t), \qquad (1)$$

where $x^{(s)}(t)$ is the relevant part of the signal, B_k are the amplitudes of each frequency component and $n(t)$ is the 'noise', which can be the actual noise or it can be an incoherent/undesired part of the data.

The method is based on the observation that the eigenvectors of the auto-correlation matrix $\boldsymbol{R} = \langle \boldsymbol{x}\boldsymbol{x}^\dagger \rangle$ (where $\boldsymbol{x}$ is the complex data vector, sampled over N regular time intervals) can be used for separating the signal and noise components. When the eigenvalues are sorted in decreasing order, the larger eigenvalues of this matrix correspond to the signal components while the eigenvalues of the noise components are all equal to the minimum eigenvalue. Using the fact that the eigenvectors are perpendicular to one another and the hypothesis that they are also perpendicular to the random noise, the method allows a very good separation of signal from noise. In practice, instead of the ensemble averaged matrix R, a forward–backward averaged $\overline{\boldsymbol{R}}$ is considered, formed from sampling the correlation matrix in smaller matrices of size $n_\mathrm{w} < N$. Furthermore, the well-known property of the singular value decomposition (SVD) is used such that the SVD of a reorganized data matrix $\boldsymbol{X}$ (such that $\overline{\boldsymbol{R}} = \boldsymbol{X}^\dagger \boldsymbol{X}$) yields the eigenvalues and eigenvectors of $\overline{\boldsymbol{R}}$ as the squares of its 'singular values' and its 'right singular vectors', respectively (see appendices A and B). The pseudo-spectrum is then directly estimated from the noise eigenvectors using the MUSIC power estimate, which can be obtained by choosing the form of the filtering function (a vector function $\boldsymbol{w}(f)$ that picks out the frequency component corresponding to the frequency f from the data, such that the power at a given frequency can be defined as $P(f) = \boldsymbol{w}^\dagger(f) \cdot R(\boldsymbol{x}) \cdot \boldsymbol{w}(f)$, see for instance [43]) to minimize the noise content:

$$P_\mathrm{MUSIC}(f) = \frac{1}{d^2} = \frac{1}{\boldsymbol{a}^\dagger(f)\boldsymbol{E}_\mathrm{noise}\boldsymbol{E}_\mathrm{noise}^\dagger\boldsymbol{a}(f)}. \qquad (2)$$

Here E_noise is a matrix whose columns are the noise eigenvectors and $\boldsymbol{a}(f)$ is a vector function of sinusoids (i.e. $a_j(f) = \mathrm{e}^{-2\mathrm{i}\pi t_j f}$). Note that here, while the maximal frequency of the vector f is fixed by the time interval between each data point (i.e. acquisition frequency), the length of this vector (which fixes the frequency resolution) is free. Assuming that the noise and the sinusoidal signals are uncorrelated, d^2 defined above would vanish and thus P_MUSIC diverge for each $f = f_k$ of the signal. In practice, the noise and the signal cannot be perfectly distinguished due to errors coming from the computation of E_noise's and noise-signal correlations, and one obtains a large narrow peak at the location of the signal frequencies. The heights of these peaks represent how distinct from the noise (i.e. significant) that particular frequency signal is. However, the heights of these peaks do not give the amplitude of the signal since the bases of the decomposition are not constant from one time sequence to another. The information of the amplitude of the signal at a given frequency is, anyway, accessible taking directly the eigenvalues: since $R(\boldsymbol{x}) \cdot \boldsymbol{e}(f) = \lambda(f)\boldsymbol{e}(f)$ (where $\boldsymbol{e}(f)$ is the eigenvector corresponding to the component with the frequency f) the eigenvalue $\lambda(f)$ is directly proportional to the square of the amplitude of the component of the signal with that frequency. Since in the MUSIC approach the eigenvalues are sorted (and positive), the square root of the first eigenvalue corresponds to the amplitude of the dominant sinusoidal component.

In practice, for evaluating the frequency content of each time sequence of interest, one has to decide the values of two parameters; n_f being the number of frequencies expected to be detected (number of expected complex sinusoids in the signal), n_w being the size of the signal subspace which corresponds to the size of the resulting averaged matrix $\overline{\boldsymbol{R}}$ when using the forward/backward averaged auto-correlation matrix. In addition, in order to access the time evolution of the Doppler frequency, the MUSIC algorithm should be applied on a reduced time sliding window, with a length of n_ws, which is then slided over the full data sequence. The shift amount (or inversely, the overlap), then determines the temporal resolution, which should be finer than the frequency of the oscillation that we want to resolve. Here, the shift is set at half the window size $n_\mathrm{shift} = n_\mathrm{ws}/2$.

In application to backscattering, we use the MUSIC algorithm to determine the Doppler frequency in sufficiently high resolution to be able to detect an oscillation of the Doppler peak. Therefore, to resolve a single frequency, the parameter n_f should be taken as 1 (which is correct when

the signal frequency spectrum is formed by a single-broad-Doppler component). The parameter n_w, which corresponds to the size of the matrix on which the eigenvalue decomposition is performed, has technical limitations: it must be larger than n_f (so that we have at least n_f signals and 1 noise components), and smaller than the length of the time sequence to be analysed (can be much smaller); however, the optimal value is not straightforward and is decided by performing several tests using a synthetic signal (see next subsection). The pseudo-spectrum P_{MUSIC} is evaluated at a frequency vector f sampled between $-f_{acq}/2$ and $f_{acq}/2$ with a number of points $n_{\Delta f}$ adapted to the desired resolution Δf (where f_{acq} is the acquisition frequency of the signal to be analysed). As described in the next subsection, the key point of using the MUSIC method is that, unlike the conventional FFT method, the frequency resolution is not limited by the width of the sliding window. In other words, considering a pure sinusoid with a frequency f, the MUSIC method can be applied on just a fraction of the full period to resolve the frequency f, as can be seen in figure 3 of [44]. Therefore, $n_{\Delta f}$, can be chosen independently to resolve the amplitude of the frequency oscillation that we want to detect keeping a high temporal resolution, by choosing a narrow sliding window (i.e. a small value of n_{ws}).

3.2. Validation and limitations of the data analysis techniques

The method introduced just above is compared with the other methods discussed in the introduction of this section using a synthetic signal $S(t)$. In order to have a reasonably realistic test-signal, the complex signal $S(t)$ is composed of a distribution of 1000 oscillators with a mean frequency equal to the frequency of the Doppler component and a frequency distribution with a width comparable to the experimental one. Furthermore, the frequencies of each of these oscillators are sinusoidally modulated (synchronously) in order to imitate the effect of the GAM. The signal is written as

$$S(t) = \sum_j \cos(2\pi F_j t + \phi_L) + i \sum_j \sin(2\pi F_j t + \phi_L) \quad (3)$$

with $F_j = f_{Dop} + \delta f_j$, where $\delta f_j = \delta f \times r_j$, $r_j = rd(j)$ with rd is normally distributed pseudorandom numbers between -1 and 1 and $\phi_L = f_{amp}(2\pi f_G)^{-1}\cos(2\pi f_G t)$. (The normalization of ϕ_L comes from the fact that the phase derivative $d\phi_L/dt \propto f_{amp}\sin(2\pi f_G t)$ should represent the oscillation of the Doppler frequency at the GAM frequency f_G with an amplitude f_{amp}). The frequency f_{amp} defines the amplitude of the oscillation and corresponds experimentally to the amplitude of the oscillation of the velocity such that $\Delta v_{amp} = 2\pi f_{amp}/k_f$ (where k_f is the wavenumber of the detected density fluctuation). The parameters f_{Dop} and δf are chosen to obtain a frequency spectrum $S(t)$ close to that measured during an ICRH Tore Supra discharge (#45510) using the X-mode channel. For the same reason, the generated time sequence is $n_{points} = 524\,000$ points long which corresponds to a time sequence of 52.4 ms. Note that due to the low level of noise in the experimental signals (signal to noise ratio is around 45 dB), no noise has been added to the synthetic signal. The jitter in the data comes from δf_j, which is random. A comparison between the mean frequency spectrum of the experimental data and synthetic signal, over the full time sequence, is shown in figure 1.

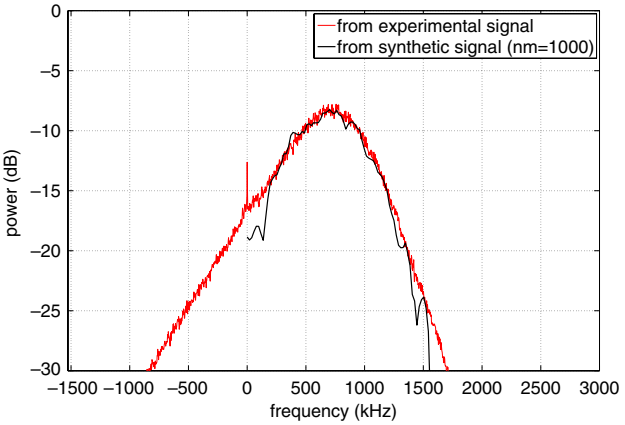

Figure 1. Comparison of the frequency spectrum measured on Tore Supra during the discharge 45510 in X-mode ($F = 78$ GHz) and the frequency spectrum of the synthetic signal $S(t)$.

In the following, the acquisition frequency is fixed at $f_{acq} = 10$ MHz (as commonly used in our system), $f_{Dop} = 700$ kHz, $\delta f = 300$ kHz and $f_G = 15$ kHz are kept constant and four different sets of parameters are used:

Case 1: $f_{amp} = 50$ kHz and $n_{points} = 524\,000$
Case 2: $f_{amp} = 20$ kHz and $n_{points} = 524\,000$
Case 3: $f_{amp} = 50$ kHz and $n_{points} = 100\,000$
Case 4: $f_{amp} = 50$ kHz and $n_{points} = 50\,000$.

As already discussed in the introduction of this section, the easiest way to extract information about the dynamics of the velocities of density fluctuations from the Doppler backscattering system is to determine the Doppler frequency directly from the derivative of the complex phase $\phi(t)$. For this, we compute the logarithmic derivative $\triangle\phi = ((I\triangle Q - Q\triangle I)/(I^2 + Q^2))$ and perform standard FFT analysis on the resulting time sequence. This technique has the advantage of being very fast and has no adjustable parameters (in contrast with the other techniques presented in the following). In addition, this method retains the high time resolution of the signal. However, when studying low-frequency modes such as GAMs ($f < 50$ kHz), the resolution of high frequency (above 50 kHz) is not really necessary. The weakness of this method comes from the fact that the phase of the experimental signal is not always well defined: the phase derivative is computed from a fraction whose denominator (the signal modulus) can reach values close to 0, which causes the instantaneous Doppler frequency computed by this method to diverge. This is mainly due to the bursty character of density fluctuations in tokamak plasmas that leads to strong and fast variations of the signal amplitude. As a result, the frequency spectrum extracted from the phase derivative is generally very noisy and is not well adapted to detect velocity oscillation of a small amplitude.

To improve the sensitivity by reducing the effect of the strong and fast amplitude variations, oscillations of the velocity are often studied using FFTs on a sliding window. This technique consists of two separate steps. First, the application of the SWFFT on the signal $S(t)$ and secondly the determination of the Doppler shift from each frequency

spectrum $\hat{S}_i(f) = \mathrm{FFT}[S(t_i : t_i + \delta t)]$ (obtained from each sliding window). SWFFT must be able to resolve the main Doppler component correctly (centered typically around 700 kHz with a width of about 300 kHz) and in the same time be able to follow a small variation of the Doppler shift (in this case $f_{\mathrm{amp}} = 20$ kHz). This requires to choose the width n_{win} carefully and the number of points n_{shift} that the window shifts at each slide. Note that during this procedure, the maximum frequency detectable is given by $f_{\mathrm{max}} = f_{\mathrm{acq}}/2$ while the frequency resolution (i.e. the minimum frequency detectable) is given by $f_{\mathrm{min}} = f_{\mathrm{acq}}/n_{\mathrm{win}}$. In order to detect an oscillation in the Doppler frequency of an amplitude f_{amp}, f_{min} must be such that $f_{\mathrm{min}} < f_{\mathrm{amp}}$. For the second step, i.e. the determination of the Doppler shift from the frequency spectrum $\hat{S}(f)$, two different methods may be used. The simplest one is to compute the weighted spectral mean, defined as $f_{\mathrm{Dop}} = \sum f \cdot \hat{S}(f) / \sum \hat{S}(f)$. In the presence of low-frequency components in the detected signal due to a contribution of the reflected signal, this method does not work correctly and each spectrum must be fitted in order to extract the maximum of the main Doppler component. This is time consuming but appears necessary sometimes for Tore Supra data (in O-mode for instance), this is not the case for the data series used here (see figure 1).

At this stage, the new signal generated from this second step has an acquisition frequency given by $f_{\mathrm{acq2}} = f_{\mathrm{acq}}/n_{\mathrm{shift}}$ and then the maximum frequency detectable $f_{\mathrm{max\,2}} = f_{\mathrm{acq}}/(2n_{\mathrm{shift}})$. The minimum frequency detectable can be at most $f_{\mathrm{min\,2}} = f_{\mathrm{acq}}/n_{\mathrm{points}}$ (the total time of the generated sequence remains the same), but from usual signal processing techniques it is better to use an averaged spectral estimator to decrease the variance and increase the detectability of the peak at the oscillation frequency. Then, unless mentionned, in the rest of the paper, to analyse the time evolution of the Doppler velocity (obtained using any of the three methods discussed here), we will use an averaging on eight Hamming windows with 50% overlap to process the generated time sequence, which decreases $f_{\mathrm{min\,2}}$ by a factor around 4 (taking into account the fact that n_{win2} should be chosen to be a power of 2). To summarize, there are two main constraints in choosing the SWFFT parameters. The width of sliding windows (n_{win}) should be large enough to satisfy $f_{\mathrm{min}} = f_{\mathrm{aqc}}/(2n_{\mathrm{win}}) < 2f_{\mathrm{amp}}$ and in the same time n_{shift} must be small enough to satisfy $f_{\mathrm{max\,2}} = f_{\mathrm{acq}}/(2n_{\mathrm{shift}}) > f_{\mathrm{G}}$. However, both parameters, n_{shift} and n_{win} are linked by the fact that the signal cannot be oversampled and then $n_{\mathrm{shift}} \geqslant n_{\mathrm{win}}/2$. Therefore a correct balance between detecting small amplitude oscillation and resolving high frequency oscillation should be found. Choosing the width of the sliding windows equal to 256 points and an overlap of 128 points is, in principle, a good compromise to detect an oscillation of the velocity with a minimal amplitude of 10 kHz ($f_{\mathrm{min}} = 20$ kHz) and a frequency up to $f_{\mathrm{max\,2}} = 40$ kHz. These are the values that will be used in the following but the efficiency of this technique depends strongly on the amplitude of the oscillation that we want to detect and on the length of the analysed signal (n_{points}).

In order to avoid these limitations, we use the MUSIC method, presented above, on a sliding window of n_{ws} points. Because we want to detect the Doppler frequency (which is a single dominant frequency in the signal), the parameter n_{f} is set to 1 (tests with higher values of n_{f} indicate that the results are not sensitive to this parameter as long as one takes the dominant frequency and that no other components such as low-frequency components are present in the experimental signal). Considering an oscillation with an amplitude f_{amp}, the number of points $n_{\Delta f}$ to sample the pseudo-spectrum over the frequency vector f must be such that the frequency resolution given by $f_{\mathrm{min}} = f_{\mathrm{acq}}/n_{\Delta f}$ is clearly finer than f_{amp}. Therefore, because here and in all the paper $f_{\mathrm{acq}} = 10$ MHz, for the case 1 ($f_{\mathrm{amp}} = 50$ kHz), $n_{\Delta f}$ should be clearly higher than 200, as it was for the SWFFT method. Similarly, considering an oscillation of frequency f_{G}, the maximal width of the sliding window, n_{ws}, which determines the temporal resolution of the Doppler frequency sequence, and thus the maximum oscillation frequency that can be detected, should be such that $n_{\mathrm{ws}} < f_{\mathrm{acq}}/(2f_{\mathrm{G}})$ (i.e. $n_{\mathrm{ws}} < 330$ in the cases considered here). Performing several tests using the case 1, with $n_{\mathrm{f}} = 1$ and $n_{\Delta f} = 512$, it appears that the best results, in detecting the oscillation of the Doppler frequency, are obtained for n_{w} from 2 to 10 and n_{ws} from 4 to 128. Note that the sensitivity of the results with the choice of these parameters is quite weak: increasing n_{w}, at fixed n_{ws}, tends to increase the 'background level' (other frequencies than the oscillation frequency) while increasing n_{ws}, at fixed n_{w}, does not affect the spectrum of the generated time sequence and just modifies the maximum accessible oscillation frequency. In order to compare with the other methods, the MUSIC algorithm has been applied to the synthetic signal $S(t)$ using the set of parameters: $n_{\mathrm{f}} = 1$, $n_{\mathrm{w}} = 6$, $n_{\mathrm{ws}} = 32$ and $n_{\mathrm{shift}} = 16$ and an FFT analysis, similar to the one used with the other methods (i.e. using an averaging of eight sliding windows, here, 6600 points, with a 50% overlap and $n_{\mathrm{fft}} = 8192$), on the time evolution of the perpendicular velocity.

Figure 2 shows frequency spectra obtained using the three different methods. In the presence of a strong oscillation in the Doppler velocity ($f_{\mathrm{amp}} = 50$ kHz) and using a long time sequence acquisition ($n_{\mathrm{points}} = 524\,000$ corresponding to a time sequence of 52.4 ms), all the methods considered can clearly detect the oscillation at $f_{\mathrm{G}} = 15$ kHz, as shown in figure 2(*a*). The ratio of the maximum of the peak over the background level, which gives the signal to noise ratio, may be used in order to evaluate the sensitivity of each method. Using the phase derivative method, the relative amplitude is around 5 as compared with 22 using the SWFFT method. The higher relative amplitude is obtained using the MUSIC method, in which the relative amplitude is around 100. Note that the error in recovering the frequency of the GAM is given here by the frequency resolution which is given by the FFT applied on the Doppler velocity and which depends on the total number of data points (for example, $\Delta f = 0.08$ kHz when using 524 000 points).

When reducing the amplitude of the oscillation of the Doppler shift down to $f_{\mathrm{amp}} = 20$ kHz (i.e. $\triangle v_{\mathrm{amp}} = 2\pi \times 20\,\mathrm{kHz}/k_{\perp}$ which gives for a typical value of $k_{\perp} = 10\,\mathrm{cm}^{-1}$ a GAM flow velocity of around $\triangle v_{\mathrm{amp}} = 125\,\mathrm{m\,s}^{-1}$), the phase derivative method starts to fail while both SWFFT and MUSIC methods remain capable of detecting the oscillation at the frequency 15 kHz (figure 2(*b*)).

When reducing the total number of points n_{points} down to $n_{\mathrm{points}} = 100\,000$, in the case with a strong oscillation in the

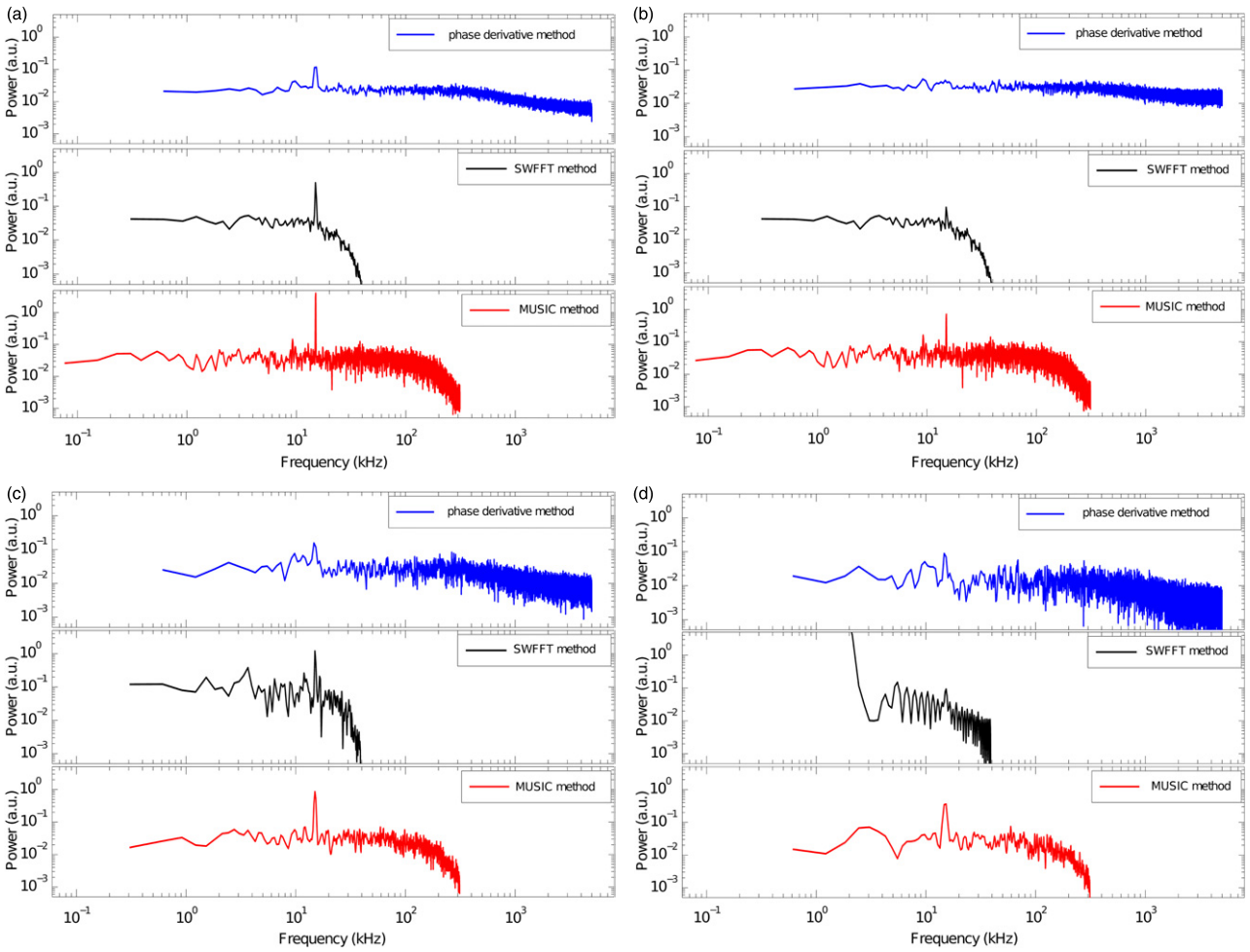

Figure 2. Synthetic signal: comparison of the normalized frequency spectrum of perpendicular velocity obtained using the three different methods for several cases: (*a*) $f_{amp} = 50$ kHz and $n_{points} = 524\,000$; (b) $f_{amp} = 20$ kHz and $n_{points} = 524\,000$; (c) $f_{amp} = 50$ kHz and $n_{points} = 100\,000$ and (d) $f_{amp} = 50$ kHz and $n_{points} = 50\,000$.

velocity (case 1), all three methods function as they should, as can be observed in figures 2(*c*) and (*d*). For $n_{points} = 50\,000$, the velocity oscillation remains visible for all methods but the relative amplitude starts to be very weak, especially using the SWFFT method.

To determine the combination of both effects of the amplitude and the total number of points, the final test has been performed using a weak amplitude oscillation in the velocity and reducing the number of data. Figure 3(*c*) shows the spectra obtained using $n_{points} = 100\,000$ in which only the MUSIC method remains capable (with difficulty) of detecting the oscillation at 15 kHz. Using only $n_{points} = 50\,000$, it becomes impossible to detect the oscillation present in the velocity as visible in figure 3(*d*). As a conclusion, for an acquisition frequency of $f_{acq} = 10$ MHz, it appears reasonable to use $n_{points} = 100\,000$, knowing that for oscillation amplitude of about $f_{amp} = 20$ kHz or lower, the detection becomes difficult. The use of the MUSIC method has two main advantages for our application. First, weaker oscillation can be detected using shorter time sequence (lower number of data point) than using phase derivative or standard SWFFT methods. Secondly, it allows us to determine the 'instantaneous' perpendicular velocity (Doppler shift) with a higher time resolution than using the standard SWFFT method (in principle up to 1 MHz).

It should be noted that in the case of very short experimental signals, one can also use a double MUSIC approach (that we call MUSIC^2) which replaces the FFT of the velocity time signal with a second MUSIC spectral estimate of the velocity signal performed over the total sequence length. This can reduce the number of points needed to detect a GAM drastically (see figure 6). This MUSIC^2 method functions down to a time signal that contains a single period of the GAM oscillation, which would be unthinkable with the SWFFT method.

4. Observation of GAMs on Tore Supra

4.1. Experimental conditions and general statistical properties

Results that are presented here were obtained by analysing the discharges of a dedicated ν^* scan performed on Tore Supra [23]. These discharges are in L-mode, and are heated using ion cyclotron resonance heating (ICRH). The particular experiment that is presented corresponds to the high collisionality case of the ν^* scan and is composed of two identical discharges, between which the set-up of the Doppler backscattering were changed. The first set-up was designed for

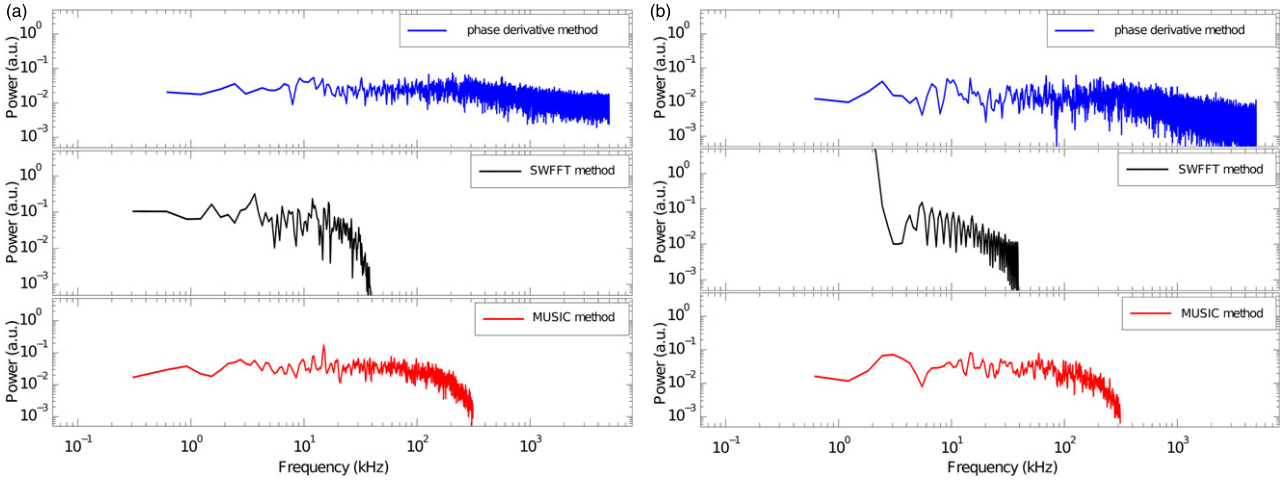

Figure 3. Synthetic signal: comparison of the normalized frequency spectrum of perpendicular velocity obtained using the three different methods for a velocity oscillation of a weak amplitude ($f_{amp} = 20$ kHz) and using $n_{points} = 100\,000$ (*a*) and $n_{points} = 50000$ (*b*).

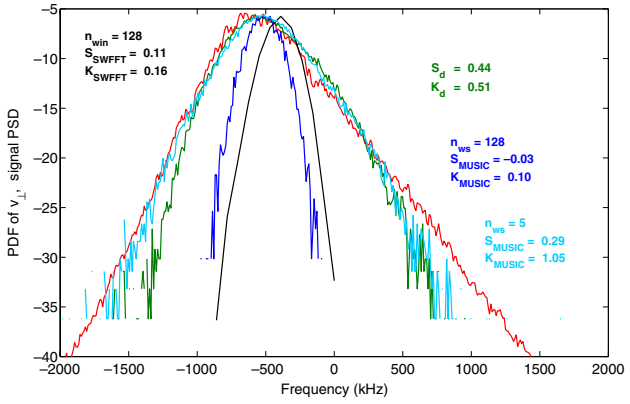

Figure 4. PDF (in arbitrary units) of the Doppler frequency time series (associated with the perpendicular velocity) obtained from SWFFT method (black) using windows of 128 points and from MUSIC algorithm with $n_{ws} = 128$ (dark blue), and with $n_{ws} = 5$ (light blue), and obtained form the phase derivative (in green). The average power spectral density of the scattering signal is shown in red.

the study of GAMs, where long time sequences were acquired (53 ms corresponding to $n_{points} = 530\,000$ data points) for each probing frequency and therefore only two probing frequencies and four incident angles were measured during the same shot. The second set-up was a standard set-up generally used for wavenumber spectrum and radial electric field measurements, short time sequences ($n_{points} = 33\,000$, i.e. a time sequence of 3.3 ms) were acquired for each probing frequency, allowing the scan of ten probing frequencies and ten incident angles during a single shot.

The time series of the Doppler instantaneous frequency obtained using the MUSIC algorithm, SWFFT and the phase derivative method are first analysed using statistical tools such as power probability Density Functions (PDF) which are compared in figure 4. It should be noted that since the first two methods use a two steps analysis (i.e. determination of the Doppler velocity and analysis of the dynamics of this velocity), the PDF of the velocity will depend on what time-scale we are looking at. When using the same time resolution for SWFFT and MUSIC ($n_{win} = n_{ws} = 128$), the different statistical moments, such as the standard deviation, the kurtosis and the skewness, are quite similar for both methods, and similar to what was obtained in [11] (close to Gaussian). However, the kurtosis and the skewness vary significantly when the time resolution is changed. If the time resolution of the Doppler velocity time series is reduced down to the turbulence correlation time or less (of the order of a microsecond, typically <10 points), the PDF obtained from MUSIC (light blue, $n_{ws} = 5$) and from phase derivative (green) departs from a Gaussian and closely follows the shape of the power spectral density of the original scattering signal (shown in red); this is what can be expected if the signal spectrum indeed reflects the fluctuation velocity time distribution [18]. The PDF statistical analysis then provides information about the dynamics of the underlying turbulence and not of the GAM.

4.2. GAM identification, radial repartition and frequency scaling

Figure 5 shows, in log–log scale, the frequency spectrum of both the perpendicular velocity of density fluctuations and the level of density fluctuations (from the time evolution of the dominant eigenvalue, $n_f = 1$) measured using Doppler backscattering system in set-up 1. The measurements are performed using the X-polarization channel of the Doppler backscattering system, the probing frequency was set to $F = 78$ GHz and the antenna tilt angle to 7.75°, which corresponds to the plasma edge around $r/a = 0.95$ and $k_\perp = 11\,\mathrm{cm}^{-1}$. The spectra are obtained using the MUSIC method to extract the Doppler frequency as well as the amplitude of the density fluctuations and applying an FFT on the time evolution of both quantities (using an averaging on eight Hamming windows with 50% overlap and $n_{fft} = 8192$). An oscillation is clearly detectable on the frequency spectrum of the velocity at a frequency of $f = 8.1$ kHz. In contrast, there are no oscillations that are distinctly observable on the frequency spectrum of the amplitude of density fluctuations. It should be noted that neither the SWFFT method (not shown here) nor the MUSIC method show no peak in the amplitude spectrum while the same oscillation (with the same frequency) is observed in the velocity.

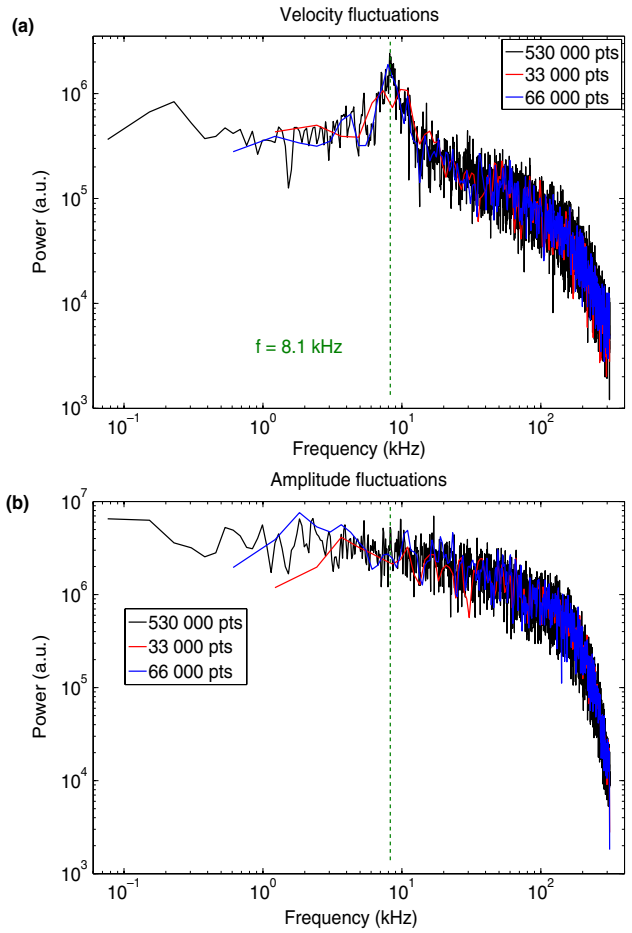

Figure 5. Experimental signal (shot TS45510): frequency spectrum of the perpendicular velocity of density fluctuations (*a*) and of the amplitude of the Doppler component (*b*) using the MUSIC algorithm with $n_f = 1$, $n_w = 4$, $n_{ws} = 32$.

Note that in order to evaluate the minimum duration of the time sequence required to detect the oscillation on the velocity, spectra presented in figure 5 have been computed considering several number of data points. The oscillation of the velocity remains undeniably detectable decreasing n_{points} down to $n_{points} = 66\,000$ for this given example. Note that decreasing the number of data point hence the length of the time sequence decreases the frequency resolution from $\Delta f = 0.08$ kHz ($n_{points} = 530\,000$) to $\Delta f = 1.2$ kHz ($n_{points} = 33\,000$).

In order to evaluate the capability of the MUSIC method as compared with the SWFFT method on experimental data, figure 6 presents the same data (as presented in the figure 5) analysed using the SWFFT and the MUSIC^2 method (introduced in the previous section). This means that the latter has been used consecutively on the complex signal to extract first the perpendicular velocity dynamics and then on the total sequence of the perpendicular velocity signal itself, instead of the standard FFT applied in section 3.2. Note that velocity time series is real and then $n_f = 2$ is necessary to detect a single frequency in a real signal. As can be observed clearly in figure 6, the SWFFT starts to fail in detecting the velocity oscillation when using 5376 points (in fact, the confidence in the method is probably very much open to question even with

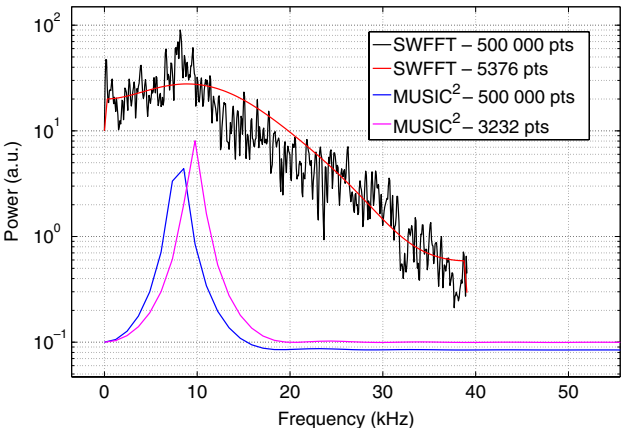

Figure 6. Experimental signal (shot TS45510): comparison of the frequency spectrum of the perpendicular velocity of density fluctuations using SWFFT for two different signal lengths (signal with 500 000 points in red and signal with 5376 points in black) and the pseudo-spectrogram obtained using double MUSIC methods with $n_f = 1$, $n_w = 4$ for the first MUSIC and $n_f = 2$, $n_w = 64$ for the second MUSIC for two different signal lengths (signal with 500 000 points in blue and signal with 3232 points in magenta).

much more points), while the double MUSIC method, remains capable of detecting distinctly the oscillation using only 3232 points. The difference between the position of the peaks for the MUSIC^2 methods with higher and lower number of points is not due to loss of accuracy but as is shown in figure 11 due to an evolution of the GAM frequency in time.

In the same spirit, a comparison between the frequency spectra of the perpendicular velocity of a synthetic signal (with a constant GAM around the experimental mean frequency of the GAM observed during the discharge 45510) and the experimental signal using the MUSIC algorithm with the same parameters are shown in figure 7. This comparison shows that the GAM component has a finite width in the experiments in contrast to the synthetic signal with constant GAM frequency, and therefore points to the fact that, in the experiments, the GAM frequency is evolving in time (which is clearly seen in figure 11).

In order to evaluate the radial extent of area where the velocity oscillation can be detected, the identical discharge with set-up 2 has been analysed and similar oscillations are detected at several probing frequencies (even using only $n_{points} = 33\,000$). Figure 8 presents the radial profile of the amplitude of the Doppler frequency oscillations, at two different wavenumbers. The amplitude in terms of velocity is then deduced taking $A(\mathrm{km\,s^{-1}}) = 2\pi A(\mathrm{kHz})/k_\perp(\mathrm{m^{-1}})$. It appears that the amplitude of this oscillation is of the order of $0.3\,\mathrm{km\,s^{-1}}$ which represents approximately 10% of the total perpendicular velocity ($v_\perp(r/a = 0.9) = 3.2\,\mathrm{km\,s^{-1}}$, which is normally a sum of the background $E \times B$ velocity and the phase velocity). These values are similar to the ones observed on ASDEX Upgrade [35]. Note that, no difference is observed between radial profiles when two different wavenumbers are investigated (i.e. using two different launching angles for the probing wave) as expected for GAMs which are oscillations of the mean poloidal flow and thus are not related to the spatial scale of the moving density fluctuation that is observed.

The oscillation detected is localized at the edge, where the safety factor is higher (in this discharge $q(r/a = 0.95) = 4$)

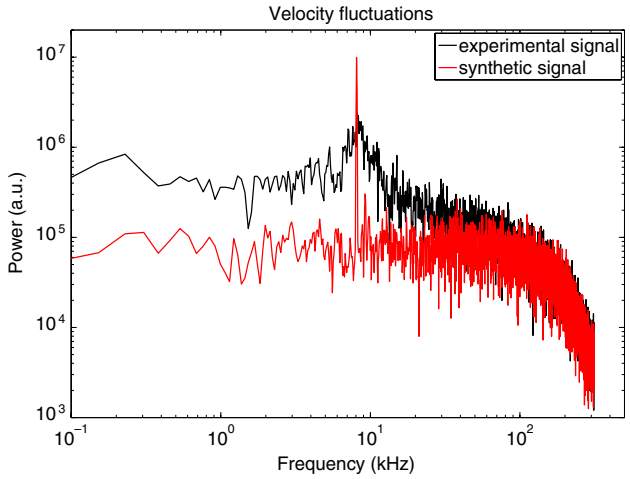

Figure 7. Comparison between spectrum of the perpendicular velocity of density fluctuations obtained from experimental data and from synthetic signal using the MUSIC algoritm. This suggests that the width of the GAM may be coming from the dynamics of the GAM, i.e. either from the frequency modulation that we observe (e.g. see figure 11) or from the auto-correlation of the GAM itself.

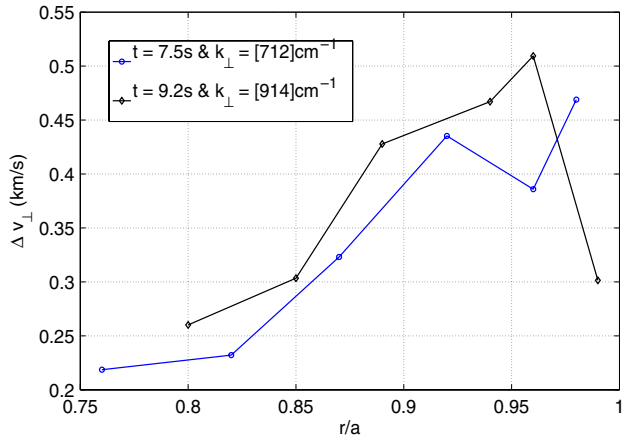

Figure 8. Radial profiles of the GAM oscillation amplitude for the discharge #45510 considered in figure 5 obtained using two different incident angles $\alpha = 5.9^\circ$ (blue) and $\alpha = 9.2^\circ$ (black).

and therefore the GAMs can be more easily excited. The radial extent is relatively wide (from $r/a = 0.95$ to $r/a = 0.75$) as compared with the observations made on ASDEX Upgrade [35].

The frequency observed is compared with the simple expression for the GAM frequency, which has been derived by [45] for a large aspect ratio $R \gg a$ (where R and a are the major and the minor plasma radii, respectively), circular plasma (both of which are reasonably valid for Tore Supra plasmas), and gives $\omega_{\mathrm{GAM}} = (2 + 1/q^2)^{1/2} C_\mathrm{s}/R$, where C_s is the ion sound speed and approximated in the following by $C_\mathrm{s} \simeq \sqrt{2T_\mathrm{e}/m_\mathrm{i}}$. Here, we consider the majority ion (i.e. deuterium). Figure 9 shows the observed frequencies during both discharges (set-up 1 and set-up 2) and the radial profiles of the quantity $C_\mathrm{s}/(2\pi R)$ and the GAM frequency $f_{\mathrm{GAM}} = \omega_{\mathrm{GAM}}/(2\pi)$ expected from the above expression. Note that the uncertainties on the experimentally observed frequencies and those that are plotted in this figure correspond to the frequency resolution of the FFT (related to n_{points}).

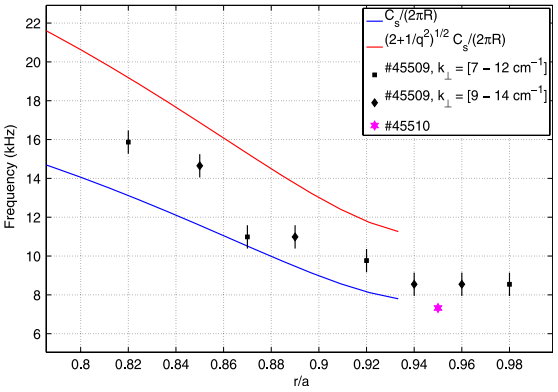

Figure 9. Radial profiles of the predicted GAM frequency for the discharge #45510 considered in figure 5 and experimental values of the frequency of the GAM observed during the similar discharges (#45510 and #45509).

Unfortunately no ECE measurements of T_e are available for $r/a > 0.93$, C_s is not evaluated at the plasma edge where the most precise measurements are made (with the smallest uncertainties obtained using set-up 1) and therefore where the frequency of the oscillations is determined with a better accuracy ($r/a = 0.95$). However, it appears from the discharge using set-up 2 that the frequency of the oscillation observed in the velocity remains in between both quantities, namely $C_\mathrm{s}/(2\pi R)$ and $(2 + 1/q^2)^{1/2} C_\mathrm{s}/(2\pi R)$. This agreement, in addition to the fact that the oscillation is observed on the flow velocity and not in the fluctuation level, and gets stronger near the edge, suggests strongly that these oscillations are indeed GAMs.

Similar oscillations in the velocity of density fluctuations (i.e. oscillations of the radial electric field) have been observed in several other discharges, including three discharges with different additional ICRH power: $P_{\mathrm{ICRH}} = 1\,\mathrm{MW}$, $P_{\mathrm{ICRH}} = 2\,\mathrm{MW}$ and $P_{\mathrm{ICRH}} = 4.5\,\mathrm{MW}$, which were otherwise identical. The frequency spectra of the Doppler frequency, measured at $r/a = 0.9 \pm 0.5$, for these three discharges are presented in figure 10 in linear–linear scale. It was observed that the frequency of the oscillation increases slightly from $f = 11\,\mathrm{kHz}$ to $f = 12.5\,\mathrm{kHz}$ when increasing the additional power. Comparing these frequencies with the radial profiles of the quantity $C_\mathrm{s}/(2\pi R)$ for each discharges shows good agreement supporting the interpretation of these observations as GAMs, since $C_\mathrm{s}/(2\pi R)(r/a = 0.9) = 8\,\mathrm{kHz}$, 9.5 kHz and 10.5 kHz, respectively, for the discharge 45500, 45498 and 45496.

4.3. GAM frequency modulation

Trying to resolve the dynamics of these oscillations, one can reanalyse the time evolution of the Doppler frequency (obtained using MUSIC algorithm) using again the MUSIC method over sliding windows scanning the full time sequence. This has been performed on the data of the discharge 45510 and is shown in figure 11.

The set of parameters used for the first MUSIC is $n_\mathrm{f} = 1$, $n_\mathrm{w} = 4$, $n_{\mathrm{ws}} = 256$ and $n_{\mathrm{shift}} = 128$. The value of n_{ws} has been increased in order to reduce the effect of the fast variations of the Doppler frequency not related to the physics of GAMs. For the second MUSIC, applied on the time evolution of the

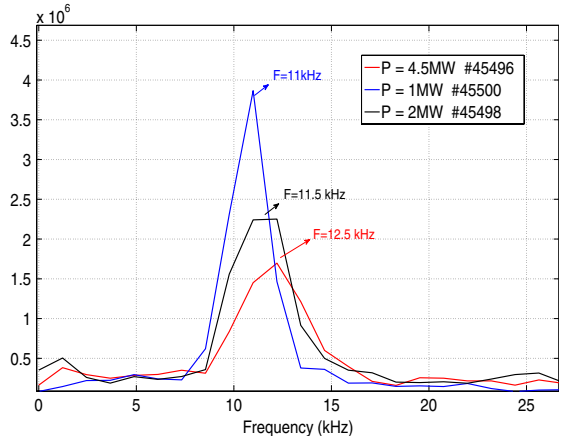

Figure 10. Frequency spectrum of the velocity of density fluctuations for different levels of additional power (ICRH) shown in linear scale.

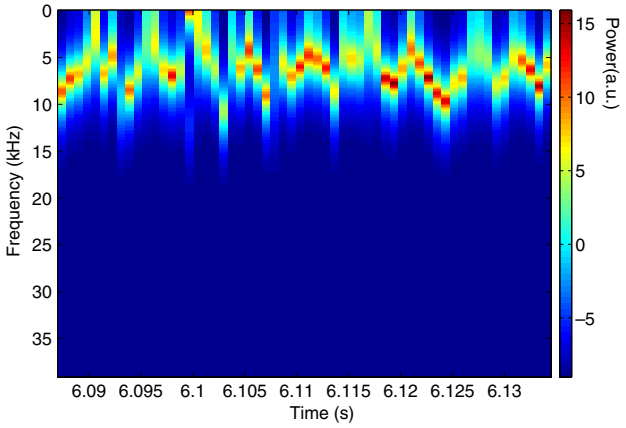

Figure 11. Time evolution of the pseudo-spectrum of the velocity of density fluctuations.

Doppler frequency, the set of parameters used is $n_{f,2} = 2$, $n_{w,2} = 8$, $n_{ws,2} = 256$ ($n_{\Delta f,2} = 512$). The choice of these parameters has been determined using a synthetic signal, similar to the signals used in the previous section, in which a time evolution of the GAM frequency has been added. Because of the high sensitivity of the results against these parameters, the use of this MUSIC[2] method requires a certain care. However, the method allows us to extract the temporal evolution of the GAM frequency as presented in figure 11. To the best of our knowledge, this is the first time such an analysis has been performed showing that the GAM frequency is modulated in time. This modulation (while plasma conditions are stationary), has a typical frequency of about 100 Hz. Such modulation may arise as a result of slow oscillations of the mean flow velocity, such as that expected to arise from the zonal flow dynamics. Temporal evolution of the *amplitude* of GAMs, and its correlation with the turbulence level have been observed on several machines such as TJ-II [46], AUG [36] and DIII-D [47] during the L-H transition, and is often related to the predator–prey oscillations [48, 49] that result from nonlinear wave interactions between turbulence and zonal modes [50], which is possibly the dominant mechanism for the spectral 'cascade' in Tore Supra [51, 52]. This method of extracting the frequency modulations of the GAM oscillations allows a secondary diagnostics for the impact of zonal flows, which perhaps has not the accuracy and the confidence that one desires of a primary diagnostics system, but can be used in conjunction with a standard long range correlation set-up [9, 53–55], which is planned on Tore Supra using the two Doppler backscattering systems.

5. Discussion

The main objective of this paper was to present the first observation of GAMs on Tore Supra plasmas using the MUSIC algorithm. Oscillations of the flow velocity (i.e. radial electric field) have been observed on several discharges using Doppler backscattering system while no clear oscillations are visible on density fluctuations (line of sight close to the equatorial plane). Using several probing frequencies during the same discharge, allows us to evaluate the radial extent of these oscillations, which are localized at the edge of the plasma, near the separatrix, between $r/a = 0.85$ and $r/a = 0.95$. The frequency of these oscillations is slightly higher than $C_s/(2\pi R)$ and slightly lower than the expected GAM frequency $(2+1/q^2)^{1/2}C_s/(2\pi R)$ and is found to scale with C_s when performing a scan in the power of the additional heating (ICRH). The observation of GAMs in Tore Supra, provides another point for the R dependence of the GAM frequency between DIII-D and JT60-U or JET, which may hopefully be useful to distinguish detailed theoretical dependencies especially among larger machines. Note for instance that, in accord with the $1/R$ dependence of the several theoretical expressions for GAM frequency, the frequency of GAMs observed on Tore Supra is lower than the frequencies observed on both DIII-D and AUG tokamaks.

In this paper, we also present the MUSIC algorithm for the Doppler backscattering signals, which we have used for detecting GAMs and validate it via numerous tests performed using a synthetic signal. This algorithm appears as a powerful data analysis method that can capture the Doppler frequency with a high temporal resolution. The key point of using the MUSIC method is that, unlike the conventional FFT method, the frequency resolution is not limited by the width of the sliding windows. Therefore, for the typical setting of the Doppler backscattering systems used on Tore Supra (acquisition frequency $f_{acq} = 10$ MHz and time sequence of $n_{points} = 100\,000$ points, i.e. 10 ms), oscillations of the flow velocity around 15 kHz (and in principle up to 1 MHz) with an amplitude down to $f_{amp} = 10$ kHz are detectable. In addition, the use of the MUSIC method may give access to the time evolution of GAMs performing a double analysis: first the determination of the time evolution of the Doppler frequency (and eventually the amplitude) and secondly the time evolution of the GAM frequency (and eventually the amplitude).

In conclusion, this study shows the possibility of studying GAMs with high precision using the Doppler backscattering system, which is particular in that it allows us to observe GAMs and their effect of turbulence characteristics such as wavenumber spectrum and amplitude of the density fluctuations simultaneously. The installation on Tore Supra of a new channel with a vertical line of sight grants access to long-range correlation studies between channels away from each other which would permit studying the physics of ZFs.

Using this capability of measuring the detailed time evolution of GAMs, the interplay between GAMs, ZFs and density fluctuations can be studied in the near future.

Acknowledgments

This work was carried out within the framework the European Fusion Development Agreement (EFDA) and the French Research Federation for Fusion Studies (FR-FCM). It is supported by the European Communities under the contract of Association between Euratom and CEA. The views and opinions expressed herein do not necessarily reflect those of the European Commission. Financial support was also received from Agence Nationale de la Recherche under contract ANR-06-BLAN-0084

Appendix A. Mathematical foundation of the MUSIC algorithm

The MUSIC algorithm assumes that the signal consists of a finite number of frequency components plus an incoherent noise part as given in (1), which takes the form

$$\boldsymbol{x} = \boldsymbol{x}^{(s)} + \boldsymbol{n} = \boldsymbol{\mathcal{A}} \cdot \boldsymbol{B} + \boldsymbol{n} \tag{4}$$

when discretized, where

$$\boldsymbol{x} = \begin{pmatrix} x_1 \\ x_2 \\ \vdots \\ x_N \end{pmatrix}$$

is the discrete complex signal vector, superscript (s) indicating the 'pure signal part', sampled over N regular time intervals as $x_i = x(t_i)$, and

$$\boldsymbol{B} = \begin{pmatrix} B_1 \\ B_2 \\ \vdots \\ B_{n_\mathrm{f}} \end{pmatrix}, \qquad \boldsymbol{n} = \begin{pmatrix} n_1 \\ n_2 \\ \vdots \\ n_N \end{pmatrix},$$

$$\boldsymbol{\mathcal{A}} = \begin{pmatrix} \mathrm{e}^{-\mathrm{i}2\pi t_1 f_1} & \mathrm{e}^{-\mathrm{i}2\pi t_1 f_2} & \cdots & \mathrm{e}^{-\mathrm{i}2\pi t_1 f_{n_\mathrm{f}}} \\ \mathrm{e}^{-\mathrm{i}2\pi t_2 f_1} & \mathrm{e}^{-\mathrm{i}2\pi t_2 f_2} & & \mathrm{e}^{-\mathrm{i}2\pi t_2 f_{n_\mathrm{f}}} \\ \vdots & & \ddots & \vdots \\ \mathrm{e}^{-\mathrm{i}2\pi t_N f_1} & \mathrm{e}^{-\mathrm{i}2\pi t_N f_2} & \cdots & \mathrm{e}^{-\mathrm{i}2\pi t_N f_{n_\mathrm{f}}} \end{pmatrix}$$

with B_i's being the coefficients (i.e. amplitudes) of the n_f frequency components. Noting that the Hermitian adjoint of (4) is $\boldsymbol{x}^\dagger = \boldsymbol{B}^\dagger \cdot \boldsymbol{A}^\dagger + \boldsymbol{n}^\dagger$, we can define the auto-correlation matrix as

$$\boldsymbol{R} = \left\langle \boldsymbol{x}\boldsymbol{x}^\dagger \right\rangle = \left\langle \boldsymbol{x}^{(s)}\boldsymbol{x}^{(s)\dagger} \right\rangle + \left\langle \boldsymbol{n}\boldsymbol{n}^\dagger \right\rangle = \boldsymbol{\mathcal{A}} \cdot \bar{\boldsymbol{P}} \cdot \boldsymbol{\mathcal{A}}^\dagger + \sigma^2 \boldsymbol{I}, \tag{5}$$

where $\bar{\boldsymbol{P}} \equiv \langle \boldsymbol{B}\boldsymbol{B}^\dagger \rangle$, assuming that the noise is not correlated with the signal (i.e. $\langle \boldsymbol{\mathcal{A}} \cdot \boldsymbol{B}\boldsymbol{n}^\dagger \rangle = 0$) and is white. Note that the components of the $N \times N$ matrix $\boldsymbol{A} \cdot \bar{\boldsymbol{P}} \cdot \boldsymbol{A}^\dagger$ can be written as

$$\begin{aligned} \boldsymbol{T}_{ij} &= \langle \boldsymbol{x}^{(s)}\boldsymbol{x}^{(s)\dagger} \rangle_{ij} = \langle \boldsymbol{\mathcal{A}} \cdot \boldsymbol{B}\boldsymbol{B}^\dagger \cdot \boldsymbol{\mathcal{A}}^\dagger \rangle_{i,j} \\ &= \sum_{m=0}^{n_\mathrm{f}} \sum_{n=0}^{n_\mathrm{f}} \langle F_m F_n^* \mathrm{e}^{\mathrm{i}2\pi(t_j f_n - t_i f_m)} \rangle \end{aligned}$$

it is easy to see that $\boldsymbol{T}^\dagger = \boldsymbol{T}$, so that $\boldsymbol{T}$ (as well as $\boldsymbol{R}$) is Hermitian, and thus has real eigenvalues. The hypothesis of statistical stationarity, which is implicit in a large number of data analysis techniques, means that the ensemble average T_{ij} cannot depend on $\tau = (t_i + t_j)/2$, but only on $t_j - t_i$, which basically means that $\boldsymbol{T}$ is also a 'Toeplitz matrix' (i.e. $T(i, j) = T(i - j)$), and thus has eigen-values that are non-negative (see appendix B for a practical demonstration of this). It is also singular, since $N > n_\mathrm{f}$ and, T_{ij} has an actual rank n_f. These two properties guarantee that the minimum eigenvalues of the auto-correlation matrix $\boldsymbol{R}$ are all equal to σ^2, which is an essential feature of $\boldsymbol{R}$ that allows the signal/noise separation.

In order to see this, we consider the eigenvalues and eigenvectors $\boldsymbol{e}_i$ of $\boldsymbol{R}$:

$$\boldsymbol{R} \cdot \boldsymbol{e}_i = \lambda_i \boldsymbol{e}_i,$$

where $\boldsymbol{e}_i$'s are the eigenvectors and λ_i's are the eigenvalues. Note that the eigenvalues of $\boldsymbol{R}$ and those of $\boldsymbol{T}$ differ by σ^2, i.e.

$$\det\left(\boldsymbol{R} - \lambda_i \boldsymbol{I}\right) = \det\left(\boldsymbol{T} + \left(\sigma^2 - \lambda_i\right)\boldsymbol{I}\right).$$

Therefore, the eigenvectors of the pure signal correlation matrix $\boldsymbol{T}$ are also the eigenvectors of the data correlation matrix $\boldsymbol{R}$. Since the rank of $\boldsymbol{R}$ is larger than the rank of $\boldsymbol{T}$ (i.e. $N > n_\mathrm{f}$) the remaining $N - n_\mathrm{f}$ eigenvectors of $\boldsymbol{R}$, all have the eigenvalue σ^2. That is, if we sort the eigenvalues of $\boldsymbol{R}$ in descending order, they satisfy: $\lambda_1 \geqslant \lambda_2 \geqslant \cdots \geqslant \lambda_{n_\mathrm{f}+1} = \lambda_{n_\mathrm{f}+2} \cdots = \lambda_\mathrm{nw} = \sigma^2$. See appendix B on the SVD for details.

Finally, for those eigenvectors with the minimum eigenvalues, we have

$$\begin{aligned} \boldsymbol{R}\boldsymbol{e}_i = \left(\boldsymbol{T} + \sigma^2 \boldsymbol{I}\right)\boldsymbol{e}_i = \lambda_i \boldsymbol{e}_i = \sigma^2 \boldsymbol{e}_i \\ \Rightarrow \boldsymbol{\mathcal{A}}^\dagger \boldsymbol{e}_i = 0\,, \end{aligned}$$

which means that those eigenvectors, which in fact correspond to noise eigenvectors are perpendicular to the signal. This is also evident when we use the eigenvectors of $\boldsymbol{R}$ as the bases, since all the eigenvectors are perpendicular to one another, and the signal can be represented using only the first n_f eigenvectors (i.e. the signal eigenvectors), and thus is perpendicular to the last $N - n_\mathrm{f}$ eigenvectors (i.e. the noise eigenvectors) with the minimum eigenvalue.

In the classical MUSIC method, the signal and the noise are assumed to be not correlated. Therefore, if we knew the noise eigenvectors perfectly, the expression

$$d^2(f) = a^\dagger(f) \boldsymbol{E}_\mathrm{noise} \boldsymbol{E}_\mathrm{noise}^\dagger a(f),$$

where $\boldsymbol{E}_\mathrm{noise}$ is a matrix whose columns are the noise eigenvectors would be exactly zero for each $f = f_i$ of the signal. The MUSIC spectral estimate is then to consider the quantity in (2), which would be infinite for each $f = f_i$ of the signal if the signal and the noise were perfectly distinguished. In practice one obtains large, narrow peaks at the locations of the signal frequencies. The heights of these peaks indicate significance (i.e. distinctness from the noise) of the corresponding frequency signals.

Appendix B. Practical implementation of the MUSIC algorithm

The expression for the spectral power estimate for the MUSIC method in (2), requires only the computation of the eigenvectors of $\boldsymbol{R}$. But the mathematical basis for its Toeplitz form relies on statistical stationarity of the ensemble average. The ensemble average in data analysis is an idealization if not an abstraction. In practice, one uses a kind of time average (or a forward–backward time average) over the data itself with some overlap, which defines $\boldsymbol{R}$ as

$$\boldsymbol{R} = \left\langle \boldsymbol{x}\boldsymbol{x}^{\dagger} \right\rangle = \frac{1}{N_{\mathrm{E}}} \sum_{n} \boldsymbol{x}_n \boldsymbol{x}_n^{\dagger}, \tag{6}$$

where $\boldsymbol{x}_n^{\mathrm{T}} = [x_n, \cdots, x_{n+nw-1}]$ with n_{w} being the size of the resulting averaged matrix, one can construct from the data of size N, a maximum of $N_{\mathrm{E}} = N - n_{\mathrm{w}} + 1$ 'ensembles' over which to compute the average. Obviously n_{w} should be larger than n_{f}, in order to resolve all the frequencies in the signal. If N_{E} is not sufficiently large one can improve the situation by performing a forward–backward average by defining the nth backwards data vector:

$$\boldsymbol{x}_n^{(b)} = \begin{pmatrix} x^*_{N-n+1} \\ x^*_{N-n} \\ \vdots \\ x^*_{N-n-nw+2} \end{pmatrix}$$

and using

$$\boldsymbol{R} \equiv \frac{1}{2N_{\mathrm{E}}} \sum_{n} \left(\boldsymbol{x}_n \boldsymbol{x}_n^{\dagger} + \boldsymbol{x}_n^{(b)} \boldsymbol{x}_n^{(b)\dagger} \right). \tag{7}$$

We will in practice use this form, since it also permits an important simplification of the computation of the eigenmodes. It also explicitly enforces a Toeplitz form for the averaged auto-correlation matrix. Note that by defining a reorganized data matrix $\boldsymbol{X}$ of the form

$$\boldsymbol{X} = \frac{1}{\sqrt{2N_{\mathrm{E}}}} \begin{pmatrix} x_K & \cdots & x_1 \\ \vdots & \ddots & \vdots \\ x_N & \cdots & x_{N-nw+1} \\ x_1^* & \cdots & x_{nw}^* \\ \vdots & \ddots & \vdots \\ x^*_{N-nw+1} & \cdots & x_N^* \end{pmatrix} \tag{8}$$

we can write the averaged auto-correlation matrix defined in (7) simply as

$$\boldsymbol{R} = \boldsymbol{X}^{\dagger} \cdot \boldsymbol{X}. \tag{9}$$

As we have noted earlier, the eigenvectors of $\boldsymbol{R}$ are also the eigenvectors of $\boldsymbol{T}$. The matrix $\boldsymbol{T}$ can also be written using (9) as $\boldsymbol{T} = \boldsymbol{X}^{(s)\dagger}\boldsymbol{X}^{(s)}$, but using the pure signal $x_i^{(s)}$'s in the definition of $\boldsymbol{X}^{(s)}$ in (8) instead of the data x_i's. A matrix $\boldsymbol{X}^{(s)}$ can be factored as

$$X^{(s)} = U \Sigma V^{\dagger}, \tag{10}$$

where $\boldsymbol{U} = [\boldsymbol{u}_1, \boldsymbol{u}_2, \ldots, \boldsymbol{u}_K]$, and $\boldsymbol{V} = [\boldsymbol{v}_1, \boldsymbol{v}_2, \ldots, \boldsymbol{v}_K]$ are unitary matrices, with $\boldsymbol{u}_i$ and $\boldsymbol{v}_i$ the left and the right singular vectors, respectively. The matrix $\boldsymbol{\Sigma}$ has the following structure:

$$\boldsymbol{\Sigma} = \begin{pmatrix} \boldsymbol{D} & 0 \\ 0 & 0 \end{pmatrix},$$

where $\boldsymbol{D} = \mathrm{diag}(\sigma_1, \sigma_2, \ldots, \sigma_\ell)$ is an $n_{\mathrm{f}} \times n_{\mathrm{f}}$ diagonal matrix of 'singular values', σ_i's. Note that, since $\boldsymbol{U}$ and $\boldsymbol{V}$ are unitary, we can write

$$X^{(s)}V = U\Sigma \qquad \text{and} \qquad \boldsymbol{X}^{(s)\dagger}\boldsymbol{U} = \boldsymbol{V}\boldsymbol{\Sigma}^{\dagger}$$

using (10), or column by column:

$$\boldsymbol{X}^{(s)}\boldsymbol{v}_i = \sigma_i \boldsymbol{u}_i \qquad \text{and} \qquad \boldsymbol{X}^{(s)\dagger}\boldsymbol{u}_i = \sigma_i \boldsymbol{v}_i. \tag{11}$$

It is clear from (11) that the right singular vectors $\boldsymbol{v}_i$ are also the eigenvectors $\boldsymbol{e}_i$ of $\boldsymbol{T}$ with the eigenvalues $\lambda_i' = \sigma_i^2$:

$$\boldsymbol{X}^{(s)\dagger}\boldsymbol{X}^{(s)}\boldsymbol{v}_i = \boldsymbol{X}^{(s)\dagger}\sigma_i\boldsymbol{u}_i = \sigma_i^2\boldsymbol{v}_i.$$

One important advantage of the SVD technique, is that it will also determine the rank n_{f} of the matrix as the number of singular values σ_i's. In equation (2), it is the eigenvectors of the noise that is needed. For this we use the eigenvectors of $\boldsymbol{R}$, which can be computed as demonstrated above for $\boldsymbol{T}$, using the SVD method. However $\boldsymbol{R}$ is a full rank matrix. Its signal eigenvectors $\boldsymbol{v}_i$ are the same with the eigenvectors of $\boldsymbol{T}$ but with eigenvalues $\lambda_i = \lambda_i' + \sigma^2$, and its noise eigenvectors all have the eigenvalue $\lambda = \sigma^2$.

Due to this observation, one uses in practice the SVD of the vector $\boldsymbol{X}$ (not $\boldsymbol{X}^{(s)}$, which is impossible to compute without knowing the noise anyways), to compute the noise eigenvectors to be used in the equation (2) above for the MUSIC spectral power estimate. The method has the further advantage that by looking at where the singular values saturate, one can estimate the number of frequencies needed to represent a given times series.

The actual algorithm we use can be summarized as follows (Note that for steps 2–4, various commercial (i.e. MATLAB™ function pmusic [56]) and open source implementations (i.e. 'pmusic' function in the 'Spectrum' library for python [57], the 'musicsp' function in the SPCToolbox [58], which works with GNU-Octave [59], etc)) of the algorithm exist. The algorithm described above is the modern version of the MUSIC algorithm due to [24] and is not linked to a particular implementation.

(1) Select a segment (of size $N = n_{\mathrm{ws}}$) of the complex signal x formed by combining the reflectometer I and Q signals (of size n_{points}), optionally with an overlap, between the segments.
(2) Construct the reorganized data matrix X as defined in equation (8) using the components of the complex signal x.
(3) Compute the SVD of the reorganized data matrix X.
(4) Take the last $n_{\mathrm{w}} - n_{\mathrm{f}}$ singular values, and the singular vectors (which are incidentally the eigenvectors of $\overline{\boldsymbol{R}}$) and use these to compute P_{MUSIC} power estimate using equation (2).
(5) Use the maximum of the P_{MUSIC} as the detected frequency for that segment.
(6) Repeat for each segment by sliding the time window by n_{shift} to construct the time series that corresponds to the Doppler frequency as a function of time.
(7) Compute the power spectrum of this $f_{\mathrm{dop}}(t)$ signal, using one of the two methods:
   (a) averaged spectral estimation (for intance the periodogram) which works if f_{dop} has sufficient number of points (see the result for instance in figure 5.

(b) Or a secondary P_{MUSIC}, which works even with less points, and therefore permits the construction of figure 11.

References

[1] Diamond P.H., Itoh S.-I., Itoh K. and Hahm T.S. 2005 *Plasma Phys. Control. Fusion* **47** R35
[2] Fujisawa A. *et al* 2004 *Phys. Rev. Lett.* **93** 165002
[3] Fujisawa A. *et al* 2008 *Phys. Plasmas* **15** 055906
[4] Tynan G.R., Moyer R.A., Burin M.J. and Holland C. 2001 *Phys. Plasmas* **8** 2691
[5] Moyer R.A., Tynan G.R., Holland C. and Burin M.J. 2001 *Phys. Rev. Lett.* **87** 135001
[6] Xu G.S., Wan B.N., Song M. and Li J. 2003 *Phys. Rev. Lett.* **91** 125001
[7] Jakubowski M., Fonck R.J. and McKee G.R. 2002 *Phys. Rev. Lett.* **89** 265003
[8] McKee G.R. *et al* 2006 *Plasma Phys. Control. Fusion* **48** S123
[9] Schmitz L., Wang G., Hillesheim J.C., Rhodes T.L., Peebles W.A., White A., Zeng L., Carter T.A. and Solomon W. 2008 *Rev. Sci. Instrum.* **79** 10F113
[10] Hamada Y., Nishizawa A., Ido T., Watari T., Kojima M., Kawasumi Y., Narihara K., Toi K. and Group J.-I. 2005 *Nucl. Fusion* **45** 81
[11] Conway G.D., Scott B., Schirmer J., Reich M., Kendl A. and the ASDEX Upgrade Team 2005 *Plasma Phys. Control. Fusion* **47** 1165
[12] Nagashima Y. *et al* 2005 *Phys. Rev. Lett.* **95** 095002
[13] Vershkov V., Shelukhin D., Soldatov S., Urazbaev A., Grashin S., Eliseev L., Melnikov A. and the T-10 team 2005 *Nucl. Fusion* **45** S203
[14] Krämer-Flecken A., Soldatov S., Koslowski H.R. and Zimmermann O. (TEXTOR Team) 2006 *Phys. Rev. Lett.* **97** 045006
[15] Zhao K.J. *et al* 2006 *Phys. Rev. Lett.* **96** 255004
[16] Clairet F., Heuraux S., Bottereau C., Molina D., Ducobu L., Leroux F. and Barbuti A. 2010 *Rev. Sci. Instrum.* **81** 10D903
[17] Sabot R., Sirinelli A., Chareau J.-M. and Giacalone J.-C. 2006 *Nucl. Fusion* **46** S685
[18] Hennequin P. Honoré C., Truc A., Qumneur A., Fenzi-Bonizec C., Bourdelle C., Garbet X., Hoang G.T. and the Tore Supra team 2006 *Nucl. Fusion* **46** S771
[19] Sabot R., Hennequin P. and Colas L. 2009 *Fusion. Sci. Technol.* **56** 1253
[20] Hennequin P. *et al* 2004 *Plasma Phys. Control. Fusion* **46** B121
[21] Vermare L., Heuraux S., Clairet F., Leclert G. and da Silva F. 2006 *Nucl. Fusion* **46** S743
[22] Gerbaud T. Clairet F., Sabot R., Sirinelli A., Heuraux S., Leclert G. and Vermare L. 2006 *Rev. Sci. Instrum.* **77** 10E928
[23] Vermare L. Hennequin P., Gürcan Ö.D., Bourdelle C., Clairet F., Garbet X. and Sabot R. 2011 *Phys. Plasmas* **18** 012306
[24] Schmidt R.O. 1986 *IEEE Trans. Antennas Propagation* **AP-34** 276
[25] Kaveh M. and Barabell A. 1986 *IEEE Trans. Acoustics Speech Signal Process.* **34** 331
[26] Swindlehurst A. and Kailath T. 1992 *IEEE Trans. Signal Process.* **40** 1758
[27] Porat B. and Friedlander B. 1988 *IEEE Trans. Acoustics Speech Signal Process.* **36** 532
[28] Jain S.K. and Singh S. 2011 *Electric Power Syst. Res.* **81** 1754
[29] Marple S.L. Jr. 1987 *Digital Spectral Analysis with Applications* (Englewood Cliffs, NJ: Prentice-Hall) p 512
[30] Honoré C., Hennequin P., Truc A. and Quemeneur A. 2006 *Nucl. Fusion* **46** S809
[31] Hennequin P. *et al* 2004 *Rev. Sci. Instrum.* **75** 3881
[32] Trier E., Eriksson L.G., Hennequin P., Fenzi C., Bourdelle C., Falchetto G., Garbet X., Aniel T., Clairet F. and Sabot R. 2008 *Nucl. Fusion* **48** 092001
[33] Hennequin P. *et al* 1999 *Proc. 26th EPS Conf. Controlled Fusion Plasma Physics (Maastricht, The Netherlands)* vol 23, p 977 http://epsppd.epfl.ch/Maas/web/pdf/p3006.pdf
[34] Conway G.D., Tröster C., Scott B., Hallatschek K. and the ASDEX Upgrade Team 2008 *Plasma Phys. Control. Fusion* **50** 055009
[35] Conway G.D. and the ASDEX Upgrade Team 2008 *Plasma Phys. Control. Fusion* **50** 085005
[36] Conway G.D., Angioni C., Ryter F., Sauter P. and Vicente J. (ASDEX Upgrade Team) 2011 *Phys. Rev. Lett.* **106** 065001
[37] Murakami T. and Ishida Y. 2001 *Acoust. Sci. Technol.* **22** 293
[38] Odendaal J., Barnard E. and Pistorius C. 1994 *IEEE Trans. Antennas Propagation* **42** 1386
[39] Godara L. 1997 *Proc. IEEE* **85** 1195
[40] Chouet B. 2003 *Pure and Appl. Geophys.* **160** 739
[41] Wang Z., Li J. and Wu R. 2005 *IEEE Trans. Med. Imaging* **24** 1308
[42] Mosher J., Lewis P. and Leahy R. 1992 *IEEE Trans. Biomed. Eng.* **39** 541
[43] Adali T. and Haykin S. 2010 *Adaptive Signal Processing: Next Generation Solutions* (New York: Wiley)
[44] Iwata T., Goto Y. and Susaki H. 2001 *Meas. Sci. Technol.* **12** 2178–84
[45] Winsor N., Johnson J.L. and Dawson J.M. 1968 *Phys. Fluids* **11** 2448
[46] Estrada T., Happel T., Hidalgo C., Ascasibar E. and Blanco E. 2010 *Europhys. Lett.* **92** 35001
[47] Schmitz L. *et al* 2011 *Shear Flow and Turbulence Suppression in Limit Cycle Oscillations Preceding the L–H Transition* (San Diego, CA: US-EU TTF)
[48] Diamond P.H., Liang Y.-M., Carreras B.A. and Terry P.W. 1994 *Phys. Rev. Lett.* **72** 2565
[49] Kim E. and Diamond P. 2003 *Phys. Plasmas* **10** 1698
[50] Chen L., Lin Z. and White R. 2010 *Phys. Plasmas* **7** 3129
[51] Gürcan Ö.D. *et al* 2009 *Phys. Rev. Lett.* **102** 255002
[52] Berionni V. and Gürcan O.D. 2011 *Phys. Plasmas* **18** 112301
[53] Pedrosa M.A., Silva C., Hidalgo C., Carreras B.A., Orozco R.O. and Carralero D. (TJ-II team) 2008 *Phys. Rev. Lett.* **100** 215003
[54] Xu Y., Jachmich S., Weynants R.R., Van Schoor M., Vergote M., Krämer-Flecken A., Schmitz O., Unterberg B., Hidalgo C. and TEXTOR Team 2009 *Phys. Plasmas* **16** 110704
[55] Liu A.D. *et al* 2009 *Phys. Rev. Lett.* **103** 095002
[56] Little J. and Shure L. 2002 *Signal Processing Toolbox User's Guide, Version 6*, Natick, MA 01760-1500
[57] Cokelaer T. 2011 *Spectrum—Spectral Analysis in Python (0.4.3)* and http://www.thomas-cokelaer.infoo/fortware/spectrum/html/contents.html
[58] Fargues M. and Brown D. 1994 Introduction to signal processing using the SPC toolbox *Conference Record of the 28th Asilomar Conf. on Signals and Systems* vol 2, pp 1298–302
[59] Eaton J.W. 2002 *GNU Octave Manual* (Network Theory Limited) ISBN 0-9541617-2-6 http://www.octave.org

5. Dynamics of the plasma via the dynamics of density fluctuations

In this paper, the first observation of GAMs on Tore Supra plasmas are presented : oscillations of the plasma flow velocity have been observed at the plasma edge in numerous discharges using DBS system in X-mode polarization (while, previously, mainly O-mode measurements were performed on Tore Supra). Using several probing frequencies during the same discharge, GAMs are found to extend between $r/a = 0.85$ and $r/a = 0.95$, with a frequency that varies with the probing radius and scales with C_s/R during a power scan, which is performed by increasing the additional heating (ICRH). The amplitude of the GAMs are usually observed to increase towards the edge, as for example in TEXTOR [100]. A significant part of this paper is devoted to the comparison of various data analysis methods for determining the instantaneous Doppler frequency. In particular, the multiple signal classification (MUSIC) algorithm [113], which is a power spectral estimation method based on the eigenmode analysis of data vectors, is presented and validated in some detail. It stands out as a powerful data analysis method to follow the Doppler frequency with a high temporal resolution due to the fact that it requires a relatively low number of points from the Doppler backscattering signal to determine the Doppler frequency. The remarkable aspect of this method is that, in contrast to Fourier analysis, MUSIC can obtain the frequency of an oscillatory signal even from a time sequence shorter than the period of oscillation. This impressive capability allows us to observe a surprising dynamics of the GAMs itself : a modulation of the GAM frequency (c.f. Figure 5 from [Publication 5]). The first observation of this behavior/characteristic is particularly interesting in the context of predator-prey dynamics and the energy exchange with the low-frequency ZF and the drift-wave turbulence in which GAM may act as a third player. These results motivate a new study based mainly on detailed comparisons of GAM properties between the experimental observations and the results from gyrokinetic simulation performed with GYSELA [114]. This work has been performed by Alexandre Storelli during his PhD [115] and published in the reference [116]. The comparison was performed using experiments from the ν^* scan (presented in the previous section) and a simulation tailored to represent, as much as possible, the plasma conditions of the high collisionality case. To summarize this work, the quantitative comparison between experiments, theoretical models and simulation highlights some limits of the current predictions of GAM frequency. While the GAM frequency from the simulation and from theoretical predictions is in fair agreement, the measured GAM frequency is below predictions. Taking into account the effects of plasma shaping and impurities helps approaching an agreement for the experimental high ν^* case. However, such effects are not large enough in the low ν^* case counterpart.

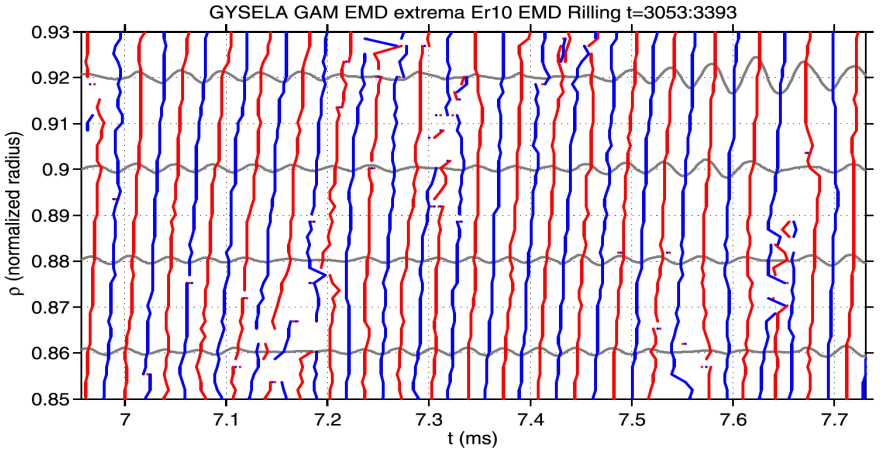

FIGURE 5.3. – Synchronization of the phase of the GAM oscillations between different radial zones. Extrema (maxima in red and minima in blue) of the velocity measured filtered at the GAM frequency from Ref. [116]

Some potential missing ingredients, such as the effect of finite orbit and trapped particles and/or the effect of the radial wavenumber of the GAM, have been identified and deeper investigation is required to elucidate the over-estimated prediction. Note that because Tore Supra plasmas are circular, no strong shape effects are expected.

Concerning the radial evolution of the GAM frequency, it follows the local sound speed both in experiments and simulations. However, in some cases, frequency steps have been detected in Tore Supra experiments while the GAM frequency in the simulations always appears to be continuous. It should be noted that the radial precision of the data analysis must be carefully evaluated, both in experimental data and simulation results.

In addition, it has been shown that GAM oscillations have an intermittent behavior, appearing as bursts in amplitude, both in the experiments and the simulation with a burst autocorrelation time of the order of $0.1ms$. In experiments, GAMs seem more coherent at some precise radii where it is more intense and where frequency steps are visible. Note however that in experiments, only few channels are available (corresponding to several probing frequency) and are not simultaneous (but only measured in a stationary phase with a small-time delay corresponding to the pattern of the sweeping of the probing wave frequency), the simulations allow analyzing all the radial positions simultaneously. Thus, it has been possible, in the simulation, to identify a pattern of mode intermittency, characterized by an outward propagation through phase synchronization at several km/s. Interestingly, over a large radial extension, this phase synchronization varies in time leading, occasionally, to phase jumps that are visible in Figure 5.3. This figure displays the maxima (red) and minima (blue) of E_r filtered around the GAM frequency. Four temporal filtered E_{r10} signals have been superimposed for the sake of clarity. It can be observed that red and blue lines are rather straight, meaning that the GAM oscillations are radially correlated. However from time to time the the phase direction is modulated or two phases merge. One can observe for example, at $t = 7.1ms$ oscillations are out of phase while at $t = 7.7ms$ there is no significant phase delay between radii. This phenomenon is obviously caused by the radial gradient of GAM frequency, which progressively desynchronizes GAM oscillators between radii. GAM frequency is lower at $\rho = 0.93$ than at $\rho = 0.85$, so the

direction of the red and blue lines turns clockwise with time. This phenomenon reaches a limit where a critical slope is reached. For example, at $t = 7.15ms$ and $\rho = 0.86$, a phase jump happens. Such jumps happen regularly, at various radii, and coincide with a low intensity of GAM, as shown by the superimposed grey curves. This phenomenon of phase synchronization is interesting to investigate deeper in the context of continuum versus eigenmode behavior of the GAM. Is a stronger synchronization between different radii can lead a GAM with a fixed frequency over a large radial extension ?

This encouraging comparison presents, however, some limitations. First, GYSELA code, which operated with an adiabatic approximation ($\delta\Phi = \delta n$) was not relevant to simulate the low collisionality case making a numerical study of collisionality effect on GAMs impossible. In addition, this simulation was limited due to the basic boundary conditions imposed at the edge of the plasma (electrostatic potential $\Phi = 0$), which probably strongly impacts the GAM behavior. New simulations are now running, including more realistic edge conditions and new comparisons are then required to carry out in this promising study.

5.2. Poloidal asymmetry of the perpendicular velocity of density fluctuations

In this section, we present a study on the poloidal asymmetry of the perpendicular velocity of density fluctuations. This work has been done comparing the radial profiles of the velocity measured using Doppler backscattering technique at two poloidal locations : at the low field side, in the equatorial plane ($\theta \sim 0°$) and at the top of the plasma ($\theta \sim 90°$). As presented in the publication included in the following, it is found that the perpendicular velocity is significantly asymmetrical for a wide range of L-mode plasma parameters in such a way that in the confined plasma between the radii $0.7 < \rho < 0.95$, density fluctuations move clearly faster in the equatorial plane than in the vertical one.

Plasma velocities

Before entering more into details, we give a brief overview of the main components of the plasma velocity. The term "plasma velocity" refers to the fluid velocity common to all the species of the plasma (i.e. $E \times B$ velocity) while the velocity detected using DBS comes from the apparent movement of the electron density fluctuations of a structure at a given spatial location of a given scale. These electron density "structures" move both as a result of their phase propagation as well as because of advection by the plasma velocity. Concerning the components of a given velocity, let us remind the reader that a tokamak plasma is a complex system, commonly described using different basis depending on the problem at hand. It is common for instance to use toroidal and parallel directions as oblique coordinates in neoclassical theory as the physical mechanisms of collisions are concentrated in these directions. In contrast, in global, experimental measurements, it is natural to use poloidal and toroidal directions as the two independent components of the velocity. Finally, in local turbulence studies, one uses the magnetic topology and therefore the directions that are parallel and perpendicular to the field lines. The plasma flow components in these different directions are governed by fundamentally different physics. These different

representations are used depending on the context. In the following, we consider both, and specify when necessary which one is considered.

From a statistical point of view, a plasma is a system composed of a large collection of different species of interacting particles : ions, electrons and neutrals. The statistical behavior of a such a system is described by the Boltzmann equation, which prescribes the evolution of the distribution functions $f_s(\mathbf{x}, \mathbf{u}, t)$ of the species s particles :

$$\frac{\partial f_s}{\partial t} + \mathbf{u} \cdot \nabla_u f_s + \frac{\mathbf{F}}{m_s} \cdot \nabla_u f_s = \left(\frac{\partial f_s}{\partial t} \right)_{collisions} \tag{5.2}$$

From the first and the second moment of the Boltzmann equation, we obtain the mass and the momentum conservation equation for the species s :

$$\frac{dn_s}{dt} + n_s \nabla \cdot \mathbf{v_s} = 0 \tag{5.3}$$

$$m_s n_s \frac{\partial \mathbf{v_s}}{\partial t} + m_s n_s (\mathbf{v_s} \cdot \nabla)\mathbf{v_s} = -\nabla p_s + n_s q_s (\mathbf{E} + \mathbf{v_s} \times \mathbf{B}) - \nabla \cdot \Pi_k + \mathbf{R_s} + \mathbf{S_s} \tag{5.4}$$

with the following definitions : $n_s = \int f_s du$ is the density, $\mathbf{v}_s = \int u f_s du$ is the fluid velocity of the species s ; p_s and Π_k are the pressure and viscosity tensors whose sum is $p_{ij} + \Pi_{\delta ij} = nm(u_i - v_i)(u_j - v_j)$; R_s is the momentum transfer due to collisions between different plasma species (i.e. friction force $R_s = \sum_k \int m_s \mathbf{v} C_{sk} d^3v$ where C_{sk} is the collision operator) ; S_s is the momentum source and includes all torques externally applied to the plasma. Note that the term $m_s n_s (\mathbf{v_s} \cdot \nabla) \mathbf{v_s}$ is negligible as compared to the viscosity tensor when the thermal velocity is much larger than the plasma velocity, which is generally the case in tokamak plasmas. Considering the stationary situation ($\frac{\partial}{\partial t} = 0$), without any external source of momentum, neglecting friction and considering an isotropic pressue ($\mathbf{P} \approx p\mathbf{I}$, with $\mathbf{I}$ the identity matrix), the momentum conservation equation (Eq. 5.4) reduce to :

$$\nabla p_s = n_s q_s (\mathbf{E} + \mathbf{v_s^{(1)}} \times \mathbf{B}) \tag{5.5}$$

This equation is the force balance equation which states that, at the lowest order, the Lorentz force is balanced by the pressure force. This equilibrium is established approximately in Alfvenic timescale (μs), which is the propagation timescale of magnetic perturbations. On longer timescales, the plasma flows and the magnetic and electric fields can evolve to very different values through intermediate states for which, to first order, the force balance equation is satisfied.

Taking the cross product of Eq.5.2 with $\mathbf{B}$, gives the perpendicular component of the first order velocity :

$$\mathbf{v}_{s\perp}^{(1)} = \frac{\mathbf{E} \times \mathbf{B}}{B^2} - \frac{1}{n_s q_s} \frac{\nabla p_s \times \mathbf{B}}{B^2} \tag{5.6}$$

The first term of the right hand side is the $E \times B$ drift, labelled $\mathbf{v}_{E\times B}$, while the second term is the co-called *diamagnetic drift*, labelled $\mathbf{v}_s^*$. Note that this drift is not a real drift

of the particles but comes from an average effect of gyro-motion in presence of a pressure gradient and can be see as "fictive velocity".

Note that, at first order, the parallel component of the velocity is not constrained by the force balance equation (Eq.5.2) and that the first order flows lie entirely on a magnetic surface. It is however often convenient in neoclassical theory to decompose vectors in their toroidal and parallel components and considering incompressible flows. The first order flows can be expressed as :

$$\mathbf{v} = \omega(\Psi) R \mathbf{e}_\varphi + U_\theta(\Psi)\mathbf{B} \tag{5.7}$$

which gives the toroidal and poloidal components written as :

$$v_\varphi = \omega(\Psi)R + v_\theta \frac{B_\varphi}{B_\theta} \tag{5.8}$$

$$v_\theta = U_\theta(\Psi) B_\theta \tag{5.9}$$

where ω and U_θ are functions of the poloidal flux Ψ, hence constant on a flux surface. Thus, in general, neither poloidal nor toroidal rotation are flux functions. In particular, poloidal rotation varies with θ, following the poloidal variation of B_θ. The "rigid rotor" toroidal rotation $\omega(\Psi)$ is corrected by a term that varies poloidally, following the variation of B_φ. Note, however, that these poloidal asymmetries remain small (i.e. of the second order).

The toroidal and the poloidal velocities are determined, in the framework of neoclassical theory, by the collisional damping in both direction ; which is depending on the collisionality regime. In the absence of external sources, the toroidal and poloidal velocities can be deduced from the parallel momentum balance (projecting Eq.5.4 on $\mathbf{B}/B$) and calculating the parallel and the perpendicular first order flows (known as "momentum approach" [117]). In the steady state, this theory predicts, in a pure plasma with circular cross section and large aspect ratio, a poloidal velocity equal to [118] :

$$v_\theta = -\frac{K}{m_i \Omega_i} \frac{dT_i}{dr} \tag{5.10}$$

with $K = -1.17$ in the banana regime, $K = 0.5$ in the plateau regime and $K = 1.7$ in the collisional regime.

If for some reason the poloidal rotation velocity happens to be different from this neoclassical prediction, collisions will tend to restore it to this neoclassical value. For example, in the banana regime, the neoclassical poloidal flow damping is caused by friction between the passing population, which carries the poloidal rotation, and the trapped particles which are locked in their magnetic well and cannot rotate. The poloidal velocity relaxes on timescales of the order of the ion collision ν_{ii}, linked to the viscosity force in the parallel direction. In addition to this damping, the poloidal rotation is submitted to a strong damping coming from toroidal magnetic equilibrium in which B_φ is larger for the inboard plasma and weaker outboard. A poloidal rotation plasma volume sees a time varying magnetic field, by which it is periodically pinched (HFS) and stretched (LFS). Through this mechanism of magnetic pumping [119] the energy of this time varying field is transferred

to the plasma in the form of kinetic energy (i.e. heat). These damping mechanims explain the generally small neoclassical predictions for poloidal rotation. However, faster poloidal rotation can arise if the plasma is subject to a poloidal torque. For instance, plasma turbulence can produce local Reynolds stress, i.e. a non-vanishing average poloidal component of the inertial term $\langle m_i n_i (\tilde{v}_i \cdot \nabla)\tilde{v}_i \rangle$ in the fluid momentum equation. This causes the plasma to rotate poloidally at a speed that is determined by the relative magnitude of the driving force and the neoclassical poloidal flow damping.

Concerning the toroidal rotation, which results from the source of momentum, transport and boundary conditions, neoclassical theory gives an explicit expression :

$$v_\phi = \frac{E_r}{B_\theta} - \frac{T_i}{eB_\theta}\left[K_n(\nu_{*i},\epsilon)\frac{1}{n_i}\frac{dn_i}{dr} + K_T(\nu_{*i},\epsilon)\frac{1}{T_i}\frac{dT_i}{dr}\right] \tag{5.11}$$

Within this treatment, the radial electric field E_r is undetermined. This degree of freedom relates to the axial symmetry of the problem, which is not resolved at first order. A full self-consistent prediction of plasma rotation requires an independent theoretical prediction for E_r, which is typically the result of momentum transport on timescales longer that the ion collisional time.

During the 1980s, it has been observed that tokamak plasmas rotate even in the absence of any obvious external sources of momentum. This natural rotation is known as *intrinsic rotation*. The origin of intrinsic rotation has been a subject of great controversy. For instance, the role of turbulence via the residual stress, has been largely studied, following different approaches[120, 121, 122, 123, 124, 125]. However, this issue remains not completely resolved and no clear consensus is adopted yet.

DBS velocity measurements and radial electric field on Tore Supra plasmas

The DBS gives the perpendicular velocity of density fluctuations whose wave-number matches the Bragg rule $k_f = -2k_i$, where k_i is the local probing wave-vector. This velocity corresponds to the movement of density fluctuations in the perpendicular direction (c.f. figure A.2) in the laboratory frame :

$$v_\perp(r, k_{\perp,f}) = v_{E\times B}(r) + v_\phi(r, k_{\perp,f}) \tag{5.12}$$

where $v_{E\times B} = -E_r/B$ is the plasma $E \times B$ velocity and v_ϕ is the phase velocity of density fluctuations. It should be mentioned that while the $v_{E\times B}$ does not depend on the wavenumber of density fluctuations since it is the plasma flow velocity not related to fluctuations (fluctuations are convected by the main plasma flow), the phase velocity naturally depends on wavenumber via the dispersion relation $v_\phi = \omega(k)/k$.

In the case of weak turbulence, standard linear theory implies that the phase velocity, which is related to the linear frequency of the locally most unstable mode, is of the order of the diamagnetic velocity. Therefore, it is generally assumed that the phase velocity remains weak as compared to the $v_{E\times B}$. This hypothesis has been tested using comparisons between $v_\perp$ measured using DBS and $v_{E\times B}$ computed using measurements from CXRS

(Charge eXchange Recombination Spectroscopy), see for example [126] and linear gyrokinetic simulations, in which the real frequency of the most unstable mode is computed, as performed in [127]. Thus, the perpendicular velocity measured using DBS is commonly used directly to evaluate the radial electric field E_r.

Note that taking the radial projection of the Eq.5.4 and considering the stationary situation ($\frac{\partial}{\partial t} = 0$) with thermal velocity much larger than the plasma velocity (which is generally the case in tokamak plasmas), neglecting friction and considering isotropic pressure, we obtain the radial force balance, which links the radial electric field to plasma velocity and to pressure gradient :

$$E_r = v_{s,\varphi} B_\theta - v_{s,\theta} B_\varphi + \frac{\nabla p_s}{n_s q_s} \tag{5.13}$$

This equation constrains simultaneously the evolution of the radial electric field E_r, the poloidal velocity v_θ and the toroidal velocity v_φ. On the other hand, the evolution of the radial electric field can be extracted from the Maxwell-Ampère equation [128] for circular plasmas showing that ambipolar particle fluxes cannot drive a radial electric field. In the frame of neoclassical theory, which describes transport of particles, momentum and energy in a plasma confined by an inhomogeneous toroidal magnetic field, accounting for collisions, neoclassical fluxes are automatically ambipolar in the case of axisymetric tokamak [129, 130] and the temporal evolution of the radial electric field should only be generated from pressure gradient and poloidal and toroidal velocities or from mechanisms that are not taken into account in the neoclassical theory.

In Tore Supra, investigations on E_r have been performed using DBS measurements in the plasma edge [131]. The particularity of Tore Supra tokamak is the presence of a relatively strong magnetic ripple (toroidal modulation of the magnetic field due to the finite number of poloidal magnetic coils), which is up to 7% at the plasmas boundary and of the order 2-3% at r/a = 0.6. In this study, it was shown that non-ambipolar fluxes of thermal ions trapped in magnetic ripple wells play a dominant role in the generation of E_r. The theoretical prediction for an ambipolar electric field arising due to ripple induced fluxes of thermal particles [132] gives :

$$E_{r,ripple} = \frac{T_i}{e}\left(\frac{\nabla n_i}{n_i} + C_{T_i}\frac{\nabla T_i}{T_i}\right) \tag{5.14}$$

where the constant C_{T_i} depends on the collisionality regime and therefore on the dominant trapping effect. For local trapping $C_{T_i} = 3.37$ [132, 127] and for the *ripple-plateau* regime (i.e. toroidal trapping) $C_{T_i} = 3/2$ [130, 127]. The comparison of the measured DBS velocity $v_\perp$ with these theoretical predictions shows a convincing agreement (Figure 5.4). The computed field has, an average tendency to be more negative than the measured one, even if it remains often within the error-bars (that are large due to the gradients of the measured quantities, especially of the T_i measurements). In particular, comparing the radial profiles of the perpendicular velocity for two discharges, a mixed result was found : an excellent agreement was observed for one discharge (c.f. figure 5.10 right), while for another discharge, for lower plasma current, the prediction is higher by a factor 1.5 (c.f. figure 5.10 left). The gap between predictions (from Eq.5.14) and measurements could be related to the contribution of the fluctuation phase velocity, which appears not to be negligible in

some cases [133]. For example, on Tore Supra, the perpendicular velocity measured using DBS at a fixed radius ($r/a = 08$) is found to vary significantly with the wavenumber of the probed fluctuations [112]. The variation reaches $1.5\,km/s$, which corresponds up the 50% of the total perpendicular velocity (see figure 5.5). This result is unexpected since this order of magnitude for the phase velocity is significantly larger than the diamagnetic velocity (which is around $500m/s$ in the discharge and at the radius considered here).

Velocity measurements using both equatorial and vertical DBS

Until this section, results presented in this manuscript have been obtained using the DBS channels (V-band in O-mode and W-band in X-mode) installed on the equatorial plane of the LFS of the Tore Supra tokamak (named DIFDOP). From 2011, measurements using a vertical system, called DREVE (Section A) with a vertical line of sight were performed. The systematic comparison of the frequency spectra detected in both equatorial ($\theta \simeq 0°$) and vertical ($\theta \simeq 90°$) planes reveals a systematic poloidal asymmetry of the perpendicular velocity of the density fluctuations. A dedicated study of this asymmetry established clearly that the density fluctuations flow faster in the equatorial plane than in the vertical plane between $r/a = 0.7$ and $r/a = 0.9$. Note that these comparisons are performed for equal probed wavenumbers in both vertical and equatorial V-band channels (see figure 5.6) to complete the following publication). Results from this study are reported ans discussed in the following publication [134], which is included next [Publication 6].

Poloidal asymmetries of flows in the Tore Supra tokamak

L. Vermare[1], P. Hennequin[1], Ö.D. Gürcan[1], X. Garbet[2], C. Honore[1], F. Clairet[2], J.C. Giacalone[2], P. Morel[1], A. Storelli[1] and the Tore Supra team[2]

[1]*LPP, CNRS, Ecole polytechnique, UPMC Univ Paris 06, Univ. Paris-Sud, Université Paris-Saclay, Sorbonne Universités, 91128 Palaiseau, France*
[2]*CEA, IRFM, F-13108 Saint-Paul-lez-Durance, France*

Simultaneous measurements of binormal velocity of density fluctuations using two separate Doppler backscattering systems at the low field side and at the top of the plasma show significant poloidal asymmetry. The measurements are performed in the core region between the radii $0.7 < \rho < 0.95$, over a limited number L-mode discharges covering a wide range of plasma conditions in the Tore Supra tokamak. A possible generation mechanism by the ballooned structure of the underlying turbulence, in the form of convective cells, is proposed for explaining the observation of these poloidally asymmetric mean flows.

Turbulent transport in magnetized plasmas is a subject of utmost importance for fusion devices such as tokamaks since it determines their confinement properties. It is now widely admitted that large scale inhomogeneous flows have a deep impact on turbulence via vortex shearing. A distinction is usually made between mean flows and time dependent zonal flows that are generated by turbulence. Zonal flows induce a scattering of large scale turbulent structures, thus participating in turbulence self-regulation. Moreover, vortex shearing due to mean or zonal flows is commonly invoked as one of the key aspects of the formation of transport barriers [1]. However, what determines (i.e. sets up and sustains) large scale flows and their gradient is not fully elucidated. One view is that non ambipolar neoclassical (i.e collisional including 3D effects) fluxes generate a radial electric field in order that the resulting charge transport stays ambipolar [2–4]. However, this would imply that the poloidal and toroidal velocity that would result, should also be neoclassical. Since toroidal rotation is rarely neoclassical [5] , one has to consider the alternative view, which is that the turbulence can generate toroidal and poloidal rotation [6], which together with the pressure gradient determine the radial electric field via the radial force balance [1]. For instance, poloidal rotation measured in the core of Ohmic L-mode plasmas of ASDEX Upgrade are found to be inconsistent with the neoclassical prediction [7].

In this Letter, we present measurements of the binormal flows at two different poloidal locations through the measurement of the perpendicular velocity of density fluctuations. Here the "perpendicular" direction refers to the binormal direction which is defined as the direction that is perpendicular both to the magnetic field line and to the radial direction on the magnetic surface.

This study has been performed in the Tore Supra tokamak using two independent Doppler Backscattering (DBS) diagnostics, simultaneously, over a wide range of L-mode plasma parameters. DBS is a diagnostic, that can be used to probe density fluctuations at a given wavenumber in different parts of the plasma. This system allows the determination of radial profiles of the perpendicular velocity of density fluctuations. Note that density fluctuations in a plasma move both as a result of plasma motion and wavelike phase propagation.

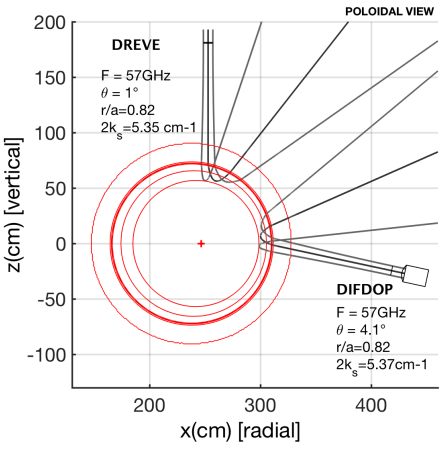

FIG. 1: Poloidal view of DBS probing beam for both equatorial and top locations computed using beam tracing code for a standard Tore Supra discharge.

The system that is installed on Tore Supra provides three DBS channels : an equatorial view ($\theta \sim 0°$) with O- and X-mode polarization channels, and a vertical view ($\theta \sim 90°$) with an O-mode polarisation channel situated at $\Delta\phi = 120°$ with respect to the former in the toroidal direction (Fig.1). In the standard set-up, probing frequencies at different antenna angles are scanned during the discharge. The measured signal is then proportional to the Fourier transform of the density fluctuations along the scattering wave vector $\mathbf{k}_{sc}$ [8]: $E_d \propto \int_{\mathcal{V}} n(\mathbf{r},t)\, e^{-i\mathbf{k}_{sc}\cdot\mathbf{r}} d^3r$ in the probed region. Frequency spectra, obtained from data analysis over a time integration between $5-10ms$, are Doppler shifted due to the movement of density fluctuations in the $\hat{\mathbf{b}}\times\hat{\mathbf{r}}$ direction [9] where $\hat{\mathbf{b}}$ and $\hat{\mathbf{r}}$ are the unit vectors along the magnetic field and in the direction normal to magnetic surfaces respectively. This shift of the peak of

the spectrum provides the mean Doppler shift frequency $\omega_{DBS} = \mathbf{k}_{sc}\mathbf{v}_\perp$ at a given radial location (an area of a few centimeters width) and at a given wavenumber, where $\mathbf{v}_\perp = \mathbf{v}_{\mathbf{E}\times\mathbf{B}} + \mathbf{v}_{ph}$ is the perpendicular velocity of density fluctuations in laboratory frame. It is commonly assumed that the $E \times B$ drift, $\mathbf{v}_{\mathbf{E}\times\mathbf{B}}$, is the dominant contribution and that the velocity measued using DBS is proportional to the radial electric field [10, 11]. However, it has been shown on Tore Supra that the phase velocity of the density fluctuations, $\mathbf{v}_{ph}$, can contribute up to 50% [12] and its contribution cannot be completely excluded.

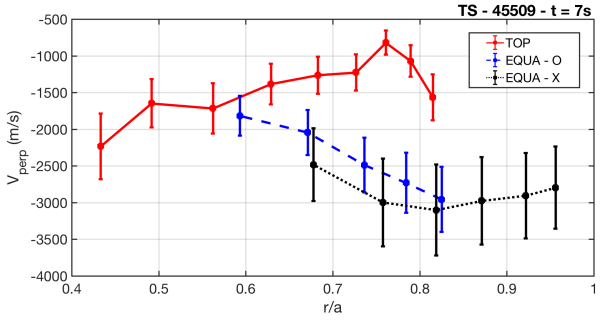

FIG. 2: Radial profiles of the perpendicular velocity of density fluctuations $\mathbf{v}_\perp$ measured using both equatorial low field side view($\theta \sim 0°$) in solid-lines and the vertical line of sight ($\theta \sim 90°$) in dashed-lines

A comparison of the perpendicular velocity of density fluctuations at different poloidal locations is presented in Fig.2 as a function of radius. Note that the velocity considered here is a mean velocity in the sense that it does not include velocity fluctuations with frequency lower than $300Hz$ (i.e. such GAMs which are resolved using adapted data analysis on shorter time sequences).

It is found that density fluctuations move in the electron diamagnetic direction (upwards in the Low Field Side) for both locations, as generally observed in Tore Supra [9, 13], where the radial electric field E_r is negative (i.e. inwards) in the confined plasma and dominated by ripple effects [14]. In addition, this comparison exhibits a clear poloidal asymmetry of the measured velocity in the region between $0.7 \leq \rho \leq 0.8$. It is found that density fluctuations move faster in the equatorial plane ($\theta \sim 0°$) and with a perpendicular velocity up to three times faster than at the top ($\theta \sim 90°$).This asymmetry seems to vanish toward the core.

To illustrate the robustness of the observation of such asymmetry, Fig.3 shows the perpendicular velocity of density fluctuations in three discharges that are representative of a wide range of Tore Supra plasma parameters (see table I). In all these three discharges, density fluctuations clearly move faster in the equatorial plane than in the vertical plane. The accessibility of the DBS systems depends on plasma parameters (mainly the density profile) and of the DBS set-up (probing frequencies and probing angle). As a consequence, measurements during these discharges cover different radial locations in the plasma, and show that the poloidal asymmetry can be observed from $r/a = 0.6$ to $r/a = 0.95$. The measured perpendicular velocity asymmetry varies between $700\,m/s$ to $2\,km/s$ in the region $0.7 \leq \rho \leq 0.95$. In addition to these observation, it should be emphases that such poloidal asymmetry is systematically observed in all discharges in which data from both locations are available.

Discharge	B_0	I_p	ICRH	n_l	q_{95}
TS-47224	3.87 T	1.12 MA	2	$5.7\,10^{19}m^{-3}$	4
TS-47491	3.87 T	0.75 MA	4.3 MW	$6\,10^{19}m^{-3}$	6.5
TS-47177	3.41 T	1.29 MA	0	$6.9\,10^{19}m^{-3}$	3.2

TABLE I: Overview of the discharges considered

The impressive amplitude of this asymmetry is not expected in these plasma conditions from well-known neoclassical effects. The simplest contributions come from the equilibrium. Since $\mathbf{v}_{\mathbf{E}\times\mathbf{B}} = \frac{\mathbf{E}\times\mathbf{B}}{B^2}$ is proportional to the inverse of the local magnetic field, and hence increases with the major radius R, a slight poloidal asymmetry is expected. Another simple contribution to the poloidal asymmetry comes from the Shafranov shift (which brings magnetic surfaces closer to each other at the LFS and makes E_r slightly higher here than at the top). Both contributions have been evaluated considering that the electrostatic potential is a flux function (i.e. toroidally and poloidally symmetric). In this case, the quantity ∇_r/B is computed from the equilibrium and lead to a poloidal asymmetry that reaches at maximum 30% which is not large enough to explain the observed asymmetry. In addition, since in this discharge without torque injection, the toroidal rotation remains weak (around few km/s) and the ICRH heating has a central deposition, none of the effects of centrifugal force and temperature's anisotropy are expected to play a significant role here.

Such asymmetry bears some similarities with observations performed in TEXTOR in ohmic plasmas [15] using Correlation Reflectometry which mentions that density fluctuations flow faster in the equatorial plane than in the vertical one in the edge of TEXTOR ohmic plasmas.

Here, after a brief discussion of the main potential effects and their limitations, a possible explanation based on the generation of asymmetric poloidal flows by turbulence is proposed.

Ripple effect is an option since non-ambipolar particle flux induced by ripple losses have been shown to be the dominant mechanism that sets the radial electric field in the plasma core [16] on Tore Supra. In this previous work, only the flux surface average of the radial electric field was derived and compared to measurments. In reality, since the magnetic ripple decreases significantly from low flied side toward high field side, a possible poloidal dependence of the radial electric field induced by ripple losses is conceivable. However, it turns out that a poloidal asymmetry is also observed in TEXTOR, where the ripple amplitude is weak ($< 1.5\%$). This suggests

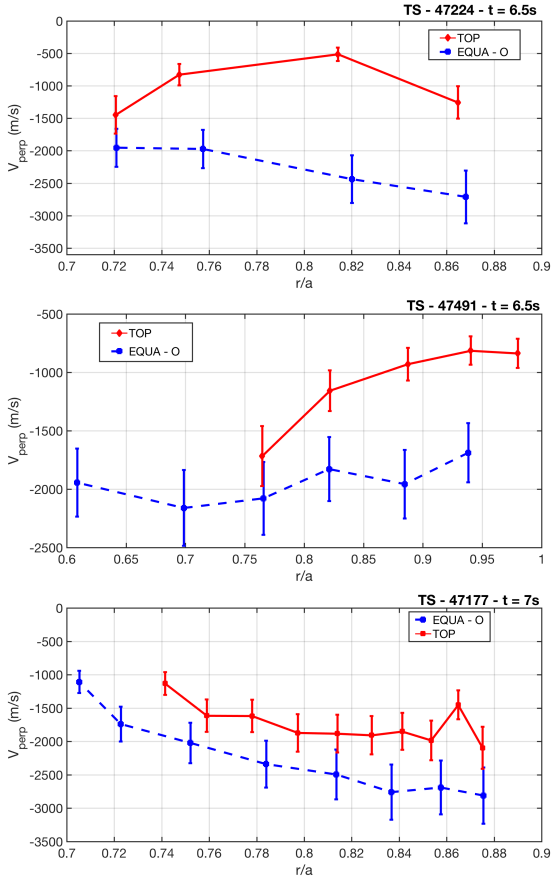

FIG. 3: Poloidal asymmetry of $\mathbf{v}_\perp$ for the different discharges (cf. Table I)

that the ripple induced friction and its impact on the radial electric field may not be the dominant effect.

We note that the poloidal asymmetry is observed at the edge where the radial electric field has been shown to be strongly related to the boundary conditions [17]. Indeed, it has been shown that the modification of flow dynamics in the scrape of layer (i.e. region of open field lines), propagates inside the plasma edge (region of closed field lines). Flows are known to be highly poloidally asymmetric in the scrape of layer [18] hence the poloidal asymmetry observed here could result from a propagation of edge flow asymmetries towards the core due to viscous effects. However, the influence of the boundary conditions has been generally visible only at the extreme edge (i.e. for $r/a > 0.9$), the large asymmetry observed at $r/a = 0.7$ appears difficult to explain by this kind of mechanism.

Concerning the role of the phase velocity, it is generally assumed that linearly, the phase velocity is given by the diamagnetic drift velocity, which is around $500m/s$ in the discharge that is considered in Figure 2. A possible poloidal asymmetry coming from the phase velocity, is therefore expected to be significantly weaker than that, which is observed. On the other hand, it has been shown in Tore Supra plasmas that the velocity measured using DBS at $r/a = 0.8$ varies significantly with wavenumber [12] implying that the phase velocity can account for 50% in the total DBS velocity (only the phase velocity is supposed to depend on wave number, the $E \times B$ velocity is in principle independent of it). This observtaion suggests that the nonlinear phase velocity is not anymore of the order of the diamagnetic velocity (or the more complete linear estimate, which is not so different from the diamagnetic velocity), but is determined by the turbulence itself. While a poloidal asymmetry coming from an asymmetry partly contained in the phase velocity cannot be totally excluded, it must be related (similarly to the mechanism proposed below) to the ballooning character of the turbulence.

These considerations motivate an explanation based on the generation of poloidal flows by turbulence. These flows are similar to zonal flows, though not axisymmetric in a poloidal section of a tokamak. An estimation based on simple arguments is presented here. $E \times B$ drift flows are ruled by an equation for the generalized evolution of plasma vorticity of the form

$$\frac{\partial}{\partial t}\left(\phi - \rho_i^2 \nabla_\perp^2 \phi\right) - \rho_i^2 \nabla \cdot \left\{\left[\left(\mathbf{V}_E + \mathbf{V}_*\right) \cdot \nabla\right] \nabla \phi\right\} = \mathcal{D}\left(\phi\right) \tag{1}$$

where $\mathbf{V}_E$ is the $E \times B$ drift velocity, $\mathbf{V}^*$ is the diamagnetic velocity, ϕ the electric potential. The linear operator $\mathcal{D}\left(\phi\right)$ covers all dissipative processes, i.e. conventional neoclassical damping, and ripple induced friction. The electric potential is then split into a large-scale component, which depends on the minor radius r and the poloidal angle θ, and small scale fluctuations. This procedure can be formalized by using a ballooning representation [19].

The vorticity equation Eq.(1) averaged over the turbulence small scales yields

$$\mu_i \delta V_\theta = -\frac{1}{r^2}\frac{\partial}{\partial r}\left[r^2 \Pi_{r\theta}\right] \tag{2}$$

where δV_θ measures the departure of the flow from is axisymmetric neoclassical value,

$$\Pi_{r\theta} = \sum_{\mathbf{k}\omega} k_\theta k_r \left(1 - \frac{\omega_{*\mathbf{k}}}{\omega}\right) \left|\phi_{k\omega}\right|^2 \tag{3}$$

is the turbulent stress tensor, μ_i is the damping rate of poloidally asymmetric flows and ω is the pulsation in the plasma frame. Here $k_\theta = \frac{-nq}{r}$ is close to a poloidal wavenumber (n is the toroidal wavenumber), while k_r is a radial wavenumber. Using a rapid distortion argument, one finds $k_r = k_\theta s(\theta - \theta_k)$ where $\theta_k \simeq \frac{1}{s}\frac{dV_\theta}{dr}\tau_k$, $s = \frac{r}{q}\frac{dq}{dr}$ the magnetic shear (q the safety factor), $\frac{dV_\theta}{dr}$ the shear rate of the mean poloidal flow, and τ_k a mode life time at wavenumber $\mathbf{k}$ [20].

This estimation of k_r agrees with the one found for a vortex distorted by magnetic and flow shears, as described in [21]. In steady-state, a local expression of the

large scale poloidal flow is found

$$\mu_i \delta V_\theta = \frac{1}{r^2}\frac{\partial}{\partial r} r^2 \left\{ \sum_{k\omega} \left(s\theta - \frac{dV_\theta}{dr}\tau_k \right) \left(1 - \frac{\omega_{*\mathbf{k}}}{\omega} \right) |V_{E\mathbf{k}\omega}|^2 \right\} \quad (4)$$

where $V_{Ek} = \frac{-inq}{r}\frac{\phi_{\mathbf{k}\omega}}{B}$ is the radial component of the turbulent $E \times B$ drift velocity. Since turbulence balloons on the low field side of a tokamak,the turbulence intensity $|V_{E\mathbf{k}\omega}|^2$ depends on the poloidal angle. This leads to a poloidal asymmetry of the plasma flow. A kinetic calculation shows that the damping rate μ_i is of the order of an inverse transit time $\mu_i \simeq \frac{v_{Ti}}{qR}$, where v_{Ti} is a thermal ion velocity and R the major radius.

In order to estimate this effect, experimental data from the discharge presented in Fig.2) have been used to evaluate the terms of the equation 4. Only the frequency and the wavenumber appearing in this equation have been evaluated from the a local linear gyrokinetic computation using the GENE code [22] in the experimental condition of the discharge considered. For this discharge, the most unstable low-k mode at $r/a = 0.8$ is found to be an ITG mode with a maximal growth rate around $k_\perp \rho_s = 0.5$, with a growth rate $\gamma = 3.2 * 10^4 s^{-1}$ and a real frequency of $\omega = 3.2 * 10^4 rad/s$. Using these values, the experimental profiles, and a friction equal to ion transit time, it is found that Eq.4 gives a poloidal velocity which rapidly varies from $200\,m/s$ at $r/a = 0.8$ to $5\,km/s$ at $r/a = 0.9$.

Since this evaluation corresponds to the equatorial plane (all profile measurements are performed in the equatorial plane) and that turbulence is strongly ballooned (flow generation can be neglected in the top), the value obtained is roughly an estimate of the poloidal asymmetry between $\theta \sim 0$ and $\theta \sim \pi/2$ velocities. Therefore, while this evaluation remains quite approximatif due to the different hypothesis used (mixing length estimate in addition to the assumptions used for the derivation of the equation 4), to the experimental error bars and to the choice of the flow damping, it is of a great interest to note that the Reynolds stress can generate an asymmetric poloidal flow with a quite large amplitude (much higher than the diamagnetic velocity) which is in agreement with the poloidal asymmetry observed ($\Delta V_\perp = 2\,km/s$). Obviously, this is only an order of magnitude estimation of the asymmetry and not a proper evaluation.

In summary, a strong poloidal asymmetry of the plasma perpendicular flow has been found in the Tore Supra tokamak. This asymmetry is observed in a broad range of conditions in L-mode plasmas. The perpendicular velocity is found to be faster on the low field side than at the top of the plasma in the measured range of radii $0.7 < \rho < 0.95$, with a ratio of velocities $v_{\perp,LFS}/v_{\perp,TOP}$ lying between 1.4 and 3. The difference between those velocities is up to $2\,km/s$. Four possible explanations for this asymmetry have been addressed. The first one relies one the contribution of the phase velocity that may participate to the observed asymmetry. The sheer magnitude of the observed asymmetry does not encourage this possibility from a linear theory perspective. In non-linear regime, a potential poloidal asymmetry of the phase velocity may contribute at some level to the observation. However, it should be noted that in this case, such poloidal asymmetry must also be proportional to the intensity of the turbulence and therefore related to the ballooning character of the turbulence. The second mechanism relies on a viscous spreading of poloidal flow asymmetries from the far edge towards the plasma core. The radial localization of the flows within the scrape-off layer make this propagation unlikely, though not impossible. The third possible explanation is based on a competition between ripple induced neoclassical friction and turbulent viscous damping of the toroidal flow, which affects in turn the poloidal flow. Turbulence ballooning and poloidal variations of the magnetic ripple amplitude result in poloidal asymmetries of the plasma flow. However, the observation of asymmetries on the TEXTOR tokamak seems to exclude this possibility (at least as the dominant effect), since the ripple amplitude is quite small in TEXTOR. Finally, the fifth possibility is the turbulent generation of large scale flows similar to zonal flows that are poloidally asymmetric. Turbulent generation of asymmetrical flows result from the tilting of turbulent structures by magnetic and mean flow shears, combined with turbulence ballooning. A balance of the turbulent Reynolds stress with Landau damping leads to a poloidal velocity that is proportional to the local intensity of turbulence (radially and poloidally) and therefore stronger in the equatorial plane. For ITG turbulence, the velocity that is generated is found to be in the electron diamagnetic direction and to decrease from the equatorial plane towards the top of the device. The order of magnitude is in agreement with the observation, which is an indication that this mechanism may be a plausible explanation of the observations. It also raises the interesting question of the feedback of these flow asymmetries on the background turbulence, via processes similar to zonal flow interaction with small scale eddies and wheter these effects can be detected with fluctuation diagnostics. A combination of these two effects, i.e. poloidal flow induced by magnetic ripple and large scale flows generated by turbulence that both predict a faster flow in the equatorial plane, appears as an encouraging explanation.

The authors thank A. Smolyakov and Y. Camenen for fruitful discussions. This work was carried out within the framework of the European Fusion Development Agreement and the French Research Federation for Fusion Studies (FR-FCM). It was supported by the European Communities under the contract of Association between Euratom and CEA. The views and opinions expressed herein do not necessarily reflect those of the European Commission.

[1] K. H. Burrell, Physics of Plasmas **4**, 1499 (1997), URL http://link.aip.org/link/?PHP/4/1499/1.

[2] E. Viezzer, T. Putterich, G. Conway, R. Dux, T. Happel, J. Fuchs, R. McDermott, F. Ryter, B. Sieglin, W. Suttrop, et al., Nuclear Fusion **53**, 053005 (2013), URL http://stacks.iop.org/0029-5515/53/i=5/a=053005.

[3] A. Bortolon, Y. Camenen, A. Karpushov, B. Duval, Y. Andrebe, L. Federspiel, O. Sauter, and the TCV Team, Nuclear Fusion **53**, 023002 (2013), URL http://stacks.iop.org/0029-5515/53/i=2/a=023002.

[4] E. Viezzer, T. Putterich, C. Angioni, A. Bergmann, R. Dux, E. Fable, R. McDermott, U. Stroth, E. Wolfrum, and the ASDEX Upgrade Team, Nuclear Fusion **54**, 012003 (2014), URL http://stacks.iop.org/0029-5515/54/i=1/a=012003.

[5] J. Rice, A. Ince-Cushman, J. deGrassie, L.-G. Eriksson, Y. Sakamoto, A. Scarabosio, A. Bortolon, K. Burrell, B. Duval, C. Fenzi-Bonizec, et al., Nuclear Fusion **47**, 1618 (2007), URL http://stacks.iop.org/0029-5515/47/i=11/a=025.

[6] P. H. Diamond and Y.-B. Kim, Physics of Fluids B: Plasma Physics **3**, 1626 (1991), URL http://link.aip.org/link/?PFB/3/1626/1.

[7] A. Lebschy, R. McDermott, C. Angioni, B. Geiger, D. Prisiazhniuk, M. Cavedon, G. Conway, R. Dux, M. Dunne, A. Kappatou, et al., Nuclear Fusion **58**, 026013 (2018), URL http://stacks.iop.org/0029-5515/58/i=2/a=026013.

[8] P. Hennequin, C. Honoré, A. Truc, A. Quéméneur, N. Lemoine, J.-M. Chareau, and R. Sabot, Review of Scientific Instruments **75**, 3881 (2004), URL http://link.aip.org/link/?RSI/75/3881/1.

[9] P. Hennequin, C. Honoré, A. Truc, A. Quéméneur, C. Fenzi-Bonizec, C. Bourdelle, X. Garbet, G. Hoang, and the Tore Supra team, Nuclear Fusion **46**, S771 (2006), URL http://stacks.iop.org/0029-5515/46/i=9/a=S12.

[10] L. Schmitz, L. Zeng, T. Rhodes, J. Hillesheim, W. Peebles, R. Groebner, K. Burrell, G. McKee, Z.Yan, G. Tynan, et al., Nuclear Fusion **54**, 073012 (2014), URL http://stacks.iop.org/0029-5515/54/i=7/a=073012.

[11] G. D. Conway, C. Angioni, F. Ryter, P. Sauter, and J. Vicente (ASDEX Upgrade Team), Phys. Rev. Lett. **106**, 065001 (2011), URL http://link.aps.org/doi/10.1103/PhysRevLett.106.065001.

[12] L. Vermare, P. Hennequin, O. D. Gürcan, C. Bourdelle, F. Clairet, X. Garbet, R. Sabot, and the Tore Supra Team, Physics of Plasmas **18**, 012306 (pages 7) (2011), URL http://link.aip.org/link/?PHP/18/012306/1.

[13] C. Honoré, P. Hennequin, A. Truc, and A. Quéméneur, Nuclear Fusion **46**, S809 (2006), URL http://stacks.iop.org/0029-5515/46/i=9/a=S16.

[14] E. Trier, L.-G. Eriksson, P. Hennequin, C. Fenzi, C. Bourdelle, G. Falchetto, X. Garbet, T. Aniel, F. Clairet, and R. Sabot, Nuclear Fusion **48**, 092001 (2008), URL http://stacks.iop.org/0029-5515/48/i=9/a=092001.

[15] A. Krämer-Flecken, Y. Xu, S. Zoletnik, and the TEXTOR team, in *39th EPS Conference & 16th Int. Congress on Plasma Physics* (2012), vol. 36F, P5.044.

[16] E. Trier, Ph.D. thesis, Ecole Polytechnique (2010), URL http://pastel.archives-ouvertes.fr/pastel-00568184.

[17] P. Hennequin, L. Vermare, N. Fedorczak, J. Bernardo, O. D. Gürcan, E. Trier, N. Stuyck, C. Fenzi, J. Gunn, P. Monier-Garbet, et al. (2010), URL ocs.ciemat.es/EPS2010PAP/pdf/P1.1040.pdf.

[18] N. Asakura, Journal of Nuclear Materials **363**, 41 (2007), ISSN 0022-3115, plasma-Surface Interactions-17, URL http://www.sciencedirect.com/science/article/pii/S0022311506006325.

[19] J. Connor, J. Taylor, and H. Wilson, Phys. Rev. Lett. **70**, 1803 (1993), URL http://link.aps.org/doi/10.1103/PhysRevLett.70.1803.

[20] P. W. Terry, Reviews of Modern Physics **72** (2000).

[21] N. Fedorczak, J. P. Gunn, J.-Y. Pascal, P. Ghendrih, G. van Oost, P. Monier-Garbet, and G. R. Tynan, Physics of Plasmas **19**, 072314 (pages 8) (2012), URL http://link.aip.org/link/?PHP/19/072314/1.

[22] F. Jenko, W. Dorland, M. Kotschenreuther, and B. N. Rogers, Physics of Plasmas **7**, 1904 (2000), http://dx.doi.org/10.1063/1.874014, URL http://dx.doi.org/10.1063/1.874014.

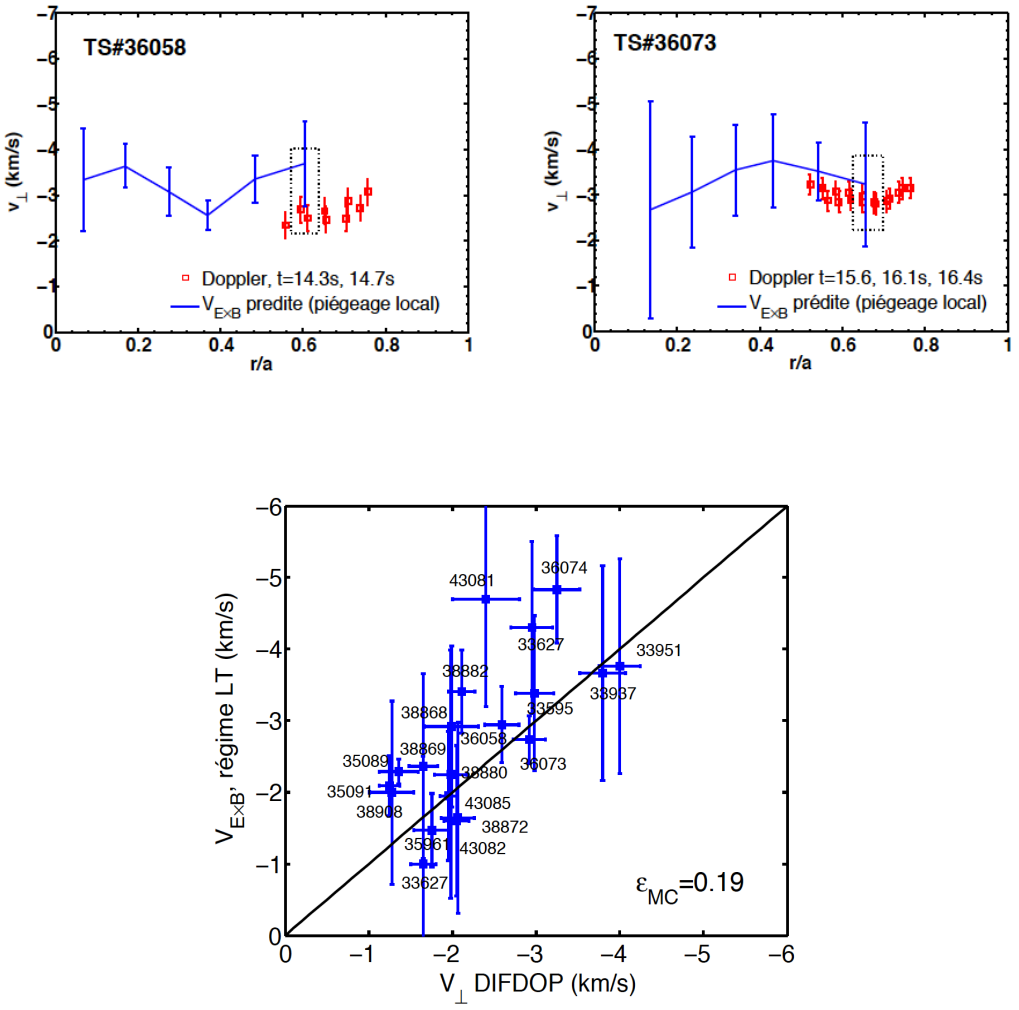

FIGURE 5.4. – Comparison between measured $v_\perp$ and the velocity predicted by $E_r \times B$ drift velocity due to ripple in the local trapping regime ($C_{T_i} = 3.37$)

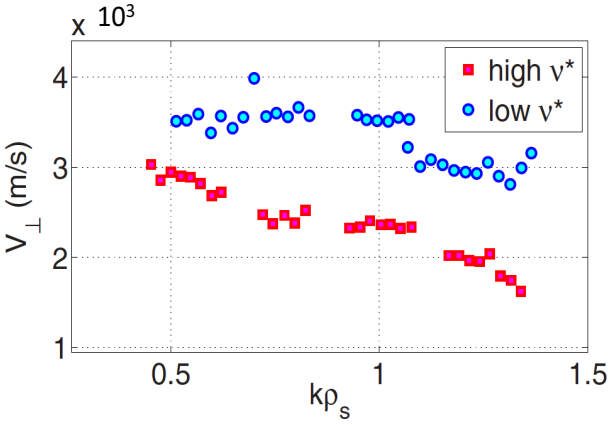

FIGURE 5.5. – Perpendicular velocity of density fluctuations as a function of the probed perpendicular wavenumber at $r/a = 0.8$ measured using DBS during a dedicated ν^* scan from reference [112]

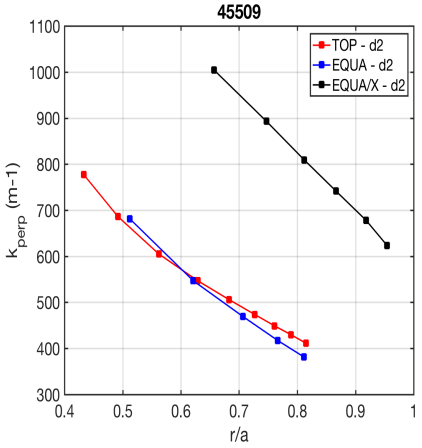

FIGURE 5.6. – Wavenumber of the density fluctuations probed as function of radial location of the measurements for the high ν^* discharge studied in the related publication (cf. Figure 2 of this publication)

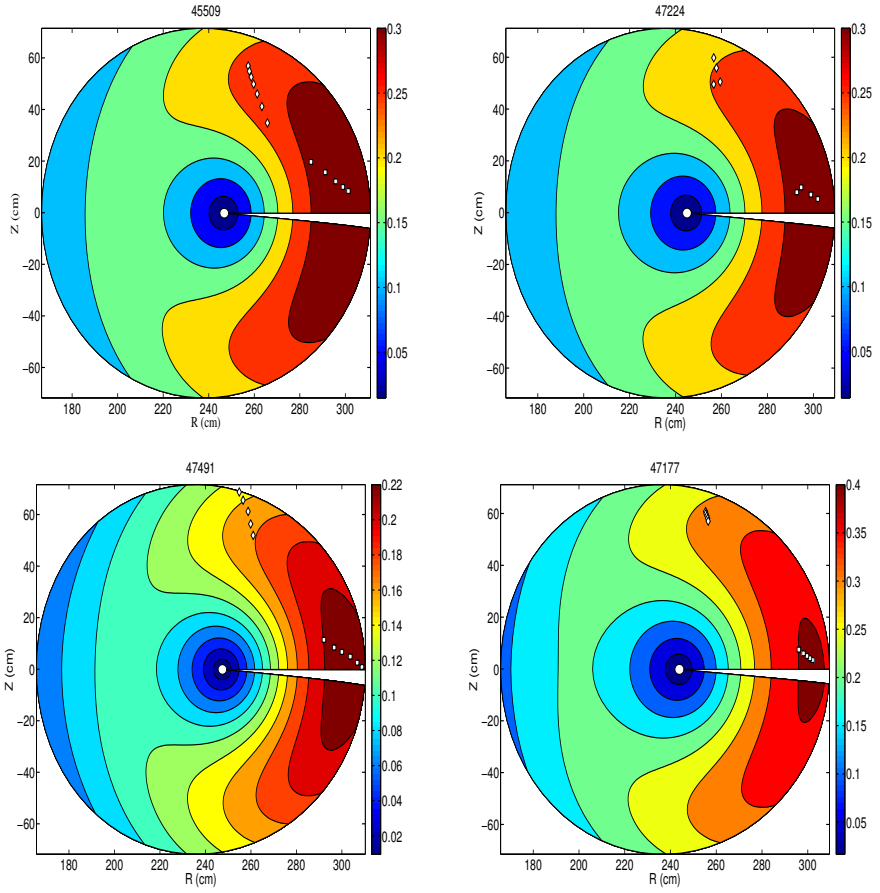

FIGURE 5.7. – Poloidal cross-section of $\frac{1}{B}|\nabla r|$ for the evaluation of its influence on the poloidal asymmetry on $v_\perp$ for a poloidally symmetric electrostatic potential ϕ and locations of DBS measurements (turning point of the probing beam for discharges presented in the following publication)

As mentioned in the related paper, the simplest contribution on the poloidal asymmetry comes from the equilibrium. Since $\mathbf{v_{E\times B}}$ is proportional to the inverse of the local magnetic field, and hence increases with the major radius R, a slight poloidal asymmetry is expected. Another simple contribution to the poloidal asymmetry comes from the Shafranov shift (which brings magnetic surfaces closer to each other at the LFS and makes $E_r = -\partial\Phi/\partial r$ slightly higher in the equatorial than at the top). These contributions (i.e. the term $|\nabla r|/B$) have been evaluated directly from the equilibrium computed using EFIT [135] for the discharges studied in the publication included above and are presented in figure 5.7. The poloidal asymmetry coming from the magnetic equilibrium reaches at maximum 30% which is not large enough to explain the total asymmetry, except maybe for the Ohmic discharge (47177) in which the asymmetry does not exceed 50% (figure 3 from [134]).

In parallel, these figures are also interesting to visualize the location of the measurements. It can be noticed, first, that the poloidal locations of the measurements are not exactly 0° and 90°, respectively, for equatorial and top system measurements. The extension of the poloidal location of the measurements changes between discharges (depending on the den-

sity profile and the diagnostic's setup). Secondly, we can see that for the discharge 45509, this extension is large enough to end up, deep inside the plasma, with measurements from top and equatorial systems at poloidal locations that are close to each other. Coherently, the radial profiles of perpendicular velocity obtained from both systems are found to meet at the radial position $r/a = 0.6$.

The other possible contributions to the poloidal asymmetry are discussed in the paper. However, in order to bring some additional materials, the different contributions are briefly repeated here. Since the contributions related to the centrifugal force and to the temperature's anisotropy are discarded (discharges without torque injection and with a central deposition of ICRH), three other options are identified :

Possible effect of phase velocity of density fluctuations

As mentioned above, it has been found that the velocity measured using DBS at $r/a = 0.8$ varies significantly with wavenumber [112] implying that the phase velocity can account for 50% in the total DBS velocity (only the phase velocity is supposed to depend on wavenumber, the $E \times B$ velocity is in principle independent of it). This observation suggests that the nonlinear phase velocity is not anymore of the order of the diamagnetic velocity (or the more complete linear estimate, which is not so different from the diamagnetic velocity), but is determined by the turbulence itself. Then a poloidal asymmetry coming from an asymmetry partly contained in the phase velocity cannot be totally excluded but should be at least two times larger than the asymmetry observed in the DBS velocity (which is the sum of the $E \times B$ velocity and the phase velocity). Note however that such poloidal asymmetry should be related (similarly to the mechanism proposed below) to the ballooning character of the turbulence.

Turbulence driven asymmetric poloidal flows

Possible theoretical explanation of observed poloidal asymmetry, with asymmetrical turbulence generated flows, has started during A. Storelli's PhD [115]. A promising explanation based on the generation of flow due to the distortion (tilting) of turbulent structures by the magnetic shear was proposed (as illustrated in figure 5.8). This explanation was inspired by a previous work in the context of SOL dynamics [136] and gives a flow with an amplitude comparable to the observation. However, the poloidal asymmetry of this generated flow was in opposite direction to the experiments (i.e. the generated flow was predicted to increase the velocity in the vertical plane as compared to the vertical one). Later, inspired by [137], an improvement of this first explanation has been proposed. The spirit remains similar to the initial proposal and the main idea is that turbulence generates flows via Reynolds stress $\tilde{v_\theta}\tilde{v_r}$. The distortion of turbulent structures by magnetic shear is used to create an asymmetry of the Reynold stress tensor and to link the poloidal velocity $\tilde{v_\theta}$ to the radial velocity $\tilde{v_r}$.

This time, the derivation is performed using a generalized equation for the evolution of the potential vorticity, in order, notably, to include finite Larmor radius effect (FLR). In this derivation, the poloidal dependence is keept, the poloidal component is retained and a scale separation is performed between large-scale fluctuations (which depend on θ and r) and small-scale fluctuations leading to the expression :

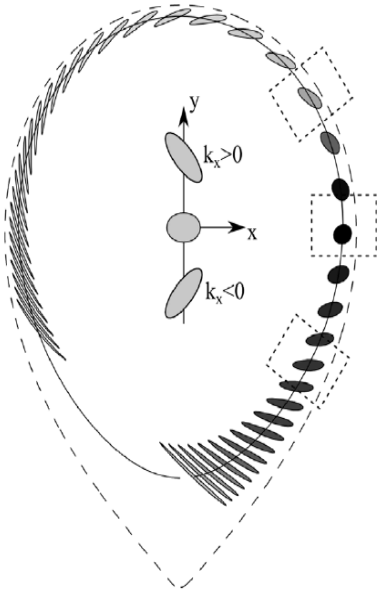

FIGURE 5.8. – Illustration of the eddy tilting due to magnetic shear. Figure is taken from [136]

$$\mu_i \delta V_\theta = \frac{1}{r^2}\frac{\partial}{\partial r} r^2 \left\{ \sum_{k\omega} \left(s\theta - \frac{dV_\theta}{dr}\tau_k \right) \left(1 - \frac{\omega^*}{\omega_{\mathbf{k}}} \right) |V_{E\mathbf{k}\omega}|^2 \right\} \tag{5.15}$$

where μ_i is the damping rate of the turbulence generated poloidal flow, δV_θ measures the departure of the flow from its axisymmetric neoclassical value V_θ, s is the magnetic shear, τ_k is the eddy life time of the mode, ω^* is the diamagnetic frequency, ω_k is the mode frequency and $V_{Ek} = \frac{-inq}{r}\frac{\tilde{\phi}_{k\omega}}{B}$ is the radial component of the turbulent $E \times B$ drift velocity. The main hypothesis of this derivation is related to the GAM contribution which is neglected (when taking the stationary state of the vorticity equation and to the damping of the turbulence generated flow. This latter is assumed to act as a friction (term in $\nabla^2\Phi$) like in the case of Zonal Flow (ZF) and GAMs instead of the usual dissipation via viscosity acting on small scales. In addition, the damping rate is estimated through previous kinetic calculation to the inverse of the transit time $\mu_i \simeq \frac{v_{Ti}}{qR}$. In order to evaluate the order of magnitude of such turbulence generated flow, an evaluation is performed using experimental data of high ν^* discharge (corresponding to the figure 2 of the publication included in this section). A linear gyrokinetic simulation (performed with the GENE code) has been used to evaluate the growth rate γ and the pulsation ω of the most unstable mode. The eddy life time τ_k is estimated taking $\tau_k = \frac{1}{\gamma}$. Since wavenumber spectrum has been measured for this discharge at $r/a = 0.8$ using DBS and is decreasing with increasing the wavenumber, the sum of the turbulent modes has been reduced to the mode with the lowest k measured with DBS which around $k_\perp \rho_s = 0.5$. From the simulation, it is found that for $k_\perp \rho_i = 0.5$, $\gamma = 0.2$ and $\omega = 0.2$ normalized to α/Cs with $Cs = 115088$ and $\alpha = 0.72$, which gives : $\gamma = 3.2 * 10^4$, $\tau_k = 1/\gamma = 31\mu s$ and $\omega = 3.2 * 10^4 rad/s$. Using the Boltzmann approximation $\tilde{\phi}_k \approx \frac{T}{e}\frac{\delta n}{n}$ which neglects the fluctuations of temperature, the velocity $V_{E\mathbf{k}\omega}$ is evaluated by $k_\theta \frac{T}{eB}\frac{\delta n}{n}$. The relative density fluctuation level is measured using fast sweep reflectometry from local

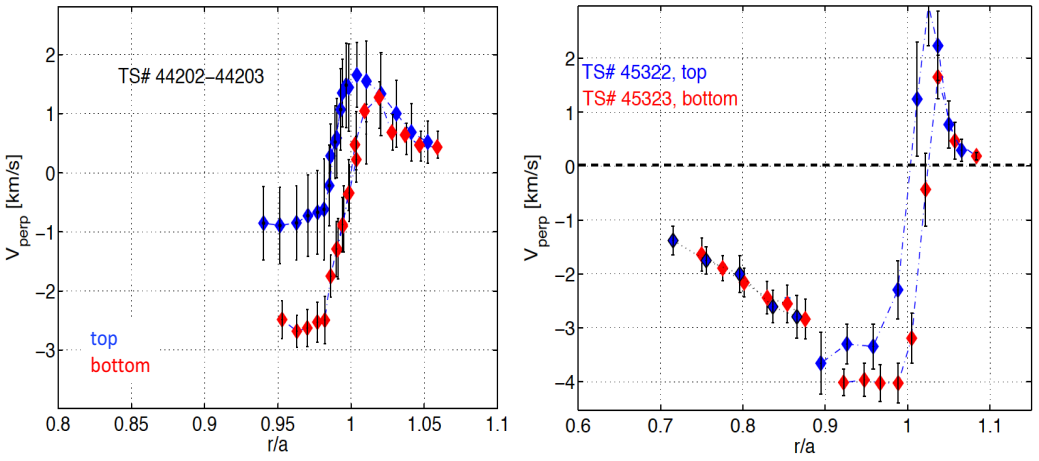

FIGURE 5.9. – Comparison of the radial profiles of perpendicular velocity measured using DBS for plasmas with two different contact points. Figures are taken from [138]

radial wavenumber spectra [39]. In fact, it is the radial derivative of this quantity which is dominant in the expression 5.15. The radial derivative of the density fluctuations changes rapidly at the edge. Thus, the experimental evaluation is performed at two different radii. At $r/a = 0.8$, the amplitude of the turbulence generated flow is estimated around $200m/s$ while at $r/a = 0.9$ it increases to $5km/s$. Even if the error-bars of this estimation are quite large, this result is interesting since it shows that such mechanism is able to create an important asymmetrical flow that can explain the experimental observations.

Spreading of far edge flow asymmetries towards the plasma core

Another possible contribution to the poloidal asymmetry is related to the spreading of edge flows. As mentioned in the publication, the poloidal asymmetry is observed at the edge where the radial electric field has been shown to be strongly related to the boundary conditions [138]. In this latter work, the flow dynamics in the Scrape Of Layer (i.e. region of open field lines) has been modified by changing the contact point (between the plasma and the outboard limiter) position. As shown in figure 5.9 taken from, reference [138], the comparison of the radial profiles of the perpendicular velocity measured using DBS in similar plasmas, with contact point situated on the top or on the bottom of the machine, shows that a modification of flow dynamics in the SOL, propagates inside the plasma edge (region of closed field lines). Since flows are known to be highly poloidally asymmetric in the SOL [139], the poloidal asymmetry observed here could result from a propagation of edge flow asymmetries towards the core due to viscous effects. However, in the example presented in the figure 5.9 (right), the influence from the SOL vanished for radial position inside $r/a = 0.9$ suggesting that the large asymmetry observed at $r/a = 0.7$ remains difficult to explain by this kind of mechanism. Nevertheless, additional experiments are required to conclude on this aspect.

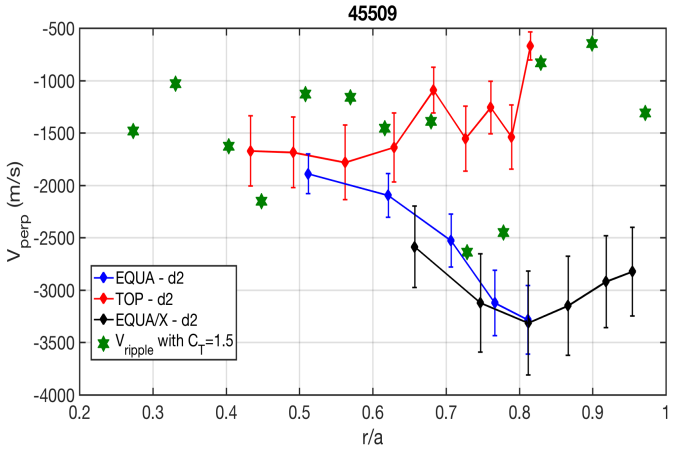

FIGURE 5.10. – Comparison of measured perpendicular velocity and the predicted velocity due to ripple in the ripple-plateau regime (i.e. $C_{T_i} = 3/2$)

Neoclassical effects related to the poloidal dependence of the toroidal magnetic field ripple in Tore Supra

Ripple effect is also a possible explanation since non-ambipolar particle flux induced by ripple losses have been shown to be the dominant mechanism that sets the radial electric field in the core of Tore Supra plasmas [131]. Because a similar poloidal asymmetry has been also observed in TEXTOR [140], where the ripple amplitude is weak ($< 1.5\%$), our first intuition was to not consider this possible explanation very seriously. However, it should be noted that in TEXTOR, the asymmetry is reported only for Ohmic discharges (and NBI with torque injection [141]) while in Tore Supra, in the case of Ohmic discharge, it has been shown that equilibrium alone may explain the asymmetry observed. Therefore, this suggests that the ripple induced friction and its impact on the radial electric field cannot be completely excluded. Figure 5.10 shows a comparison of the measured radial profile of the perpendicular velocity in both locations (equatorial and vertical planes) and the prediction obtained using 5.14 for the high ν^* discharge (idem figure 2 from [134]). In this discharge, the collisionality is higher than in the discharges presented previously (5.4), $\nu_{ii} > (Nq)^2\omega_{0bi}$, where N is the number of toroidal coils and $\omega_{bi} = \epsilon^{3/2} v_{th}/qR$ is the bounce frequency of toroidally trapped particles. This condition corresponds to the ripple-plateau regime (i.e. $K = 1.5$). For the predicted values, error-bars are rather large, especially at the edge, but inside $r/a = 0.7$ the prediction seems to be closer to the top measurements than to the equatorial ones, in agreement with the generation of asymmetrical flows by turbulence proposed below. However, it must be noted that the expression 5.14 has been derived using a non-ambipolar flux averaged over the poloidal direction, cancelling a possible θ dependence. Since the magnetic ripple depends on θ, a possible poloidal asymmetry of the radial electric field induced by ripple is conceivable. This aspect is the subject of an ongoing theoretical work.

6. Perspectives

The perspectives of my research activity can be separated into two major parts : one, which contains, in some sense, the *direct* continuity of the different works presented in this report and a second one, which will open a new research area in my activity, related to the L-H transition.

Among the studies addressed in this manuscript, some parts of them have been stopped due to the shutdown of the Tore Supra tokamak in 2013 and will restart in the WEST tokamak, others, which are still under investigation will continue. Concerning the characterization of turbulence, the detailed comparison of turbulence spatial scales, through the k-spectrum, between experiments and gyrokinetic simulations is a difficult task. However, progress made over the last few decades in computing science, resources and our understanding, make this more and more precise and relevant. In the future, the study of the role of large scale structure such as Zonal Flow on the k-spectrum will continue, using simple models and gyrokinetic simulations in parallel. In addition, the radial evolution of the turbulence amplitude, in the edge region, sometimes called *no manś land*, will be studied with the GYSELA code with a specific care in performing simulations with conditions as similar as possible to the experimental conditions. This entire work is part of the process of precise comparisons based on multiple turbulence characteristics, such as turbulence amplitude, frequency spectrum, k-spectrum and correlation lengths. On the experimental side, a new diagnostic, based on Upper Hybrid Resonnance Scattering (UHRS) will be installed in WEST to measure small scale fluctuations related to electronic turbulence. Such measurements should allow studying the interplay between ion and electron scale turbulence.

In addition, the investigations on GAMs will also continue through new comparisons with gyrokinetic simulations, especially on GAM frequency and spatial structure and performing new studies, coupling if possible new experiments and gyrokinetic simulations with kinetic electrons on GAM damping, including both Landau damping and collisional damping. A project is planned in order to study the transition from eigenmode to continuum mode and the role of a possible synchronization of GAM oscillators.

The puzzling observation of the largely varying phase velocity with the probing wavenumber merits additional investigations. Experimental work in WEST, TCV and AUG should be performed and numerical studies must be dedicated to this subject. In the same spirit, a specific study of turbulence generated flows with GYSELA is ongoing and new experimental investigations on the poloidal asymmetry is planned for the next year in AUG (installation of a vertical DBS). In parallel, the poloidal asymmetry of the velocity measured on Tore Supra plasma motivates additional theoretical investigations on the poloidal dependence of the radial electric field related to the presence of magnetic ripple.

Since the bulk of our experimental results are from the radial region at the interface between edge end core plasma, an important evolution of my research activity will consist

of including more and more of these different issues, considering edge turbulence and intensifying our efforts to investigate the coupling between edge and core dynamics.

This aspect offers a perfect transition to a topic that we plan to investigate in detail in WEST plasmas : the L-H transition. Our project on this subject will focus on the dynamics of the key ingredients of this transition : the flows and the turbulent density fluctuations. It will address the multi-scale dynamics and the interplay between flows and turbulence approaching the L-H transition via simultaneous measurement of equilibrium sheared flows, turbulence and turbulence generated sheared flows. The main motivation of this project is to improve our understanding on the synergy between the role of the mean radial electric field profile (mean flows) and the turbulence generated flows in the L-H transition, and in addition to establish a link between the dependencies of the power threshold of the L-H transition and the physical mechanisms involved in the transition.

The project will be subdivided into three main tasks : the characterization of turbulence and flows in L-mode plasmas in different turbulence regimes ; the establishment of the H-mode regime in the WEST tokamak and the study of the sensitivity of the L-H transistion with respect to plasma conditions ; the measurements of flows and turbulence during the L-H transition.

The first task is to investigate the L-mode phase and has two main objectives. The first goal is to establish the link between the core turbulence and/or the edge dynamics and the shape of the radial profile of the flows which are key ingredients in the transition to H-mode. The second goal is to determine the link between the characteristics of flows and turbulence and the accessibility of the L-H transition, i.e., the power threshold scaling. As mentioned above, the power threshold depends on several plasma parameters, including the plasma density (the dependence of which is non-monotonic, having a minimum), the toroidal magnetic field, the main ion species, the direction of the magnetic field gradient drift relative to the position of the X-point and the height of the X-point. The second objective of this task would be in particular the determination of whether these dependencies may be mediated by underlying effects on the turbulence and flows. This task will be mainly carried out in the WEST tokamak, but maybe also completed by TCV measurements.

The second task will be related to the L-H transition in the WEST configuration. Since we have a comprehensive knowledge of the radial electric field profile in Tore Supra plasmas before the WEST upgrade (having accumulated 10 years of DBS measurements), the first step will be to compare our observations of turbulence and flows in L-mode in this new configuration with similar observations performed on Tore Supra. This comparison should help in understanding the role of the plasma shaping in the edge dynamics and core turbulence. For example, it should help in determining how strongly the radial electric field profile is influenced, in a circular plasma, by the presence of a strong ripple, and how this dependence is modified in shaped plasmas. In addition, the influence of the aspect ratio, which will be up to twice as large in WEST than in Tore Supra, on turbulence characteristics and flow profiles, will be investigated. The second step will be to follow and assist the achievement of the first H-mode on this tokamak. Preliminary analysis based on existing scaling laws indicates that achieving the H-mode on WEST should not be problematic. However, since the calculation of the threshold power results from an extrapolation with large error bars for some parameters such as aspect ratio and ripple, the accessibility to H-mode in WEST may in fact not be straightforward ; however, this difficulty can be turned into

an advantage in that it may add new points to constrain the empirical scaling laws. Once the H-mode becomes routine in WEST, more systematic studies of power threshold will be undertaken, to fully characterize the scenario with high aspect ratio and large ripple.

The third task will be performed in parallel to the others and will consist of a direct investigation of the L-H transition, through measurements performed during the transition. This part is the most challenging one for several experimental reasons. The transition is generally quite fast and changes in the density profile are drastic. One possible solution is to slow down the transition, by approaching the power threshold very slowly, or to access a regime in between the L and H phases. Such scenarios have been obtained in the DIII-D and AUG tokamaks and should, in principle, be accessible in TCV and WEST.

A. Measurements of density fluctuations using Doppler BackScattering

Different types of diagnostic systems are used in order to measure and characterize density fluctuations in the hot core of magnetized plasmas where probes and cameras are not usable. Among those are two major diagnostic families which rely on scattering of electromagnetic waves on plasma fluctuations. On one hand, there is reflectometry that uses microwave frequency range to probe the plasma up to a cut-off layer, where the refractive index vanishes and the probing wave gets reflected. In this case, the probing wave reflected from the plasma is detected and analyzed to extract information about the density fluctuations in the vicinity of the cut-off layer. Major advantages of this method are high sensitivity and good localization of the measurement. On the other hand, there are wave-scattering systems based on the detection of waves scattered by the fluctuations of the plasma [30, 142, 143]. The choice of the angle between the emitter and the receptor, permits selecting the spatial scale of the detected fluctuations (elastic scattering). This selectivity in wavenumber is the main advantage of this kind of system.

The Doppler backscattering system combines advantages from both reflectometry and scattering techniques.

Diagnostic aspects of the Doppler backscattering technique

Principle of the measurements

This technique is based on the detection of the field backscattered on density fluctuations in the vicinity of the cut-off layer. The detected field comes from collective scattering, in the sense that the power of the scattered signal is due to the existence of coherent structures (fluctuations) which involve a large number of particles. This collective scattering comes mainly from electrons, lighter than ions. All the the electrons located in the scattering area are accelerated by the electric field of the incident probing wave $E_i(r,t) = E_{i0} \exp i(\omega t - \overrightarrow{k_i}.\overrightarrow{r_i})$ (which has an angular frequency ω and a wavenumber k_i) and then emit dipolar electromagnetic radiation of the same frequency in all directions, in the form of a spherical wave. The detector collects the superposition of these radiations coming from all electrons. In far field approximation (i.e. distance between the antenna and the scattering area much larger than the size of the scattering area and than the probing wavenumber), the collective electric field can be written as :

$$E_d = E_i \frac{e^{-i\vec{k}.\vec{R}}}{R} \sum_{j=1} e^{i\vec{k_f}.\vec{r_j}} \tag{A.1}$$

$\vec{k}_f$, the probed fluctuation wave vector, obeys the Bragg selection rule which writes $\vec{k}_f = -2\vec{k}_i$ in the case of backscattering, with $\vec{k}_i$ the local wave-vector of the probing beam (cf. Figure 1 from [Publication 3]).

In practice, the probing wave is chosen in the microwave range (typically from 50 to 75 GHz for O-mode corresponding to cut-off density from $3 * 10^{19} m^{-3}$ to $7 * 10^{19} m^{-3}$ in O-mode) and is launched in oblique incidence with respect to the normal of iso-index surfaces, so that no or little reflected signal is received, and thereby only the back-scattered signal is detected by the emitter antenna, which also serves as a receptor.

This technique thus provides the instantaneous spatial Fourier analysis of density fluctuations, $\tilde{n}(\vec{k}, t) = \int_V n(\vec{r}, t) e^{i\vec{k}.\vec{r}} d\vec{r}$, acting as a band pass filter in k-space around $k = k_0 sin\alpha$ at the cut-off layer. Due to the movement of density fluctuations, the detected signal is Doppler shifted by $\triangle\omega = \vec{k}_f.\vec{v_f}$. This allows the determination of the velocity of the selected density fluctuations at the cut-off layer, corresponding to the movement of the density fluctuations in laboratory frame, which corresponds to the sum of the $E \times B$ drift, written as $v_f = v_{E\times B} + v_\phi$ where $v_{E\times B}$ is the $E \times B$ velocity plus the phase velocity of density fluctuations v_ϕ. Due to the geometry of the apparatus, the Doppler back-scattering system detects density fluctuations that flow inside the plasma with a selectivity in the direction both perpendicular to the magnetic field lines and perpendicular to the radial direction (cf. schema in Figure A.2), called *bi-normal* direction, or *perpendicular* direction (this labelled commonly used may be however misleading since it may correspond also to the radial direction). The radial localization of the measurements is provided by two combined effects : a propagation effect and an effect linked to an intrinsic characteristic of the plasma turbulence. First, back-scattering processes are strongly amplified close to the cut-off layer due to swelling of the incident field near the cut-off layer. Secondly, the probed wavenumber k_f, have their highest values far from the cut-off and decrease along the beam trajectory down to the cut-off, while the physical fluctuation energy decreases as a power law at large radial wavenumbers, which makes the contribution at small k dominant, close to the cut-off.

Technical aspects

The system installed on Tore Supra has two channels in the equatorial plane : one of which operates in the V-band frequency range (50-75 GHz) in ordinary polarization (i.e. O-mode) and a second one covers the W-band (75-110 GHz) in extra-ordinary polarization (i.e. X-mode). In addition, in 2010, a complementary channel has been installed on the top of the machine with a vertical line of sight. This latter operates in the V-band with an ordinary polarization (see. A.1).

Basically, the three channels are based on the same microwave scheme initially used on the high sensitive reflectometers installed on Tore Supra from 2000 [145]. During the decade covered in the present report, technical improvements have been regularly made, however the scheme of principle remains quite similar to the one presented in Figure A.3.

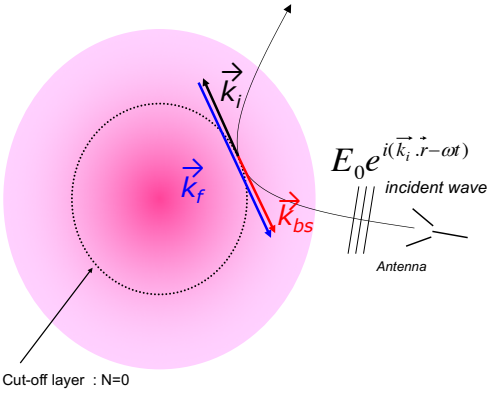

FIGURE A.1. – Illustration of the principle of the Doppler backscattering system

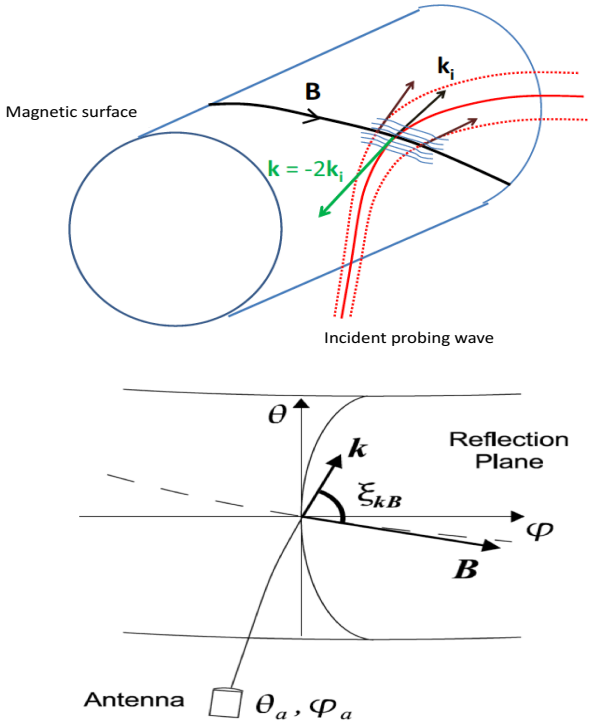

FIGURE A.2. – Illustration of the bi-normal direction (figure from [127] and of the reflection plane (figure from [144])

	O-mode	X-mode
DIFDOP (equatorial plane)	V-band (50-75 GHz)	W-band (75-110 GHz)
DREVE (vertical plane)	V-band (50-75 GHz)	

TABLE A.1. – DBS systems installed on Tore Supra

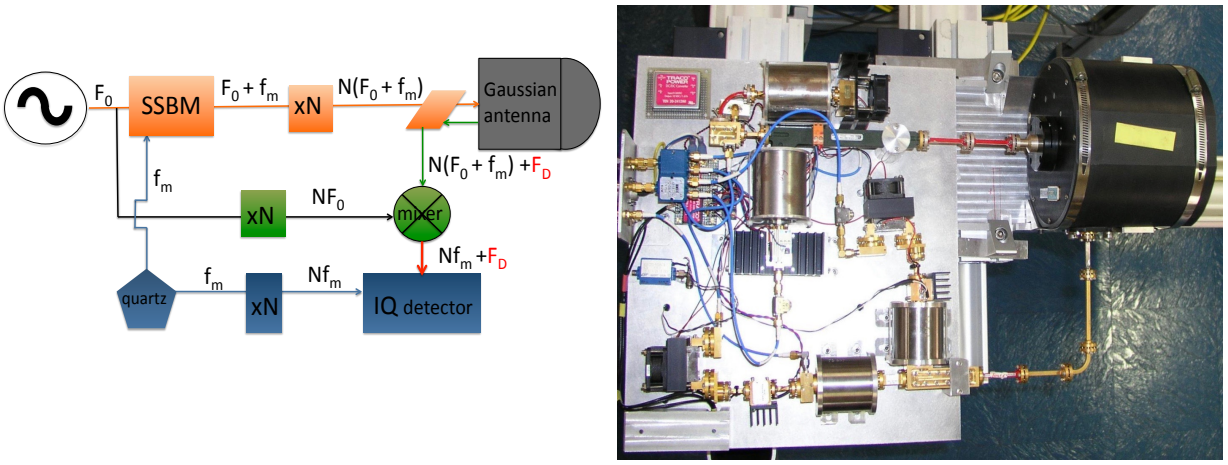

FIGURE A.3. – Electronical scheme and a corresponding picture of the DIFDOP system

All three channels implement an heterodyne detection : the source signal, produced by a synthesizer with ultra low phase noise, typically operating in the range 12.5 to 19 GHz, is split in a probing arm and a reference arm (local oscillator "LO"). The probing signal is frequency shifted by use of a single sideband modulator [146] to $F_0 + F_m$ with very high rejection levels of harmonics and $F_0 - F_m$ component. The intermediate frequency F_m is provided by 100 MHz quartz. These signals are set to the V-band and W-band ranges by the use of active multipliers (respectively, quadrupleur N=4 and sextupleur N=6). It is then sent to the plasma through a high gain antenna via a high directivity coupler, to separate emission and reception signals. The LO signal is also send through active multipliers (N=4 and N=6) to get signal at $N \times F_0$, which feeds a mixer together with the received signal, frequency shifted to $N \times F_0 + N \times F_m + F_S$, where F_S characterizes the Doppler effect on scatterers in the plasma. The output signal at the intermediate frequency $N \times F_m + F_S$ is sent to an I/Q detector to mix it with the $N \times F_m$ quartz signal to get real and imaginary parts of the scattering signal at the Doppler frequency F_S. Modulation and demodulation are performed with the same quartz oscillator. More detailed description of this system can be found in Ref. [52].

The scattering volume is controlled by Gaussian optics (to reduce small-angle scattering related to the diffraction of the probing beam), however, due to the long distance between the antenna and the plasma, the waist of the Gaussian beam remains distant from the scattering zone in contrast with the conditions of the analysis of optical mixing in scattering experiments reported in [147] and with other similar systems [148, 149]. The antenna is motorized in order to vary the tilt angle (in poloidal direction) during a single discharge (capability available only for the equatorial system DIFDOP).

To fulfil the Bragg selection condition near the cutoff layer, the beam wave-vector should have a small toroidal component since the density fluctuations are nearly aligned along the magnetic field lines [142, 150] ($k_{\|} << k_{\perp}$). The beam is thus launched with a small (fixed) toroidal tilt angle so that the wave-vector makes at the cut-off an angle ξ_{kB} with the poloidal plane nearly equal to the pitch angle of the magnetic field lines (around 5° depending on the safety factor profile). This condition is not critical due to the beam slight divergence,

Mode name	Acquisition frequency	Samples per step	Number of frequency steps	Number iterations	Delay between iterations
Wavenumber	$10MHz$	66000	4	13	$100ms$
Frequency	$10MHz$	33000	15	5	$100ms$
Long steps	$10MHz$	530000	4	1	

TABLE A.2. – Example of set-up for both DIFDOP and DREVE systems

but is important to get a good sensitivity. Note that in the vertical system DREVE, the antenna has no toroidal angle.

Set-up and capabilities

As mentioned previously, probing frequency can be varied from $50GHz$ to $75GHz$ for both, equatorial and vertical, V-band systems in O-mode, and from $75GHz$ to $110GHz$ for the W-band in X-mode. The probing angle of the equatorial system can be scanned by varying the inclination of the GOLA antenna during the discharge from 1° to 6°. Depending of the plasma parameters (mainly the electronic density for the O-mode and the density and the magnetic field for the X-mode), the channels installed in the equatorial plan allow to probe the plasma from $r/a = 0.6$ to $r/a = 0.9$ (where a is the minor radius) with wavenumber $k_\perp = 3 - 20cm^{-1}$ (for the O-mode) and from $r/a = 0.85$ to $r/a \geq 1$ with $k_\perp = 2 - 25cm^{-1}$ (for the X-mode). Concerning the vertical system DREVE, the probing angle can be changed only in between discharges in a reduce angle (due to the accessibility in the machine) from $-1°$ to 3°. This system therefore gives access to the plasma from $r/a = 0.6$ to $r/a = 0.85$ with wavenumber $k_\perp = 6 - 10cm^{-1}$.

In order to probe different locations the probing frequency is scanned by steps lasting typically 10ms to allow for stationary measurements and statistical analysis (typically Fourier). In the default set-up, a pattern of 10 steps frequency (typically 10ms) is repeated 11 times during which the antenna angle is slowly varied.

The three channels use a similar acquisition set-up. In-phase ($I = Acos\phi$) and Quadrature ($Q = Asin\phi$) signals are sampled at 10MHz (and possibly up to $100MHz$). The main limitation comes from the memory card which has a maximum of 4 Mega samples for each acquisition channel. However, since the acquisition card can be emptied during the discharge (data are transferred to the PC acquisition), it allows some flexibility. In the standard set-up for instance, data are transferred between each frequency pattern repetition. The time delay between each block of 10 steps must be long enough, typically 100ms, to transfer the 10^6 samples (i.e. 10 steps fo $10ms$ sampled at 10 MHz). This mode requires then a long stationary phase, at least 2s, to complete all the iterations of the probing frequency pattern. To illustrate this mode of operation, an example is plotted in Figure **??**. In order to reduce the measurement time, another possibility is to acquire several blocks of steps before to empty the memory card. The steps must be shorter or the number of step lower, or both of them. To illustrate this flexibility, examples of some set-up used in the work presented in this report are summarised in Table A.2. A continuous acquisition at a single probing frequency during 0.5 s is also used for statistical and dynamical studies.

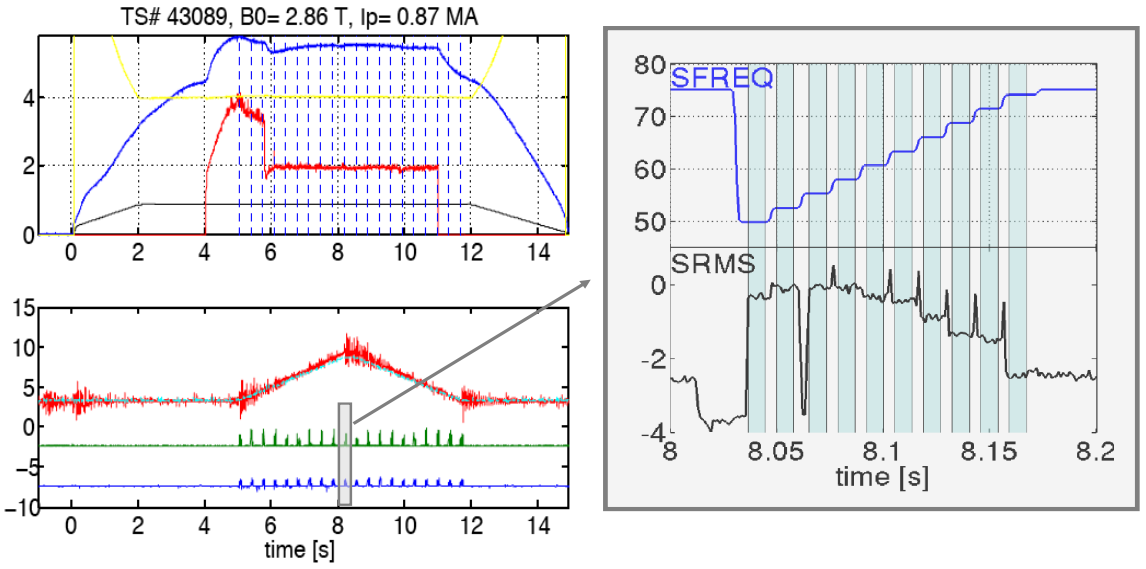

FIGURE A.4. – Set-up

Vertical Doppler backscattering system installed on Tore Supra

From 2010, a new channel (V-band in O-mode), called DREVE, has been implemented on the top of the tokamak with a vertical line of sight. It has been designed to study long range correlation with the V-band channel of the DIFDOP system. Therefore, in addition to their positions at two separate poloidal angle ($\theta \sim 0°$ and $\theta \sim 90°$), DIFDOP and DREVE are also situated at two separate toroidal positions with an angle $\Delta\varphi = 120°$ (see Figure A.5). Except for the positions and the line of sight, DREVE system is identical to the V-band of the DIFDOP system.

Measurements and interpretation

The interpretation of DBS measurements is strongly related to the spatial distribution of the scattering phenomena. This key issue has been studied numerically [126, 151, 152, 153] and analytically [154, 155, 41, 156] for Doppler reflectometry in which scattering is generally assumed to occur in the cut-off layer vicinity. The case of low turbulence level is investigated in the framework of linear theory, using the Born approximation, which assumes that the fluctuations amplitude is small enough to neglect multiple scattering. For Doppler reflectometry, it has been shown that, in the linear regime, the received signal consists of backscattering occurring in vicinity to the turning point, especially when using focused beam [156]. As for standard reflectometry, the scattering efficiency is found to be inversely proportional to the square of the radial wavenumber of the probing wave at the scattering location. At high turbulence level, small-angle multiple scattering can occur (far from the cut-off), reducing the localization of the measurement and complicating its interpretation. The turbulence level at which occurs the transition from "linear" to "non-linear regime" is not straightforward to determine and briefly addressed in Non-linear effects. To give an

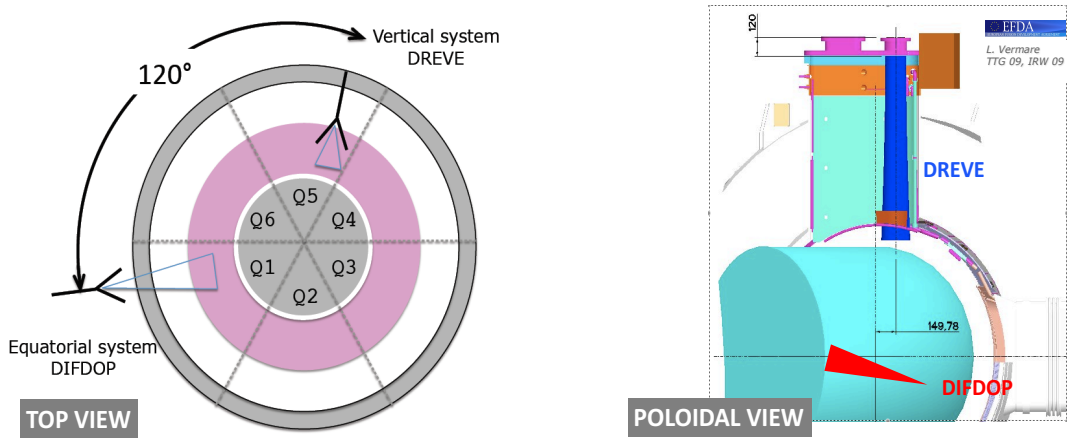

FIGURE A.5. – Top view and a poloidal/3D view of the implantation of both DFIDOP and DREVE systems on the tokamak Tore Supra)

order of magnitude and a general view, it is reasonable to consider that the condition for "linear regime" is fully valid in the major part of the confined plasma where $\delta n/n < 1\%$. At the periphery of the plasma (i.e $r/a > 0.85$), where the amplitude of fluctuations can be above 1% and can reach 10% at the extreme edge (close to the separatrix), reflectometry and DBS signals must be analyzed carefully. Note, however, that signatures of non-linear regime are generally clearly visible on the measurements allowing a simple selection of the reasonable data (see. A.13).

Localization and scale of the fluctuations detected

Concretely, the interpretation of DBS measurements requires the knowledge of the radial position where occur the main backscattering phenomena and the wavenumber of the probing beam at this position. To simulate the propagation of the probing microwave in the "real" plasma, the computation would be ideally performed using a *"full-wave code"* which resolves the interaction between density fluctuations and the probing wave by solving the Maxwell's equations in the presence of a plasma permittivity tensor including the real density fluctuations. In this case, all propagation phenomena (forward scattering, single backscattering, small-angle multiple scattering...) are taken into account and "linear" as well as "non-linear" regimes can be correctly treated. However, since "real" density fluctuations are exactly what we tend to determine and characterize, the perfect simulations with real density fluctuations are not available yet (even if turbulence codes reach high level of refinement, they are not able to predict perfectly density fluctuations). Secondly, since the beam propagation computation has to be done for each data acquisition sequence (in the order of 50 triggers per shots), the systematic use of "full wave" simulations is not realistic (due to their cost in term of computation time and resources).

Nevertheless, as mentioned above, in the linear regime the signal is dominated by backscattering occurring at the turning point, which can be determined using a ray tracing code. Therefore, the determination of the radial position and the wavenumber of the probing wave at the cut-off layer (i.e turning point) are performed using a 3-D beam tracing

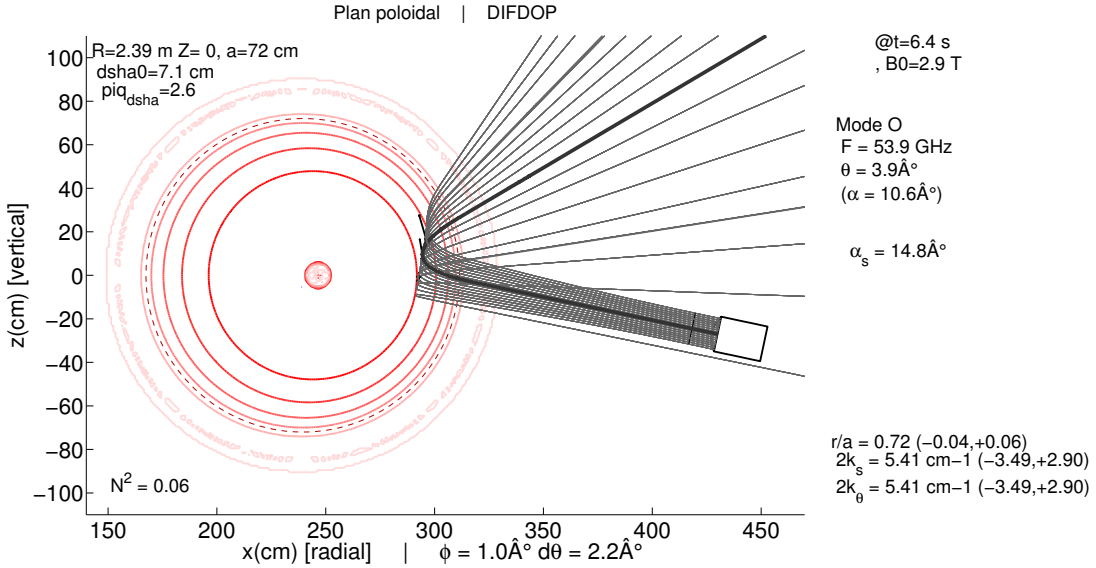

FIGURE A.6. – Beam tracing for DIFDOP system for probing frequency $F = 51.9$ GHz in O-mode for a typical Tore Supra discharge in a poloidal view. In this illustration, the number of rays per radius ($nbrayr$) has been set to 9. Bold rays correspond to the rays computed in the set-up routinely ($nbrayr = 2$)

code [144] which requires much less time than "full-wave" simulation. This code simulates the propagation of a Gaussian beam in a stationary plasma. The optical index is calculated from a radial density profile (measured using fast-sweep reflectometers [157]) mapped on the magnetic equilibrium ; the magnetic field is also needed for the optical index calculation in the case of extra-ordinary polarization. The Gaussian beam is computed via several rays to describe beam size and wave vector resolution evolution. Generally, one central ray and four peripheral rays (corresponding to an intensity reduced to $1/e^2$) are computed. The equations of propagation are resolved using the WKB (Wentzel-Kramers-Brillouin), which means that the refractive index is varying slowly (i.e the length of inhomogeneity is much larger than the local probing wavenumber) and that the equation could be solved locally. Each ray tracing computation, gives access to the radial position of the turning point of the probing wave and of its wavenumber at this position. The spatial resolution and the wave-number selectivity $\triangle k$, related to the refraction of the Gaussian beam during its propagation, can be evaluated directly from the beam tracing code [158, 151] considering the several computed rays. Examples of beam tracing computation are presented in Figure A.7 for both equatorial and vertical systems in O-mode polarization. In addition, an example of measurements mapping for O-mode for a typical Tore Supra discharge is shown on Figure A.8. It should be noted that changing the probing frequency changes mainly the radial position of the measurements but also changes slightly the probed wavenumber. On the other side, changing the probing tilt angle changes mainly the probed wavenumber but also change slightly the radial position of the measurements.

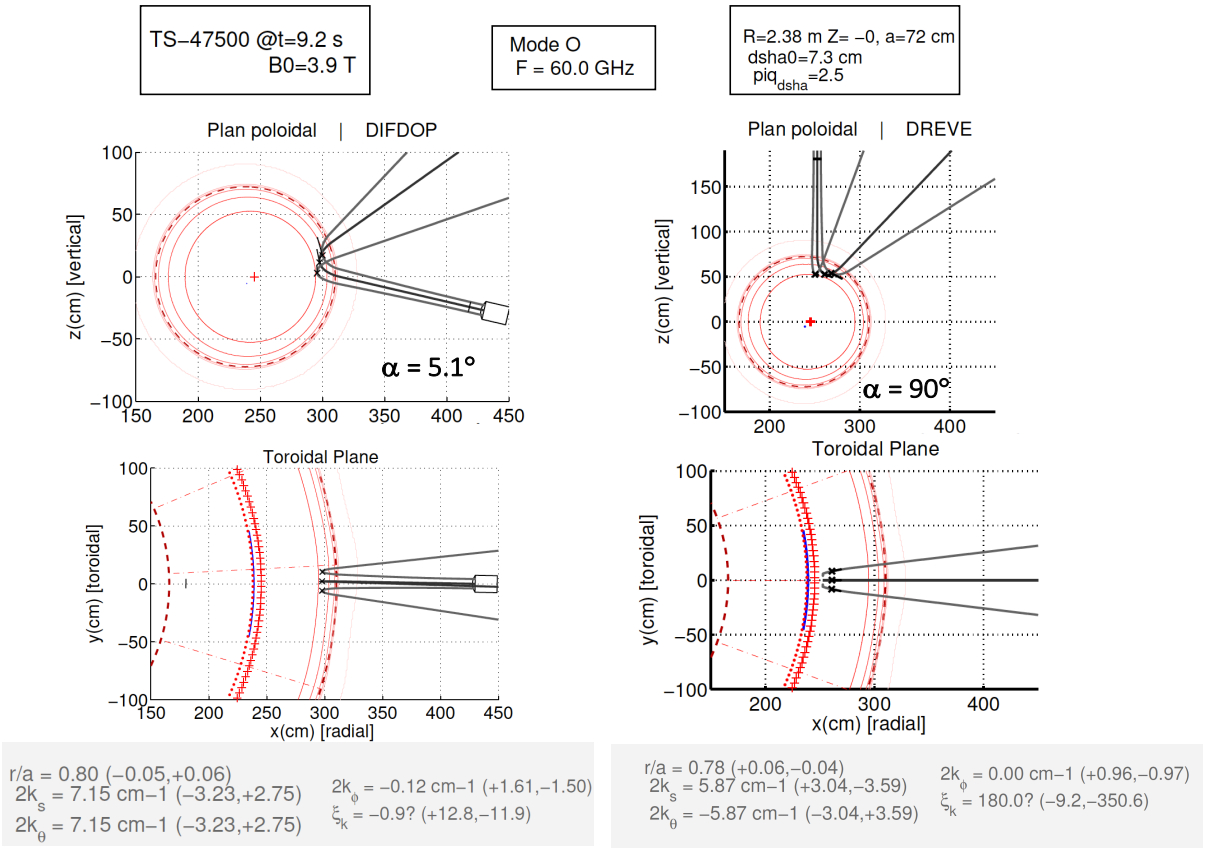

FIGURE A.7. – Beam tracing for DIFDOP and DREVE systems for probing frequency $F = 51.9$ GHz in O-mode for a typical Tore Supra discharge in a poloidal view computed in the set-up routinely used

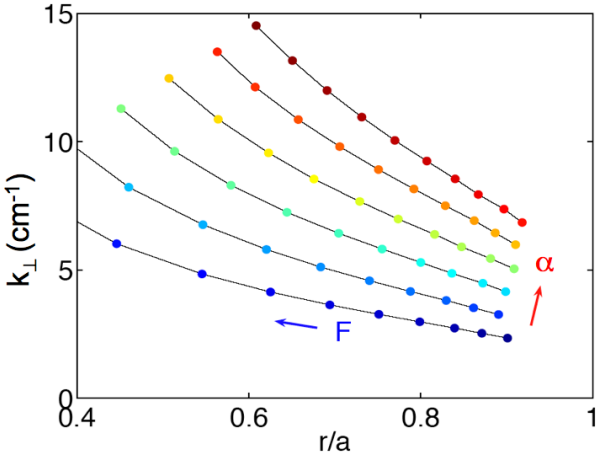

FIGURE A.8. – Mapping r/a vs. k of Doppler backscattering system (V-band, O-mode) measurements for a typical Tore Supra discharge

Frequency spectrum

The time analysis of the detected signal (at a given probing frequency and at a given probing tilt angle) gives access to the frequency spectrum of density fluctuations at a given radial position and at a given scale. An example is presented in Figure A.9. This spectrum is Doppler shifted due to the movement of detected density fluctuations and its amplitude is proportional to the intensity of density fluctuations. From the set of frequency spectra measured during a single discharge for several couples of probing beams frequency and probing tilt angle, wavenumber spectrum of density fluctuations or velocity of these fluctuations can be evaluated.

The shape of the frequency spectrum is related to several effects : the width of the probing beam which determines the spatial location extension, the distribution function of the density fluctuations velocity (statistics of the turbulent movement) and depending on the time integration of the analysis, the presence of velocity fluctuations.

The localization of the measurement related to the probing beam is discussed in the previous subsection.

The frequency spectrum is obtained from the Fourier transform of correlation function of the scattered field E_d, which can be written as [159] :

$$\begin{aligned} C(\tau) &\propto \langle \textstyle\sum_{i,j} exp(i\,\overrightarrow{k}.(\overrightarrow{r_i}(t) - \overrightarrow{r_j}(t+\tau)))\rangle_t \\ &\propto \langle \textstyle\sum_{i,j} exp(i\,\overrightarrow{k}.(\overrightarrow{r_i}(t) - \overrightarrow{r_j}(t)))exp(i\,\overrightarrow{k}.\Delta(\tau)\rangle_t \end{aligned} \tag{A.2}$$

Assuming a normal probability distribution function for the turbulent displacement Δ, the last term which contains the time/frequency information is proportional to :

$$F(k,\tau) =< e^{i\overrightarrow{k}.\overrightarrow{\Delta}_\tau} >= e^{-k^2<\Delta^2>/2} \tag{A.3}$$

To evaluate $< \Delta^2 >$, hypothesis are made for the statistics of the turbulent movement : the turbulent macroscopic motions can be described using the classical statistical Lagrangian analysis [159]. In this approach, the dynamics of a particle with a velocity v is described through the mean square value of the displacement $< \Delta^2 >$ where $\Delta(\tau) = r_j(t+\tau) - r_j(t)$. For time longer than the Lagrangian velocity correlation time $\tau_L = \int_0^\infty C_v(\tau)d\tau$ (where $C_v(\tau) =< v(0)v(\tau) > /u^2$, $u^2 =< v^2 >$), this displacement corresponds to a diffusive transport (i.e $< \Delta^2 >= 2u^2\tau_L\tau = 2D\tau$) while for shorter time, $\tau \ll \tau_L$, it has the signature of a convective transport behavior. The transition between diffusive or convective behavior can be modelled by a fast decreasing function for the velocity correlation as proposed by Taylor [160] $C_v = e^{-\tau/\tau_L}$, which leads to $< \Delta^2 >= 2u^2\tau_L^2(\frac{\tau}{\tau_L} - 1 + e^{-\tau/\tau_L})$.

The correlation function reads :

$$F(k,\tau) =< e^{i\overrightarrow{k}.\overrightarrow{\Delta}_\tau} >= e^{-k^2u^2\tau_L^2(\frac{\tau}{\tau_L}-1+e^{-\tau/\tau_L})} \tag{A.4}$$

the Fourier transform is then numerically computed to fit the experimental Power Spectral Density (PSD).

In this report, no proper study on statistics of the turbulent movement are presented and this aspect appeared only through the fitting process performed using : or a Gaussian function which corresponds to the convective character of turbulence, when $ku\tau_L \gg 1$, or a Lorentzian function translating the diffusive character of the fluctuations when $ku\tau_L \leq 1$

or the test function labelled "T" corresponding to the intermediate regime described above (A.4), which is able to very well reproduced the measured frequency spectra (see. Figure A.9).

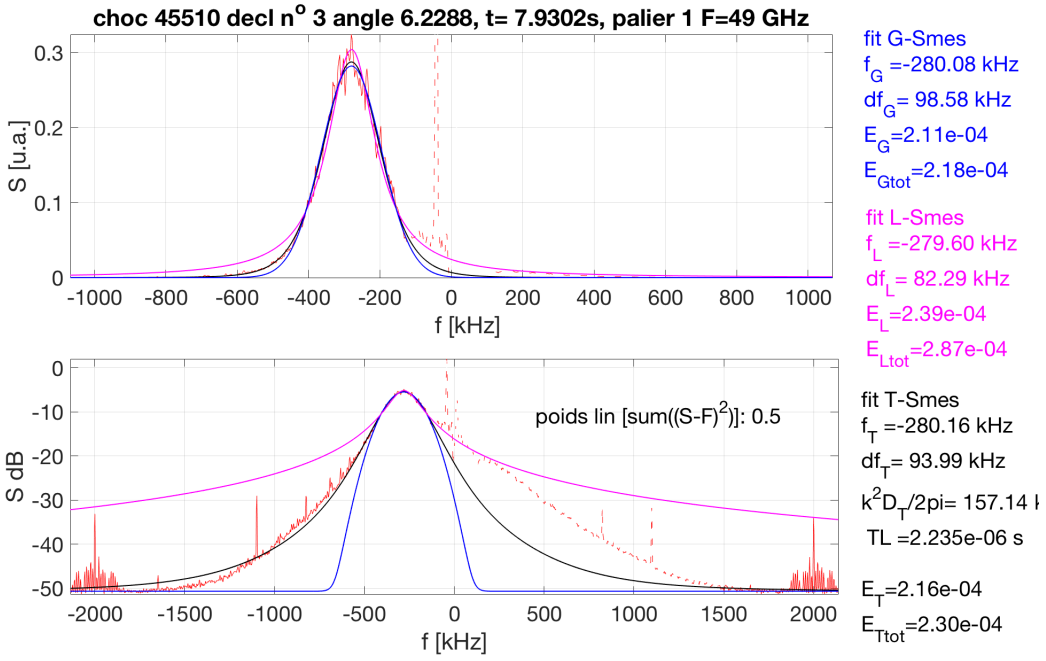

FIGURE A.9. – Example of frequency spectrum and fitting functions for an O-mode step frequency measurement

In practice, the time analysis is performed using a Power Spectral Density (PSD) estimate using the Welch algorithm (averaged spectral estimator). For a given time sequence of N_{point}, PSD are calculated using Fast Fourier Transform (FFT) on typical time windows of N_{fft} points with a certain overlap between each window. The resulting spectrum is the average of all PSD. Depending of the context of the analysis, N_{fft} and the number of points of the overlap (N_{over}) are adapted to the characteristic studied. For a given step frequency of N_{point}, one can choose to average all the time sequence or to subdivide the total time sequence in shorter time windows (of N points), for example to extract a time evolution of the fluctuations velocity. Note that, all data analysis is based on the hypothesis that the plasma conditions are stationary, at least, during each frequency step. Figure A.10 shows frequency spectra corresponding to time sequences of different length for a given very long (one of the longest achievable, i.e. $N_{point} = 529920$) step frequency.

Depending of the time integration of the measurements (determined by N), the Doppler shift related to the maximum of the spectrum will correspond either to an "equilibrium" velocity (for large value of N) or to the "fluctuations" of the velocity (for smaller value of N). Of course, the limit between what can be labelled as "equilibrium velocity" and "fluctuations" depends of the frequency of the dynamics processes that are considered.

From the set of frequency spectra measured during a simple discharge for several couples of probing beams frequency and probing tilt angle, wavenumber spectrum of density fluctuations or velocity of these fluctuations can be evaluated. For both wavenumber spectrum

and velocity determination, the three fitting functions discussed just above are used to describe the shape of the frequency spectrum.

When evaluating the velocity, the Doppler frequency shift f_D can be obtained either from a direct evaluation of the maximum of the raw frequency spectrum, or using these fitting functions. Note that f_D does not change much depending on the method or function choose. Nevertheless, for a given total time length for the analysis (fixed N), varying N_{fft} modifies both, the frequency resolution and the averaging (by changing the number of windows). An illustration on this aspect is presented in Figure A.11. For increasing the time resolution one could decrease both N and N_{fft} but is therefore limited by the frequency resolution. To study the fluctuations of the velocity about few kHz with an amplitude around ($300m/s$ which corresponds typically to $50kHz$ in term of Doppler frequency oscillations), data analysis based on the Multiple Signal Classification (MUSIC) algorithm has been used. The MUSIC algorithm [113] is a power spectral estimation method based on the Eigenmode analysis of data vectors, which can provide a fine estimation of the frequency content of the signal, with high temporal resolution [161, 162, 163]. This method allows the determination of the Doppler frequency with a relatively low number of points from the detected backscattering signal, and gives therefore access to a kind of "instantaneous" velocity. For more details see Section 5.1.

Concerning the determination of the wavenumber spectrum, the time analysis parameters are chosen is order to get a well resolved frequency spectra (i.e. with a N large enough and an intermediate N_{fft}). The integration of the power spectral density is performed using the "T" function (chosen because of its excellent agreement with raw spectra). As visible in Figure A.9 comparing E_G, E_L and E_T, Gaussian function gives generally close values and Lorentzian function, gives slight different results (due to the tails of the spectrum not contain in this function).

Non-linear effects

At high turbulence level, the probing wave can experience non-linear propagation phenomena before and after the vicinity of the cut-off layer. For example, it has been shown using fast sweep reflectometry that non-linear effects affect the detected signal already for amplitude level around 1%. In this context, the determination of the radial wavenumber spectrum of density fluctuations appears questionable while some characteristics, as the amplitude of density fluctuations seems more robust [39]. For DBS, both analytic and numerical studies have addressed this issue. Analytically, E.Z Gusakov has first study the transition from linear to non-linear scattering regime, using a one-dimensional model, in the context of correlation reflectometry [41]. Under several hypothesis, it derived a criteria for this transition defined as the situation in which the probing line is no longer observable in the reflected spectrum, leading to :

$$\frac{\omega^2 l_c x_c}{c^2} \frac{\delta n^2}{n_c^2} ln \frac{x_c}{l_c} \gg 1 \tag{A.5}$$

where ω is the angular frequency of the probing wave, $l_c x$ is the correlation length of density fluctuations, x_c is the cut-off layer position and $\delta n/n_c$ is the relative density fluctuations amplitude at the cut-off.

It shows that in the non-linear regime the probing beam is affected by small angle scattering reducing diagnostic's localization and leading to a broadening of the reflected signal frequency spectrum. In this context, E.Z. Gusakov studied precisely the case of Doppler reflectometry, within the framework of Born approximation in order to evaluate its spatial and wavenumber resolution [156] and also when the multiple forward scattering of the probing wave is dominant [42] for determining the limitations of measurements interpretation. It demonstrated that the frequency shift is not influenced by the absolute amplitude of the turbulence and gives information on the density fluctuations velocity averaged over the vicinity of the cut-off (which has a radial extension that depends on the density profile and turbulence distribution). In the case of uniform plasma velocity profile, the frequency shift formed by the nonlinear mechanisms coincides with the linear Doppler effect, while, in the more realistic case of non-uniform velocity profile, the "non-linear" spectrum shift corresponds to an averaged velocity as illustrated in A.12. This result means that in the presence of a strong local gradient in the radial electric field, as observed in the edge of Tokamak plasmas, the measured DBS velocity may be smoother as compare to the real one. However, concerning the width of the frequency spectrum, it is shown that in the multiple scattering regime, it is much larger than that in the linear case (see from (c) Figure A.12) and it is found to be proportional to the turbulence amplitude and to the probing trajectory length (cf. Eq 24 from [42]). This result is observable in measurements performed using X-mode channel at the plasma edge, as illustrated in Figure A.13, leading to distorted wavenumber spectrum Figure A.14.

In addition to these analytic studies, 2D full-wave codes are used with realistic density fluctuations (simply modeled from some basic characteristics, or determined using first principle turbulence codes) and experimental density profile to measure the perpendicular k-spectrum and the perpendicular velocity of the density fluctuations [43, 164, 165, 74]. Such simulations confirm that the measurement of the velocity is quite robust and does not depend too much on the turbulence level. However, numerical results show that the relationship between the scattered wave amplitude and the turbulence level is linear only at low turbulence levels and short radial correlation lengths, otherwise, the relationship becomes non-linear and the changes in the scattered wave amplitude do not reflect the changes in the turbulence level. This effect is more pronounced in X mode compared to O mode and depends on the density profile shape. Non-linear scattering processes distort the wavenumber spectrum, especially in X-mode polarization [74]. The comparison between k-spectrum obtained using O-mode and X-mode 2D full wave simulations with density fluctuations coming from first principle code turbulence exhibits a clear flattening of the X-mode k-spectrum. This result explains the different k-spectrum shapes obtained in AUG from the measurements in O-mode and X-mode [75].

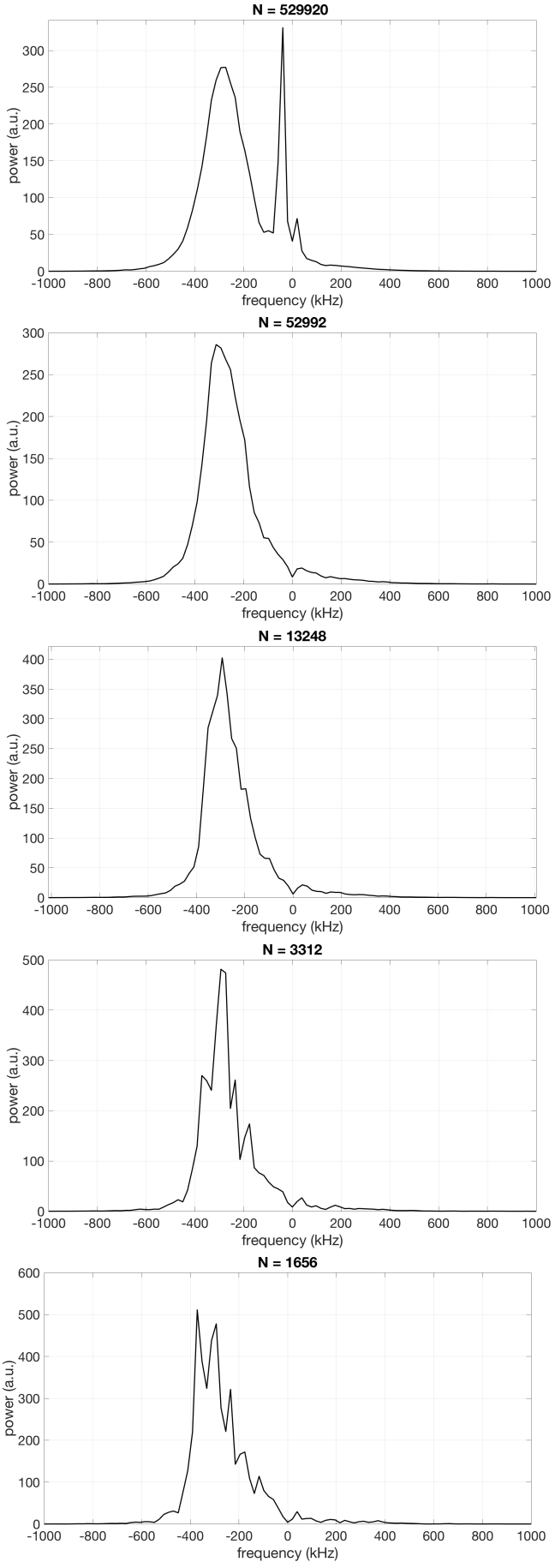

FIGURE A.10. – Example of frequency spectrum using time analysis on different time lenght for an O-mode step frequency measurement

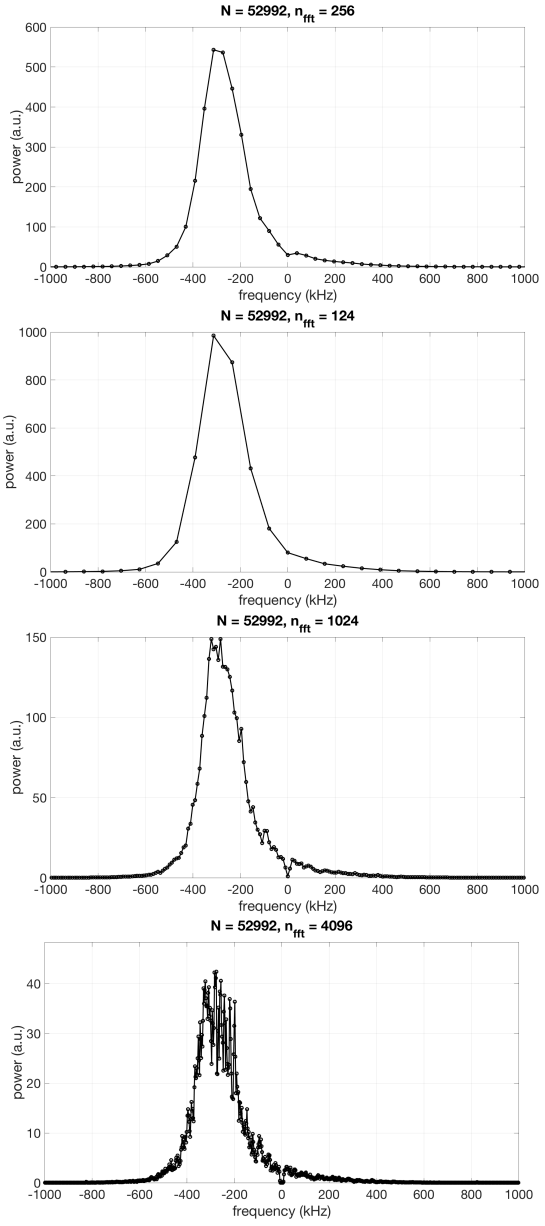

FIGURE A.11. – Example of frequency spectrum using time analysis on different FFT number for an O-mode step frequency measurement

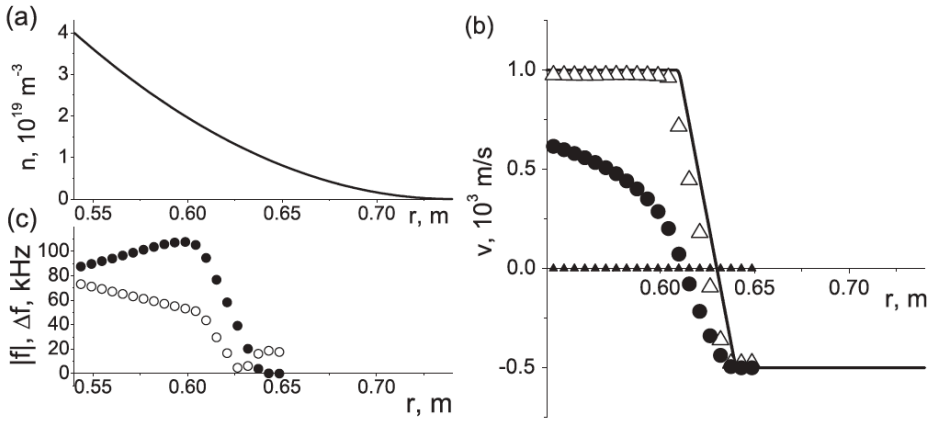

Figure 2. The signal spectrum evolution. (*a*) Assumed density profile *r* denotes the minor radius. (*b*) Assumed poloidal velocity profile (——), cut-off positions (▲) and measured poloidal velocity profile in nonlinear (●) and linear (△) diagnostics regimes. (*c*) The absolute value of frequency shift (○) and width (●) of the signal spectrum related to different probing frequencies (plotted via the corresponding cut-off position).

FIGURE A.12. – Results from analytic investigations on multiple scattering effect in Doppler reflectometry from [42]

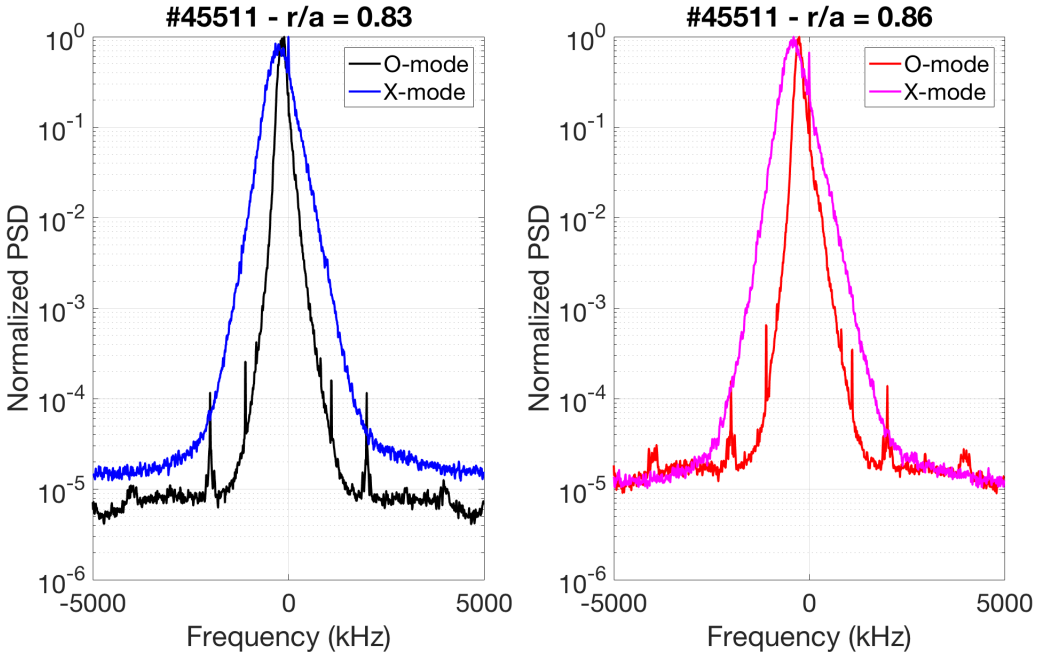

FIGURE A.13. – Comparison of frequency spectra detected using O-mode and X-mode channel at the same radial localization (but different wavenumbers). The wide form of the frequency spectrum in X-mode suggests non-linear regime)

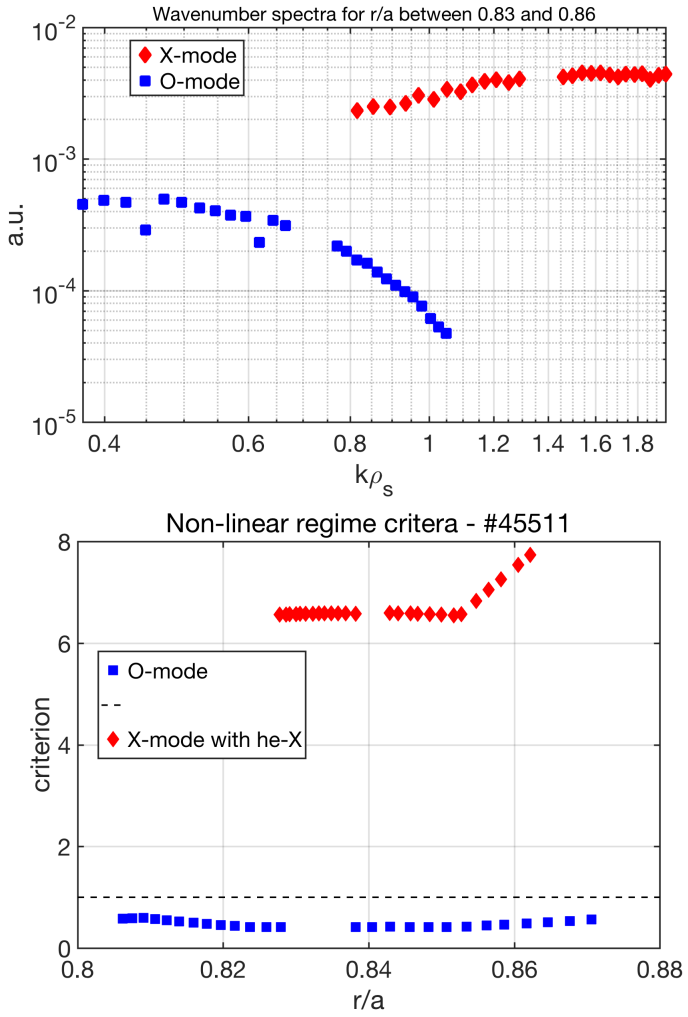

FIGURE A.14. – Evaluation of the wavenumber spectrum for O-mode and X-mode data at the same radial localization ($r/a = [0.83 - 0.86]$ for the discharge 45511. The flat form of the spectrum in X-mode is the typical signature of non-linear regime (top). Evaluation of the non-linear regime critera A.5 for the measurements presented above (bottom) taking density fluctuations intensity from fast sweep reflectometry and a correlation lenght $l_c = 10\rho_i$

Bibliographie

[1] S. Coda, M. Porkolab, and K. H. Burrell. Signature of turbulent zonal flows observed in the DIII-D tokamak. *Phys. Rev. Lett.*, 86 :4835–4838, May 2001.

[2] Z. Lin, T. S. Hahm, W. W. Lee, W. M. Tang, and P. H. Diamond. Effects of collisional zonal flow damping on turbulent transport. *Physical Review Letter*, 83(18) :3645–3648, 1999.

[3] G. R. Tynan, A. Fujisawa, and G. McKee. A review of experimental drift turbulence studies. *Plasma Physics and Controlled Fusion*, 51(11) :113001, 2009.

[4] H. Biglari, P. H. Diamond, and P. W. Terry. The influence of sheared poloidal rotation on edge turbulence. *Phys. Fluids B*, 2(1) :1–4, 1990.

[5] F. Wagner, G. Becker, K. Behringer, D. Campbell, A. Eberhagen, W. Engelhardt, G. Fussmann, O. Gehre, J. Gernhardt, G. v. Gierke, G. Haas, M. Huang, F. Karger, M. Keilhacker, O. Klüber, M. Kornherr, K. Lackner, G. Lisitano, G. G. Lister, H. M. Mayer, D. Meisel, E. R. Müller, H. Murmann, H. Niedermeyer, W. Poschenrieder, H. Rapp, H. Röhr, F. Schneider, G. Siller, E. Speth, A. Stäbler, K. H. Steuer, G. Venus, O. Vollmer, and Z. Yü. Regime of Improved Confinement and High-β in Neutral-Beam-Heated Divertor Discharges of the ASDEX Tokamak. *Phys. Rev. Lett.*, 49 :1408–1412, Nov 1982.

[6] E. Viezzer, T. Putterich, G.D. Conway, R. Dux, T. Happel, J. C. Fuchs, R. M. McDermott, F. Ryter, B. Sieglin, W. Suttrop, M. Willensdorfer, E. Wolfrum, and the ASDEX Upgrade Team. High-accuracy characterization of the edge radial electric field at asdex upgrade. *Nuclear Fusion*, 53(5) :053005, 2013.

[7] E. Viezzer, T. Putterich, C. Angioni, A. Bergmann, R. Dux, E. Fable, R.M. McDermott, U. Stroth, E. Wolfrum, and the ASDEX Upgrade Team. Evidence for the neoclassical nature of the radial electric field in the edge transport barrier of asdex upgrade. *Nuclear Fusion*, 54(1) :012003, 2014.

[8] P. H. Diamond, Y.-M. Liang, B. A. Carreras, and P. W. Terry. Self-regulating shear flow turbulence : A paradigm for the L to H transition. *Phys. Rev. Lett.*, 72 :2565–2568, Apr 1994.

[9] K. H. Burrell. Effects of E $timesB$ velocity shear and magnetic shear on turbulence and transport in magnetic confinement devices. *Physics of Plasmas*, 4(5) :1499–1518, 1997.

[10] L. Chôné, P. Beyer, Y. Sarazin, G. Fuhr, C. Bourdelle, and S. Benkadda. L-H transition dynamics in fluid turbulence simulations with neoclassical force balance. *Physics of Plasmas*, 21(7) :070702, 2014.

[11] ITER Physics Expert Group on Confinement, Transport, ITER Physics Expert Group on Confinement Modelling, Database, and ITER Physics Basis Editors. Chapter 2 : Plasma confinement and transport. *Nuclear Fusion*, 39(12) :2175, 1999.

[12] J.G. Cordey. An error analysis of dimensionless confinement scaling experiments. *Nuclear Fusion*, 49(5) :052001, 2009.

[13] B. B. Kadomtsev. *Sov. J. Plasma Phys.*, 1 :295, 1975.

[14] J.W. Connor and J.B. Taylor. Scaling laws for plasma confinement. *Nuclear Fusion*, 17(5) :1047, 1977.

[15] P. B. Snyder and G. W. Hammett. Electromagnetic effects on plasma microturbulence and transport. *Physics of Plasmas*, 8(3) :744–749, 2001.

[16] J. Candy. β-scaling of transport in microturbulence simulations. *Physics of Plasmas*, 12(7), 2005.

[17] G. L. Falchetto, J. Vaclavik, and L. Villard. Global-gyrokinetic study of finite β effects on linear microinstabilities. *Physics of Plasmas*, 10(5) :1424–1436, 2003.

[18] I. Holod, D. Fulton, and Z. Lin. Microturbulence in DIII-D tokamak pedestal. II. Electromagnetic instabilities. *Nuclear Fusion*, 55(9) :093020, 2015.

[19] J Citrin, J Garcia, T Görler, F Jenko, P Mantica, D Told, C Bourdelle, D R Hatch, G M D Hogeweij, T Johnson, M J Pueschel, and M Schneider. Electromagnetic stabilization of tokamak microturbulence in a high-beta regime. *Plasma Physics and Controlled Fusion*, 57(1) :014032, 2015.

[20] J. Garcia, C. Challis, J. Citrin, H. Doerk, G. Giruzzi, T. Görler, F. Jenko, P. Maget, and JET Contributors. Key impact of finite-beta and fast ions in core and edge tokamak regions for the transition to advanced scenarios. *Nuclear Fusion*, 55(5) :053007, 2015.

[21] C. C. Petty, T. C. Luce, D. C. McDonald, J. Mandrekas, M. R. Wade, J. Candy, J. G. Cordey, V. Drozdov, T. E. Evans, J. R. Ferron, R. J. Groebner, A. W. Hyatt, G. L. Jackson, R. J. La Haye, T. H. Osborne, and R. E. Waltz. β-scaling of transport on the DIII-D Tokamak : Is transport electrostatic or electromagnetic ? *Physics of Plasmas*, 11(5) :2514–2522, 2004.

[22] D. C. McDonald, J. G. Cordey, C. C. Petty, M. Beurskens, R. Budny, I. Coffey, M. de Baar, C. Giroud, E. Joffrin, P. Lomas, A. Meigs, J. Ongena, G. Saibene, R. Sartori, I. Voitsekhovitch, and JET EFDA contributors. The β scaling of energy confinement in ELMy H-modes in JET. *Plasma Physics and Controlled Fusion*, 46(5A) :A215, 2004.

[23] H. Urano, T. Takizuka, H. Takenaga, N. Oyama, Y. Miura, and Y. Kamada. Confinement degradation with β for ELMy H -mode plasmas in JT-60U tokamak. *Nuclear Fusion*, 46(8) :781, 2006.

[24] M. Kotschenreuther, G. Rewoldt, and W.M. Tang. Comparison of initial value and eigenvalue codes for kinetic toroidal plasma instabilities. *Comp. Phys. Comm.*, 88 :128, 1995.

[25] S. Maeyama, T.-H. Watanabe, and A. Ishizawa. Suppression of ion-scale microtearing modes by electron-scale turbulence via cross-scale nonlinear interactions in tokamak plasmas. *Phys. Rev. Lett.*, 119 :195002, Nov 2017.

[26] D. C. McDonald, L. Laborde, J. C. DeBoo, F. Ryter, M. Brix, C. D. Challis, P. de Vries, C. Giroud, J. Hobirk, D. Howell, E. Joffrin, T. C. Luce, J. Mailloux,

V. Pericoli-Ridolfini, A. C. C. Sips, K. Thomsen, and JET EFDA Contributors. JET confinement studies and their scaling to high-β_N ITER scenarios. *Plasma Physics and Controlled Fusion*, 50(12) :124013, 2008.

[27] Ö. D. Gürcan. *Turbulent nonlocal phonemena in magnetized plasmas.* HDR. 2017.

[28] D.L. Brower, W.A. Peebles, and Jr. N.C. Luhmann. The spectrum, spatial distribution an scaling of microturbulence in the TEXT tokamak. *Nuclear Fusion*, 27(12), 1987.

[29] TFR-Group and A. Truc. Turbulent spectrum analysis in TFR Tokamak plasmas. *Plasma Phys. Control. Fusion*, 26(9) :1045–1062, 1984.

[30] E. Mazzucato. Small-scale density fluctuations in the Adiabatic Toroidal Compressor. *Physical Review Letter*, 36(14) :792–794, Apr 1976.

[31] C.P. Ritz, D.L. Brower, T.L Rhodes, R.D. Bengtson, S.J. Levinson, Jr. N.C. Luhmann, W.A. Peebles, and E.J Powers. Characterization of tokamak edge turbulence by far-infrared laser scattering and langmuir probes. *Nuclear Fusion*, 27(7), 1987.

[32] R. J. Fonck, G. Cosby, R. D. Durst, S.F. Paul, N. Brtez, S. Scott, E. Synakowski, and G. Taylor. Long-wavelength density turbulence in the TFTR tokamak. *Physical Review Letter*, 70(24) :3736–3739, 1993.

[33] G. R. McKee, C. C. Petty, R. E. Waltz, C. Fenzi, R. J. Fonck, J. E. Kinsey, T. C. Luce, K. H. Burrell, D. R. Baker, E. J. Doyle, X. Garbet, R. A. Moye, C. L. Rettig, T. L. T. L. Rhodes, D. W. Ross, R. G. M. Staebler, R. Sydora, and M. R. Wade. Nondimensional scaling of turbulence characteristics and turbulent diffusivity. *Nuclear Fusion*, 41(9) :1235–1242, 2001.

[34] S. E. Parker, W. W. Lee, and R. A. Santoro. Gyrokinetic simulation of ion temperature gradient driven turbulence in 3D toroidal geometry. *Physical Review Letters*, 71(13), 1993.

[35] P. Hennequin, R. Sabot, C. Honoré, G. Hoang, X. Garbet, A. Truc, C. Fenzi, and A. Quéméneur. Scaling laws of density fluctuations at high-k on Tore Supra. *Plasma Physics and Controlled Fusion*, 46(12B) :B121–B133, 2004.

[36] A. Semet, A. Mase, W. A. Peebles, N. C. Luhmann, and S. Zweben. Study of low-frequency microturbulence in the microtor tokamak by far-infrared laser scattering. *Physical Review Letters*, 45(6) :445–448, Aug 1980.

[37] A. Casati, T. Gerbaud, P. Hennequin, C. Bourdelle, J. Candy, F. Clairet, X. Garbet, V. Grandgirard, Ö. D. Gürcan, S. Heuraux, G. T. Hoang, C. Honoré, F. Imbeaux, R. Sabot, Y. Sarazin, L. Vermare, and R. E. Waltz. Turbulence in the Tore Supra tokamak : Measurements and validation of nonlinear simulations. *Physical Review Letters*, 102(16) :165005, 2009.

[38] R. Leybros. *Etude des vitesses de dérive fluide dans le plasma de bord des tokamaks : Modélisation numérique et comparaison simulation/expérience.* PhD Thesis. 2015.

[39] L. Vermare. *Mesure de l´activité magnétohydrodynamique et de la micro-turbulence par réflectomètrie à balayage.* PhD Thesis. 2005.

[40] T. Gerbaud, F. Clairet, R. Sabot, A. Sirinelli, S. Heuraux, G. Leclert, and L. Vermare. Comparison of density fluctuation measurements between O-mode and X-mode reflectometry on Tore Supra. *Rev. Sci. Inst.*, 77(10) :10E928, 2006.

[41] E. Z. Gusakov and A. Yu Popov. Non-linear theory of fluctuation reflectometry. *Plasma Physics and Controlled Fusion*, 44(11) :2327, 2002.

[42] E. Z. Gusakov, A. V. Surkov, and A. Yu Popov. Multiple scattering effect in doppler reflectometry. *Plasma Physics and Controlled Fusion*, 47(7) :959, 2005.

[43] E. Blanco and T. Estrada. Study of doppler reflectometry capability to determine the perpendicular velocity and the k-spectrum of the density fluctuations using a 2d full-wave code. *Plasma Physics and Controlled Fusion*, 50(9) :095011, 2008.

[44] A. Hasegawa and K. Mima. Pseudo-three-dimensional turbulence in magnetized nonuniform plasma. *Phys. Fluids*, 21(1) :87–92, 1978.

[45] A. Hasegawa and M. Wakatani. Plasma edge turbulence. *Physical Review Letter*, 50(9) :682–686, 1983.

[46] Ö. D. Gürcan, P. Hennequin, L. Vermare, X. Garbet, and P. H. Diamond. Shell models and the possibility of application to fusion plasmas. *Plasma Phys. Control. Fusion*, 52(4) :045002, 2009.

[47] P. W. Terry, D. A. Baver, and Sangeeta Gupta. Role of stable eigenmodes in saturated local plasma turbulence. *Physics of Plasmas*, 13(2) :022307, 2006.

[48] P. W. Terry, A. F. Almagri, G. Fiksel, C. B. Forest, D. R. Hatch, F. Jenko, M. D. Nornberg, S. C. Prager, K. Rahbarnia, Y. Ren, and J. S. Sarff. Dissipation range turbulent cascades in plasmas. *Physics of Plasmas*, 19(5) :055906, 2012.

[49] A A Schekochihin, S C Cowley, W Dorland, G W Hammett, G G Howes, G G Plunk, E Quataert, and T Tatsuno. Gyrokinetic turbulence : a nonlinear route to dissipation through phase space. *Plasma Physics and Controlled Fusion*, 50(12) :124024, 2008.

[50] G.G. Plunk, S.C Cowley, A. Schekochihin, and T. Tatsuno. Two-dimensional gyrokinetic turbulence. *Journal of Fluid Mechanics*, 664 :407, 2010.

[51] M. Barnes, F. I. Parra, and A. A. Schekochihin. Critically balanced ion temperature gradient turbulence in fusion plasmas. *Phys. Rev. Lett.*, 107 :115003, Sep 2011.

[52] P. Hennequin, C. Honoré, A. Truc, A. Quéméneur, N. Lemoine, J-M Chareau, and R. Sabot. Doppler backscattering system for measuring fluctuations and their perpendicular velocity on Tore Supra. *Review of Scientific Instruments*, 75(10) :3881–3883, 2004.

[53] P. Hennequin, C. Honoré, A. Truc, A. Quéméneur, C. Fenzi-Bonizec, C. Bourdelle, X. Garbet, and G.T. Hoang. Fluctuation spectra and velocity profile from doppler backscattering on Tore Supra. *Nuclear Fusion*, 46(9) :S771, 2006.

[54] X.L Zou. *Poloidal rotation measurement in Tore Supra by reflectometry.* 26th EPS Conf. Plasma Phys. 1999.

[55] K M Novik and A D Piliya. Enhanced microwave scattering in plasmas. *Plasma Physics and Controlled Fusion*, 36(3) :357, 1994.

[56] D. G. Bulyiginskiy, A. D. Gurchenko, E. Z. Gusakov, V. V. Korkin, M. M. Larionov, K. M. Novik, Yu. V. Petrov, A. Yu. Popov, A. N. Saveliev, V. L. Selenin, and A. Yu. Stepanov. Radar upper hybrid resonance scattering diagnostics of small-scale fluctuations and waves in tokamak plasmas. *Physics of Plasmas*, 8(5) :2224–2231, 2001.

[57] E. Z. Gusakov, A. D. Gurchenko, A. B. Altukhov, V. V. Bulanin, L. A. Esipov, M. Yu Kantor, D. V. Kouprienko, S. I. Lashkul, A. V. Petrov, and A. Yu Stepanov. Investigation of small-scale tokamak plasma turbulence by correlative UHR backscattering diagnostics. *Plasma Physics and Controlled Fusion*, 48(12B) :B443, 2006.

[58] A.D. Gurchenko, E.Z. Gusakov, A.B. Altukhov, A.Yu Stepanov, L.A. Esipov, M.Yu. Kantor, D.V. Kouprienko, V.V. Dyachenko, and S.I. Lashkul. Observation of the ETG mode component of tokamak plasma turbulence by the UHR backscattering diagnostics. *Nuclear Fusion*, 47(4) :245, 2007.

[59] C. Tröster. *Development of a flexible Doppler reflectometry system and its application to turbulence characterization in the ASDEX Upgrade tokamak*. PhD Thesis Ludwig-Maximilians-Universität München. 2008.

[60] W. A. Peebles, T. L. Rhodes, J. C. Hillesheim, L. Zeng, and C. Wannberg. A novel, multichannel, comb-frequency doppler backscatter system. *Review of Scientific Instruments*, 81(10) :10D902, 2010.

[61] T. Happel, T. Estrada, E. Blanco, V. Tribaldos, A. Cappa, and A. Bustos. Doppler reflectometer system in the stellarator TJ-II. *Review of Scientific Instruments*, 80(7) :073502, 2009.

[62] Z. Lin, T. S. Hahm, W. W. Lee, W. M. Tang, and R. B. White. Turbulent transport reduction by zonal flows : Massively parallel simulations. *Science*, 281 :1835, 1998.

[63] F. L. Hinton and M. N. Rosenbluth. Dynamics of axisymmetric E×B and poloidal flows in tokamaks. *Plasma Phys. Control. Fusion*, 41(3A) :A653, 1999.

[64] W.X. Wang, P.H. Diamond, T.S. Hahm, S. Ethier, G. Rewoldt, and W. M. Tang. Nonlinear flow generation by electrostatic turbulence in tokamaks. *Physics of Plasmas*, 17 :072511, 2010.

[65] F. Merz and F. Jenko. Nonlinear interplay of TEM and ITG turbulence and its effect on transport. *Nuclear Fusion*, 50 :054005, 2010.

[66] K. Mikki and P.H. Diamond. Role of the geodesic acoustic mode shearing feedback loop in transport bifurcations and turbulence spreading. *Physics of Plasmas*, 17 :032309, 2010.

[67] T. Estrada, E. Ascasibar, E. Blanco, A. Cappa, P. H. Diamond, T. Happel, C. Hidalgo, M. Liniers, B. Ph. van Milligen, I. Pastor, D. Tafalla, and the TJ-II Team. Spatial, temporal and spectral structure of the turbulence flow interaction at the L-H transition. *Plasma Physics and Controlled Fusion*, 54(12) :124024, 2012.

[68] F. Fernández-Marina, T. Estrada, and E. Blanco. Turbulence radial correlation length measurements using doppler reflectometry in TJ-II. *Nuclear Fusion*, 54(7) :072001, 2014.

[69] L. Schmitz, C. Holland, T. L. Rhodes, G. Wang, L. Zeng, A. E. White, J. C. Hillesheim, W. A. Peebles, S. P. Smith, R. Prater, G. R. McKee, Z. Yan, W. M. Solomon, K. H. Burrell, C. T. Holcomb, E. J. Doyle, J. C. DeBoo, M. E. Austin, J. S. deGrassie, and C. C. Petty. Reduced electron thermal transport in low collisionality h-mode plasmas in DIII-D and the importance of TEM/ETG-scale turbulence. *Nuclear Fusion*, 52(2) :023003, 2012.

[70] U. Stroth, A. Banon Navarro, G. D. Conway, T. Goerler, T. Happel, P. Hennequin, C. Lechte, P. Manz, P. Simon, A. Biancalani, E. Blanco, C. Bottereau, F. Clairet, S. Coda, T. Eibert, T. Estrada, A. Fasoli, L. Guimarais, Ö. Gürcan, Z. Huang, F. Jenko, W. Kasparek, C. Koenen, A. Krämer-Flecken, M.E. Manso, A. Medvedeva, D. Molina, V. Nikolaeva, B. Plaum, L. Porte, D. Prisiazhniuk, T. Ribeiro, B.D. Scott, U. Siart, A. Storelli, L. Vermare, and S. Wolf. Experimental turbulence studies for gyro-kinetic code validation using advanced microwave diagnostics. *Nuclear Fusion*, 55(8) :083027, 2015.

[71] J. C. Hillesheim, N. A. Crocker, W. A. Peebles, H. Meyer, A. Meakins, A. R. Field, D. Dunai, M. Carr, N. Hawkes, and the MAST Team. Doppler backscattering for spherical tokamaks and measurement of high-k density fluctuation wavenumber spectrum in MAST. *Nuclear Fusion*, 55(7) :073024, 2015.

[72] A. D. Gurchenko, E. Z. Gusakov, D. V. Kouprienko, S. Leerink, A. B. Altukhov, J. A. Heikkinen, S. I. Lashkul, L. A. Esipov, and A. Yu Stepanov. Observation of turbulence exponential wave number spectra at ion sub-Larmor scales in FT-2 tokamak. *Plasma Physics and Controlled Fusion*, 52(3) :035010, 2010.

[73] T. Happel, T. Estrada, E. Blanco, C. Hidalgo, G. D. Conway, U. Stroth, and TJ-II Team. Scale-selective turbulence reduction in h-mode plasmas in the TJ-II stellarator. *Physics of Plasmas*, 18(10) :102302, 2011.

[74] C. Lechte, G. D. Conway, T. Goerler, C. Troester-Schmid, and the ASDEX Upgrade Team. X-mode Doppler reflectometry k-spectral measurements in ASDEX Upgrade : experiments and simulations. *Plasma Physics and Controlled Fusion*, 59(7) :075006, 2017.

[75] T. Happel, T. Goerler, P. Hennequin, C. Lechte, M. Bernert, G. D. Conway, S. J. Freethy, C. Honore, J. R. Pinzon, U. Stroth, and The ASDEX Upgrade Team. Comparison of detailed experimental wavenumber spectra with gyrokinetic simulation aided by two-dimensional full-wave simulations. *Plasma Physics and Controlled Fusion*, 59(5) :054009, 2017.

[76] E. Z. Gusakov and A. Yu Popov. Two-dimensional non-linear theory of radial correlation reflectometry. *Plasma Physics and Controlled Fusion*, 46(9) :1393, 2004.

[77] P. H. Diamond, S.-I. Itoh, K. Itoh, and T. S. Hahm. Zonal flows in plasma - a review. *Plasma Physics and Controlled Fusion*, 47(5) :R35–R161, 2005.

[78] T. S. Hahm, M. A. Beer, Z. Lin, G. W. Hammett, W. W. Lee, and W. M. Tang. Shearing rate of time dependent E×B flow. *Physics of Plasmas*, 6(3) :922–926, 1999.

[79] K. Itoh, K. Hallatschek, and S-I. Itoh. Excitation of geodesic acoustic mode in toroidal plasmas. *Plasma Physics and Controlled Fusion*, 47(3) :451, 2005.

[80] R. E. Waltz and C. Holland. Numerical experiments on the drift wave zonal flow paradigm for nonlinear saturation. *Physics of Plasmas*, 15(12) :122503, 2008.

[81] G. D. Conway, C. Angioni, F. Ryter, P. Sauter, and J. Vicente. Mean and oscillating plasma flows and turbulence interactions across the L-H confinement transition. *Phys. Rev. Lett.*, 106 :065001, Feb 2011.

[82] N. Winsor, J. L. Johnson, and J. M. Dawson. Geodesic Acoustic Waves in Hydromagnetic Systems. *Physics of Fluids*, 11(11) :2448–2450, 1968.

[83] P. Angelino, X. Garbet, L. Villard, A. Bottino, S. Jolliet, Ph. Ghendrih, V. Grandgirard, B. F. McMillan, Y. Sarazin, G. Dif-Pradalier, and T. M. Tran. The role of plasma elongation on the linear damping of zonal flows. *Physics of Plasmas*, 15(6) :062306, 2008.

[84] V. B. Lebedev, P. N. Yushmanov, P. H. Diamond, S. V. Novakovskii, and A. I. Smolyakov. Plateau regime dynamics of the relaxation of poloidal rotation in tokamak plasmas. *Physics of Plasmas*, 3(8) :3023–3031, 1996.

[85] T. Watari, Y. Hamada, A. Fujisawa, K. Toi, and K. Itoh. Extension of geodesic acoustic mode theory to helical systems. *Physics of Plasmas*, 12(6) :062304, 2005.

[86] H Sugama and T H Watanabe. Collisionless damping of geodesic acoustic modes. *Phys. Plasmas*, 72(Part 6) :825–828, 2006.

[87] A. Fujisawa, T. Ido, A. Shimizu, S. Okamura, K. Matsuoka, H. Iguchi, Y. Hamada, H. Nakano, S. Ohshima, K. Itoh, K. Hoshino, K. Shinohara, Y. Miura, Y. Nagashima, S.-I. Itoh, M. Shats, H. Xia, J. Q. Dong, L.W. Yan, K. J. Zhao, G. D. Conway, U. Stroth, A. V. Melnikov, L.G. Eliseev, S.E. Lysenko, S. V. Perfilov, C. Hidalgo, G. R. Tynan, C. Holland, P. H. Diamond, G. R. McKee, R. J. Fonck, D. K. Gupta, and P. M. Schoch. Experimental progress on zonal flow physics in toroidal plasmas. *Nuclear Fusion*, 47(10) :S718, 2007.

[88] K. J. Zhao, T. Lan, J. Q. Dong, L. W. Yan, W. Y. Hong, C. X. Yu, A. D. Liu, J. Qian, J. Cheng, D. L. Yu, Q. W. Yang, X. T. Ding, Y. Liu, and C. H. Pan. Toroidal Symmetry of the Geodesic Acoustic Mode Zonal Flow in a Tokamak Plasma. *Phys. Rev. Lett.*, 96 :255004, Jun 2006.

[89] L. W. Yan, J. Cheng, W. Y. Hong, K. J. Zhao, T. Lan, J. Q. Dong, A. D. Liu, C. X. Yu, D. L. Yu, J. Qian, Y. Huang, Q. W. Yang, X. T. Ding, Y. Liu, and C. H. Pan. Three-dimensional features of GAM zonal flows in the HL-2A tokamak. *Nuclear Fusion*, 47(12) :1673, 2007.

[90] K. J. Zhao, J. Q. Dong, L. W. Yan, W. Y. Hong, T. Lan, A. D. Liu, J. Qian, J. Cheng, D. L. Yu, Y. Huang, H. D. He, Yi. Liu, Q. W. Yang, X. R. Duan, X. M. Song, X. T. Ding, and Y. Liu. Characteristics of geodesic acoustic mode zonal flow and ambient turbulence at the edge of the HL-2A tokamak plasmas. *Physics of Plasmas*, 14(12) :122301, 2007.

[91] T. Lan, A. D. Liu, C. X. Yu, L. W. Yan, W. Y. Hong, K. J. Zhao, J. Q. Dong, J. Qian, J. Cheng, D. L. Yu, and Q. W. Yang. Spectral characteristics of geodesic acoustic mode in the HL-2A tokamak. *Plasma Physics and Controlled Fusion*, 50(4) :045002, 2008.

[92] M. G. Shats and W. M. Solomon. Experimental evidence of self-regulation of fluctuations by time-varying flows. *Phys. Rev. Lett.*, 88 :045001, Jan 2002.

[93] M G Shats, H Xia, and M Yokoyama. Mean $E \times B$ flows and GAM-like oscillations in the H-1 heliac. *Plasma Physics and Controlled Fusion*, 48(4) :S17, 2006.

[94] G. D. Conway, B. Scott, J. Schirmer, M. Reich, A. Kendl, and the ASDEX Upgrade Team. Direct measurement of zonal flows and geodesic acoustic mode oscillations in ASDEX Upgrade using Doppler reflectometry. *Plasma Phys. Control. Fusion*, 47(8) :1165, 2005.

[95] L. Schmitz, G. Wang, J. C. Hillesheim, T. L. Rhodes, W. A. Peebles, A.E. White, L. Zeng, T. A. Carter, and W. Solomon. Detection of zonal flow spectra in DIII-D by dual-channel Doppler backscattering system. *Rev. Sci. Inst.*, 79(10F113), 2008.

[96] J. C. Hillesheim, W. A. Peebles, T. A. Carter, L. Schmitz, and T. L. Rhodes. Experimental investigation of geodesic acoustic mode spatial structure, intermittency, and interaction with turbulence in the DIII-D tokamak. *Physics of Plasmas*, 19(2) :022301, 2012.

[97] A. D. Gurchenko, E. Z. Gusakov, A. B. Altukhov, E. P. Selyunin, L. A. Esipov, M. Yu Kantor, D. V. Kouprienko, S. Lashkul, A. Yu Stepanov, and F. Wagner. Spatial structure of the geodesic acoustic mode in the FT-2 tokamak by upper hybrid resonance Doppler backscattering. *Plasma Physics and Controlled Fusion*, 55(8) :085017, 2013.

[98] A. Fujisawa. A review of zonal flow experiments. *Nuclear Fusion*, 49(1) :013001, 2009.

[99] G D Conway, C Tröster, B Scott, K Hallatschek, and the ASDEX Upgrade Team. Frequency scaling and localization of geodesic acoustic modes in ASDEX Upgrade. *Plasma Physics and Controlled Fusion*, 50(5) :055009, 2008.

[100] A. Krämer-Flecken, S. Soldatov, D. Reiser, M. Kantor, and H. R. Koslowski. Investigation of geodesic acoustic modes and related zonal flows at TEXTOR. *Plasma Physics and Controlled Fusion*, 51(1) :015001, 2009.

[101] T. Ido, Y. Miura, K. Kamiya, Y. Hamada, K. Hoshino, A. Fujisawa, K. Itoh, S.-I. Itoh, A. Nishizawa, H. Ogawa, Y. Kusama, and JFT-2M group. Geodesic acoustic mode in JFT-2M tokamak plasmas. *Plasma Physics and Controlled Fusion*, 48(4) :S41, 2006.

[102] C. A. de Meijere, S. Coda, Z. Huang, L. Vermare, T. Vernay, V. Vuille, S. Brunner, J. Dominski, P. Hennequin, A. Krämer-Flecken, G. Merlo, L. Porte, and L. Villard. Complete multi-field characterization of the geodesic acoustic mode in the TCV tokamak. *Plasma Physics and Controlled Fusion*, 56(7) :072001, 2014.

[103] G. Merlo. *Flux-tube and global grid-based gyrokinetic simulations of plasma microturbulence and comparisons with experimental TCV measurements*. PhD Thesis. 2016.

[104] Z. Gao, K. Itoh, H. Sanuki, and J. Q. Dong. Eigenmode analysis of geodesic acoustic modes. *Physics of Plasmas*, 15(7) :072511, 2008.

[105] F. Zonca and L. Chen. Radial structures and nonlinear excitation of geodesic acoustic modes. *EPL (Europhysics Letters)*, 83(3) :35001, 2008.

[106] F. Clairet. Fast sweeping reflectometry upgrade on Tore Supra. *Review of Scientific Instruments*, 81 :10D903, 2010.

[107] R. Sabot, A. Sirinelli, J.-M. Chareau, and J.-C. Giacalone. A dual source D-band reflectometer for density profile and fluctuations measurements in Tore-Supra. *Nuclear Fusion*, 46(9) :S685, 2006.

[108] M. Jakubowski, R. J. Fonck, and G. R. McKee. Observation of coherent sheared turbulence flows in the DIII-D tokamak. *Phys. Rev. Lett.*, 89 :265003, Dec 2002.

[109] Y. Hamada, A. Nishizawa, T. Ido, T. Watari, M. Kojima, Y. Kawasumi, K. Narihara, K. Toi, and JIPPT-IIU Group. Zonal flows in the geodesic acoustic mode frequency range in the JIPP T-IIU tokamak plasmas. *Nuclear Fusion*, 45(2) :81, 2005.

[110] G. R. McKee, D. K. Gupta, R. J. Fonck, D. J. Schlossberg, M. W. Shafer, and P. Gohil. Structure and scaling properties of the geodesic acoustic mode. *Plasma Phys. Control. Fusion*, 48(4) :S123, 2006.

[111] L. Vermare, S. Heuraux, F. Clairet, G. Leclert, and F. da Silva. Density fluctuation measurements using X-mode fast sweep reflectometry on Tore Supra. *Nuclear Fusion*, 46(9) :S743–S759, 2006.

[112] L Vermare, P Hennequin, Ö. D. Gürcan, C Bourdelle, F Clairet, X. Garbet, and R. Sabot. Impact of collisionality on fluctuation characteristics of micro-turbulence. *Phys. Plasmas*, 18(1) :012306, 2011.

[113] R. O. Schmidt. Multiple emitter location and signal parameter estimation. *IEEE Transactions on Antennas and Propagation*, AP-34(3) :276–280, 1986.

[114] V. Grandgirard, Y. Sarazin, P. Angelino, A. Bottino, N. Crouseilles, G. Darmet, G. Dif-Pradalier, X. Garbet, Ph. Ghendrih, S. Jolliet, G. Latu, E. Sonnendr¨ucker, and L. Villard. Global full- f gyrokinetic simulations of plasma turbulence. *Plasma Physics and Controlled Fusion*, 49(12B) :B173, 2007.

[115] A. Storelli. *Etude du transport turbulent dans les plasmas du tokamak Tore Supra : observation des écoulement perpendiculaires stationnaires et du mode acoustique géodésique*. PhD Thesis. 2015.

[116] A. Storelli, L. Vermare, P. Hennequin, Ö. D. Gürcan, G. Dif-Pradalier, Y. Sarazin, X. Garbet, T. Görler, Rameswar Singh, P. Morel, V. Grandgirard, P. Ghendrih, and Tore Supra team. Comprehensive comparisons of geodesic acoustic mode characteristics and dynamics between Tore Supra experiments and gyrokinetic simulations. *Physics of Plasmas*, 22(6), 2015.

[117] S.P. Hirshman and D.J. Sigmar. Neoclassical transport of impurities in tokamak plasmas. *Nuclear Fusion*, 21(9) :1079, 1981.

[118] Y. B. Kim, P. H. Diamond, and R. R. Groebner. Neoclassical poloidal and toroidal rotation in tokamaks. *Physics of Fluids B : Plasma Physics*, 3(8) :2050, 1991.

[119] Thomas H. Stix. Decay of poloidal rotation in a tokamak plasma. *The Physics of Fluids*, 16(8) :1260–1267, 1973.

[120] Ö. D. Gürcan, P. H. Diamond, T. S. Hahm, and R. Singh. Intrinsic rotation and electric field shear. *Phys. Plasmas*, 14(4) :042306, 2007.

[121] A. G. Peeters, C. Angioni, and D. Strintzi. Toroidal momentum pinch velocity due to the coriolis drift effect on small scale instabilities in a toroidal plasma. *Phys. Rev. Lett.*, 98 :265003, Jun 2007.

[122] T. S. Hahm, P. H. Diamond, O. D. Gurcan, and G. Rewoldt. Nonlinear gyrokinetic theory of toroidal momentum pinch. *Physics of Plasmas*, 14(7) :072302, 2007.

[123] C. J. McDevitt and P. H. Diamond. Transport of parallel momentum by drift-alfvÃ©n turbulence. *Physics of Plasmas*, 16(1) :012301, 2009.

[124] Y. Camenen, A. G. Peeters, C. Angioni, F. J. Casson, W. A. Hornsby, A. P. Snodin, and D. Strintzi. Transport of parallel momentum induced by current-symmetry breaking in toroidal plasmas. *Phys. Rev. Lett.*, 102 :125001, Mar 2009.

[125] Ö. D. Gürcan, P. H. Diamond, P. Hennequin, C. J. McDevitt, X. Garbet, and C. Bourdelle. Residual parallel reynolds stress due to turbulence intensity gradient in tokamak plasmas. *Physics of Plasmas*, 17(11) :112309, 2010.

[126] M. Hirsch, E. Holzhauer, J. Baldzuhn, B. Kurzan, and B. Scott. Doppler reflectometry for the investigation of propagating density perturbations. *Plasma Physics and Controlled Fusion*, 43(12) :1641, 2001.

[127] E. Trier. *Champ électrique radial dans les plasmas de tokamak non axi-symétrique : étude par réflectométrie Doppler*. PhD Thesis. 2010.

[128] K. C. Shaing. Stability of the radial electric field in a nonaxisymmetric torus. *The Physics of Fluids*, 27(7) :1567–1569, 1984.

[129] P. H. Rutherford. Collisional diffusion in an axisymmetric torus. *The Physics of Fluids*, 13(2) :482–489, 1970.

[130] A. H. Boozer. Enhanced transport in tokamaks due to toroidal ripple. *The Physics of Fluids*, 23(11) :2283–2290, 1980.

[131] E. Trier, L. G. Eriksson, P. Hennequin, C. Fenzi, C. Bourdelle, G. Falchetto, X. Garbet, T. Aniel, F. Clairet, and R. Sabot. Radial electric field measurement in a tokamak with magnetic field ripple. *Nuclear Fusion*, 48(9), 2008.

[132] J. W. Connor and R. J. Hastie. Neoclassical diffusion arising from magnetic-field ripples in tokamaks. *Nuclear Fusion*, 13 :221–225, 1973.

[133] G.D. Conway, C. Angioni, R. Dux, F. Ryter, A.G. Peeters, J. Schirmer, C. Troester, CFN Reflectometry Group, and the ASDEX Upgrade team. Observations on core turbulence transitions in ASDEX Upgrade using Doppler reflectometry. *Nuclear Fusion*, 46(9) :S799, 2006.

[134] L. Vermare, P. Hennequin, Ö.D. Gürcan, X. Garbet, C. Honore, F. Clairet, J. C. Giacalone, P. Morel, A. Storelli, and the Tore Supra team. Poloidal asymmetries of flows in the Tore Supra tokamak. *Physics of Plasmas*, 25(2) :020704, 2018.

[135] L.L. Lao, H. St. John, R.D. Stambaugh, A.G. Kellman, and W. Pfeiffer. Reconstruction of current profile parameters and plasma shapes in tokamaks. *Nuclear Fusion*, 25(11) :1611, 1985.

[136] N. Fedorczak, P. Manz, S. Chakraborty Thakur, M. Xu, and G. R. Tynan. Zonal flow shear amplification by depletion of anisotropic potential eddies in a magnetized plasma : idealized models and laboratory experiment. *Plasma Physics and Controlled Fusion*, 55(2) :025011, 2013.

[137] X. Garbet, Y. Asahi, P. Donnel, C. Ehrlacher, G. Dif-Pradalier, P. Ghendrih, V. Grandgirard, and Y. Sarazin. Impact of poloidal convective cells on momentum flux in tokamaks. *New Journal of Physics*, 19(1) :015011, 2017.

[138] P. Hennequin, L. Vermare, N. Fedorczak, J. Bernardo, Ö. D. Gürcan, É. Trier, N. Stuyck, C. Fenzi, J.P. Gunn, P. Monier-Garbet, et al. The effect of SOL flows on edge and core radial electric field and rotation in Tore Supra. 34A, P1.1040, 2010.

[139] N. Asakura. Understanding the SOL flow in L-mode plasma on divertor tokamaks, and its influence on the plasma transport. *Journal of Nuclear Materials*, 363 :41 – 51, 2007.

[140] A. Krämer-Flecken, Y. Xu, S. Zoletnik, and the TEXTOR team. Poloidal rotation asymmetry and relation to turbulence. In *39th EPS Conference & 16th Int. Congress on Plasma Physics*, volume 36F, P5.044, 2012.

[141] S. Soldatov, A. Krämer-Flecken, G. Van Wassenhove, M. de Bock, and TEXTOR-Team. The poloidal asymmetry in perpendicular plasma rotation and radial electric field measured with correlation reflectometry at TEXTOR. In *34th EPS Conference on Plasma Phys. Warsaw*, volume 31F, P2.059, Warsaw, July 2007.

[142] A. Truc, A. Quemeneur, P. Hennequin, et al. ALTAIR - an infrared-laser scattering diagnostic on the tore-supra tokamak. *Rev. Sci. Inst.*, 63(7) :3716–3724, 1992.

[143] C.M. Surko and R.E. Slusher. Study of the Density Fluctuations in the Adiabatic Toroidal Compressor Scattering Tokamak Using CO_2 Laser. *Physical Review Letters*, 37(26) :1747, 1976.

[144] C. Honoré, P. Hennequin, A. Truc, and A. Quemeneur. Quasi-optical gaussian beam tracing to evaluate doppler backscattering conditions. *Nuclear Fusion*, 46(9) :S809–S815, 2006.

[145] R. Sabot, F. Clairet, C. Honoré, C. Bottereau, J.-M. Chareau, F. Gabillet, P. Hennequin, S. Heuraux, G. Leclert, A. Sirinelli, A. Truc, and L. Vermare. Advances of reflectometry on tore-supra : From edge density profile to core density fluctuations. *International Journal of Infrared and Millimeter Waves*, 25(2) :229–246, Feb 2004.

[146] J.-M. Chareau F. Clairet R. Sabot, C. Bottereau and M. Paume. Single sideband modulator, a key component of tore-supra heterodyne reflectometers. *Rev. Sci. Inst.*, 75(8) :2656, 2004.

[147] E. Holzhauer and J.H. Massig. An analysis of optical mixing in plasma scattering experiments. *Plasma Physics*, 20(9) :867–877, 1978.

[148] M. Hirsch and E. Holzhauer. Doppler reflectometry with optimized temporal resolution for the measurement of turbulence and its propagation velocity. *Plasma Phys. Control. Fusion*, 46(4) :593, 2004.

[149] V. Bulanin and M. Efanov. Spatial and spectral resolution of the plasma doppler reflectometry. *Plasma Physics Reports*, 32(1) :47, 2006.

[150] P Devynck, X Garbet, C Laviron, J Payan, S K Saha, F Gervais, P Hennequin, A Quemeneur, and A Truc. Localized measurements of turbulence in the Tore Supra tokamak. *Plasma Physics and Controlled Fusion*, 35(1) :63, 1993.

[151] V. Bulanin. *Simulation of microwave scattering in Doppler reflectometry experiment*, volume 26B of *29th EPS Conf. Plasma Phys.* 2002.

[152] V. Bulanin, A. Petrov, and M. Yefanov. Broadening of Scattering Spectra in Reflectometry Experiment. *Proceedings, 30th EPS Conference on Plasma Physics, St Petersburg, ECA*, 27J :P2.55, 2003.

[153] E. Blanco, T. Estrada, and J. Sánchez. Doppler reflectometry studies using a two-dimensional full-wave code. *Plasma Physics and Controlled Fusion*, 48(5) :699, 2006.

[154] E. Z. Gusakov. *Two dimensional theory of fluctuation reflectometry diagnostics*, volume 25A of *28th EPS Conf. Plasma Phys.* 2001.

[155] L. G. Bruskin, A. Mase, N. Oyama, and Y. Miura. Fluctuation reflectometry of azimuthally symmetric plasmas. *Plasma Physics and Controlled Fusion*, 44(11) :2305, 2002.

[156] E. Z. Gusakov and A. V. Surkov. Spatial and wavenumber resolution of doppler reflectometry. *Plasma Physics and Controlled Fusion*, 46(7) :1143, 2004.

[157] F. Clairet, C. Bottereau, J.M. Chareau, and R. Sabot. Advances of the density profile reflectometry on TORE SUPRA. *Rev. Sci. Inst.*, 74 :1481, 2003.

[158] M Hirsch, E Holzhauer, J Baldzuhn, and B Kurzan. Doppler reflectometry for the investigation of propagating density perturbations. *Rev. of Sci. Instrum.*, 72(1, Part 2) :324–327, 2001.

[159] P. Hennequin et al. Analysis of density fluctuation frequency spectra in Tore Supra as a tool studying plasma motion and transport properties. In *Proceed. 26th EPS Conf. Control. Fusion Plasma Phys., Maastricht*, volume 23, page 977, 1999.

[160] J.O. Hinze. *Turbulence :*. McGraw-Hill classic textbook reissue series. McGraw-Hill, 1975.

[161] M. Kaveh and A. Barabell. The statistical performance of the MUSIC and the minimum-norm algorithms in resolving plane waves in noise. *Acoustics, Speech and Signal Processing, IEEE Transactions on*, 34(2) :331 – 341, apr 1986.

[162] A.L. Swindlehurst and T. Kailath. A performance analysis of subspace-based methods in the presence of model errors. I. The MUSIC algorithm. *Signal Processing, IEEE Transactions on*, 40(7) :1758 –1774, jul 1992.

[163] B. Porat and B. Friedlander. Analysis of the asymptotic relative efficiency of the music algorithm. *Acoustics, Speech and Signal Processing, IEEE Transactions on*, 36(4) :532 –544, apr 1988.

[164] F da Silva, S Heuraux, N Lemoine, C Honoré, P Hennequin, M Manso, and R Sabot. Global full-wave simulation of the Tore-Supra doppler reflectometer. *Rev. Sci. Inst.*, 75(10, Part 2) :3816–3818, 2004. 15th Topical Conference on High-Temperature Plasma Diagnostics, San Diego, CA, APR 19-22, 2004.

[165] Carsten Lechte. Investigation of the Scattering Efficiency in Doppler Reflectometry by Two-Dimensional Full-Wave Simulations. *IEEE Transactions on Plasma Sciences*, 37(6, Part 2) :1099–1103, JUN 2009.